**ENHANCEMENT OF THE POWER CONVERSION EFFICIENCY OF ORGANIC SOLAR CELLS BY SURFACE PATTERNING OF AZOBENZENE THIN FILMS**


**AMÉLIORATION DE L'EFFICACITÉ DE CONVERSION D'ÉNERGIE DES CELLULES SOLAIRES ORGANIQUES PAR LA STRUCTURATION EN SURFACE DE COUCHES MINCES D'AZOBENZÈNE**


A Thesis Submitted to the Division of Graduate Studies
Of the Royal Military College of Canada
by

**Geneviève Ginette Thérèse Tadeson, CD**
**Captain**

In Partial Fulfillment of the Requirements for the Degree of
Master of Science


April 2019

This work is dedicated to my grandmother, Ginette Fauquet, for her gift of a constant quest for knowledge mixed with a hint of stubbornness. Mamie, merci d'être la plus belle corbeille de fruits.

**ABSTRACT**

  In order for organic solar cells to take their place in the energy market and be a serious alternative to fossil fuels, their photon-to-electron power conversion efficiency must be improved. Efficiency enhancements of organic solar cells can potentially be achieved by increasing the amount of light absorbed by the active layer. Two solutions for increasing the light absorption in organic solar cells were explored in this thesis. The first solution consisted in using surface relief gratings on a Disperse Red 1 functionalized glass-forming azobenzene compound to couple the light by surface plasmon resonance in inverted organic solar cells. Technical difficulties in the fabrication of inverted solar cells prevented further research in this area. The second method used to increase the light absorption consisted in integrating patterned azobenzene thin films in organic solar cells to scatter the light, thus increasing the optical path of the light inside the active area. Azobenzene thin films were patterned with randomized nanostructures fabricated by corona poling or with crossed gratings inscribed via laser interference lithography. The patterned films were then bleached (or made transparent) and thermally stabilized by an ultraviolet exposure before being incorporated in P3HT:PC$_{61}$BM and PTB7:PC$_{61}$BM solar cells. The large size of the nanostructures created by corona poling caused a disadvantageous forward to total scattering ratio, resulting in a reduction of the solar cells' efficiencies. However, the solar cells with the azobenzene thin films patterned by crossed gratings showed significant efficiency enhancements. Best results were achieved with root-mean-square roughness, $R_q$, and maximum roughness, $R_{qmax}$, of the azobenzene thin films of $R_q/R_{qmax} =$ 3.9 /41 nm and $R_q/R_{qmax} =$ 3.6/52 nm for P3HT:PC$_{61}$BM and PTB7:PC$_{61}$BM solar cells, respectively. The patterned azobenzene thin films resulted in marked increases in short-circuit current density and photon-to-electron conversion efficiency. Efficiency enhancements of 133%, from 1.37% to 3.19%, were observed for P3HT:PC$_{61}$BM solar cells, while efficiency enhancements of 302%, from 0.53% to 2.13%, were observed for PTB7:PC$_{61}$BM solar cells.

# RÉSUMÉ

Pour que les cellules solaires organiques prennent leur place sur le marché de l'énergie et constituent une alternative sérieuse aux combustibles fossiles, leur efficacité de conversion de l'énergie lumineuse à électrique doit être améliorée. Il est potentiellement possible d'améliorer l'efficacité des cellules solaires organiques en augmentant la quantité de lumière absorbée par la couche active. Deux solutions pour augmenter l'absorption de la lumière dans les cellules solaires organiques ont été explorées dans cette thèse. La première solution consistait à utiliser des réseaux de diffraction sur un composé d'azobenzène de verre moléculaire Disperse Red 1 pour coupler la lumière par résonance de plasmon de surface dans des cellules solaires organiques inversées. Des difficultés techniques dans la fabrication de ces cellules solaires inversées ont empêché la poursuite des recherches dans ce domaine. La deuxième méthode utilisée pour augmenter l'absorption de la lumière consistait à intégrer des minces couches nano-structurées d'azobenzène dans des cellules solaires organiques afin de disperser la lumière, augmentant ainsi le parcours optique de la lumière dans la couche active. Des couches minces d'azobenzène ont été structurées avec des nanostructures aléatoires fabriquées par effet corona ou avec des réseaux de diffraction croisés inscrits via une lithographie d'interférence au laser. Les films structurés ont ensuite été décolorés et stabilisés thermiquement par une exposition aux rayons ultraviolets avant d'être incorporés dans des cellules solaires P3HT:PC$_{61}$BM et PTB7:PC$_{61}$BM. Les grandes tailles des nanostructures créées par l'effet corona ont entraîné un rapport défavorable de diffusion direct par rapport à la diffusion totale, ce qui a entraîné une réduction de l'efficacité des cellules solaires. Cependant, les cellules solaires avec les couches minces d'azobenzène structurées par des réseaux croisés ont montré des améliorations d'efficacité significatives. Les meilleurs résultats ont été obtenus avec une rugosité quadratique moyenne, $R_q$, et une rugosité maximale, $R_{qmax}$, des couches minces d'azobenzène de $R_q/R_{qmax} = 3,9/41$ nm et $R_q/R_{qmax} = 3,6/52$ nm pour les cellules solaires P3HT:PC$_{61}$BM et PTB7:PC$_{61}$BM, respectivement. Les couches minces d'azobenzène structurées ont entraîné une augmentation marquée de la densité de courant de court-circuit et de l'efficacité de conversion des photons en électrons. Une augmentation de l'efficacité de 133%, de 1,37% à 3,19%, a été observée pour les cellules solaires P3HT:PC$_{61}$BM, tandis qu'une augmentation de l'efficacité de 302%, de 0,53% à 2,13%, a été observée pour les cellules solaires PTB7: PC$_{61}$BM.

# CONTENTS

| | |
|---|---|
| AFM | atomic force microscope |
| Ag | Silver |
| Al | Aluminium |
| AM | Air Mass |
| a-Si | amorphous silicon |
| BCP | Bathocuproine |
| Ca | Calcium |
| CB | Chlorobenzene |
| CCD | charged coupled device |
| CdTe | cadmium telluride |
| $CO_2$ | carbon dioxide |
| $Cs_2CO_3$ | cesium carbonate |
| DCM | Dichloromethane |
| DIO | 1,8-diiodooctane |
| DMSO | Dimethyl sulfoxide |
| DR1 | Disperse Red 1 |
| EG | ethylene glycol |
| EM | electro-magnetic |
| EPBT | energy payback time |
| *et al.* | *et alia* (and others) |
| ETL | electron-transport layer |
| FF | fill factor |
| GaAs | gallium arsenide |
| gDR1 | Disperse Red 1 Molecular Glass |
| $H_2SO_4$ | sulfuric acid |
| HCl | hydrochloric acid |
| $HNO_3$ | nitric acid |
| HOMO | Highest Occupied Molecular Orbital |
| HTL | hole-transport layer |
| IPCE | Internal Photon to Current Efficiency |
| ITO | indium-tin-oxide |
| LED | light-emitting diode |
| LiF | lithium fluoride |
| LSPR | localized surface plasmon resonance |
| LUMO | Lowest Unoccupied Molecular Orbital |
| MDMO-PPV | poly[2-methoxy-5-(3,7-dimethylocxylogy)-1,4-phenylenevinylene] |
| $MoO_3$ | molybdenum trioxide |
| N | Nitrogen |
| $N_2$ | Dinitrogen |
| NP | Nanoparticle |
| o-DCB | 1,2-dichlorobenzene |
| OLED | organic light-emitted diode |
| P3HT | poly(3-hexylthiophene) |
| PBDTT-C-T | poly[4,8-bis-(2-ethylhexyloxy)-benzo(1,2-b:4,5-b')dithiophene)-2,6-diyl-alt-(4-(2-ethylhexanoyl)-thieno[3,4-b]thiophene-)-2-6-diyl)] |
| $PC_{61}BM$ | [6,6]-phenyl-C61-butyric acid methyl ester |
| $PC_{71}BM$ | [6,6]-phenyl-C71-butyric acid methyl ester |

| | |
|---|---|
| PCE | power conversion energy |
| PDMS | Polydimethylsiloxane |
| PEDOT | Poly(3,4-ethylenedioxythiophene) |
| PEG | polyethylene glycol |
| PMMA | Poly(methyl methacrylate) |
| PSS | poly(styrene sulfonate) |
| PTB7 | poly({4,8-bis[(2-ethylhexyl)oxy]benzo[1,2-b:4,5-b']dithiophene-2,6-diyl}{3-fluoro-2-[(2-ethylhexyl)carbonyl]thieno[3,4-b]thiophenediyl}) |
| RMS | root mean square |
| RPM | revolutions per minute |
| Si | Silicon |
| SNOM | scanning optical microscopy |
| SP | surface plasmons |
| SPR | surface plasmon resonance |
| SRGs | surface relief gratings |
| SRH | Shockley-Read-Hall |
| STM | scanning tunneling microscope |
| t coal equiv. | ton of coal equivalent |
| t coal equiv./a | ton of coal equivalent per year |
| TIS | Total Integrated Scatter |
| TX-100 | Triton X-100 |
| USD | United States Dollars |
| UV | Ultraviolet |
| Wt | Weight |
| w/v | weight/volume |
| ZnO | zinc oxide |

**ROMAN SYMBOLS**

| | |
|---|---|
| $2D$ | two dimensions |
| $3D$ | three dimensions |
| $A$ | area |
| $\boldsymbol{B}$ | magnetic field vector |
| $c$ | the speed of light in free space, $\sim 3.00 \times 10^8$ m/s |
| $\boldsymbol{D}$ | electric displacement vector |
| $\boldsymbol{E}$ | electric field vector |
| $\boldsymbol{E_0}$ | amplitude of the electrical field vector |
| $f_e$ | probability that an electron occupies a specified energy state |
| $h$ | Planck's constant, $\sim 6.63 \times 10^{-34}$ m$^2$kg/s |
| $\boldsymbol{H}$ | magnetic field vector |
| $k$ | Boltzmann's constant, $\sim 1.38 \times 10^{-23}$ m$^2$kg/s$^2$K |
| $k$ | wavenumber |
| $\boldsymbol{k}$ | wavevector |
| $k_0$ | magnitude of the wavevector in free space |
| $k_{sp}$ | dispersion relation |
| $I$ | current |
| $I$ | irradiance (W/m$^2$) |
| $I_{max}$ | maximum current |
| $I_{sc}$ | short-circuit current |
| $J_{max}$ | maximum current density |
| $J_{mp}$ | current density at the point of maximum power |
| $J_{sc}$ | short-circuit current density |
| $l$ | length |
| $m$ | order of diffraction |
| $n$ | refractive index of a material |
| $\boldsymbol{p}$ | momentum |
| $P$ | power |
| $P_R$ | power loss per unit area |
| $P_{in}$ | maximum input energy |
| $P_{max}$ | maximum output energy |
| $\boldsymbol{r}$ | position vector |
| $R$ | laser beam ray |
| $R$ | resistance |
| $R_0$ | theoretical reflectance |
| $R_S$ | series resistance |
| $R_{SH}$ | shunt resistance |
| $R_q$ | root mean square roughness |
| $R_{qmax}$ | maximum roughness |
| $t$ | time |
| $t$ | thickness |
| $T$ | absolute temperature |
| $V$ | electrical potential |
| $V$ | voltage |

| | |
|---|---|
| $V_{mp}$ | voltage at the point of maximum power |
| $V_{oc}$ | open-circuit voltage |
| $w$ | width |

## GREEK SYMBOLS

| | |
|---|---|
| $\varepsilon$ | dielectric permittivity of a material |
| $\tilde{\varepsilon}$ | complex dielectric permittivity of a material |
| $\varepsilon_0$ | dielectric permittivity in free space, $\sim 8.85 \times 10^{-12}$ m$^3$s$^4$A$^2$/kg |
| $\varepsilon_c$ | energy level of the conduction band |
| $\varepsilon_e$ | energy level of an electron |
| $\varepsilon_f$ | Fermi level |
| $\varepsilon_G$ | band gap |
| $\varepsilon_{FC}$ | electron-associated quasi-Fermi level |
| $\varepsilon_{FV}$ | hole-associated quasi-Fermi level |
| $\varepsilon_r$ | relative dielectric permittivity of a material |
| $\varepsilon_r'$ | real portion of the relative dielectric permittivity |
| $\varepsilon_v$ | energy level of the valance shell |
| $\eta$ | efficiency |
| $\theta$ | angle |
| K | grating vector |
| $\lambda$ | wavelength |
| $\lambda_{sp}$ | surface plasmon excitation wavelength |
| $\Lambda$ | grating spacing |
| $\mu_{eh}$ | chemical potential |
| $\mu_r$ | relative magnetic permeability of a material |
| $\rho$ | resistivity of a material |
| $\sigma$ | conductivity of a material |
| $\phi$ | phase shift between two light rays |
| $\omega$ | angular frequency |
| $\omega_p$ | plasma frequency of a metal |
| $\Omega$ | Ohm |

## OPERATORS

| | |
|---|---|
| $A$ | scalar |
| $\boldsymbol{A}$ | vector |
| $\boldsymbol{A}_o$ | amplitude of vector A |
| $A_x$ | x-component of the vector A |
| $A_y$ | y-component of the vector A |
| $A_z$ | z-component of the vector A |
| $\nabla \boldsymbol{A}$ | gradient of vector A |
| $\langle \boldsymbol{A} \rangle$ | time average of vector A |
| $\overline{AB}$ | segment length from point A to B |

**ELECTRONIC SYMBOLS**

| | |
|---|---|
| ↑ (circle) | current source |
| —⊣⊢+ | DC voltage source |
| —▷⊢ | diode |
| —◇◇◇— | resistor |

# 1 INTRODUCTION

## 1.1 BACKGROUND

### 1.1.1 Global Energy Situation

Our consumption of fossil energy has been rising exponentially since the beginning of the twentieth century and it is expected to reach a peak in the next two decades[1], a point where it will then decrease as our reserves are used up. While it is possible that our reserves of fossil energy will continue to grow as a result of continued exploration, the depletion of fossil energy reserves is a lesser problem than the negative long-lasting effects resulting from its combustion. The current global consumption of fossil energy produces 2.2 x $10^{10}$ tons of carbon dioxide ($CO_2$) per year[1]. Taking into consideration a consumption growth of 1% per year, the $CO_2$ concentration in the atmosphere is expected to double within 100 years[1]. This is a major issue as $CO_2$, like all triatomic molecules, is a good absorber in the infrared region. An increase in $CO_2$ in the atmosphere would therefore lead to an increase in absorption of the solar radiation, causing in turn an increase in heat emission back to the Earth. This phenomenon is known as "Greenhouse Effect", which is associated with negative consequences to human health and the threat of global climate change[2].

Under the 2009 Copenhagen Accord, Canada has pledged to reduce its 2005 $CO_2$ emission levels by 17% by 2020[3], and under the 2015 Paris Agreement by 30% by 2030[4]. However, Environment Canada's projections tabulated in 2016[5] shown in Figure 1.1 below predicts that not only will Canada miss its committed targets, but will be 5% above its 2014 $CO_2$ emissions level by 2020 and 11% above 2014 level by 2030. This trend calls for a greater emphasis on identifying and implementing alternative sources of energy.
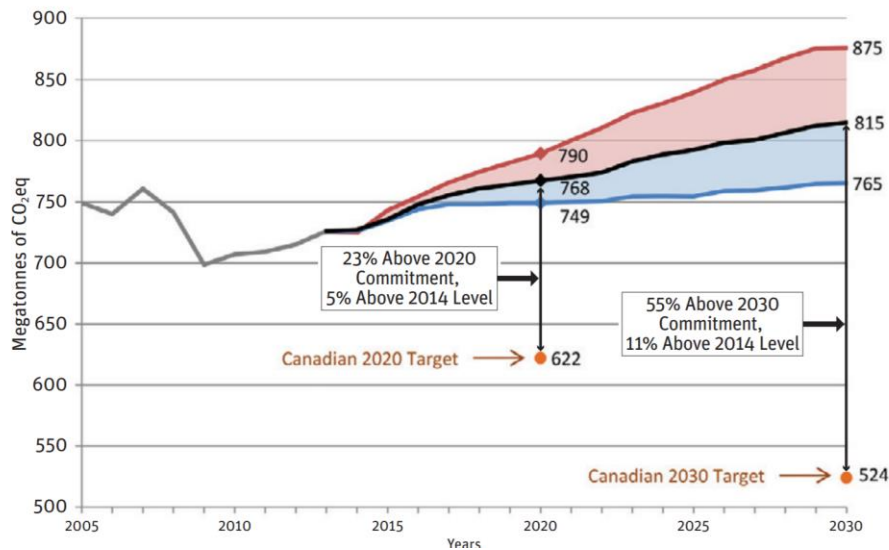


Figure 1.1. Canada's $CO_2$ emissions projections for 2020 and 2030. According to Environment Canada's projection, Canada will not only miss its committed target, but be above current emission levels. Adapted from (Hughes, 2016)[5].

As sustainable alternatives to fossil fuels, renewable energy sources such as hydropower, wind power, and solar energy are on the rise[2]. However, the negative impacts of those "green" solutions, such as impacts on the environment, wildlife and air pollution, are often overlooked. For example, hydroelectric reservoirs needed to generate hydropower can emit 48-82 teragrams ($10^{12}$ grams) of $CO_2$ per year into the atmosphere[6] – not withstanding other effects such as habitat loss, biodiversity loss, environment degradation due to access roads and power lines, etc.

Solar energy offers a potential solution in the quest of green energy. The energy of fossil fuels is often given in metric tons of coal equivalent (t coal equiv.), with 1 t coal equiv. = 8200 kilowatts-hour (kWh)[1] and the consumption of 1 t coal equiv. per year (t coal equiv./a) amounting to 0.94kW. The Sun produces an energy of 1.8 x $10^{14}$ t coal equiv./a, which is more than sufficient to meet our current global energy consumption of 13.2 x $10^9$ t coal equiv./a[1]. The increased interest in solar energy resulted in the global expansion of solar photovoltaic capacity – the capacity to transform solar energy to electrical energy – by 33% from 228 gigawatts (GW) in 2015 to 303 GW in 2016[6].

### 1.1.2 Solar Cells Evolution

Although there has been an increased interest in the scientific community in solar energy, photovoltaic technology is not new. In 1839, Edmund Becquerel observed that light incident on a silver coated electrode immersed in an electrolyte could produce an electric current[7]. In 1876, using selenium, William Adams and his student Richard Day showed for the first time that electric power could be produced by a solid under illumination[8]. Soon after, in 1883, Charles Fritts constructed the first solar cell panel by coating selenium with a thin layer of gold. This first solar cell achieved a power conversion efficiency (PCE), which is the ability to transform solar energy into electrical energy, in the order of 1-2%[8]. The first silicon solar cell, reported in 1941 by Russel Ohl, had an efficiency, based on the description of the device, estimated at 1%[7]. Major improvements in efficiencies occurred in the early 1950s with the development of crystal growth and junction diffusion techniques, and the refinement of cells and contact designs. Bell Laboratories, researching applications for remote communication stations[7], fabricated a cell with 6% efficiency in 1954, and achieved 10% efficiency within 18 months[8]. However, these early cells had a production cost of around $200USD per Watt, and therefore were not at that time serious contenders for the production of energy other than for space applications where reliability outweighed costs[9]. The next significant improvements in solar cell efficiencies occurred during the oil crisis of the 1970s with the development of shallow junctions, enhanced antireflection coatings and surface texturing[10]. A third phase began in the early 1980s with progress in surface passivation, bulk lifetimes, contact passivation and light trapping in the cell[10]. Figure 1.2 shows the history of confirmed research solar cell efficiencies.
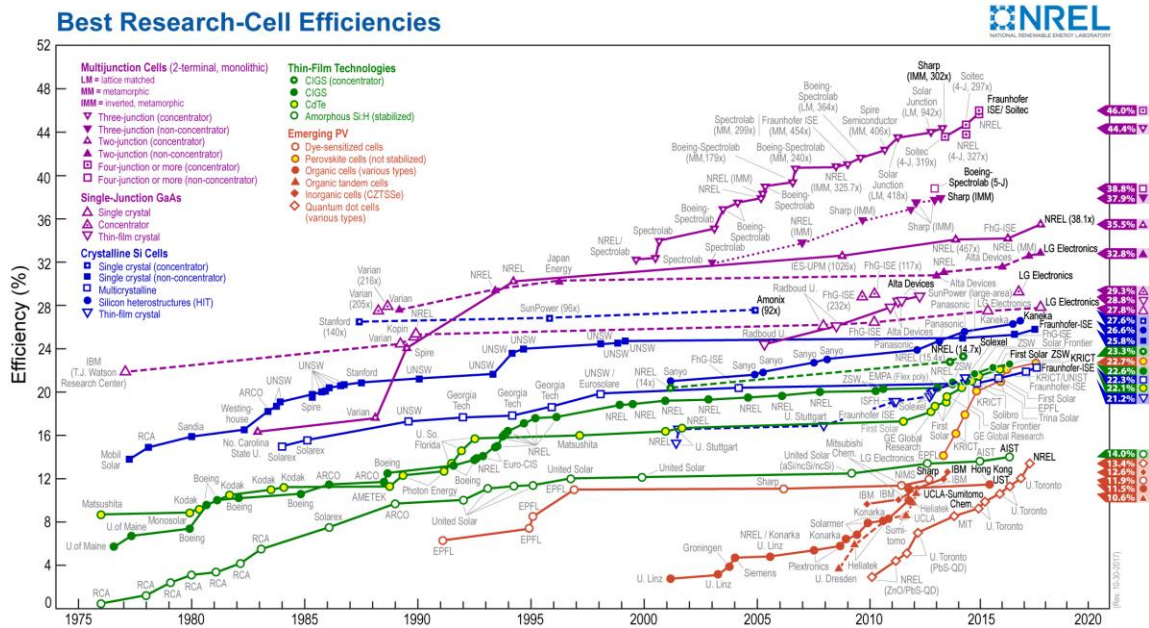
Figure 1.2. Best research solar cell efficiencies. The efficiency of conventional first-generation solar cell (in blue in the graph) has plateaued around 25%. Courtesy of the National Renewable Energy Laboratory, Golden, CO[11].

As it can be seen from the above graph, the performance of conventional, or first generation, solar cells (in blue in Figure 1.2) such as crystalline silicon cells has now reached a steady-state with only minor improvements in the last 20 years and a maximum efficiency for a single crystal silicon cell without concentrator of 25.8%. Some multi-junction and gallium arsenide cells have progressed beyond 30%, however the cost of these devices is commercially not advantageous[12]. Second generation solar cells concentrated on reducing manufacturing cost, and are mainly made of thin films of amorphous silicon (a-Si) and chalcogenides such as cadmium telluride (CdTe) [12, 13]. However, a-Si exhibits a low efficiency of 14%[11] and is almost extinct in terrestrial applications[14]. CdTe devices, with a more attractive conversion efficiency of 22.1%[11], are however unlikely to be widely commercialized due to the scarcity of tellurium and the high toxicity of cadmium[12]. Organic solar cells are considered an emerging technology and can be subdivided in three main categories: dye sensitized, small molecules and polymer solar cells[13]. In 2008, Konarka Technologies attempted to commercialized polymer-fullerene solar cells, with their initial modules reaching efficiency about 3-5%[15]. However, they were not able to penetrate the photovoltaic market and filed for bankruptcy a few years later[16]. While there is a lot of focus on improving the efficiencies of organic solar cells, they have yet to reach the point of commercialization.

### 1.1.3 Energy Payback Time

While sunlight is free, solar energy conversion to electricity is conventionally done using photovoltaic cells, a process which has some drawbacks. The environmental impact of a green

3

technology can be assessed using the energy payback time (EPBT) indicator. EPBT for a solar cell is defined as the time it takes to generate the same amount of energy as was expended during its life cycle, including manufacturing, usage and disposal[13]. Figure 1.3 presents a comparison of the EPBT of different solar cells.
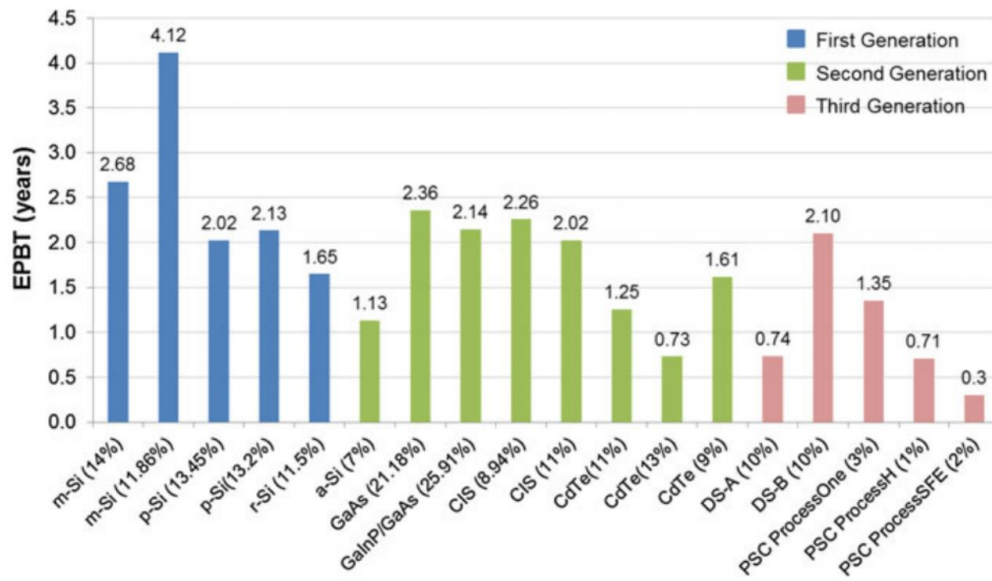


Figure 1.3. Energy payback time of selected solar cells. Within the third-generation solar cells, ProcessOne are indium-tin-oxide (ITO) based solar cells, ProcessH is ITO-free solar cells, and ProcessSFE is metal- and ITO-free solar cells. The efficiencies of the cells are indicated in brackets. Adapted from (Angmo *et al.*, 2014)[13].

The lowering of the EBPT requires either a decrease in manufacturing costs, or an increase in the efficiency of the solar cell. While inorganic solar cells have now reached efficiencies in the 25% range, a 2010 report puts their energy cost at $396.10USD per megawatt-hour (MWh) compared to $100.40USD per MWh for fossil fuel[17]. Organic solar cells, despite having low efficiencies compared to their inorganic counterparts, have the advantage of low manufacturing costs as they can be solution-processed using techniques such as ink-printing, spray coating or spin coating, all of which require relatively little equipment. Furthermore, solar cells require at least one of their electrodes to be transparent to the visible spectrum. Indium-tin-oxide (ITO) has been commonly used as an electrode in research solar cells, due to its high conductivity and transmission in the visible region of the solar spectrum. However, cost analysis reveals that the use of ITO is not compatible with low-cost production due to its scarcity and requirements for high preparation temperature and vacuum-based energy-intensive deposition techniques[13]. Therefore, if the efficiency of ITO-free organic solar cells could be further improved, they could become an attractive alternative to conventional solar cells and, ultimately, to fossil fuels. As previously mentioned, organic solar cells can be subdivided in dye-sensitized, small-molecule and polymer

solar cells. This thesis focuses on the efficiency enhancement of ITO-free polymer organic solar cells.

## 1.2   RECENT DEVELOPMENTS IN POLYMER ORGANIC SOLAR CELLS

Polymer organic solar cells, compared to their inorganic counterparts, offer many advantages such as environmental friendliness, low-cost and ease of fabrication, mechanical flexibility and versatility of chemical structure[18], but their relative low efficiency still limits their practical use. However, with recent developments, commercialization may be only a few years away. Some of these developments, such as the development of bulk-heterojunction solar cells, advances in materials, plasmonic solar cells and scattering through surface patterning, will be discussed below. Also, recent developments on the patterning of azobenzenes, a group of chemical compounds with interesting photoisomerization properties useful to write Surface Relief Gratings (SRGs), will be presented.

### 1.2.1   Bulk-Heterojunction Solar Cells

Photoconductivity in an organic material, anthracene, was first observed by Pochettino in 1906[19]. The first polymer solar cells appeared in the 1980s and consisted of a single absorbing polymer sandwiched between two electrodes. However, these simple devices had efficiencies below 0.1%[19] since, as it will be further explained in Chapter 2 of this thesis, a single organic layer could not efficiently separate the holes and electrons generated by the absorption of the photons[20] – a process essential to convert the solar energy into electrical energy. The first pioneering work on polymer solar cells was the introduction by Tang in 1986 of a second organic layer, resulting in a bilayer cell with a donor and acceptor layers that brought the efficiency to around 0.9%[19, 20]. While this bilayer structure improved the separation of charges, poor charge transport within each layer was still limiting the efficiency of the solar cells[20, 21]. In 1992, Sariciftci et al.[22] reported a conjugated polymer/fullerene bilayer solar cell. The next breakthrough came with Yu et al.'s[23] development of a bulk-heterojunction structure by mixing soluble polymers and fullerenes to create a network of electron donor and acceptor materials[18]. The morphology control of polymer: fullerene solar cells was then thoroughly studied and a solvent change from toluene to chlorobenzene lead to an efficiency improvement to 2.5%[20].

### 1.2.2   Advancement in Materials

While early solar cells used poly[2-methoxy-5-(3,7-dimethylocxylogy)-1,4-phenylenevinylene] (MDMO-PPV) as a polymer, the introduction of poly(3-hexylthiophene) (P3HT) polymers saw an efficiency increase, when used in conjunction with fullerene derivative [6,6]-phenyl-C61-butyric acid methyl ester ($PC_{61}BM$), to 4-5% due to a better absorption of visible light up to wavelengths of 650 nanometers (nm)[20]. Recently, various polymers have been developed with increasing optical range, such as poly({4,8-bis[(2-ethylhexyl)oxy]benzo[1,2-b:4,5-b']dithiophene-2,6-diyl}{3-fluoro-2-[(2-ethylhexyl)carbonyl]thieno[3,4-b]thiophenediyl}), commonly known as PTB7, which has an absorption range reaching 750 nm and was able to achieve an efficiency of 9.2% when used with the fullerene [6,6]-phenyl-C71-butyric acid methyl ester ($PC_{71}BM$)[20].

Regardless of the choice of polymer or fullerene chosen, the active material must be sandwiched between two electrodes, with one of the electrodes needing to be transparent to allow absorption of the light. ITO has been a popular choice for a transparent bottom electrode, but as discussed in section 1.1.3, it is responsible for the majority of the production costs. Extensive researches have therefore been carried out to find ITO alternatives, including nanomaterials (e.g.

carbon nanotubes, graphene, metal nanowires and metal nanogrids), metals, metal oxides and solution-processed polymers[13]. While solution-processed polymers have been used as a bottom electrode in organic solar cells since the beginning of the century, they originally suffered from low conductivity[23] and therefore were not considered effective replacements to ITO. Furthermore, there were major difficulties in using them as top electrode due to wettability issues with the electrode solution would not spread well over the active material. However, recent developments in both the conductivity[23, 24] and the wettability[25-33] issues, which will be further discussed in Chapter 2 of this thesis, are now not only making solution-processed transparent electrode an attractive alternative to ITO, but also offers the flexibility of a transparent top electrode. This flexibility is of particular interest for the design of plasmonic solar cells.

### 1.2.3 Plasmonic Organic Solar Cells

Free electrons in metals behave like a gas known as a plasma. Under the right conditions, the electrons in the plasma can collectively oscillate. The quanta associated with the collective oscillations of the free electron gas density are known as plasmons[17]. If properly engineered, metallic nanostructures can be used to enhance light absorption by localized surface plasmon resonance (LSPR) or surface plasmon resonance (SPR), phenomena predicted by Ritchie[34] and demonstrated by Powell and Swan[35]. Both LSPR and SPR can give rise to enhanced electrical near fields. The enhanced electric field, through light coupling, can improve light absorption. In LSPR, the plasmon is confined to the surface of nanoparticles, which need to be of size comparable or smaller than the wavelength of light to excite the plasmon. In SPR, under the right conditions, the light can be coupled at the interface of a structured metal/absorber layer, forming a wave of electrons propagating laterally into the cell[36]. The later is of interest to this thesis and the theory behind SPR is further explained in Chapter 2 of this thesis. Figure 1.4 illustrates the two types of plasmonic solar cells.



(a)                 (b)
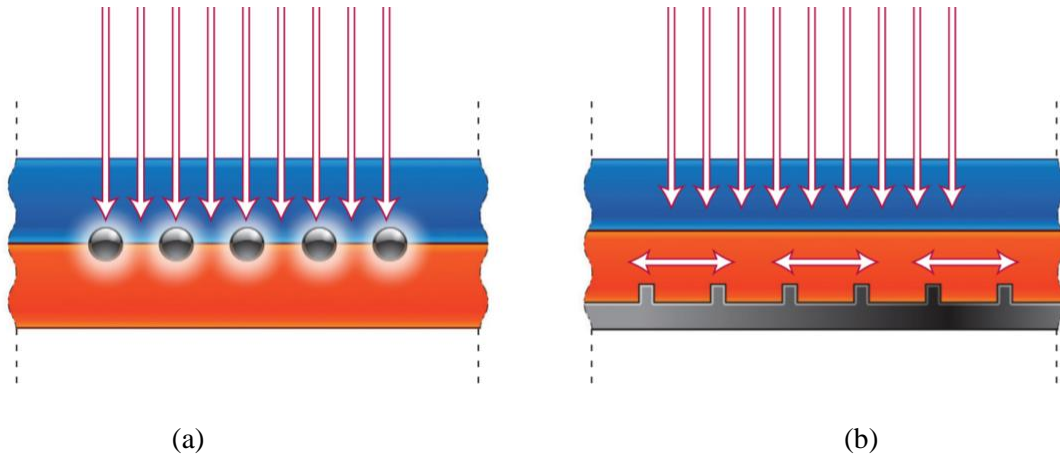
Figure 1.4. Plasmonic solar cells geometries. In (a), metallic nanoparticles act as subwavelength antennae to create a strong electric field near the nanoparticles, a phenomenon known as LSPR while in (b), the structured metal at the metal/absorber interface act as a light coupler to excite SPR, which results in an electrons wave propagating laterally in the cell. Adapted from (Atwater and Polman, 2010)[36].

Plasmons resonance have been used in several fields of study, including biosensing[37-39], imaging[40-42], integrated circuits[43, 44], and light-emitting diodes[45-47]. Several studies have also been published on the use of LSPR[42, 48, 49] to increase the efficiency of solar cells. For example, the incorporation of silver nanoparticles in amorphous silicon (a-Si) solar cells effectively improved the absorption near the optical wavelength of 625 nm, resulting in a 10.2% higher external quantum efficiency compared to a reference device[14]. In organic solar cells, enhanced efficiencies have been demonstrated for solar cells doped with silver nanoparticles[36], and an efficiency increase from 3.05% to 3.69% has been reported using electrodeposited silver nanoparticles on a transparent electrode[50].

On the other hand, the use of SPR in solar cells, and particularly in organic solar cells, is relatively less explored. Most studies used SRGs to excite the SPR. Soft lithography[51-54] and laser lithography[55-57] have both been used to inscribe the SRGs used in solar cells. In the former, an efficiency increase from 3.6% to 4.1% was noted using linear gratings with P3HT:$PC_{61}$BM solar cells, while an efficiency increase to 4.3% was observed with crossed gratings[54]. Figure 1.5 shows an example of linear and crossed gratings.



(a)                                                                         (b)
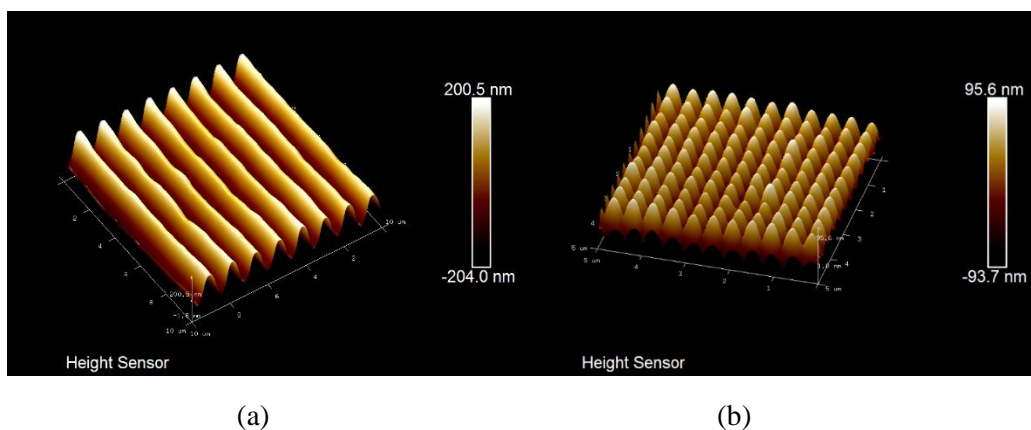
Figure 1.5. Atomic Force Microscope (AFM) images of (a) a linear grating and (b) a crossed grating.

An efficiency enhancement from 7.2% to 7.3% was also demonstrated on PTB7:$PC_{71}$BM[52]. In an interesting study using the donor poly[4,8-bis-(2-ethylhexyloxy)-benzo(1,2-b:4,5-b')dithiophene)-2,6-diyl-alt-(4-(2-ethylhexanoyl)-thieno[3,4-b]thiophene-)-2-6-diyl)] (PBDTT-C-T), both nanoparticles and gratings were incorporated to excite LSPR and SPR in a PBDTT-C-T:$PC_{71}$BM device. While the control (as-cast) solar cell had an efficiency of 7.59%, the efficiency of the device with grating only (SPR), nanoparticles only (LSPR) and grating and nanoparticles (SPR and LSPR) were respectively $8.38\pm0.20$ %, $8.11\pm0.20$ % and $8.79\pm0.15$ %[53]. In the cases where laser lithography was used to inscribe the SRGs, photocurrent enhancements were demonstrated with polarized incident light on a single grating structure[57], and enhancements similar in magnitude but broader in optical range were also shown when using a parallel

superimposed grating structure[56]. However, while the photocurrent enhancements were promising, the efficiencies of those solar cells under standard test conditions using unpolarized light were not measured and reported.

### 1.2.4    Scattering through Surface Patterning

Another method to improve the efficiency of solar cells is to trap the light within the cell, thus increasing the chance that the light would be absorbed and its energy converted into electrical energy. In conventional silicon solar cells, this is often achieved by texturing the surface of the cell which causes the light to scatter. The light then acquires an angular trajectory thus extending its effective path within the absorber, which in turns increases the absorption probability[58, 59]. The same technique cannot be used in thin film organic solar cells as the surface roughness would exceed the film thickness.

In organic solar cells, scattering is often used in conjunction with LSPR by doping one of the layers with metallic nanoparticles, as illustrated in Figure 1.6. In this figure, the light scattered from the nanoparticle has an extended optical path. Furthermore, some of the light reflected by the back electrode will be blocked from escaping the active layer by the nanostructure, thus effectively trapping the light within the solar cell.
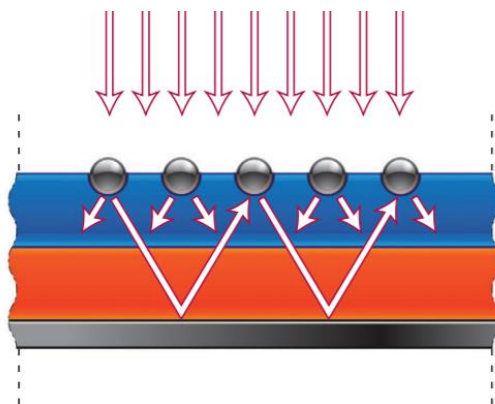


Figure 1.6. Metal nanoparticles acting as scattering centers in a thin film solar cell. The nanoparticles also act as top reflectors for the light reflected by the bottom electrode. Adapted from (Atwater and Polman, 2010)[36].

In organic solar cells, both silver and gold nanospheres have been used as scattering centers to improve light absorption[60-62]. However, it can be difficult to separate the contribution from the scattering and the LSPR to the efficiency enhancement[17]. Metallic nanowires[63], nanocubes[64], and nanoprisms[65] have also been used. Unfortunately, due to the size and shape of the metallic nanostructures, the efficiency enhancement is limited to a narrow spectral range, typically around 100 nm[65].

### 1.2.5 Photo-induced Nanostructures in Azobenzene Films

The photo-induced fabrication of nanostructures in azobenzene polymer thin films was first reported by Rochon *et al.* [66] in 1995 in the form of SRGs. This report noted that the azobenzene underwent a trans-cis-trans photo-isomerization when exposed to a laser light and that SRGs could be inscribed in a single step using interference beams – a technique further detailed in Chapter 2 of this thesis. Furthermore, the process is easily controllable and multiple patterns on a single point can be inscribed by superposition[56]. Random nanoscale surface patterning have also been achieved on azobenzene thin films upon the application of an electric field, through a process called corona poling[67]. This process created randomized nanostructures, but with size controllable through temperature and exposure time.

While azobenzenes are a popular materials for the optical inscription of SRGs and the subsequent excitation of SPR in solar cells, this material has a strong absorption in the visible spectrum below 600 nm[68]. Furthermore, azobenzene nanostructures can be collapsed by heating above the glass transition temperature of this material, typically above 80 degrees Celsius (C°)[67, 69]. Those drawbacks limit azobenzene applications in solar cells as not only would the transmission of light be negatively affected, but the nanostructure could be destroyed during high temperature annealing which is often required in the manufacturing of solar cells, notably when using the P3HT:$PC_{61}$BM organic blend[18]. However, it is possible to transfer the surface relief patterns inscribed on azobenzene films to a more stable material, such as polydimethylsiloxane (PDMS), through nano-imprint lithography[51-54]. Furthermore, some researchers have reported an increased transmission of azobenzene films in the visible range after ultraviolet (UV) treatment[68, 70, 71]. One single example was found in the literature using UV-treated azobenzene nanostructures to improve the efficiency of organic light-emitted diodes (OLEDs)[70] – however none was found for the efficiency enhancement of solar cells.

### 1.3 RESEARCH GOAL

In order for organic solar cells to take their place in the energy market and be a serious alternative to fossil fuels, their power conversion efficiency needs to be improved – particularly if using ITO-free solar cells which are more environmentally friendly, but typically have lower efficiencies. One way to enhance the efficiency of these solar cells is to increase the amount of light absorbed by the active layer. Two possible solutions for efficiency enhancements in organic solar cells are explored in this thesis.

The first solution consists of using azobenzene crossed gratings to couple the light within the solar cell through the excitation of SPR. As discussed in section 1.2.3, linear and crossed gratings have been successfully used in the past to increase the efficiency of P3HT:$PC_{61}$BM solar cells[54]. This was achieved using a bottom illuminated direct structure, i.e. a structure with a transparent bottom anode and metal top cathode. However, inverted structures, i.e. with a bottom cathode and top anode, are becoming the dominating geometry due to advantages such as improved lifetime, air and moisture stability[31, 72, 73]. Only one example was found in the literature of SPR used in inverted P3HT:$PC_{61}$BM solar cells[56]. This study demonstrated an increase in the photocurrent of inverted P3HT:$PC_{61}$BM solar cells[56], but solar cell efficiency measurements were not reported because of the difficulties encountered at that time with making a transparent top electrode. Furthermore, linear gratings were also used in the improvement of direct structure PTB7:$PC_{71}$BM solar cells[52], but no example was found in the literature on using these solar cells with superimposed gratings to excite SPR, either in a direct or inverted structure. The work presented in this thesis is an attempt at solving these deficiencies by using inverted PTB7:$PC_{61}$BM

solar cells with a SRGs metal bottom electrode and ultra-thin metal or solution-processed transparent top electrode.

The second method to improve the efficiency of ITO-free organic solar cells explored in this thesis uses scattering principles. As organic solar cells need to remain as thin films with thickness typically less than 500 nm, this can be done by scattering the light before it enters the solar cell. The optical path of the light within the solar cell would then be extended without increasing the physical thickness of the cell. This thesis will attempt to use UV-treated azobenzene structures integrated in both P3HT:PC$_{61}$BM and PTB7:PC$_{61}$BM solar cells to scatter the light and improve the efficiency of the solar cells. A literature review did not reveal any similar techniques to enhance the efficiency of solar cells, although this method has been used in the past to scatter light from OLEDs in thin films[70]. Two UV-treated azobenzene nanostructures will be explored: the first surface patterning will be done through corona poling, while the second will consist of using crossed gratings. This thesis will also explore the effects of the nanostructures' physical features, particularly surface roughness and transmission, on the efficiency enhancements of the solar cells.

## 1.4 STRUCTURE OF THE THESIS

This thesis is divided in five chapters. In the first chapter, the global energy situation was discussed. Solar energy was offered as a viable alternative energy source to fossil fuel energy, a source of energy with fast depleting reserves and an important contributor to global climate change. The early history of solar cells' evolution was then presented, starting with Edmund Becquerel's observation that light could produce an electric current. It was then shown that first generation solar cells, based on inorganic materials, have now plateaued in terms of their efficiency to convert solar energy into electrical energy and that they not only suffer from high manufacturing costs but also have high energy payback time, making them a less than ideal green technology. Organic solar cells, with their easy of fabrication, low manufacturing cost and environment friendliness could be worthwhile replacements if their efficiencies could be further increased. Recent developments in polymer organic solar cells, including the introduction of bulk-heterojunction solar cells, advancement in materials, plasmonic solar cells and the use of nanostructures to scatter the light within the solar cells, as well as surface patterning of azobenzene thin films were then discussed. The goal of this thesis was then presented: the enhancement of the power conversion efficiency of ITO-free polymer organic solar cells by surface patterning of azobenzene thin films, either by using superimposed gratings to excite SPR in inverted PTB7:PC$_{61}$BM solar cells or by using UV-treated nanoscale structures to scatter the light within P3HT:PC$_{61}$BM and PTB7:PC$_{61}$BM solar cells.

The second chapter of this thesis is a theoretical overview where some notions introduced in the Chapter 1 are further explored. This chapter is divided in five sections. The chapter begins with the theory of first generation inorganic solar cells and explains how solar energy is transformed first into chemical energy and then into electrical energy. In the second section, common parameters used in the characterization of solar cells are presented. Organic solar cells, including charges formation and extraction and common architectures and materials, are then introduced. The next section is dedicated to plasmonic organic solar cells with a focus on the SPR dispersion relation, excitations, diffraction gratings and plasmonic solar cells architectures. The last section explores the possibility of scattering light through surface patterning of azobenzene thin films to improve the absorption probability.

The experimental procedures used in this thesis are detailed in Chapter 3. The first section of this chapter details materials and solutions preparations, while the second section describes

processing and testing equipment and set-ups. In the third section, the designs, fabrication steps and processing parameters for the control solar cells without SPR are specified. The last section details the fabrication procedures of azobenzene nanostructures and their integration in the solar cells. Two surface patterning techniques are explored: crossed gratings through laser beams interference and corona poling by inducing an electrical-field while heating an azobenzene film above its glass temperature. The UV-treatment of azobenzene films to improve transparency is also detailed. Finally, the processing parameters for the different layers of the solar cells used in this thesis are summarized.

The experimental results are presented in Chapter 4. In the first section of this chapter, the ITO-based solar cells, using P3HT:$PC_{61}$BM as active layer materials, are characterized and analyzed. While the goal of this thesis is to improve the efficiency of ITO-free polymer organic solar cells, this step was necessary to confirm appropriate fabrication procedures. As ITO/P3HT:$PC_{61}$BM-based solar cells are well studied with known efficiency values between 2-4%, they were chosen as control cells. The next section discusses issues with fabricating a solar cell with a transparent top electrode – a structure required for the integration of the bottom metal structured electrode needed to excite SPR. Two transparent electrodes are investigated: an ultra-thin metal electrode and a spin-coated electrode. Results for spin-coated transparent bottom electrode solar cells are presented in the third section and are used as references for measuring the efficiency improvement of the solar cells incorporating scattering nanostructures. Solar cells made with azobenzene thin films patterned by corona poling are then presented. Finally, solar cells with azobenzene thin films patterned by crossed gratings, using both P3HT:$PC_{61}$BM and PTB7:$PC_{61}$BM as active organic material, are discussed.

The thesis concludes with Chapter 5, which includes consideration for future work.

## 2   THEORETICAL OVERVIEW

This chapter covers the necessary theory to understand the work contained in this thesis and is divided in five sections. First, the photovoltaic process – the process in which solar energy is transformed into electrical energy – will be explored from a basic level using well-studied first generation inorganic solar cells and pn-heterojunctions. Common parameters used in the characterization of solar cells and limitations of energy conversion will then be presented. The concepts seen in the first two sections will then be applied to the emerging organic solar cells in the third section. Common organic solar cell architectures and materials will also be introduced. The next section is dedicated to plasmonic organic solar cells with a focus on how diffraction gratings can excite surface plasmons in a solar cell. The last section explores the possibility of scattering light through the surface patterning of azobenzene thin films to improve the absorption probability.

### 2.1   INORGANIC SOLAR CELLS

First generation solar cells were made of inorganic semiconductors, with silicon being a popular choice. This section includes a brief introduction to semiconductors before exploring how the solar energy is transformed first into chemical energy and then into electrical energy.

### 2.1.1   Semiconductors

In terms of electricity, materials fall within two main categories: conductors and insulators. A conductor is a material in which the electrons can move freely, i.e. if a potential difference is applied to the conductor, the electrons can be made to drift in one direction, thus forming an electric current. On the other hand, materials in which there is no or little free electron movements when a potential difference is applied are called insulators or non-conductors. These materials have their electrons bound within their molecules. For example, silicon, a common inorganic solar cell material, has a total of 14 electrons distributed on three shells. Since the first and second shell can only contain a maximum of two and eight electrons respectively, the outer occupied shell, called the valence shell, contains the remaining four electrons. Most atoms need eight electrons on their valence shell to be stable. To remain stable, a pure - or intrinsic - silicon atom forms covalent bonds with its neighbours by sharing its valence electrons with four more silicon atoms. As a result, each atom has eight electrons on its valence shell as illustrated in Figure 2.1.
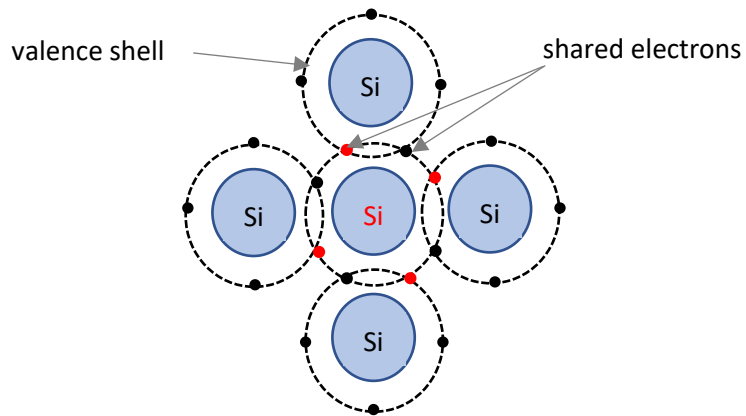
Figure 2.1. Pure silicon crystal lattice. Each silicon atom shares its valence electrons to form stable bonds with the neighbouring atoms.

At absolute zero temperature, there are no free electrons in a pure silicon crystal lattice, making it a good isolator. However, at solar cells operating temperature, electrons can gain enough energy to escape from their bonds on the valence shell to a now partially occupied new outer band, the conduction band, with the space left behind by the electrons called "holes". The band gap ($\varepsilon_G$) of a semiconductor is the minimum energy required to excite an electron from the bound state on the valence shell into a free state on the conduction band. With the electrons free to move in the crystal lattice, this potentially allows for an electric current, and thus silicon is considered a semi-conductive material.

Conductivity in a semiconductor can be increased by doping, which is the intentional introduction of impurities in a material. A n-type semiconductor is one in which impurities, called donors, have more valence electrons than needed for chemical bonding with neighbouring atoms. A p-type semiconductor is one which was doped with atoms, called acceptors, having less valence electrons than is necessary for chemical bonding with neighbouring atoms. For silicon lattices, phosphorus or arsenic atoms are the most common donors, whereas boron or indium are common acceptors[1]. Figure 2.2 illustrates n-type and p-type doped silicon lattices.
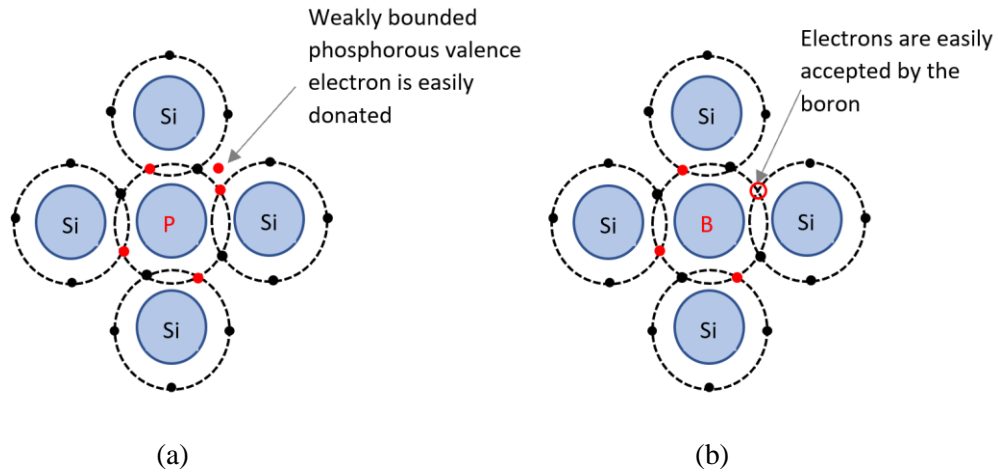
Figure 2.2. Doping of silicon with (a) phosphorus (n-type) and (b) boron (p-type). At non-absolute temperatures, the extra weakly bounded phosphorous valence electron in (a) is easily donated to the conduction band of a neighbouring silicon atom, while in (b) the holes in the lattice from the boron atom allow silicon electrons to move in the lattice.

The distribution of electrons and holes in the conduction and valence bands of a semiconductor follows a Fermi-Dirac distribution. For example, the probability $f_e$ that in equilibrium an electron occupies a state with energy $\varepsilon_e$ is[1]:

$$f_e(\varepsilon_e) = \frac{1}{exp\left[(\varepsilon_e - \varepsilon_f)/kT\right] + 1} \tag{2.1}$$

where $T$ is the absolute temperature, $k$ is Boltzmann's constant, and $\varepsilon_f$ is the Fermi level, which can be defined as the work required to add an electron to a given system. The closer the Fermi-Dirac distribution value is to 1, the higher the chance that this state is occupied by an electron. In a pure semiconductor, the Fermi level lies within the bandgap. However, as illustrated in Figure 2.3, doping moves the Fermi level towards the conduction band for an n-type semiconductor (i.e. increasing the probability that an electron occupies a conduction band) or towards the valence shell for a p-type semiconductor (i.e. increasing the probability that a hole occupies a valence shell). As it will be seen in the next section, the doping of semiconductor materials allows the formation of a current when p-type and n-type materials are combined.
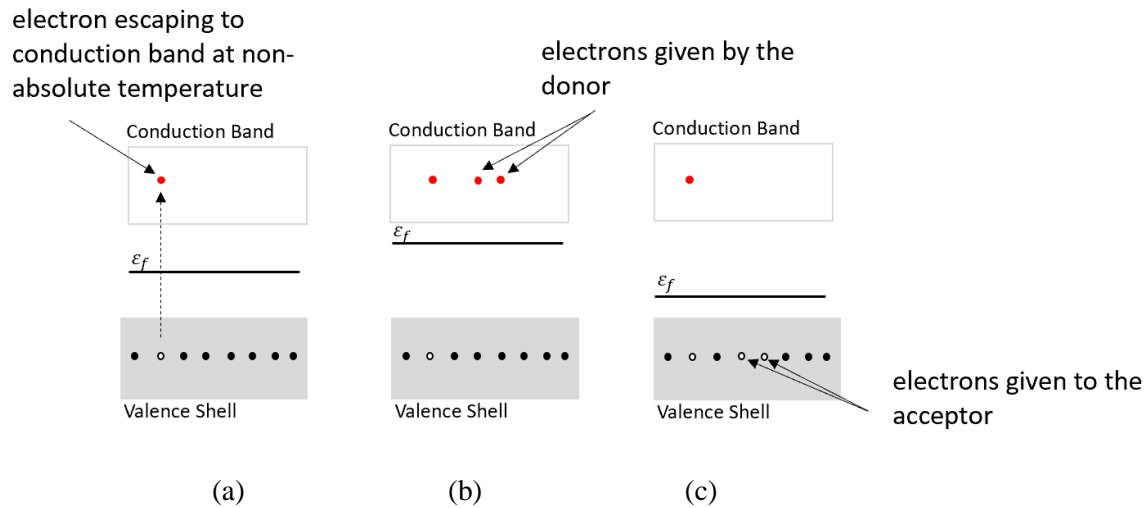
Figure 2.3. Fermi levels in an (a) intrinsic semiconductor, (b) n-type semiconductor and (c) p-type semiconductor at non-absolute temperatures. In (a) the Fermi level lies within the bandgap. In (b), unbonded electrons from the valence band of the donor are being donated to the conduction band of the semiconductor, thus there is an increase probability of electrons occupying the conduction band. In (c), the semiconductor donated some of its valence electrons to the valence shell of an acceptor, thus leaving holes in the valence shell of the semiconductor.

### 2.1.2 Conversion of Solar Energy into Chemical Energy

The first step in a photovoltaic process is the absorption by the semiconductor of solar energy to produce chemical energy. The amount of energy that will be available for transformation into chemical energy depends on both the generation of electron-hole pairs created through the absorption of photons and the losses caused by the recombination of some of those electrons and holes.

Albert Einstein[74], in his 1905 paper on the photoelectric effect, theorized that quanta of light, now called photons, could penetrate a material at the atomic level and, with enough energy, eject an electron. As mentioned earlier, $\varepsilon_G$ of a semiconductor is the minimum energy required to excite an electron from its bound state on the valence shell into a free state on the conduction band. As long as a photon has an energy $\geq \varepsilon_G$, the absorption of the photon's energy allows an electron to transition from the valence shell to the conduction band[1]. The absorption of photons by a semiconductor creates electrons in the conduction band and holes in the valence shell, thus both the electron and hole densities are greater in an illuminated semiconductor than in the dark. Therefore, the electron-associated Fermi level $\varepsilon_{FC}$, is closer to the conduction band than in the dark, while the hole-associated Fermi level $\varepsilon_{FV}$ is closer to the valence band than in the dark[1, 9]. This means that there are two Fermi levels in an illuminated semiconductor, called quasi-Fermi levels[1, 9]. Figure 2.4 shows the quasi-Fermi levels for a semiconductor in the dark (in equilibrium) and under illumination (under bias).
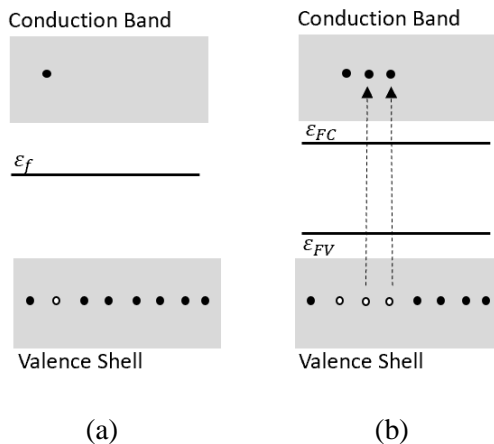
Figure 2.4. Quasi-Fermi levels for a semiconductor (a) in the dark and (b) illuminated. Under illumination, the absorption of the photons' energy causes the electrons to transition to the conduction band, increasing both the electron concentration in the conduction band and the hole concentration in the valence shell.

The difference in the quasi-Fermi levels $\varepsilon_{FC} - \varepsilon_{FV}$ represents the free energy per electron-hole pair: this is the chemical potential $\mu_{eh}$ of a solar cell[1]. A large difference in quasi-Fermi levels means that the solar cell is easily capable of absorbing the photon's energy and producing electron-hole pairs. Thus, such a solar cell would have a good chemical potential.

Unfortunately, not all electron-hole pairs created by the absorption of photons will be available for eventual conversion to electrical energy. There are three basic types of recombination in the bulk of the semiconductor: radiative recombination, Auger recombination and Shockley-Read-Hall (SRH) recombination[1]. These recombination mechanisms are illustrated in Figure 2.5.
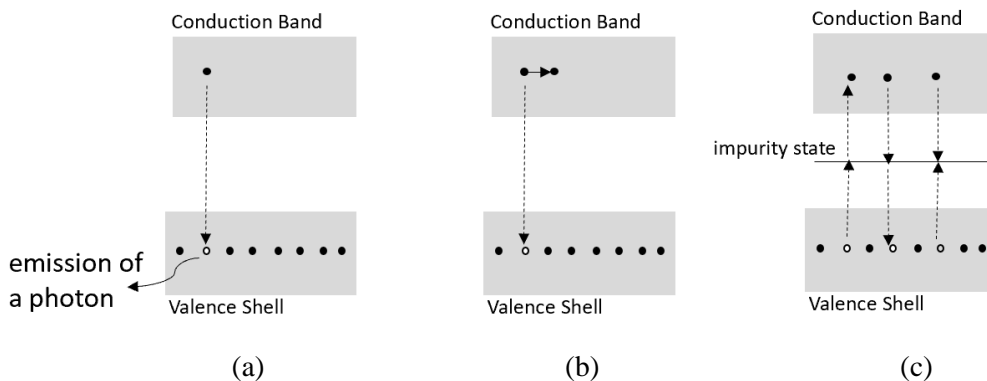


Figure 2.5. (a) Radiative, (b) Auger, and (c) SRH recombination. In (a), the energy from the recombination of the electron and hole is emitted in the form of a photon. In (b), the energy from the recombination is transferred to another electron. In (c), electrons and holes are trapped by impurities within the band gap.

In radiative recombination, an electron from the conduction band combines with a hole in the valence shell and releases a photon (this process is basically the reverse of the absorption of the photon's energy by the electron)[1]. In Auger recombination, just as in radiative combination, an electron from the conduction band combines with a hole in the valence band. However, the energy set free during recombination is transferred to another electron or hole, instead of emitted in the form of a photon[1]. Another significant recombination in solar cells is the recombination via impurities, also known as SRH recombination[1]. This recombination can be viewed as a two-step process. First, a defect, either unintentional or introduced through doping, with energy in the "forbidden region" with energy between the conduction and valence shell, traps an electron (or hole), with dissipation of the energy to the lattice. The electron (or hole) then moves to the valence shell (or conduction band), once again dissipating energy to the lattice, eliminating a hole (or electron). Alternatively, if the impurities are closed to the middle of the forbidden zone, both electrons and holes have high chance of being captured and recombining at the impurity state level[1]. The dissipation of energy to the lattice in small multiple steps ease the recombination process, and therefore the purity of solar cell material is critical in achieving good solar cells.

The amount of energy available for transformation into chemical energy therefore depends on both the generation of electron-hole pairs through the absorption of photons (gains) and the recombination of the electrons and holes (losses), mainly through radiative, Auger, and SRH and recombination. The chemical potential of a solar cell $\mu_{eh}$ was previously defined as the difference in quasi-Fermi energies $\varepsilon_{FC} - \varepsilon_{FV}$. When $\mu_{eh} \neq 0$ in an illuminated semiconductor, the energy from the absorbed photons, less the recombination losses, has been converted into chemical energy and could potentially be harvested as electrical energy.

### 2.1.3    Conversion of Chemical Energy into Electrical Energy
To transform the potential chemical energy $\mu_{eh}$ into electrical energy, a structure with two terminals which can produce a charge current and an electrical voltage at its terminals is required. Given that pn-junctions are the most widely used structures in the fabrication of solar cells[9], the conversion of chemical energy into electrical energy will be examined from a pn-junction perspective, though other mechanisms are possible.

### *2.1.3.1    Transport of Electrons and Holes*
The electrons and holes produced by the absorption of the photons need to be transported to the terminals of an external circuit to produce electrical energy. This transportation is the result of forces acting on the electrons and holes. To simplify, let's first assume that the electrical potential is uniform, but that the concentrations of carriers is nonuniform. As illustrated in Figure 2.6, the electrons would spread out to minimize their statistical potential energy. This movement is sometimes referred to as "diffusion current"[9].
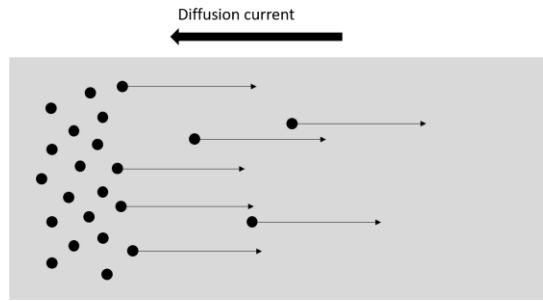
Figure 2.6. Diffusion current in a semiconductor. The electrons spread as a result of non-uniform concentration of charges. As the current is defined, by convention, as the direction of movement of a positive charge, the diffusion current is in the opposite direction of the movement of the electrons.

Let's now assume spatially uniform electrons and holes concentrations. In this case the only driving force on the particles would be an electric field $E = -\nabla V$, where $V$ is the electrical potential[1]. As illustrated in Figure 2.7, the electrons would move to reduce their electrical potential energy, a motion sometimes referred to as "drift current"[9].
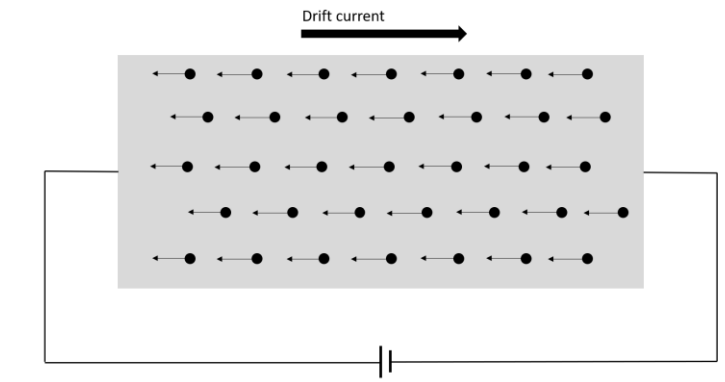


Figure 2.7. Drift current in a semiconductor. The direction of the drift current depends on the polarity of the applied electrical field.

Let's now apply these two cases to a pn-junction. When combining a n-type and p-type material, initially, the greater chemical potential of the electrons in the n-type and holes in the p-type material would drive a "diffusion current" (electrons in the n-material would tend to move to the p-material and holes in the p-material would tend to move to the n-material). This movement would lead to a positive build up of charges in the n-material and negative charges in the p-material. The build-up of charges would create an electrical potential leading to a "drift current" opposing

the "diffusion current" until the driving forces no longer exit and the junction is in a state of electrochemical equilibrium[1]. Therefore, the overall current could be considered as the sum of the opposite currents: a statistical "diffusion" current depending on carrier concentration and an electrical potential "drift" current[9]. In general terms, while mathematically useful, "diffusion" and "drift" currents have no physical meaning. The current is not a result of the addition of two other currents, but the result of the addition of two forces acting on the particles, the gradient of the chemical potential and the gradient of the electrical energy, into a resultant force: the gradient of the electrochemical potential[1]. But transporting electrons and holes is not sufficient to produce electrical energy. The electron-hole pairs need to be separated since extracting them pairwise along the same path would not provide a charge current as the pairs are electrically neutral.

### 2.1.3.2 *Separation of Electrons and Holes*

It was shown above that the driving force on the electrons and holes is the gradient of the electrochemical potential, which can be thought of as the gradient of the quasi-Fermi level. Figure 2.8 shows the quasi-Fermi levels between the valence shell and conduction band of an illuminated n-type semiconductor.
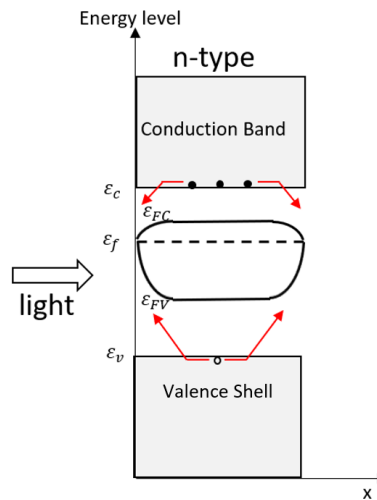


Figure 2.8. Quasi-Fermi levels in a n-type material, where $\varepsilon_c$ and $\varepsilon_v$ are the energy level of the conduction band and valence shell, respectively. The gradients of the quasi-Fermi levels $\varepsilon_{FC}$ and $\varepsilon_{FV}$ drive the electrons and holes toward the surfaces. However, as the material is symmetrical, there is no preferential path for the carriers and therefore no current.

Inside the semiconductor, the illumination generates electrons and holes, and therefore a chemical potential $\mu_{eh} = \varepsilon_{FC} - \varepsilon_{FV} \neq 0$. At the surfaces, the electrons and holes generated by the illumination recombine and therefore the quasi-Fermi levels at both surfaces have the same value $\varepsilon_f$ as in the dark. This results in gradients for the two quasi-Fermi levels, which drive the electrons and holes in the bulk of the semiconductor toward both the front (left on the figure) and back (right on the figure) surfaces. As this is a n-type material, there is a larger conductivity of electrons in the conduction band, and therefore the gradient of $\varepsilon_{FC}$ is smaller than the gradient of $\varepsilon_{FV}$ (for a p-type

material, the gradient of $\varepsilon_{FV}$ would be smaller)[1]. However, as this material is symmetrical, no current would be generated as there is no preference for the transport of electrons and holes in opposite directions. Furthermore, the electrodes required to transport the electrical energy into an external circuit pose a new challenge: in a metal, electrons move freely. Large losses of carriers by surface recombination at the metal contact can therefore only be avoided by allowing only one type of carrier at the contact[1].

This dilemma can be resolved by using a pn-heterojunction, which is made of an absorbing semiconductor sandwiched between two semiconductors with different energy gaps where the valence shells and conduction bands of the materials are not at the same energy level[1]. Figure 2.9 shows such an arrangement.
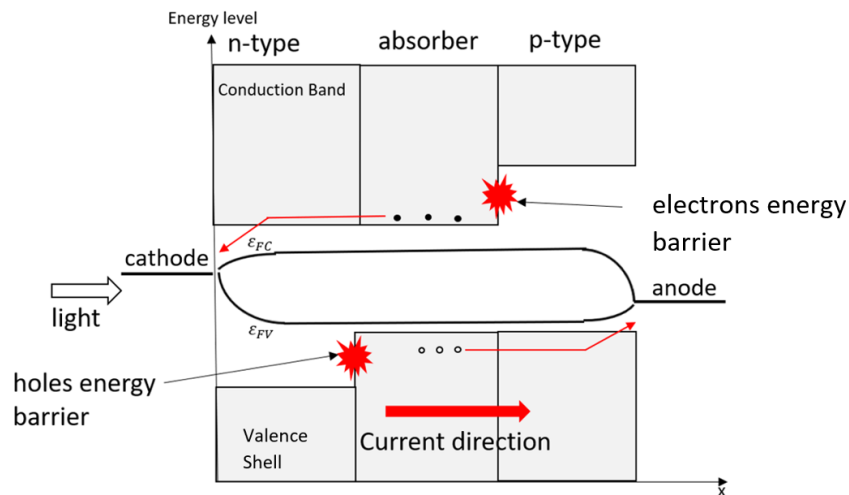


Figure 2.9. Quasi-Fermi levels in a pn-heterojunction. The differences in energy gaps of the material create energy barriers allowing only one type of carriers at the electrodes.

Just like in Figure 2.8, the quasi-Fermi levels join at the surfaces. Electrons are driven by a small $-\varepsilon_{FC}$ gradient in the n-type material where they will be collected by the cathode, while holes are driven by a small $\varepsilon_{FV}$ gradient in the p-type material where they will be collected by the anode[1]. While the forces driving the electrons to the hole contact and the holes to the electron contact are much larger, the large band gaps in the materials act as barriers. In the n-type material, the energy barrier prevents the injection of holes from the valence shell of the absorber into the n-type material, thus preventing large recombination losses at the anode. Similarly, a larger band gap on the right causes an energy barrier preventing the electrons from reaching the anode. Therefore, a pn-heterojunction satisfies the requirements to have semi-permeable membranes to prevent interface recombination at the metal contact, while allowing a difference of the quasi-Fermi levels in the absorber. Many materials can be doped to achieve this purpose but, for solar cell applications, it is not enough to have a large band gap. As seen in section 2.2.1, preventing energy gap in the

forbidden zone to avoid SRH recombination is also important. A material with this combination is not common, but silicon and other III-V compounds, such as those based on gallium arsenide, are viable options[1].

## 2.2    CHARACTERIZATION OF SOLAR CELLS

The pn-heterojunction is a structure capable of producing electron-hole pairs by the absorption of photons, separating the charges and transporting them to terminals in the desired direction. However, collecting carriers will not by itself generate power. As power is a function of both current and voltage, two specific cases will be examined: short-circuit current ($I_{sc}$) and open-circuit voltage ($V_{oc}$). Other parameters of importance in the characterization of solar cells, namely fill factor (FF), shunt and series resistance ($R_{SH}$ and $R_S$ respectively), and PCE, will also be presented.

### 2.2.1    Short-Circuit Current

The short-circuit current $I_{sc}$ is the current through the solar cell when the voltage across the solar cell is zero and is therefore the largest current which may be drawn from the solar cell. To remove the dependence of the solar cell area, the short-circuit current density $J_{sc}$ is commonly used as a solar cell parameter[9], with:

$$J_{sc} = \frac{I_{sc}}{active\ area\ of\ solar\ cell} \qquad (2.2)$$

The short-circuit current is linked to the internal quantum efficiency of the solar cell, that is to the number of photons absorbed by the material resulting in electron-hole pairs, and external quantum efficiency of the solar cell, which includes the effect of reflection[75, 76]. Generally, a large $J_{sc}$ requires the absorber to be as thick as possible to maximize the absorption of photons[1]. Junction depths of 400 to 600 nm are typical for crystalline silicon cells[76].

### 2.2.2    Open-circuit Voltage

The open-circuit voltage $V_{oc}$ is the voltage across the solar cell when the current through the cell is zero and is therefore the maximum voltage available from a solar cell. It can be defined as the separation of quasi-Fermi levels $\varepsilon_{FC} - \varepsilon_{FV}$ at which generation and recombination of electron-hole pairs is in equilibrium[1] and is therefore largely dependent of the bandgap of the chosen material[75]. However, the thickness of the cell also affects the open-circuit voltage. As the rate of generation of electron-hole pairs per volume is greatest near the top surface, a reduction in the thickness of the cell implies an increase in the separation of the Fermi levels. $V_{oc}$ is therefore maximal when the thickness of the cell approaches zero[1].

Since power is a function of both current and voltage, that is $P = IV$, both a high short-circuit current (thick solar cell) and high open-circuit voltage (thin solar cell) are desirable to maximise the power generated. These two requirements are competing each other. Since the gain in the open-circuit voltage from a reduction of thickness does not compensate for the short-circuit current loss[1], a thicker cell generally produces more power. However, when the thickness of the cell exceeds the diffusion length, i.e. the length after which the electrons and holes are likely to recombine, the extra thickness does not generate photocurrent[9], and any additional thickness would therefore reduce the performance of the cell.

### 2.2.3 Fill Factor

As was seen above, the maximum current density available from a solar cell is the short-circuit current density $J_{sc}$, while the maximum voltage is the open-circuit voltage $V_{oc}$. Since the voltage is zero under short-circuit condition and the current density is also zero at the open-circuit condition, the solar cell at those two points will not produce any power. At some point before $V_{oc}$ is reached, the current density-voltage product is maximum. This point corresponds to the maximum power point, that is:

$$d(JV) = d(J)V + Jd(V) = 0 \tag{2.3}$$

and thus

$$\frac{d(J)}{d(V)} = -\frac{J}{V} \tag{2.4}$$

Therefore, the maximum power point occurs when the tangent to the characteristic J-V curve of a solar cell forms the same angle with a vertical line as the line connecting the origin to the maximum power point. Figure 2.10 illustrates the geometrical construction of the maximum power point from a typical J-V characteristic curve of a solar cell where $J_{mp}$ and $V_{mp}$ are respectively the current density and voltage at the point of maximum power.
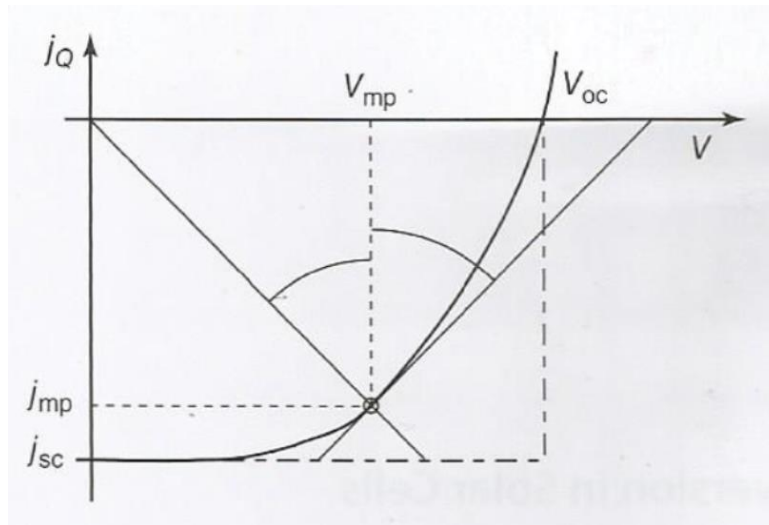


Figure 2.10. Geometrical construction of the maximum power point of a solar cell. The maximum power point occurs when the tangent to the characteristic J-V curve of a solar cell forms the same angle with a vertical line as the line connecting the origin to the maximum power point. Adapted from (Würfel and Würfel, 2016)[1].

The fill factor FF is an important parameter of the solar cell and is defined as the ratio of the maximum power to the product of $I_{sc}$ and $V_{oc}$[1] or, when using the current density parameters, by the equation:

$$FF = \frac{J_{mp}V_{mp}}{J_{sc}V_{oc}} \tag{2.5}$$

Graphically, it is related to the area of the largest rectangle which will fit in the J-V characteristic curve, and is affected by both the shunt and series resistance of the solar cell[75].

### 2.2.4 Shunt and Series Resistance

A solar cell can be modelled by a current source in parallel with a diode, a shunt resistance $R_{SH}$ and a series resistance $R_S$, as illustrated in Figure 2.11.
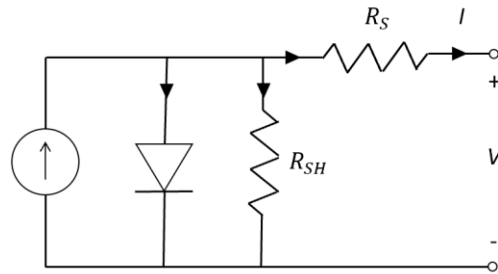


Figure 2.11. Equivalent circuit of a solar cell. A solar cell may be modelled by a current source in parallel with a diode, a shunt resistance and a series resistance.

The efficiency of the solar cell is negatively impacted by low $R_{SH}$ and high $R_S$. Low $R_{SH}$ is a result of manufacturing defects such as pinholes where the two electrodes are not isolated. Such defects can cause current leakage and a lowering of the $V_{oc}$. In cases of short-circuits, the solar cell may be rendered non-functional. $R_{SH}$ can be estimated from the inverse of the slope at the $J_{sc}$ point of the J-V characteristic curve. On the other hand, $R_S$ is estimated from the inverse of the slope at the $V_{oc}$ point of the J-V characteristic curve. $R_S$ is mainly affected by poor morphology of the active layer, recombination at the material interfaces, the contact resistance and the sheet resistance of the electrodes.[1, 13, 75] A high $R_S$ negatively impacts the efficiency of the solar cells by reducing the FF[77-79]. A further increase in $R_S$ will also decrease the current density of the solar cells, as modeled in Figure 2.12.
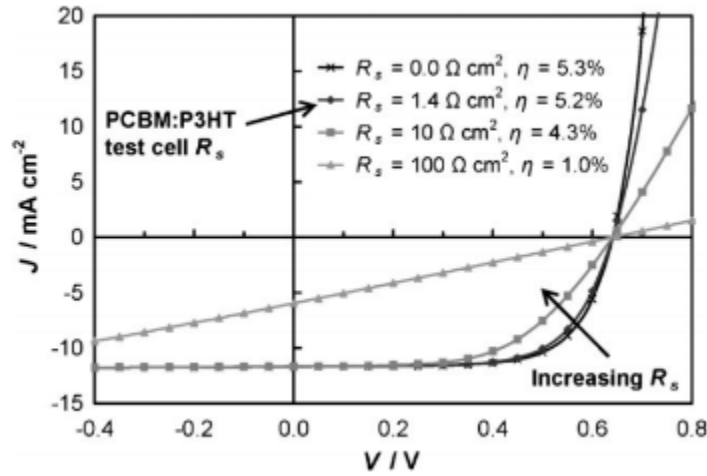
Figure 2.12. Modeled effect of $R_S$ variation on the J-V characteristics of a P3HT:PC$_{61}$BM cell. An increase in $R_S$ results a decrease in FF, current density and efficiency. Adapted from (Servaites *et al.*,2010)[77].

### 2.2.5 Efficiency of Solar Cells

While $J_{sc}$, $V_{oc}$, FF, $R_{SH}$ and $R_S$ are commonly used parameters to characterize solar cells, the most used parameter to compare solar cells is the power conversion efficiency PCE (also written as $\eta$), which is defined as the ratio of maximum output energy from the solar cell $P_{max}$ to input energy from the sun $P_{in}$. The efficiency can be expressed using the following known parameters of the solar cell[80]:

$$PCE = \frac{P_{max}}{P_{in}} = \frac{V_{OC}I_{SC}FF}{P_{in}} = \frac{V_{OC}J_{SC}FF}{P_{in} \times Active\ Area} \tag{2.6}$$

Historically, the measurements of solar cells efficiencies were laboratory-dependent. Today, standard solar spectrums are used for the $P_{in}$ and differences between recognized test centres are in the order of magnitude of less than 1%[10] of the PCE value. The air mass (AM) coefficient defines the direct optical path length through the Earth's atmosphere, expressed as a ratio relative to the path length at the zenith[81], as illustrated in Figure 2.13.

24
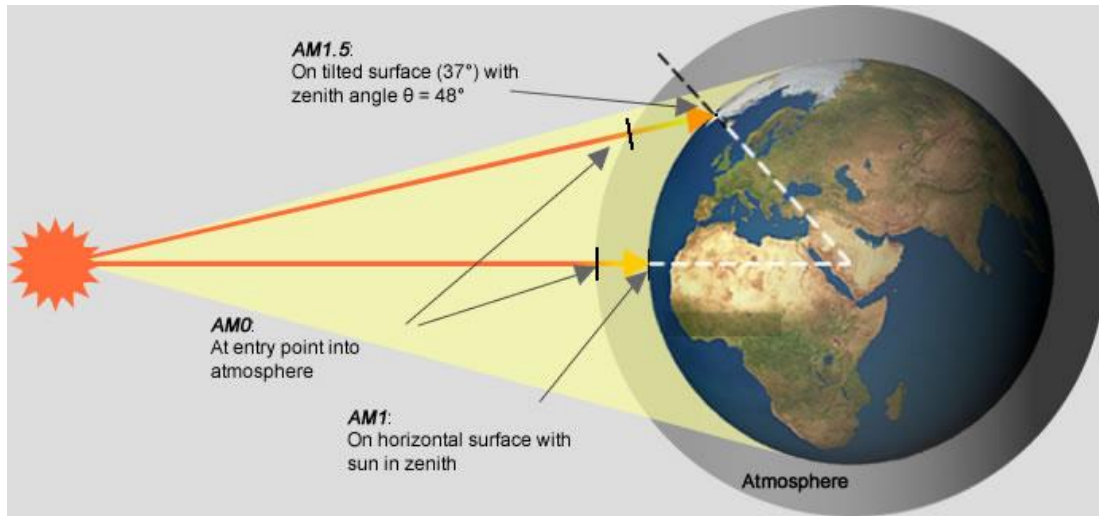
Figure 2.13. Length of the path through the atmosphere in relation to the shortest length for different solar spectrum. AM0 is typically used to test solar cells for spatial application, while AM1.5 is used to test solar cells for terrestrial application. Adapted from (Green Rhino Energy, 2016)[82].

The solar spectrum outside the atmosphere is designated by Air Mass 0 (AM0). This spectrum is typically used to predict the performance of solar cells in space. As solar radiation is partially absorbed during its passage through the atmosphere, mainly by gases such as water vapor, carbon dioxide, ozone and oxygen[83], a different solar spectrum is needed for terrestrial applications. The spectrum at the equator is called AM1. However, solar panels do not generally operate under exactly one atmosphere's thickness. Many of the world's major population centres, and hence solar installations and industry, lie in mid-latitudes. The specific value of AM1.5 (solar zenith angle 48.2˚) has been selected in the 1970s for standardization purposes[84]. The latest AM1.5 standard pertaining to photovoltaic applications is available in ASTM G-173-03(2006)[85]. Figure 2.14 shows different AM spectra.
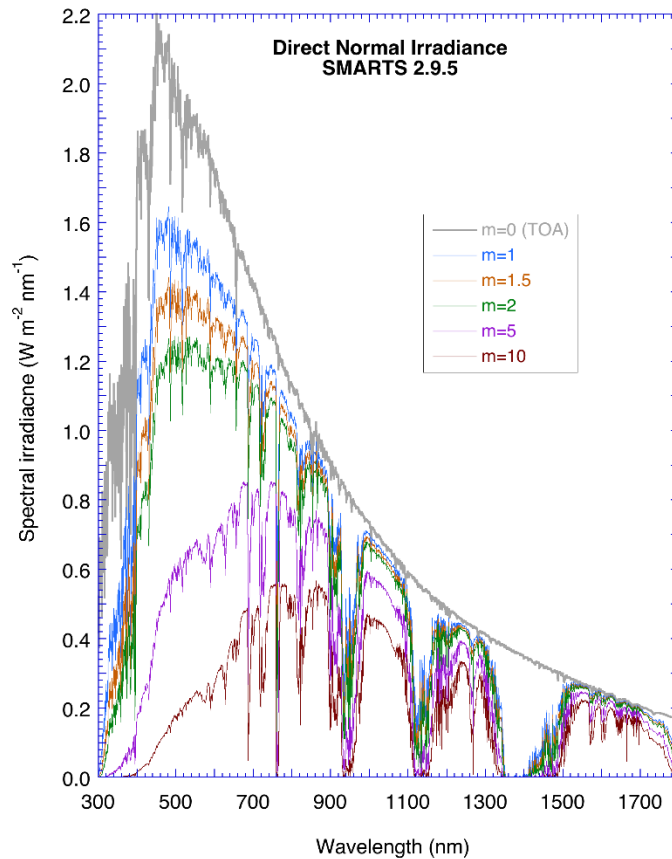
Figure 2.14. Irradiance spectra for increasing air mass. The solar radiation has been partially absorbed through its passage through the atmosphere in AM1 compared to AM0. AM1.5 shows even more absorption due to a longer path through the atmosphere. Adapted from (Wikipedia, 2013)[86].

With the concept of efficiency in solar cells explained, it is of interest to know what the ultimate theoretical efficiency limit would be. The Shockley-Queisser limit is the maximum theoretical efficiency limit for a pn-junction cell without concentration of sunlight. It was calculated by William Shockley and Hans Queisser in 1961[87]. The limit is based on the principle of detailed balance of the fluxes (i.e. the photon flux into a device should equate to the flux - photons or electrons - out of the device), assuming that each excitation produces one electron-hole pair and that the only recombination mechanism is a radiative recombination[88].

According to the Shockley-Queisser limit, not all the energy of the incident photons will be converted into electrical energy. As long as the energy from a photon is superior to the bandgap, the generation of electrons and holes depends on the number of excitation events, not the amount of energy absorbed. Any extra energy is lost in a process known as thermalization, that is the dissipation of energy in excess of equilibrium in photoexcited electrons[89]. Thermalization losses account for most of the inefficiency. However, the Shockley-Queisser limit also considers losses

from photons, with energy less than the bandgap, that will not be able to produce electron-hole pairs and other less limiting factors[87]. Losses from thermalization and non-absorption of photons below the bandgap represent 33% and 23% respectively of the incident solar energy[90]. With this limit, a theoretical efficiency can be calculated as a function of the bandgap of the solar cell material. Figure 2.15 shows the efficiency as a function of bandgap for a pn-junction under an AM1.5 spectrum.
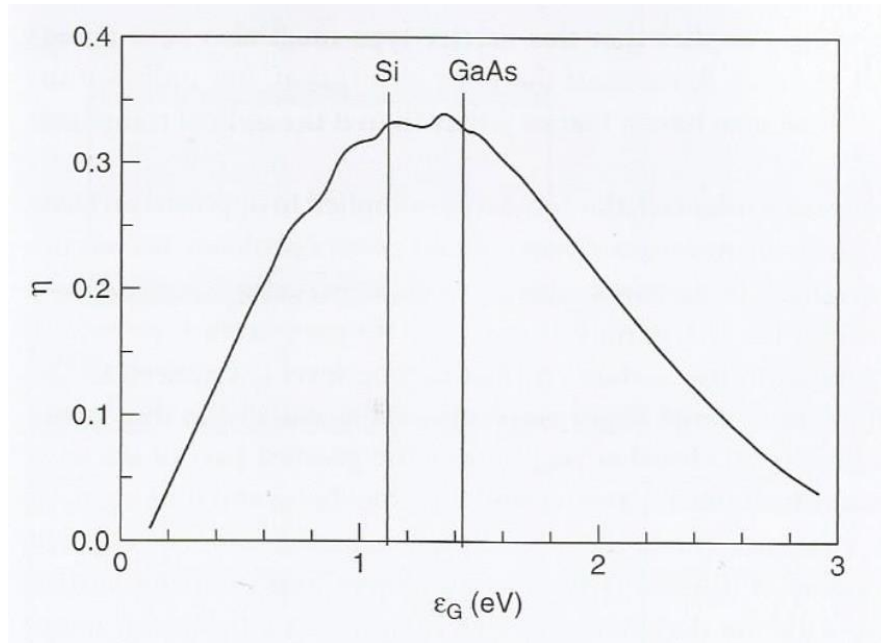


Figure 2.15. Efficiency $\eta$ of a solar cell with radiation recombination only under AM1.5 as a function of bandgap. Adapted from (Würfel and Würfel, 2016)[1].

From this graph, it can be seen that semiconductors with an energy gap between 1 and 1.5 eV, in particular silicon (Si) and gallium arsenide (GaAs), are suitable solar cell materials[1]. Crystalline silicon is a widely used material in solar cell applications[9] as it offers numerous advantages: at 27.7%, it is the second most abundant element in the Earth's crust after oxygen[7], it is also non-toxic and forms an oxide layer that protects it when exposed to air[1].

While silicon offers many advantages, it has a weak absorption and must therefore have a thickness in the order of several hundred $\mu m$[9]. The development of thin film solar cells has been driven by the desire to keep manufacturing costs down. However, the absorption decreases with thinner materials and the performance of thin film solar cells have yet to surpass those of conventional solar cells. This is therefore an intense area of research within the scientific community, with a particular focus on thin films organic solar cells.

## 2.3 ORGANIC SOLAR CELLS

Organic solar cells, with their relative low cost and manufacturing advantages such as roll-to-roll, large area scalability and processability on flexible substrates[91], are attractive alternatives to their inorganic counter parts. Despite the various advantages, organic solar cells have some limitations including low carrier mobility and short exciton life-time[22, 92, 93]. This section of the thesis is dedicated to the theory behind organic solar cells, including charge formation and extraction, and common organic solar cell materials.

### 2.3.1 Charge Formation and Extraction in Organic Solar Cells

A polymer is a macromolecule composed of repeated subunits called monomers. Conventional polymers (e.g. plastics) are considered insulators, but there exists a peculiar class of polymers, called conjugated polymers, that can behave as semiconductors[94, 95]. At this point, it is useful to note some specific terminology. For organic molecules (often in solution), the terms "Highest Occupied Molecular Orbital" (HOMO) and "Lowest Unoccupied Molecular Orbital" (LUMO) are often used[1, 17]. When in bulk (solid), organic semiconductors also have valence and conduction bands, which are close to the HOMO and LUMO of individual molecules.

As in inorganic solar cells, organic solar cells absorb solar energy to generate electron-holes pairs. However, when electrons and holes are generated, they attract each other due to Coulomb forces. Because of the large dielectric permittivity of inorganic semiconductors, the binding energy is small at room temperature and electrons and holes are essentially free particles. On the other hand, organic semiconductors often consist of molecules that have smaller dielectric permittivity and are only weakly bound to each other. This means that the binding energies are usually much larger for organic semiconductors and the electrons and holes remain bound together, in a state called exciton[1]. Due to the bound state of the electron-holes pairs, charge separation differs in organic solar cell from the previously studied pn-heterojunction of an inorganic solar cell. In early organic polymer solar cells, a bilayer heterojunction structure was used to separate the charges, but the development of bulk-heterojunction greatly contributed to efficiency improvements.

A bilayer heterojunction consists of a stack of two materials, a donor (often a polymer) and an acceptor (often a fullerene). Figure 2.16 shows the energy levels in an organic bilayer polymer/fullerene heterojunction. In the first material (the donor), the photons generate excitons. By choosing a second material (the acceptor) with a LUMO level lower than the LUMO level of the first material, the electrons in the donor material may tunnel out of their bound states into the LUMO of the acceptor material. Those electrons would now be free electrons while the holes remain in the first material. A third material on the left side, called a hole-transport layer (HTL), is also required as a semi-permeable membrane for the holes[1], ensuring electrons are not collected by the anode.
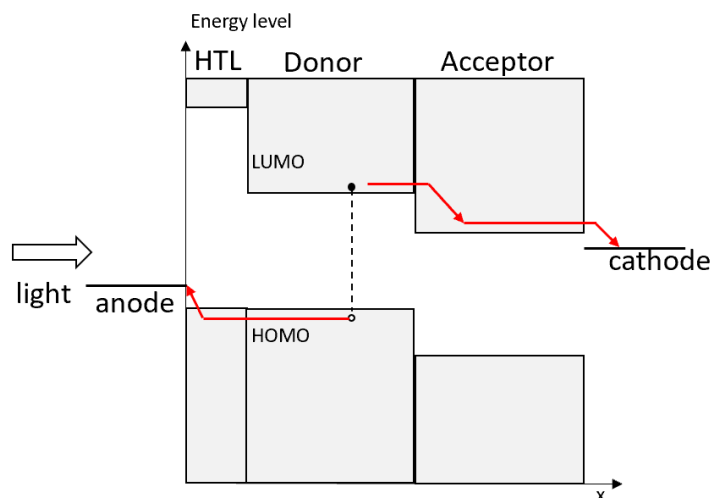
Figure 2.16. Energy levels in an organic polymer/fullerene solar cell. The absorption of photons generates excitons in the donor materials. The electrons are then funneled into a second material with lower LUMO level.

Ideally, the distance of the exciton to the donor/acceptor interface should be similar to the exciton diffusion length in order to limit recombination. In conjugated polymers, the diffusion length is in the order of 10-20 nm[13, 96]. Solar cells fabricated using bilayers can only separate excitons that are generated within the diffusion length. This poses a conundrum: if the active material is too thin, the solar cell would suffer from low light absorption, but high recombination losses would negatively impact thicker devices. An alternate approach to the bilayer is to mix the donor and acceptor materials during processing to create a bulk-heterojunction.

In a bulk-heterojunction, the organic semiconductors form a random network of separated fingers and islands, as illustrated in Figure 2.17. This geometry results in an enhancement of the short circuit photocurrent of several orders of magnitude[93], making it an attractive approach. All-polymer solar cells based on absorption-complimentary polymer donor and acceptor have also shown promising results[97, 98].
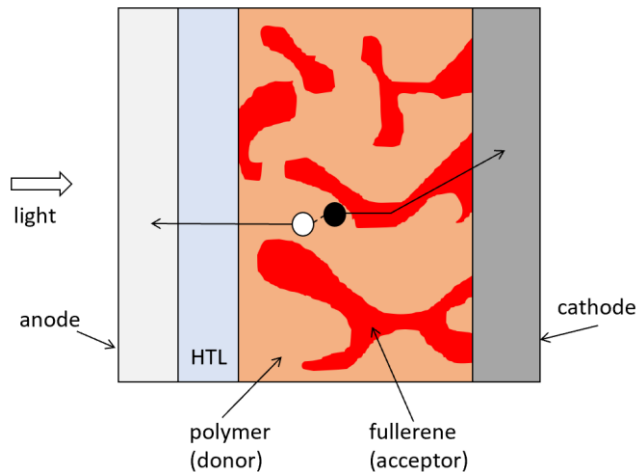
Figure 2.17. Charge separation in a bulk-heterojunction. Excitons are by the absorption of the photon energy in the polymer. Due to the reduced distance to the fullerene, the electrons can be funneled out before they recombined. A hole-transport layer provides a semi-permeable membrane, blocking the electrons from reaching the cathode.

### 2.3.2    Organic Solar Cells Architectures

Two different architectures are commonly used in bulk-heterojunction organic solar cells: a direct structure and an inverted structure. In a direct structure, the bottom electrode is a high work-function conductor such as ITO, gold or silver. This electrode is used as an anode to collect the holes. The top electrode is a lower work-function conductor, such as aluminium, which collects the electrons. In an inverted structure, the electrodes are inverted with the lower-function electrode being at the bottom. Either architecture could be top or bottom illuminated – however in both cases the electrode being illuminated should be transparent to allow the absorption of the solar energy by the active material of the solar cell. Figure 2.18 shows a schematic of direct and inverted organic solar cell structures, though due to the difficulty of processing a transparent top cathode, the direct top illuminated architecture (Figure 2.18a) is seldom used. Nonetheless, it may have a found a niche in flexible solar cells[99-101].
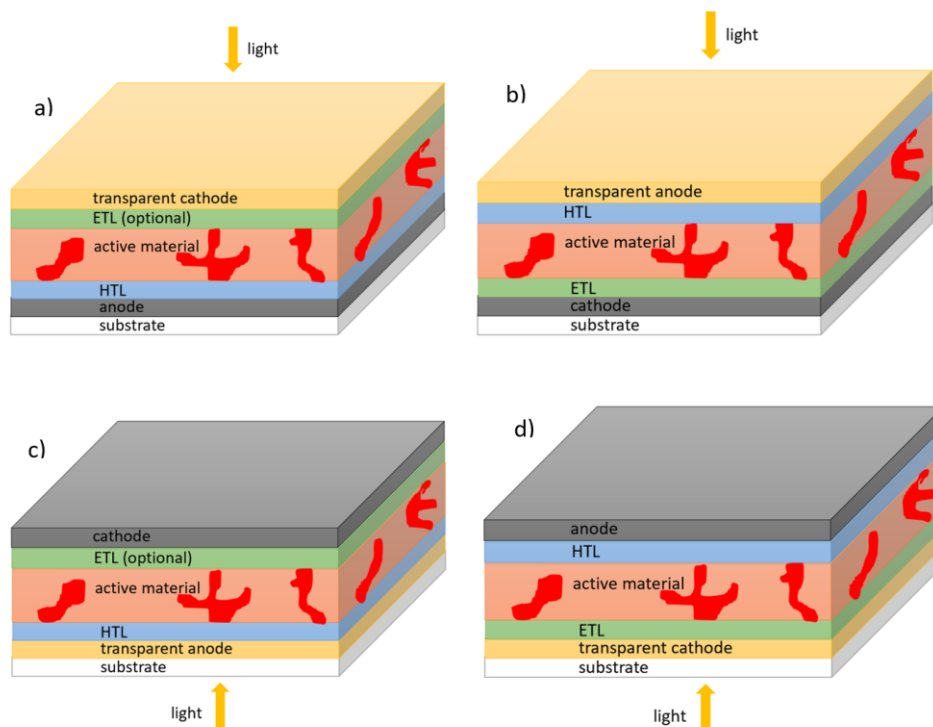
Figure 2.18. Architectures of bulk-heterojunction organic solar cells. Top illuminated solar cells are illustrated in a) with a direct structure and in b) with an inverted structure, while bottom illuminated solar cells are illustrated in c) with a direct structure and in d) with an inverted structure.

As seen in section 2.3.1, a HTL blocking electrons and transporting holes is sandwiched between the anode and the active material to separate the charges. In a direct structure, while not strictly required to have a functional solar cell, an Electron-Transport layer (ETL) is often added in order to achieve good performance[31]. It is believed that this additional layer improves the efficiency of the solar cells by preventing exciton quenching by the metal cathode[102, 103].

The inverted geometry (Figure 2.18b and d) has a few advantages over the direct geometry. With direct solar cells, the top electrode is often made of low work function metals, such as aluminium, which are prone to oxidation and degradation. This can be avoided in inverted solar cells by using higher work function metals, such as gold or silver, as top electrode[31]. However, in inverted solar cells, the ETL is not optional as it acts as a planarization layer to prepare the cell for the deposition of the active layer – a role that the HTL likewise plays in direct solar cells[13]. Furthermore, it has been widely reported that polymer/fullerene blends suffer from a vertical phase separation during film formation with the fullerene (electron acceptor) concentrating at the bottom of the film[31, 75, 104, 105]. Thus, as illustrated in Figure 2.19, inverted solar cells with a bottom cathode (electron collecting electrode) can advantageously exploit this phase separation - provided they have a proper ETL to avoid exciton quenching, which would be more severe than in a direct structure. Indeed, no example of inverted solar cells without an ETL was found in the literature.
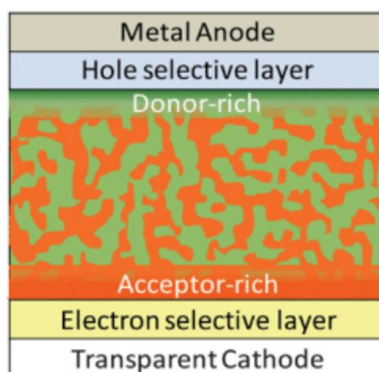
Figure 2.19. Schematic illustration of the vertical separation of a polymer:fullerene blend in an inverted solar cell. The fullerene, the electron acceptor, concentrates at the bottom of the cell during film formation. The inverted cell structure, with a bottom cathode, can therefore exploit this phase separation. Adapted from (Yip and Jen, 2012)[75].

### 2.3.3    Organic Solar Cells Materials

As discussed previously, organic solar cells are often made with an active material composed of a polymer-fullerene blend, interfacial layers, and electrodes. The following paragraphs discuss some commonly used materials in the fabrication of organic solar cells.

#### 2.3.3.1    *Active Layer*

Two frequently used polymer:fullerene blends are discussed in this section: P3HT:PC$_{61}$BM and PTB7:PC$_{71}$BM. The polymer P3HT is frequently used as a donor material in organic solar cells[13, 72]. While soluble in organic solvents, P3HT produces long, narrow fibrils which form paths for charge transportation once crystallized[19, 106]. The fullerene PC$_{61}$BM is a common acceptor in heterojunction solar cells[13]. It has a high electron affinity, good conductance and is transparent in the visible range[19]. For optimized performance, P3HT should be slightly in excess in a P3HT:PC$_{61}$BM blend[72] with a (1:0.8) ratio. Figure 2.20 shows the effect of different ratios of P3HT:PC$_{61}$BM blends on the J-V characteristic curve of a solar cell.
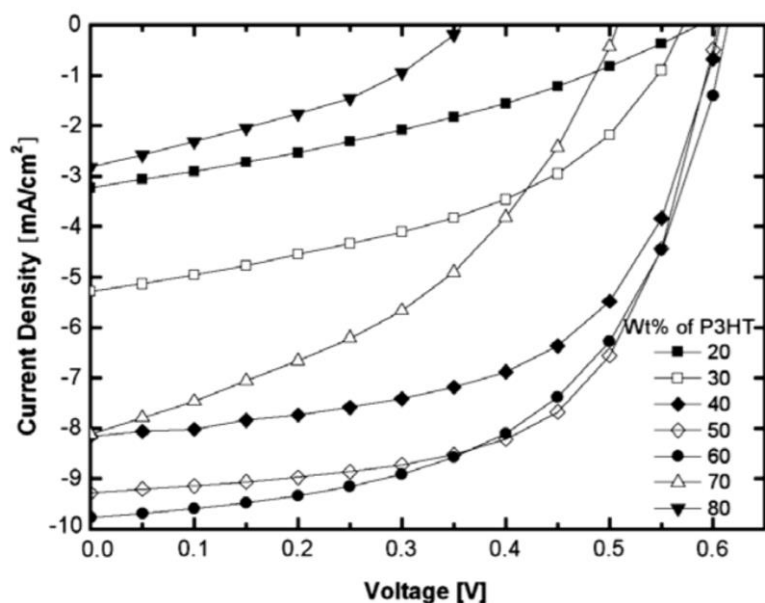
Figure 2.20. Effect of different ratios of P3HT:PC$_{61}$BM blends on the J-V characteristic curve of a solar cell. Best results are achieved when P3HT:PCBM ratio of (1:0.8). Adapted from (Baek *et al.*, 2010)[104].

The thickness of the active layer also plays an important role in the overall efficiency. If the active layer is too thin, not enough light would be absorbed for the generation of excitons, but if the material is too thick, the electrons and holes would recombine within the active layer before they have time to reach the interfacial layers. Figure 2.21 shows the relationship between active layer thickness and efficiency based on a survey of 579 papers dealing with P3HT:PC$_{61}$BM heterojunction solar cells. Based on this graph, the efficiency reaches a maximum when the active layer thickness is about 90 nm.
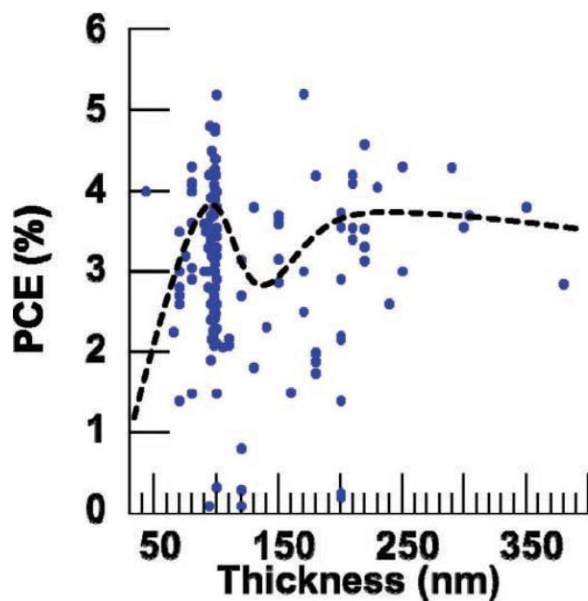
Figure 2.21. Efficiency as a function of P3HT:PC$_{61}$BM active layer thickness. The dots represent the reported thickness and associated efficiencies. A thickness of 90 nm produces the maximum efficiency and has been the choice of several studies. Adapted from (Dang *et al.*, 2011)[72].

P3HT:PC$_{61}$BM also requires thermal annealing for best results[18, 72, 107, 108]. As shown in Figure 2.22, the P3HT and PC$_{61}$BM form networks allowing for the passage of electrons and holes after annealing.
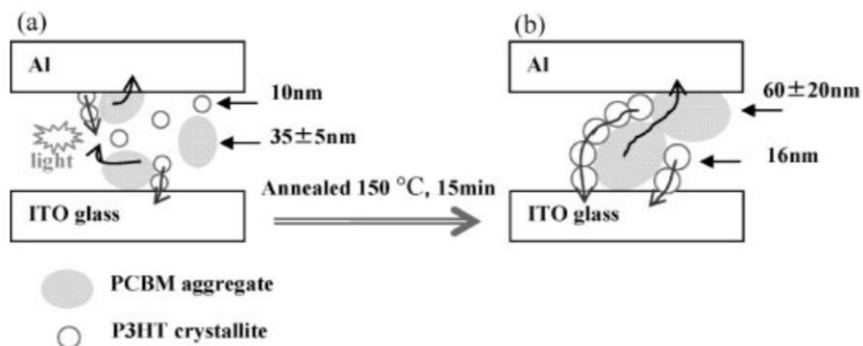


Figure 2.22. Schematic representation of P3HT:PC$_{61}$BM blends a) in non-annealed solar cell and b) after annealing at 150˚C for 15 minutes. The annealed device shows a good percolated network allowing for the passage of electrons and holes to the electrodes. Adapted from (Chiu *et al.*, 2008)[107].

In this thesis, a second polymer with low band gap and optimized absorption spectrum is also used: PTB7. PTB7 is normally used with the fullerene $PC_{71}BM$, a common acceptor for low band gap donor polymer[108] as it has an extended absorption spectrum that compliments the one from PTB7 and significantly increases the $J_{sc}$[108]. The additive 1,8-diiodooctane (DIO) is often added to the blend as it was shown to increase charge generation rate, reduce recombination and increase the electrons mobility, resulting in a three-fold increase in efficiency, though at the expense of a decrease in device stability[108-112]. Contrary to $P3HT:PC_{61}BM$ solar cells where P3HT is in excess, $PTB7:PC_{71}BM$ solar cells are normally made with a 1:1.5 ratio[109, 110, 113-115]. While the P3HT blend beneficiated from thermal annealing, PTB7 blends can lose their efficiency if thermally annealed[20, 114]. This is because the P3HT blend typically uses a lower ratio of acceptor, such as 1:0.8. However, in the case of higher acceptor ratio such as the 1:1.5, thermal annealing causes the acceptor molecules to diffuse inside the donor domains, thus preventing their crystallization[114, 115]. Instead, $PTB7:PC_{71}BM$ solar cells can be slowly dried under nitrogen atmosphere[116].

### 2.3.3.2 *Interfacial Layers*

Interfacial layers, be it HTL or ETL, are inserted between the active layer and the electrodes. The material chosen should take into consideration the energy level alignment to ensure charge selectivity[75]. Figure 2.23 shows the energy levels of some commonly used materials in organic solar cells. Other important requirements include, amongst others: promoting Ohmic contact formation between electrodes and the active layer, having a large bandgap to confine excitons in the active layer, be conductive to reduce resistive losses, having low absorption in the visible range, and be chemically and physically stable[75]. Some common interfacial layer materials meeting those requirements are listed discussed below.
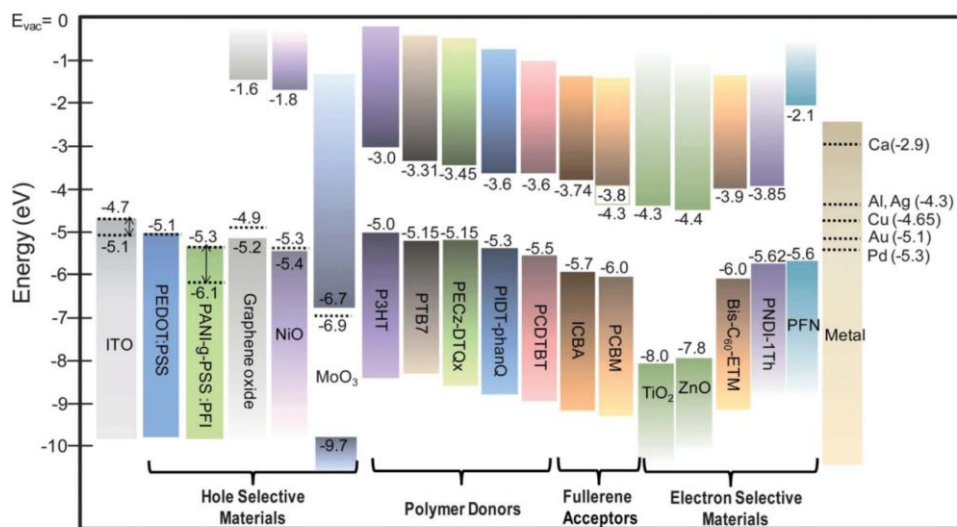


Figure 2.23. Energy levels of some common components used in organic solar cells. Adapted from (Yip and Jen, 2012)[75].

Poly(3,4-ethylenedioxythiophene):poly(styrene sulfonate) (PEDOT:PSS) is the most commonly used HTL[13, 75, 117] due to its good film-forming properties, high transparency, thermal stability[23], and high work function of 5.0-5.2 eV matching the HOMO level of P3HT and PTB7 polymers[31]. PEDOT is a highly conductive[24] conjugated polymer but is not soluble in comment solvents[118]. PSS, an insulating and hydrophilic polymer[24] is added to EDOT during polymerization to improve the solubility of PEDOT in water[13]. However, as organic layers used in solar cells are hydrophobic, care must be taken to chose a formulation with a high wettability when this HTL is used in an inverted structure in order to ensure the HTL spread well over the active layer[31].

While selecting an anode is straightforward with the availability of high work function metals such as gold or silver, the selection of the cathode poses a challenge. Most energy levels of low work function metals - such as aluminum - or transparent oxides – such as ITO – do not match well with the LUMO level of the acceptors[31]. Furthermore, when conjugated polymers come into contact with a metal cathode, it was found that the metal atoms diffuse into the polymer, creating a layer that increases the electron injection barrier and lower the FF of the solar cells[19]. A properly chosen ETL can therefore improve the efficiency of the solar cell by not only matching the energy levels of the active layer and electrodes, but also by providing a protective layer preventing the diffusion of the metal into the active layer. In direct solar cells, lithium fluoride (LiF), calcium (Ca) and bathocuproine (BCP) are often used as ETL[75, 102, 119, 120], while zinc oxide (ZnO) is often used in inverted solar cells[13]. Figure 2.24 shows the effect of adding a Ca or BCP ETLs in a direct structure solar cell.
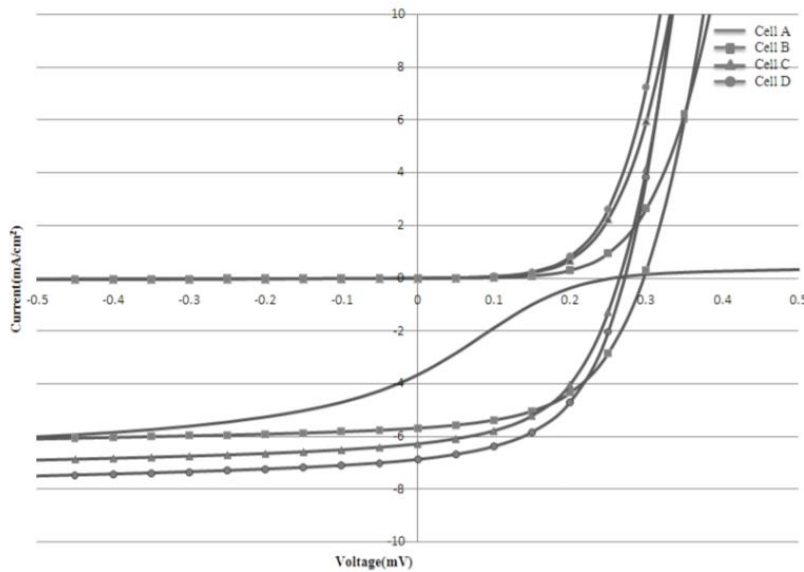


Figure 2.24. Effect of interfacial layers between the active layer and the cathode in a direct structure solar cell. Cell A is a reference device, Cell B, C, and D include respectively interfacial layers of Ca, BCP, and BCP + Ca. Adapted from (Kim *et al.*, 2010)[120].

### *2.3.3.3 Electrodes*

The active material and interfacial layers are sandwiched between two electrodes: the anode, the hole-collecting electrode, and the cathode, the electrons collecting electrode. The front electrode should be transparent to allow absorption of the light by the active material, while the back one should ideally be reflective to reflect non-absorbed light back into the cell. ITO is commonly used as the transparent electrode in organic solar cells. However, as discussed in section 1.1.3, it is responsible for the majority of the production costs and, as such, finding a low-cost replacement is crucial for the commercial feasibility of organic solar cells. Alternatives should be optically transparent and have a high conductivity, two parameters which are often conflicting[13] as transparency normally implies thinner material while conductivity is increased with material thickness. Commercially available ITO usually have a conductivity of 4000 S/cm and a transmittance of $> 80\%$[13]. Alternatives to ITO include nanomaterials (e.g. carbon nanotubes, graphene, metal nanowires and metal nanogrids), metal, metal oxides and polymers[13]. In this thesis, two alternatives were considered: ultra-thin metal and transparent polymer electrodes.

To use metal as an alternative, the film must be ultra-thin for a reasonable transmittance of the light through the metal. However, a reduction in thickness also leads to an increase in sheet resistance. For thin metal films, the ideal thickness has been found to be around 5-10 nm for aluminium (Al), silver (Ag) and gold (Au)[13, 121, 122], with silver having the highest conductivity at room temperature. With a deposition rate of 0.2 nm/s, a thickness of at least 10 nm is required to achieved continuous film formation for silver - a thickness known as the percolation thickness[122]. Metals also exhibit a high reflectance, which was calculated to be 63% in a 10 nm thick layer of silver[13, 121, 123]. As light reflected is not available for absorption by the active material, this represents a significant loss. The combination of the high conductivity of a metal and the high transmission of a transition metal oxide such as molybdenum trioxide ($MoO_3$) offers a promising approach. The top layer of a $MoO_3$/Ag/$MoO_3$ tri-layer anode serves as a transparent conducting refractive index matching layer, reducing the large amount of reflection and lowering series resistance, while the bottom layer acts as a HTL to improve hole collection[121]. Nguyen *et al.*[122] showed that optimized layers thicknesses for the stack is $MoO_3$(20 nm)/Ag (10 nm)/$MoO_3$(35 nm). This combination achieved a maximum transmittance of 86% at a wavelength of 465 nm and an averaged transmittance of 70% in the visible range (350-800 nm).

Another alternative to ITO is to use polymeric transparent conductors, which also have for advantage that they can be solution processed and are therefore compatible with mass production techniques. Highly conductive grades of PEDOT:PSS can be used as a combined HTL and transparent conductor, and have been used both as a bottom or top electrode[124]. Regular grade PEDOT:PSS used as HTL has a conductivity around 1 to 10 S/cm [13], three orders of magnitude lower than that of ITO (4000 S/cm), and therefore is not a suitable candidate for a transparent electrode. Higher conductivity formulations of PEDOT:PSS, such as Heraeus Clevios[TM] PH1000, are now commercially available. With secondary doping, such as the addition of dimethyl sulfoxide (DMSO) or ethylene glycol (EG), and chemical or thermal post-treatment[23, 24], PEDOT:PSS have been successfully employed in organic solar cells as ITO replacements[13, 25-28, 33, 91, 117, 124, 125]. A high conductivity of 4380 S/cm, achieved by sulfuric acid ($H_2SO_4$) post-treatment, has also been reported[23]. Figure 2.25 shows the timeline of different treatment used to improve the conductivity of PEDOT:PSS.
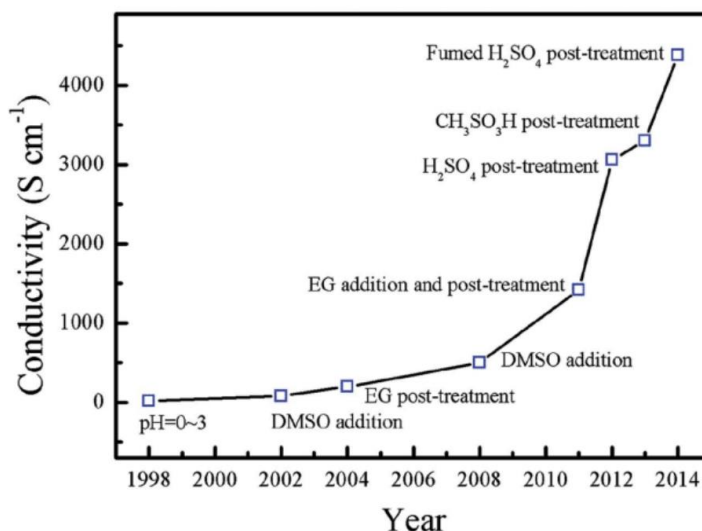
Figure 2.25. Timeline of PEDOT:PSS treatment aimed at improving its conductivity. Adapted from (Shi *et al.*, 2015)[23].

As discussed earlier in section 2.3.3.2, the spin-coating of an aqueous solution of PEDOT:PSS on an hydrophobic active layer poses an additional challenge in an inverted structure. While some formulations of PEDOT:PSS, such as Heraeus Clevios[TM] HTL Solar, include surfactants to improve their wettability, the highly conductive PEDOT:PSS grade PH1000 cannot be used as is on top of the active layer without additional treatment. Several strategies have been used to address this issue, a popular one being the use of additive such as Zonyl FS-300[31-33], Triton X-100 (TX-100)[29, 30], methanol[28], polyethylene glycol (PEG)[25, 26], EG[25-27]. Oxygen, nitrogen and argon plasma treatments have also been used to reduce the hydrophobic nature of the active layer[27]. Another approach has been the use of dual – or multiple - layers, with the first layer being a formulation with higher wettability but lower conductive of PEDOT:PSS and PH1000 as the top layer[124, 126]. Regular PEDOT:PSS and PH1000 blends have also been successfully employed[126].

This section of the thesis focused on the theory behind organic solar cells. Conjugated polymers were shown to be able to absorb the solar energy, generating bound electrons and holes in the form of excitons that could be dissociated with a second material. The mixing of the two materials into a bulk-heterojunction greatly improved the efficiency of organic solar cells. Direct and inverted structures were explored, and common materials used in the fabrication of organic solar cells were presented. Despite various advantages, organic solar cells need to remain thin due to short exciton lifetime, a limitation which negatively impacts their efficiencies. Plasmonic organic solar cells, with enhancement from light coupling, offers a potential solution.

## 2.4    PLASMONIC ORGANIC SOLAR CELLS

When excited by an oscillating electro-magnetic (EM) wave (i.e. by light) at optical frequencies, the free electrons in a metal will oscillate. Under the right conditions, the electrons can coherently and collectively oscillate, generating a longitudinal wave of electrons, as illustrated in Figure 2.26. The wave of electron density and associated induced EM field is referred to as surface plasmons (SP)[17, 127].
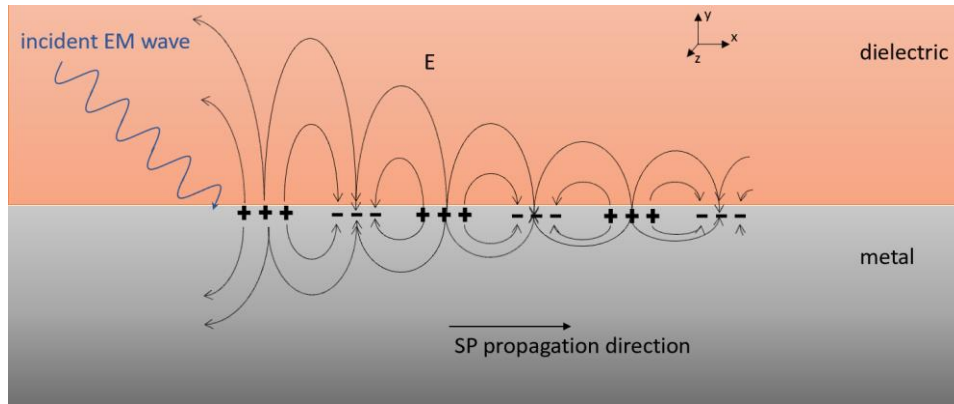
Figure 2.26. Surface plasmons schematic. The charge density oscillations induce an evanescent EM wave at the interface propagating in the *x*-direction and exponentially decaying in the *y*-direction.

While often used as an optical monitor of changes in the local environment in fields such as electrochemistry and biosensing [128, 129], SPR can give rise to enhanced optical near-fields which is of interest in the study of solar cell efficiency enhancements[17]. In this section, plasmonic organic solar cells will be studied by first examining light as an EM wave, before looking at the SPR dispersion relation and excitation. Two-beam interference theory will then be introduced. The end of this section then uses the interference theory to show how SRGs can be patterned on azobenzene thin films to excite SPR in organic solar cells.

### 2.4.1 The Electro-Magnetic Evanescent Wave

Before discussing SPR in more detail, a mathematical description of an EM evanescent wave is required. An EM wave consists of oscillating electric and magnetic fields, denoted $E$ and $H$ respectively, which are orthogonal to each other and transverse to the direction of propagation[130], as illustrated in Figure 2.27.
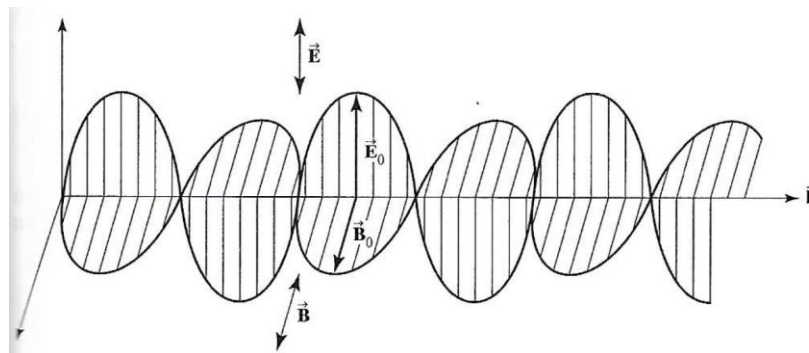


Figure 2.27. An electro-magnetic wave. In this graph, the magnetic field $H$ is denoted as $B$. The electric field $E$, the magnetic field $B$, and wavevector $k$ are mutually perpendicular. Adapted from (Pedrotti *et al.*, 2007)[130].

An EM wave travelling $\boldsymbol{k}$ direction can be described by its electrical field[127, 130]:

$$E = E_o \exp(-j\omega t - j\boldsymbol{k} \cdot \boldsymbol{r}) \tag{2.7}$$

where $\boldsymbol{E_o}$ is the amplitude of the electrical field, $\omega$ it the angular frequency, $\boldsymbol{k}$ is the wavevector and $\boldsymbol{r}$ is the position vector.

At the interface between two media with different indices of refraction $n_1$ and $n_2$, the wave will be refracted, as illustrated in Figure 2.28– in this case with $n_1 < n_2$.
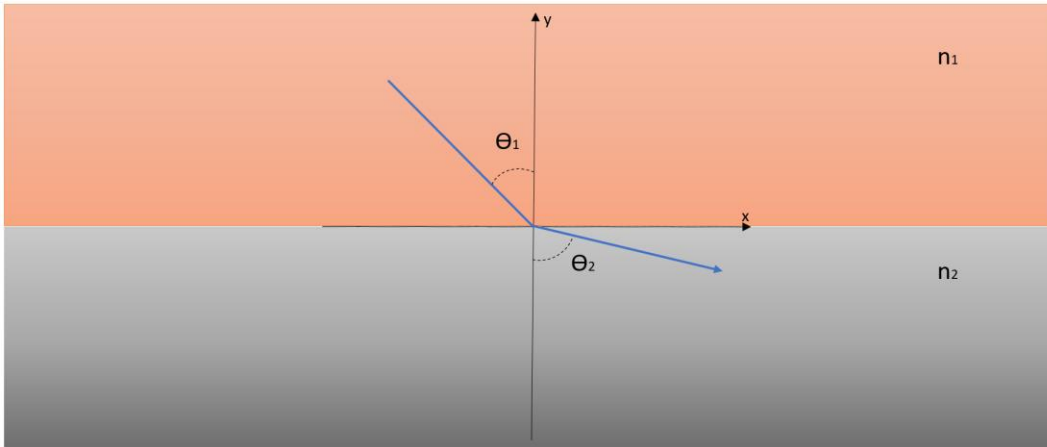


Figure 2.28. Refraction of a wave at the interface of two media with different index of refraction. In this case, $n_1 < n_2$.

Using Snell's law of refraction[127, 130], one obtains:

$$n_1 \sin\theta_1 = n_2 \sin\theta_2 \tag{2.8}$$

where $\theta_1$ and $\theta_2$ are the angles of incidence and transmission, respectively. For a SPR wave to exist and propagate in the $x$-direction, one must have:

$$k_{x,1} = k_{x,2} \equiv k_x \tag{2.9}$$

The magnitude of the wavevector of a wave propagating in $x$-direction is given by[127]:

$$k = \sqrt{k_x^2 + k_y^2} = n\frac{2\pi}{\lambda} = n\frac{\omega}{c} = \omega\sqrt{\mu\varepsilon} \tag{2.10}$$

40

where $n$ is the refractive index of the medium, $\lambda$ is the wavelength of the wave, $c$ is the propagation velocity in vacuum, $\mu$ is the permeability and $\varepsilon$ is the permittivity of the medium. Thus, rearranging Equation (2.10) for medium 2 and geometry:

$$k_{y,2}^2 = k_2^2 - k_{x,2}^2 = \left(\frac{2\pi}{\lambda}\right)^2 (n_2^2 - n_2^2 \sin^2 \theta_2) \qquad (2.11)$$

Using Equation (2.8) in Equation (2.11):

$$k_{y,2}^2 = \left(\frac{2\pi}{\lambda}\right)^2 (n_2^2 - n_1^2 \sin^2 \theta_1) = n_1^2 \left(\frac{2\pi}{\lambda}\right)^2 \left(\frac{n_2^2}{n_1^2} - \sin^2 \theta_1\right) \qquad (2.12)$$

If $n_1 > n_2$, such as would be the case for most dielectric/metal interface, $k_{y,2}$ would be purely imaginary for $sin\theta_1 > \frac{n_2}{n_1}$. Therefore, the wave at the interface would not only be parallel to the surface in the $x$-direction, but also exponentially decaying in the $y$-direction. The complex fields in the two media can be written as:

$$\boldsymbol{E_1} = \left(E_{x,1}, E_{y,1}, 0\right) \exp - j\left(k_{x,1}x + k_{y,1}x\right) \qquad (2.13)$$

$$\boldsymbol{H_1} = \left(0,0, H_{z,1}\right) \exp - j\left(k_{x,1}x + k_{y,1}x\right) \qquad (2.14)$$

$$\boldsymbol{E_2} = \left(E_{x,2}, E_{y,2}, 0\right) \exp - j\left(k_{x,2}x + k_{y,2}x\right) \qquad (2.15)$$

$$\boldsymbol{H_2} = \left(0,0, H_{z,2}\right) \exp - j\left(k_{x,1}x + k_{y,2}x\right) \qquad (2.16)$$

### 2.4.2 Surface Plasmon Dispersion Relation

The relation between the angular frequency and the wavevector for a SPR at the dielectric/metal interface of two half-infinite media, called the dispersion relation[127, 128], can be derived from Maxwell's equations[131]. Maxwell's fourth equation for oscillating films is given by[131]:

$$\nabla \times \boldsymbol{H} = \sigma \boldsymbol{E} - j\omega\varepsilon \boldsymbol{E} = -j\omega \left(\varepsilon + \frac{\sigma}{\omega}\right) \boldsymbol{E} = j\omega \tilde{\varepsilon} \boldsymbol{E} \qquad (2.17)$$

with

$$\varepsilon = \varepsilon_0 \varepsilon_r \qquad (2.18)$$

$$\tilde{\varepsilon} = \varepsilon + j\frac{\sigma}{\omega} = \varepsilon' + j\varepsilon'' \qquad (2.19)$$

where $\varepsilon$ and $\sigma$ are the permittivity and the conductivity of the medium, respectively. The permittivity can be expressed as a product of a relative permittivity $\varepsilon_r$ and the free-space permittivity $\varepsilon_0$. The complex permittivity, $\tilde{\varepsilon}$, can be divided in a real and imaginary part. The real part of the complex permittivity, $\varepsilon'$, is a measure of a material's ability to store energy, while the imaginary part, $\varepsilon''$, is a measure of how lossy a material is to an electric field[131]. Applying equation (2.17) to the set of equations (2.13) to (2.16):

$$k_{y,1} H_{z,1} = -\omega \widetilde{\varepsilon_1} E_{x,1} \tag{2.20}$$

$$k_{y,2} H_{z,2} = -\omega \widetilde{\varepsilon_2} E_{x,2} \tag{2.21}$$

Solar cell materials are generally non-magnetic[132], which implies that the magnetic field is continuous at the interface. $E_x$ is also continuous at the interface, since there is no boundary orthogonal to $E_x$. As there are no free charges, the normal component of the electric displacement field $D_y$ is also continuous[131]. As $\boldsymbol{D} = \varepsilon \boldsymbol{E}$ for a linear medium[131], it is the discontinuity in the relative permittivity which force $E_y$ to change. Therefore, using these boundary conditions with Equations (2.20) and (2.21):

$$\frac{\varepsilon_1}{k_{y,1}} = \frac{\widetilde{\varepsilon_2}}{k_{y,2}} \tag{2.22}$$

The magnitude of the wavevectors can also be expressed in terms of the relative permittivity of the media and the magnitude of the light wavevector. Recalling Equation (2.10), one can obtain:

$$k_{y,1}^2 = \omega^2 \mu_1 \varepsilon_1 - k_x^2 \tag{2.23}$$

$$k_{y,2}^2 = \omega^2 \mu_2 \widetilde{\varepsilon_2} - k_x^2 \tag{2.24}$$

Dividing Equations (2.23) by (2.24):

$$\frac{k_{y,1}^2}{k_{y,2}^2} = \frac{\omega^2 \mu_1 \varepsilon_1 - k_x^2}{\omega^2 \mu_2 \widetilde{\varepsilon_2} - k_x^2} \tag{2.25}$$

Using Equations (2.22) in (2.25) and assuming that the relative permeability is unity for non-magnetic materials:

$$k_x = \omega \sqrt{\frac{\mu_0 \varepsilon_1 \widetilde{\varepsilon_2}}{\widetilde{\varepsilon_2} + \varepsilon_1}} \tag{2.26}$$

Therefore, the SPR dispersion relation $k_{SP}$ for a flat interface is:

$$k_{SP} = k_x = \frac{\omega}{c} \sqrt{\frac{\varepsilon_{r,1} \widetilde{\varepsilon_{r,2}}}{\widetilde{\varepsilon_{r,2}} + \varepsilon_{r,1}}} \tag{2.27}$$

where

$$c = \frac{1}{\sqrt{\mu_0 \varepsilon_0}} \tag{2.28}$$

For an evanescent wave to exist at the interface, $k_{sp}$ must have a real part. This condition is met, from Equation (2.27), when:

$$\frac{\varepsilon_{r,1}\varepsilon'_{r,2}}{\varepsilon_{r,1} + \varepsilon'_{r,2}} > 0 \tag{2.29}$$

In the case where medium 1 is a dielectric and medium 2 is a metal, $\varepsilon_{r,1} > 0$ and $\varepsilon'_{r,2} < 0$ since metals contain a large number of free electrons for frequencies below the plasma frequency of the metal – which is generally in the UV region[127]. Therefore, the numerator of Equation (2.29) is negative. Consequently, the denominator of Equation (2.29) also needs to be negative. This implies that $\varepsilon'_{r,2} < -\varepsilon_{r,1}$ or, i.e., that the commonly accepted SPR condition is when the permittivity changes sign at the dielectric-metal interface[127-129, 132].

### 2.4.3 Excitation of Surface Plasmons Resonance

With the SPR condition established, the next step in understanding SPR is to see how it can be excited. According to the electron model of an electron gas, neglecting damping, the real part of relative permittivity of metal at optical frequency is given by [17, 127]:

$$\varepsilon'_r = 1 - \frac{\omega_p^2}{\omega^2} \tag{2.30}$$

where $\omega_p$ is the plasma frequency and is an intrinsic property of metals. Substituting Equation (2.30) into Equation (2.27):

$$k_x = \frac{\omega}{c}\sqrt{\frac{\varepsilon_{r,1}\left(1 - \frac{\omega_p^2}{\omega^2}\right)}{\varepsilon_{r,1} + 1 - \frac{\omega_p^2}{\omega^2}}} = \frac{\omega}{c}\sqrt{\frac{\varepsilon_{r,1}(\omega^2 - \omega_p^2)}{(\varepsilon_{r,1} + 1)\omega^2 - \omega_p^2}} \tag{2.31}$$

Recalling that the wavevector of light is:

$$k_0 = \frac{\omega}{c} \tag{2.32}$$

and as $\varepsilon_{r,1} \geq 1$ (medium 1 being a dielectric material), the wavevector of a SPR is always larger that that of a light. According to the de Broglie relation[133], the momentum $\boldsymbol{p}$ and wavevector $\boldsymbol{k}$ are related by:

$$\boldsymbol{p} = \frac{2\pi}{h}\boldsymbol{k} \tag{2.33}$$

where $h$ is the Planck constant. Consequently, a SPR always has a larger momentum than a photon at the same frequency. This implies that light shining on a flat metal cannot simultaneously provide the correct angular frequency and wavevector. Therefore, additional momentum must be provided to excite SPR. Nevertheless, coupling of photons into SPR can be achieved by using either photon tunneling in the total internal geometry (Kretschmann and Otto configurations) or diffraction effects[127, 128, 134], as illustrated in Figure 2.29.
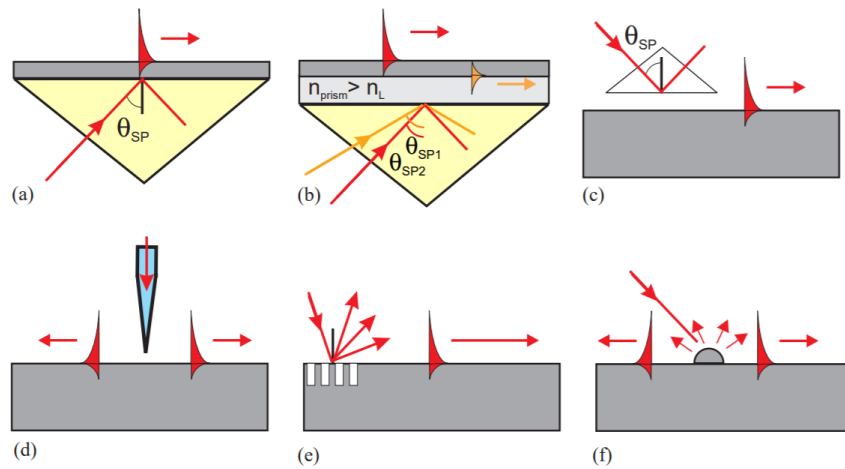
Figure 2.29. Surface plasmon excitation configurations. (a) Kretschmann geometry, (b) two-layer Kretschmann geometry, (c) Otto geometry, (d) excitation with a near-field scanning optical microscopy (SNOM) probe, (e) diffraction on a grating, and (f) diffraction on surface features. Adapted from (Zayats *et al.*, 2005)[134].

Of particular interest for this thesis is the excitation by diffraction on a grating. Diffraction gratings are made of periodic diffracting elements separated by a distance comparable to the wavelength of incident light, often in a sinusoidal shape, and can be reflective or transmissive. The light will be diffracted by the grating into multiple orders, with the $0^{th}$ order (m=0) being light that is not diffracted. By convention, beams diffracted to the right of the $0^{th}$ order are considered positive orders, while beams diffracted to the left have negative orders. Figure 2.30 shows the diffraction of light using a reflective grating.
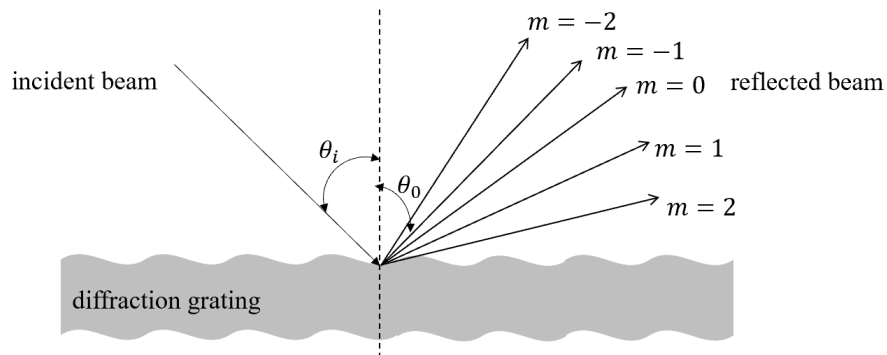


Figure 2.30. Diffraction of light with a reflective grating. The 0th order correspond to a reflection angle equal to the incident angle $\theta_i = \theta_0$ (i.e. no diffraction).

In this thesis, diffraction gratings will be manufactured on azobenzene thin films by laser lithography using a Lloyd's mirror interferometer. An understanding of two-beam interference theory is useful to comprehend this technique.

### 2.4.4 Two-Beam Interference

Let's consider two plane waves travelling at the same frequency combining at point P, as illustrated in Figure 2.31.
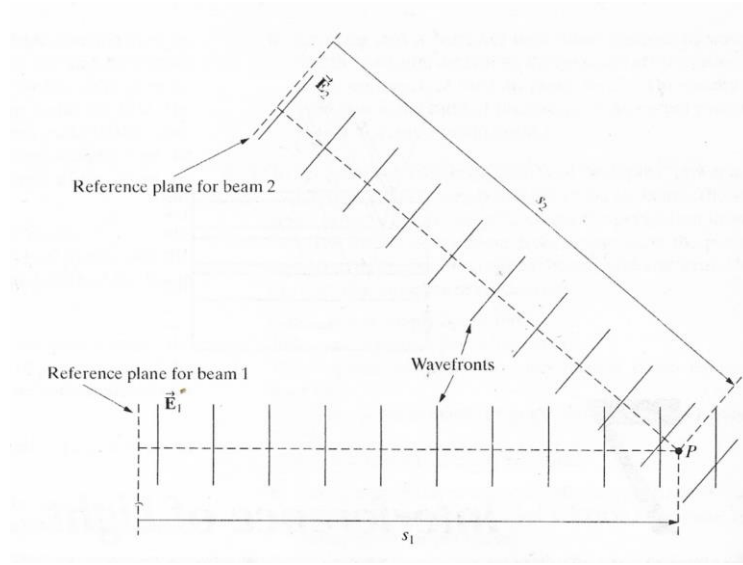


Figure 2.31. Two travelling plane waves interference, where $s_1$ and $s_2$ are the distances traveled by each beam from their sources to point P. Adapted from (Pedrotti *et al.*, 2007)[130].

The waves can be expressed in terms of their electric fields[130]:

$$E_1 = E_{01}\cos(ks_1 - \omega t + \phi_1) \tag{2.34}$$

$$E_2 = E_{02}\cos(ks_2 - \omega t + \phi_2) \tag{2.35}$$

where $E_0$ is the amplitude of the electrical field, $k = \frac{2\pi}{\lambda}$ is the amplitude of the wavevector, $s$ is the distance traveled by each beam from its respective source to point P, $\omega$ is the angular frequency, and $\phi$ represents the phase of a wave at its source at time $t = 0$. Given the principle of superposition[130], the electric field at point P is given by:

$$E_P = E_1 + E_2 \tag{2.36}$$

The irradiance $I$ (W/m$^2$) at any point is given by[130]:

$$I = \varepsilon_o c \langle E^2 \rangle \tag{2.37}$$

Therefore, using Equation (2.36) in Equation (2.37):

$$I_p = \varepsilon_o c \langle E_p^2 \rangle = \varepsilon_o c \langle (E_1 + E_2) \cdot (E_1 + E_2) \rangle \tag{2.38}$$

$$I_p = \varepsilon_o c \langle E_1 \cdot E_1 + E_2 \cdot E_2 + 2E_1 \cdot E_2 \rangle \tag{2.39}$$

$$I_p = I_1 + I_2 + I_{12} \tag{2.40}$$

where $I_1$ and $I_2$ are the irradiance of the individual beams and $I_{12}$ is the interference term. The interference term can provide either enhancement (constructive interference) or diminution (destructive interference) of the irradiance. Using Equations (2.34) and (2.35), the interference term can be rewritten as:

$$I_{12} = \varepsilon_o c \langle 2E_{01} \cdot E_{02} \cos(ks_1 - \omega t + \phi_1) \cos(ks_2 - \omega t + \phi_2) \rangle \tag{2.41}$$

Defining $\alpha \equiv ks_1 - \omega t + \phi_1$ and $\beta \equiv ks_2 - \omega t + \phi_2$, the notation of Equation (2.41) can be simplified:

$$I_{12} = \varepsilon_o c \langle 2E_{01} \cdot E_{02} \cos(\alpha - \omega t) \cos(\beta - \omega t) \rangle \tag{2.42}$$

Using the identity $2\cos(A)\cos(B) = \cos(A + B) + \cos(B - A)$[135], Equation (2.42) becomes:

$$I_{12} = \varepsilon_o c E_{01} \cdot E_{02} \langle \cos(\alpha + \beta - 2\omega t) + \cos(\beta - \alpha) \rangle \tag{2.43}$$

As the first term in the time average is taken over a rapidly oscillating cosine function, Equation (2.43) reduces to:

$$I_{12} = \varepsilon_o c E_{01} \cdot E_{02} \langle \cos(\beta - \alpha) \rangle = \varepsilon_o c E_{01} \cdot E_{02} \langle \cos(\delta) \rangle \tag{2.44}$$

where $\delta = \beta - \alpha = k(s_2 - s_1) + \phi_2 - \phi_1$ is defined as the phase difference between $E_1$ and $E_2$. Now, using the fact that the time average of the square of a rapidly oscillating cosine function is $\frac{1}{2}$, the irradiance of the two beams can be written as:

$$I_1 = \varepsilon_o c \langle E_1^2 \rangle = \varepsilon_o c E_{01}^2 \langle \cos^2(\alpha - \omega t) \rangle = \frac{1}{2} \varepsilon_o c E_{01}^2 \tag{2.45}$$

$$I_2 = \varepsilon_o c \langle E_2^2 \rangle = \varepsilon_o c E_{02}^2 \langle \cos^2(\beta - \omega t) \rangle = \frac{1}{2} \varepsilon_o c E_{02}^2 \tag{2.46}$$

Using Equations (2.43), (2.45) and (2.46) in (2.40), the irradiance at a point P resulting from the interference of two travelling plane waves can finally be written as:

$$I_p = I_1 + I_2 + 2\sqrt{I_1 I_2}\cos(\delta) \tag{2.47}$$

From Equation (2.40), the interference yields a maximum irradiance (constructive interference) when $\cos(\delta) = 1$, which occurs when $\delta = 2m\pi$ where $m$ is an integer. Recalling that $\delta = k(s_2 - s_1) + \phi_2 - \phi_1$, the constructive interference occurs when:

$$k(s_2 - s_1) + \phi_2 - \phi_1 = 2m\pi \tag{2.48}$$

which, using $k = \frac{2\pi}{\lambda}$, simplifies to:

$$(s_2 - s_1) + \phi_2 - \phi_1 = m\lambda \tag{2.49}$$

### 2.4.5 Diffraction Grating Equation

The two-beam interference theory can be used to derive the diffraction grating equation required for the fabrication of SRGs. Figure 2.32 below illustrate two rays incident on successive elements of the grating separated by a distance $\Lambda$, known as the grating spacing.
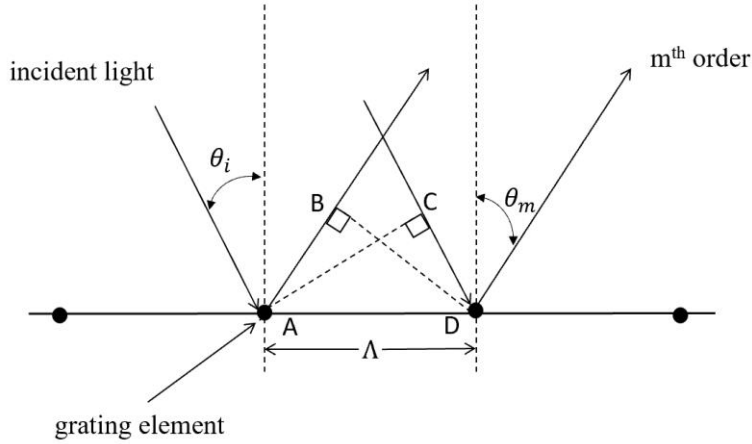


Figure 2.32. Light diffraction by two consecutive elements of a reflective grating elements separated by a distance $\Lambda$.

The optical path difference between rays from successive elements is given by:

$$\overline{AB} - \overline{CD} = \Lambda(\sin\theta_m - \sin\theta_i) \tag{2.50}$$

As previously discussed, in order for the interference to be maximum, the optical path difference must be equal to an integer multiple of the wavelength of the incident light, yielding:

$$m\lambda = \Lambda(\sin\theta_m - \sin\theta_i) \tag{2.51}$$

Rewriting Equation (2.51) in terms of the magnitude of the wavevector and isolating the diffracted angle, one obtains:

$$k\sin\theta_m = k\sin\theta_i \pm \frac{2\pi m}{\Lambda} \tag{2.52}$$

where $k\sin\theta_i$ and $k\sin\theta_m$ are the vector components of the incident and diffracted light perpendicular to the grating grooves and $\frac{2\pi}{\Lambda}$ is the magnitude of the grating vector K. Recalling that a SPR always has a larger momentum than a photon of the same frequency, the grating must increase the $x$-component of the incident light wavevector at the metal-dielectric interface, which is provided by the term $\frac{2\pi m}{\Lambda}$ of Equation (2.52), if the incident light is perpendicular to the grating grooves (with p-polarized light for a grating oriented as per Figure 2.30). Crossed-gratings would therefore allow for two polarization directions to excite surface plasmons and thus further increase the absorption of solar cells.

Finally, using the real portion of Equations (2.27) in (2.52) and $k = \frac{2\pi}{\lambda}$, and assuming a lossless dielectric material, an expression for the wavelength that will excite SPR $\lambda_{SP}$ can be derived:

$$\frac{\omega}{c}\sqrt{\frac{\varepsilon_{r,1}\varepsilon'_{r,2}}{\varepsilon_{r,1} + \varepsilon'_{r,2}}} = k\sin\theta_i \pm \frac{2\pi}{\Lambda} \tag{2.53}$$

$$\frac{2\pi}{k} = \left(\sqrt{\frac{\varepsilon_{r,1}\varepsilon'_{r,2}}{\varepsilon_{r,1} + \varepsilon'_{r,2}}} \pm \sin\theta_i\right)\Lambda \tag{2.54}$$

$$\lambda_{SP} = \left(\sqrt{\frac{\varepsilon_{r,1}\varepsilon'_{r,2}}{\varepsilon_{r,1} + \varepsilon'_{r,2}}} \pm \sin\theta_i\right)\Lambda \tag{2.55}$$

where $\varepsilon'_{r,2}$ is the real portion of the metal relative permittivity. This condition can also be written in terms of the refractive index of the dielectric $n_1$, using the relationship between the refractive index and the relative permittivity $n = \sqrt{\varepsilon_r}$:

$$\lambda_{SP} = n_1\left(\sqrt{\frac{\varepsilon'_{r,2}}{n_1^2 + \varepsilon'_{r,2}}} \pm \sin\theta_i\right)\Lambda \tag{2.56}$$

For solar cell applications, one would need to design a grating to excite SPR within the absorption range of the active material. For example, PTB7:PC$_{71}$BM has a peak absorption around

675 nm[123]. At this wavelength, its index of refraction is 2.12, while the real portion of the permittivity of aluminium is 60.00[123]. A grating spacing of 342 nm would therefore be appropriate to excite an SPR in this solar cell. As illustrated in Figure 2.33, the grating could be incorporated either as the top electrode in a direct bottom illuminated solar cell, or as the bottom electrode in an inverted top illuminated solar cell. In a direct cell structure, the active layer would need to be patterned prior to the ETL deposition since the ETL is typically to thin to be patterned, which can be achieved by using a PDMS stamp[51-54]. In an inverted structure, a layer of azobenzene can be spin-coated on the substrate and patterned by laser lithography prior to cathode deposition[55, 56]. This technique is explored further in the next section.



(a)                                                    (b)
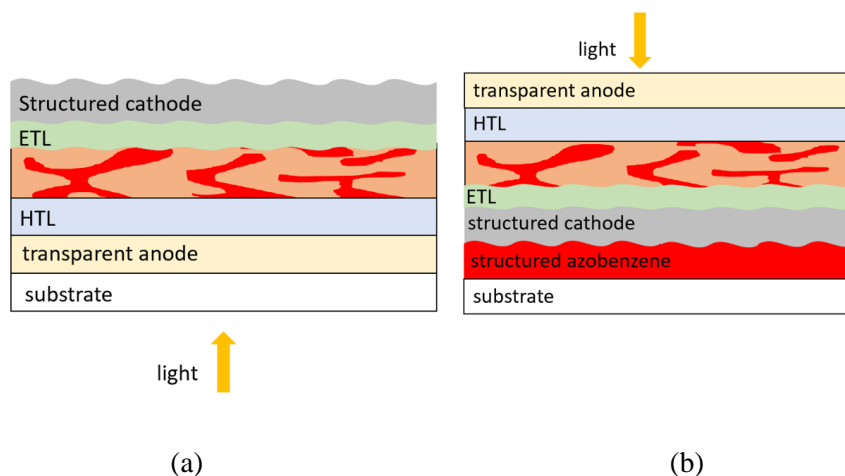
Figure 2.33. Organic solar cell structures for surface plasmons. For the direct structure in (a), the ETL can be patterned using a PDMS stamp before evaporation of the cathode. For the inverted structure in (b), a layer of azobenzene can be patterned via laser lithography before deposition of the cathode.


### 2.4.6    Surface Relief Gratings on Azobenzene Thin Films

Azobenzene is a chemical compound composed of two benzene rings linked by two nitrogen (N) atoms sharing a double bond. It exists mainly as a *trans* isomer (with the two rings oriented in opposing directions) but can be converted to a *cis* isomer (with the rings oriented in the same direction) upon absorption of specific wavelength of light. The mechanism of photoisomerization in azobenzene material is still not well understood, with two possible pathways proposed: a rotation about the N=N bond, or an inversion around the N atom[136], as illustrated in Figure 2.34. The molecules can also relax back to the *trans* form upon irradiation or when heated [67, 69].
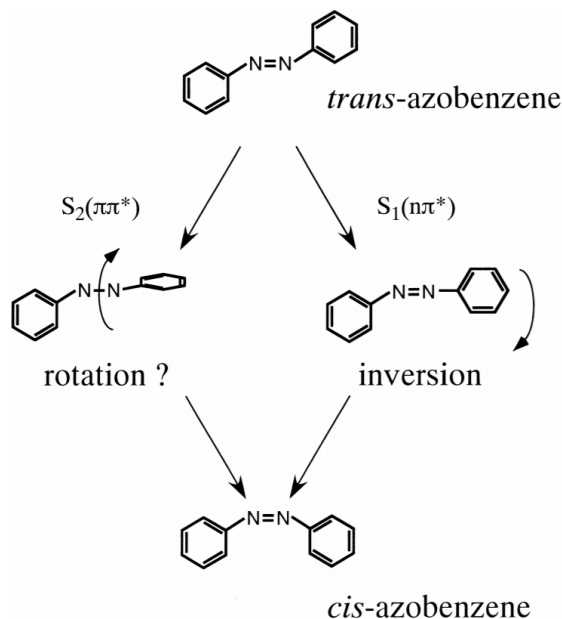
Figure 2.34. Possible mechanisms for the isomerization of azobenzene molecules from the *trans* to the *cis* form. A rotation about the N=N bond or inversion around the N atom have been proposed. Adapted from (Fujino *et al.*, 2002)[136].

As mentioned in section 1.2.5, photo-induced fabrication of SRGs on azobenzene polymer thin films was first reported by Rochon *et al.*[66] in 1995. This report noted that the azobenzene underwent a trans-cis-trans photo-isomerization when illuminated by a polarized laser beam. The trans-cis-trans cycles cause a motion of the azobenzene chromophores, which drag the molecules to which they are grafted[137]. By using an interference pattern with illuminated and dark areas, localized mass transport of the material occurs with the azobenzene molecules moving away from the areas of high irradiance into darker areas. This results in the interference pattern being photo-mechanically imprinted onto the azobenzene film. Figure 2.35 depicts a basic set-up with a Lloyd's mirror interferometer that can be used to inscribe gratings on thin azobenzene films without the use of a mask. This set-up also includes a quarter-wavelength plate to circularly polarize the laser beam, as polarization of the light was found to affect SRGs formation[137], with only the azobenzene molecules having a component dipole parallel to the light polarization direction being able to photo-isomerize[138]. Therefore, a circular polarized light was necessary to ensure that azobenzene molecules of any orientation within the thin film would be able to undergo the *trans-cis-trans* isomerisation.
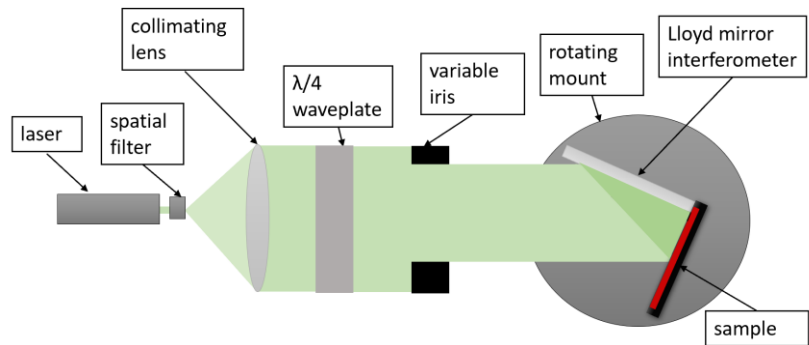
Figure 2.35. Top-view schematic of grating inscription set-up . A lens collimates the laser beam, which is then circularly polarized before irradiating the Lloyd's mirror interferometer.

A top-view of the Lloyd's mirror interferometer set-up is shown in Figure 2.36. The mirror and the sample have an angular separation of 90°. The sample mount is adjusted so that half of the laser beam is directly incident on the sample, while the other half is incident on the mirror. After striking the mirror, the half-beam is reflected onto the sample, interfering with the direct half-beam.
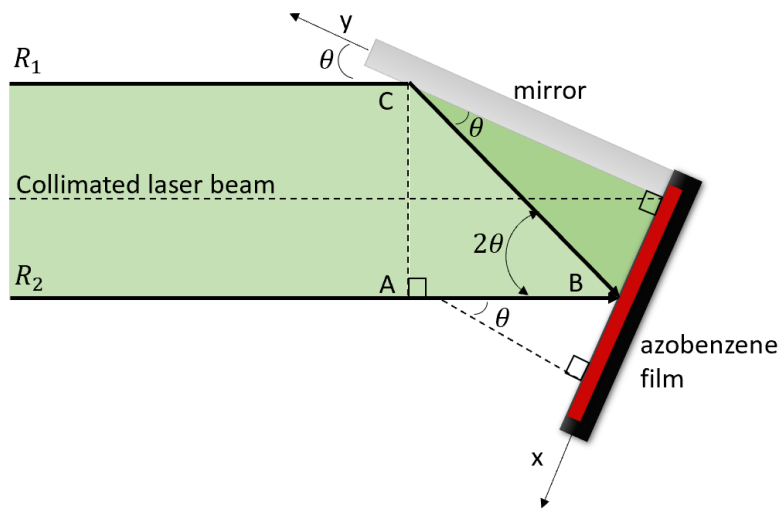


Figure 2.36. Top-view of the Lloyd's mirror interferometer. The mirror and sample form and angular angle of 90°. Half of the collimated laser bean illuminates the sample directly, while the other half is first reflected by the mirror, generating an optical path length difference and interference pattern.

Since the two interfering beam halves – the one reflected by the mirror, $R_1$, and the direct half, $R_2$, come from the same source, the condition for constructive interference, Equation (2.49), can be rewritten as:

$$s_2 - s_1 = m\lambda + \frac{\lambda}{2} \tag{2.57}$$

where the term $\frac{\lambda}{2}$ has been added to take into account the phase change due the mirror reflection. The left side of Equation (2.57) is the net path difference between the two beam halves, as illustrated in Figure 2.36. The condition for constructive interference with a Lloyd's mirror set-up therefore becomes:

$$\overline{CB} - \overline{AB} = m\lambda + \frac{\lambda}{2} \tag{2.58}$$

Using the cartesian coordinates established in Figure 2.36:

$$\overline{CB} = \frac{x}{\sin\theta} \tag{2.59}$$

$$\overline{AB} = \overline{CB}\cos(2\theta) = \frac{x}{\sin\theta}\cos(2\theta) \tag{2.60}$$

Substituting Equations (2.59) and

(2.60) in (2.58):

$$\frac{x}{\sin\theta}(1 - \cos(2\theta)) = m\lambda + \frac{\lambda}{2} \tag{2.61}$$

Using the double angle formula $\cos(2A) = 1 - 2\sin^2 A$ [135]:

$$x = \frac{\lambda}{2\sin\theta}\left(m + \frac{1}{2}\right) \tag{2.62}$$

The distance between two maxima is known as the grating spacing ($\Lambda$), and can therefore be given by:

$$\Lambda = \frac{\lambda}{2\sin\theta} \tag{2.63}$$

With a Lloyd's mirror interferometer, a SRGs with a sinusoidal pattern can be imprinted in the azobenzene film[66, 139]. The grating spacing can be controlled by modifying the angle of incidence or the wavelength of the laser beam, while the grating depth depends on both the beam irradiance and exposure time[137].

In this section, the concept and mathematics necessary to design SRGs capable of exciting SPR in an organic solar cell were explored. SRGs written on azobenzene thin films by laser lithography can be used to pattern metal electrodes in a solar cell, which would provide the additional momentum needed to excite SPR. As SPR can couple the light in the solar cell and give rise to enhanced optical near-fields, exciting SPR has the potential for significant efficiency improvement.

## 2.5    SCATTERING THROUGH SURFACE TEXTURING OF AZOBENZENE THIN FILMS

Efficiency enhancement of organic solar cells through scattering is also explored in this thesis. For solar cell applications, optical losses consist of light which has enough energy to generate electron-hole pairs but is reflected or transmitted instead of absorbed. Surface texturing can minimize reflection by deflecting the photons onto the semiconductor. The pyramid or inverted pyramid shapes are commonly used in industry, with random pyramid arrays obtained via etching of crystalline silicon reducing reflectivity by 10 %[140]. However, surface texturing is mostly used to scatter the light in the active material, which has for effect to increase the optical path length of the light within the active layer without increasing the thickness of the cell. In this section, the possibility of scattering light through surface patterning of azobenzene thin films to improve the absorption probability is explored. First, the scalar scattering theory is introduced. Corona poling is then shown as a way to create randomized nanostructures on azobenzene thin films. Finally, the bleaching of azobenzene films is discussed.

### 2.5.1    Scalar Scattering Theory

The theory of light scattering in solar cells was initially developed for conventional cells where the absorbing film is typically many light wavelengths thick. With a rough interface, the light propagation directions inside the material is randomized. This results in a much longer propagation distance inside the material and hence a substantial absorption enhancement. That theory demonstrated that absorption enhancement could reach a maximum factor of $4n^2$, where n is the refractive index of the active layer[141]. By roughening both the front and back layers, an optical path length enhancement on the order of 50 times is possible, though in practice enhancements of about 10 times have been reported[9]. For thin films, some of the basic assumptions in the conventional theory are no longer applicable, and an absorption enhancement factor of $12 \times 4n^2$ has been numerically demonstrated[142]. Thus, there is a potential for substantial improvement of the efficiency of organic solar cells through light scattering.

In 1961, Bennett and Porteous came up with the concept of Total Integrated Scatter (TIS, the total amount of light scattered by a surface) and found a functional relationship between TIS and surface roughness[143]:

$$TIS(R_q) = R_0 \left[ 1 - e^{-\left( \frac{4\pi R_q \cos \theta_i}{\lambda} \right)^2} \right] \tag{2.64}$$

where $R_0$ is the theoretical reflectance of the surface, $R_q$ is the root mean square (RMS) roughness of the surface, $\theta_i$ is the angle of incidence on the surface, and $\lambda$ is the wavelength of light. According to this equation, a rougher surface would scatter the light more efficiently than a smoother one.

When encountering a rough surface, light can be scattered forward or backward, as illustrated in Figure 2.37. The proportion of backward to forward scattering depends on the reflectance of the material, its surface roughness, the indices of refraction of both materials, the wavelenght and angle of incidence. Evidently, for solar cell applications, the proportion of forward scattering should be optimized.
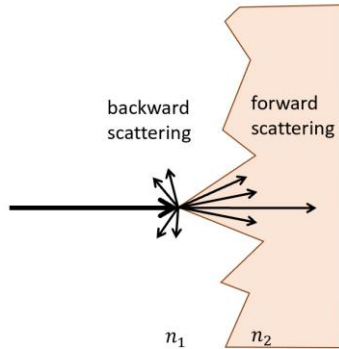


Figure 2.37. Backward and forward scattering of incident light at the interface of a rough surface.

Due to the quasi-random character of the nano-textured surfaces, the mathematical treatment of the scattering problem is highly non-trivial. However, the effect of the size of the nanostructure can be deducted from experimental results. In one of those experiment, Baek *et al*. [60] incorporated silver nanoparticles (AgNPs) in the PEDOT:PSS layer of PTB7:PC$_{71}$BM inverted solar cells. They found that, initially, increasing the AgNPs size led to an enhancement of the efficiency due to increase $J_{sc}$ – a result consistent with the theory that scattered light improves the absorption of photons by the active material. However, a further increase in AgNPs size caused a sharp reduction in the portion of forward scattering and, consequently, in the efficiency of the solar cell. For their particular design, they found that 67 nm was an optimized size for the nanoparticles[60].

(a)

(b)
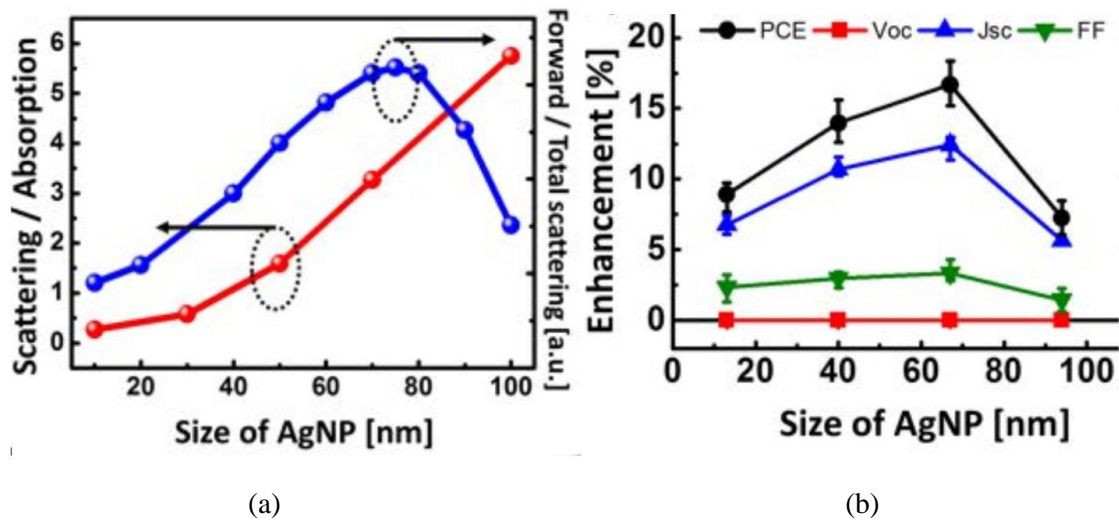
Figure 2.38. Effects of the size of silver nanoparticles embedded in the PEDOT:PSS layer of an organic solar cell. In (a) the blue line shows that the ratio of forward scattering to total scattering raises with particle size, reaching a maximum around 70 nm before sharply decreasing (here, the arrows are simply an indication of that the blue line is associated with the right-hand scale, and the red line with the left-hand scale). In (b) the enhancement of the PCE follows a similar pattern. Adapted from (Baek *et al.*, 2013)[60].

In this thesis, nanoparticles are not incorporated in the solar cells. Instead, the scattering of the light is achieved by texturing azobenzene thin films. One of the random texturing techniques explored is the use of corona poling.

### 2.5.2    Corona Poling of Azobenzene Thin Films

In a corona discharge, a neutral fluid such as air is ionized by a current flowing from an electrode with a high potential, generating a plasma around the electrode. Corona poling consists of using corona discharge to modify the electro-optic properties of materials, often to reorient the molecules dipoles, as illustrated in Figure 2.39. Poling a polymer while heating it close to its glass transition temperature increases the mobility of the molecules and allows dipole rotation. The temperature is then decreased while poling is still applied to fix the molecules in their new orientation.
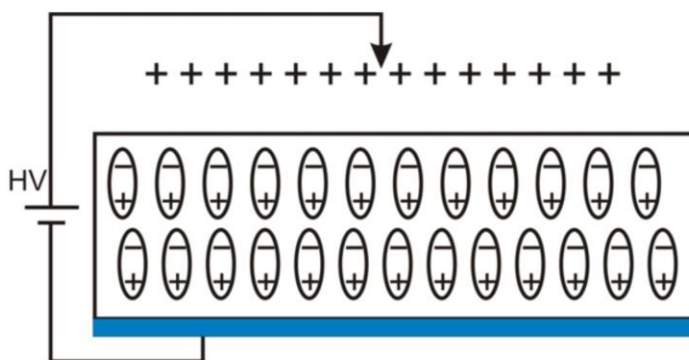
Figure 2.39. Schematic of a corona poling process. A high voltage is applied to an electrode, ionizing the surrounding air. This causes an alignment of the dipole in the material. Adapted from (Rahman, 2007)[144].

By applying voltage pulses with a scanning tunneling microscope (STM) tip, Alemani *et al.*[145] showed that azobenzene molecules around the tip had an increased height. As this process was reversible by applying subsequent pulses, they attributed this phenomenon to a lowering of the isomerization barrier due to the electric field, causing *trans* to *cis* isomerization. Ten years later, Umezawa *et al.*[67] found that selective and reversible nanoscale surface patterning of azobenzene thin films could be obtained by prolonged corona poling if the temperature was increased above the glass temperature. Under those conditions, the corona poling caused a dewetting of the film and a surface instability, creating randomized spherical and irregularly-shaped nanostructures as illustrated in Figure 2.40. These nanostructures had diameters and heights ranging from 200-1000 nm and could be controlled via temperature and exposure time.
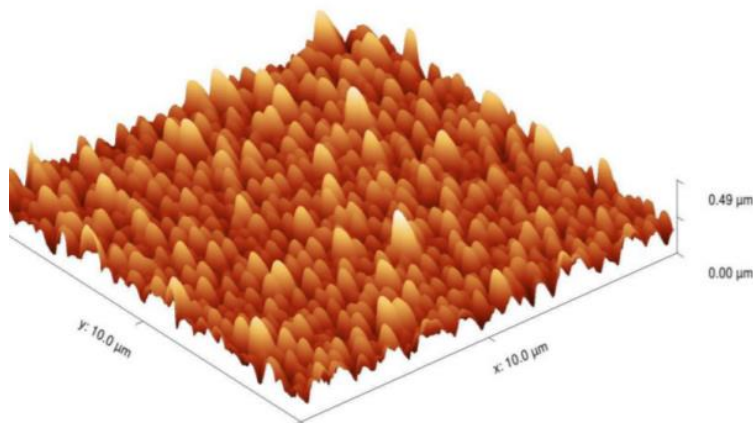


Figure 2.40. AFM scan of an electric-field-induced nanoscale surface patterning in azobenzene thin film. The film was exposed to an 8kV corona voltage at 80˚C for 30 minutes. Adapted from (Umezawa *et al.*, 2016) [67].

While corona poling provides a way to texture azobenzene thin films, such textured films can not be used as is in solar cells due to the high absorbance of azobenzene in the visible spectrum. Photobleaching of the films is therefore required to allow transmission of the light through the azobenzene film to the solar cell active layer.

### 2.5.3    Photobleaching of Azobenzene

As discussed above, azobenzene can undergo a *trans-cis-trans* isomerization cycle when exposed to a laser light. This exposure also causes a decrease of the optical activity. Bellini *et al.* [137] showed that the transmittance of a thin layer of disperse red 1 azobenzene (DR1) doped poly(methyl methacrylate) (PMMA) exposed to a laser beam of irradiance $I_0 = 15$ mW/mm$^2$, increased from 30% to 50% in 2 seconds, and 95% after 40 minutes of exposure. While they found that the fast optical loss was reversible, the slow optical activity resulting from a prolonged exposure was irreversible. Another study found that the transmittance of azobenzene films was also dependent on intensity of the laser beam[146], as illustrated in Figure 2.41. Like Bellini *et al.*, that study found the bleaching to be reversible with subsequent exposure in the order of 20-100 ms, as long as the intensity of the laser remained below 200 mW/cm$^2$. A higher irradiance was found to produced irreversible bleaching of the azobenzene films – which is the desirable outcome in this thesis.
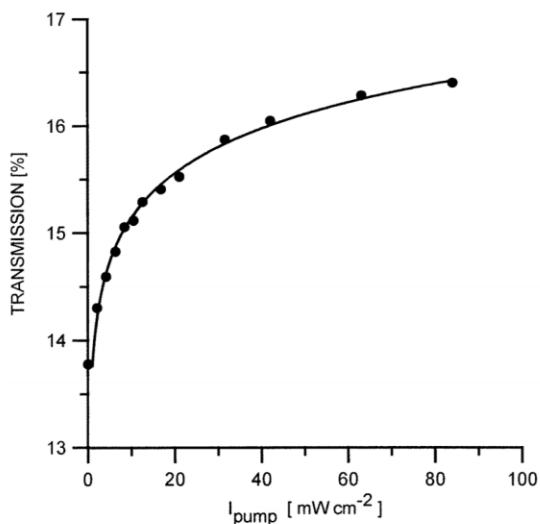


Figure 2.41. Transmission at a wavelength of 543.5 nm of azobenzene illuminated by a 532 nm laser. The transmission increases with the laser intensity. Adapted from (Miniewicz *et al.*, 1998) [146].

While some authors have attributed the irreversibility of the bleaching of the azobenzene films to a balance between *trans* and *cis* forms[137], another possible explanation is that optical damage from the irradiation alters the chemical structure of the molecules[147]. In this model, illustrated in

Figure 2.42, the *trans* isomer absorbs the energy from a photon and transforms to its *cis* form but relaxes to the ground state of a modified molecule from which no back conversion to the original molecule is possible.
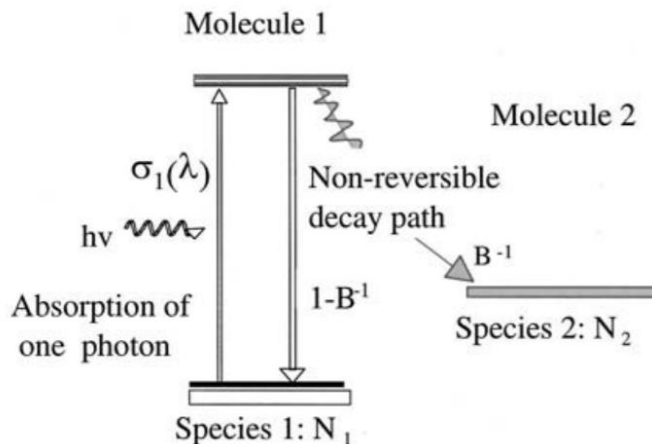


Figure 2.42. Model for the photodegradation process of azobenzene molecules. Initial molecules are raised to the *cis* excited state be means of absorption of a photon, but decay to new species instead of relaxing back to their *trans* ground state, making the process irreversible. Adapted from (Galvan-Gonzalez *et al.*, 2000)[147].

Evidence of this model can be found by close inspection of the absorption spectrum of an irradiated azobenzene film over time. Figure 2.43 shows an example of such spectrum.
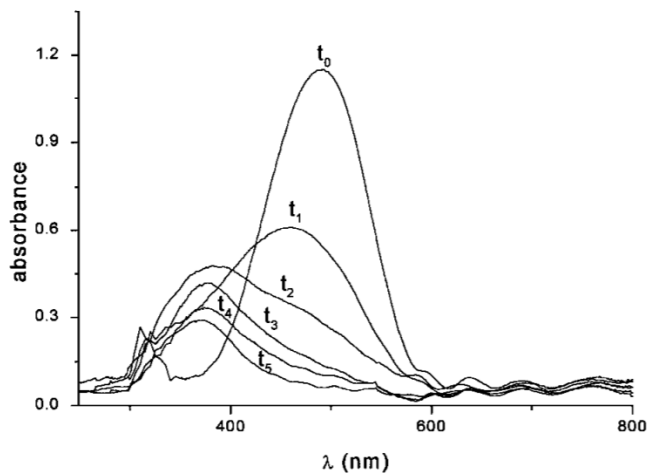
Figure 2.43. Evolution of the absorption spectrum of an DR1 azobenzene thin film upon 488 nm, 20 W/cm$^2$ irradiation. $t_0, t_1, t_2, t_3, t_4$ and $t_5$ correspond to irradiation times of 0, 5 minutes, 20 minutes, 60 minutes, 2 hours and 20 hours respectively. Adapted from (Galvan-Gonzalez *et al.*, 1999)[148].

As it can be seen in Figure 2.43, there are two peaks in the spectrum changing over time, one near 300 nm and one near 490 nm. Galvan-Gonzalez *et al.*[147] speculated that the two peaks were the result of two effects occurring simultaneously: a reversible *trans–cis* isomerization and an irreversible photo-oxidation. The behaviour of the peak near 300 nm corresponds to the reversible *trans-cis* isomerization process, which first gets stronger and then decreases as more and more molecules are damaged from continued photo-exposure. Similar results where achieved by exposure to UV light, which also causes a *trans* to *cis* isomerization of the azobenzene molecules[149-152]. Just as it was the case with laser irradiation, short exposure where found to be reversible, but longer ones resulted in an irreversible process.

Interestingly, Takase *et al.*[153, 154] and Kimura *et al.*[152] found that previously written SRGs could not only be bleached by UV light irradiation, but also became thermally stable due to photocrosslinking, even at a temperature of 150˚C, which is above the glass temperature of azobenzene films. This effect is an important development for solar cell applications which often requires annealing at high temperatures. Therefore, azobenzene thin films, patterned either through laser lithography or corona poling, can be UV treated to bleach and thermally stabilize their nanostructures. The incorporation of those patterned azobenzene thin films in a solar cell is studied in this thesis for its potential to scatter the light within the active layer and thus increase the efficiency of the solar cell.

This chapter covered the theory and mathematical background to understand the work contained in this thesis. While this thesis focuses on the efficiency enhancement of ITO-free organic solar cells through patterning of azobenzene thin films, the photovoltaic process was explained through first generation inorganic solar cells. Common parameters used in the characterization of solar cells, including $J_{sc}$, $V_{oc}$, FF, $R_{SH}$, $R_S$, and PCE were presented. Parallels where then made between inorganic solar cells and organic solar cells, with a focus on organic materials used in solar cells. Finally, the theories of surface plasmons and light scattering through patterning of azobenzene thin film were detailed, as those two techniques will be employed in this thesis to enhance the efficiency of solar cells. Experimental procedures are detailed in the next chapter, while results and discussions are included in Chapter 4.

# 3 EXPERIMENTAL PROCEDURES

This chapter outlines the experimental procedures used in this thesis. It includes materials, handling and storage, substrates and solutions preparation, processing and test equipment, fabrication of control solar cells, and incorporation of nanostructures into solar cells. A table summarizing the processing parameters for the different solar cell designs used in this thesis is included at the end of this chapter.

## 3.1 MATERIALS, HANDLING AND STORAGE

Materials used in this thesis include polymers, fullerenes, solvents, surfactants, glass slides, metal wires, silver paste, azobenzene, and other common chemical products. Polymers P3HT (SOL4106, molecular weight (Mw) 50-70 kilodaltons (KDa)), PTB7 (SOL4700M, Mw 50-100 KDa) and fullerene $PC_{61}BM$ (SOL5061) were purchased from Solaris Chem Inc. Three grades of PEDOT:PSS were purchased from Ossila: Al 4083, a regular grade PEDOT:PSS used as an HTL in direct structure solar cells, HTL Solar, a PEDOT:PSS with surfactant which is used as an HTL in an inverted structure, and PH1000, a highly conductive PEDOT:PSS suitable for the fabrication of transparent electrodes. ITO coated glass slides with a surface resistivity of 15-25 $\Omega$/square, silver conductive paste, solvents chlorobenzene (CB), 1,2-dichlorobenzene (o-DCB) and dichloromethane (DCM), surfactants EG and PEG, aluminium and silver wires were purchased from Sigma-Aldrich (now Millipore-Sigma). Soda lime glass slides (No. 2947) were purchased from Corning Glass Works. The additive DMSO was purchased from Caledon. The surfactant TX-100 was purchased from Rohm & Hass Company. The azobenzene molecular glass was fabricated in house as per section 3.2.2. A Dowsil 184 silicon elastomer kit was used to fabricate PDMS. Other common chemicals used in this thesis include acetone, isopropanol, hydrochloric acid (HCl) and nitric acid ($HNO_3$).

The polymers and fullerenes used in this thesis are sensitive to oxygen and light. They were therefore wrapped in aluminium foil and stored in a nitrogen-filled glovebox. All handling of polymers and fullerenes, including opening vials, measuring quantities, mixing and filtering were done inside the Nitrogen-filled glovebox. The PEDOT:PSS was kept in the fridge. The other materials were stored at room temperature in ambient air. Once prepared, polymer:fullerene solutions were sealed and wrapped in aluminium foil. To prevent agglomeration, prepared polymer:fullerene and azobenzene molecular glass solutions were kept at all times in a mechanical shaker. The solutions were double-filtered with a 0.45 µm filter prior to first use, and they were re-filtered prior to each subsequent use.

## 3.2 SUBSTRATE AND SOLUTIONS PREPARATION

### 3.2.1 Substrate Preparation

An etching solution was prepared to pattern the ITO bottom electrodes. The solution consisted of mixing 225 millimetres (ml) of HCl and 75 ml of $HNO_3$ in 300 ml of distilled water. The solution was then vigorously shaken for 15 minutes and stored at room temperature under ambient air. This solution was briefly remixed before each use. ITO slides were patterned by applying cellophane tape on the desired areas, then soaking the slide in a small amount of etching solution for 15 minutes under a laboratory chemical fume hood. The cellophane tape was then removed, and the substrate was cleaned. Figure 3.1 shows the schematic of a patterned-ITO slide

with two 6.25 millimetres (mm) width stripe electrodes. Other ITO slides were also prepared with 2 mm width stripe electrodes.
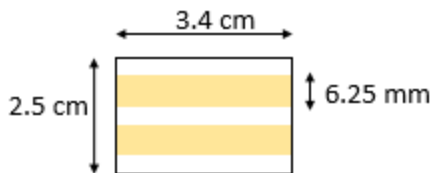


Figure 3.1. Patterned ITO. Two stripe electrodes of 6.25 mm (or 2 mm) width have been patterned from an ITO covered slide.

For the ITO-free solar cells, glass slides were cut to dimensions 3.4 cm x 2.5 cm. All slides were cleaned with liquid dish soap followed by a series of ultrasonic baths of detergent water, acetone, isopropanol and deionized water for ten minutes each, with a deionized water rinse between each bath. The slides were then kept in deionized water until used. Immediately prior to use, the slides were dried in an oven at 120°C for 15 minutes and blown with nitrogen to remove any dust particles.

### 3.2.2    Solutions Preparation

Small quantities of P3HT:PC$_{61}$BM solution were prepared by first mixing 0.093 grams (g) of P3HT in 2 ml of CB and 0.074 g of PC$_{61}$BM in 2 ml of CB inside a nitrogen-filled glovebox. Once sealed and wrapped in aluminium foil, the vials were transferred to a mechanical shaker and shaken overnight. This was followed by a one-hour sonification to ensure the powders were completely dissolved. The vials were then transferred back to the glovebox and the solutions were mixed to form a P3HT:PC$_{61}$BM (1:0.8) 25 mg/ml in CB solution. A P3HT:PC$_{61}$BM solution in o-DCB was also prepared in a similar manner as the previous solution, using 0.080 g of P3HT, 0.064 g of PC$_{61}$BM and  4 ml of o-DCB to obtain a  P3HT:PC$_{61}$BM (1:0.8) 2% weight/volume (w/v) P3HT/o-DCB solution. A PC$_{61}$BM solution in DCM was prepared by mixing 0.020 g of PC$_{61}$BM in 4 ml of DCM to obtain a 0.5% w/v solution. Though PTB7 is normally paired with PC$_{71}$BM, PC$_{61}$BM was used in this thesis due to its relative low cost. Upon manufacturer recommendation, a ratio of (1:2) was used. 0.040 g of PTB7 and 0.080 g of PC$_{61}$BM were mixed in 4 ml of CB to create a PTB7: PC$_{61}$BM (1:2) 30 mg/ml in CB solution.

To improve the conductivity of PH1000, 0.6 g of DMSO was added to 12 g of PH1000 to create a solution of PH1000 + 5% weight (wt) of DMSO. This solution was mixed in a mechanical shaker for one hour before being filtered with a 0.45 µm filter. The solution was stored in a fridge but shaken again in the mechanical shaker for an hour prior to each use. To improve the wettability of the PH1000, several solutions with surfactants were also made. Solutions were made with the addition of  10% wt isopropanol, 2%  wt PEG, 0.5% wt TX-100, and a mix of 7%  wt EG + 0.25% wt TX-100.

PDMS stamps were fabricated by mixing 10 g of silicone in 1g of curing agent from a Dowsil 184 silicone elastomer kit in a petri dish. The dish was then put in a vacuum chamber for 30 minutes before being heated at 75˚C for 30 minutes, producing a 2 mm thick PDMS stamp.

In 2014, a research group from Queen's University and the Royal Military College of Canada developed an azobenzene chromophore with a mexylaminotriazine backbone, a combination referred to as Disperse Red 1 Molecular Glass (gDR1)[155]. Compared to its azo-polymer counterpart, gDR1 is easily synthesized and is produced at a higher yield. It was therefore selected as the azobenzene chromophore for this thesis. Small quantities of azobenzene solution were prepared by dissolving 0.18 g of gDR1 in 5.82 g of DCM and shaking the mixture in a mechanical shaker for one hour, creating gDR1 3% wt in DCM solutions.

### 3.3    PROCESSING AND TEST EQUIPMENT

### 3.3.1    Processing Equipment
The following equipment was used for the fabrication of the solar cells:  an OHAUS Precis Standard scale, a 300 µl - 30 µl Hamilton pipette, a 1 ml – 100 µl Hamilton pipette, a Fisher Vortex Genie 2 mechanical shaker, a Branson PC620 ultrasonic bath, a Yamato vacuum oven ADP-21 equipped with a nitrogen bottle to anneal the samples under nitrogen atmosphere, a MBraun Unilab nitrogen-filled glovebox equipped with a spin-coater, and a Key High Vacuum Products KV-301 physical vapor evaporator controlled by a Varian Turbo-V 301-AG vacuum controller and Sigma Instrument SQM-160 rate/thickness monitor, along with in-house built evaporation masks. An ORC HmW-6238 UV lamp was used to bleach the azobenzene films. To pattern the azobenzene thin films, two set-ups were used, a SRGs inscription station and a corona poling station, both of which are described below.

### 3.3.1.1    *Surface Relief Grating Inscription Station*
Figure 3.2 shows the equipment set-up used for writing SRGs on azobenzene thin films following the methodology explained in section 2.4.6. The beam from a Coherent Verdi V5 diode-pumped continuous wave laser with an irradiating wavelength of 532 nm set at 416 mW/cm$^2$ irradiance, was passed through a 25 µm spatial filter to reduce its Gaussian profile. The beam was then collimated using a collimating lens and it was circularly polarized with a quarter-wave plate. A variable iris was used to control the diameter of the laser beam incident on a Lloyd's mirror interferometer.
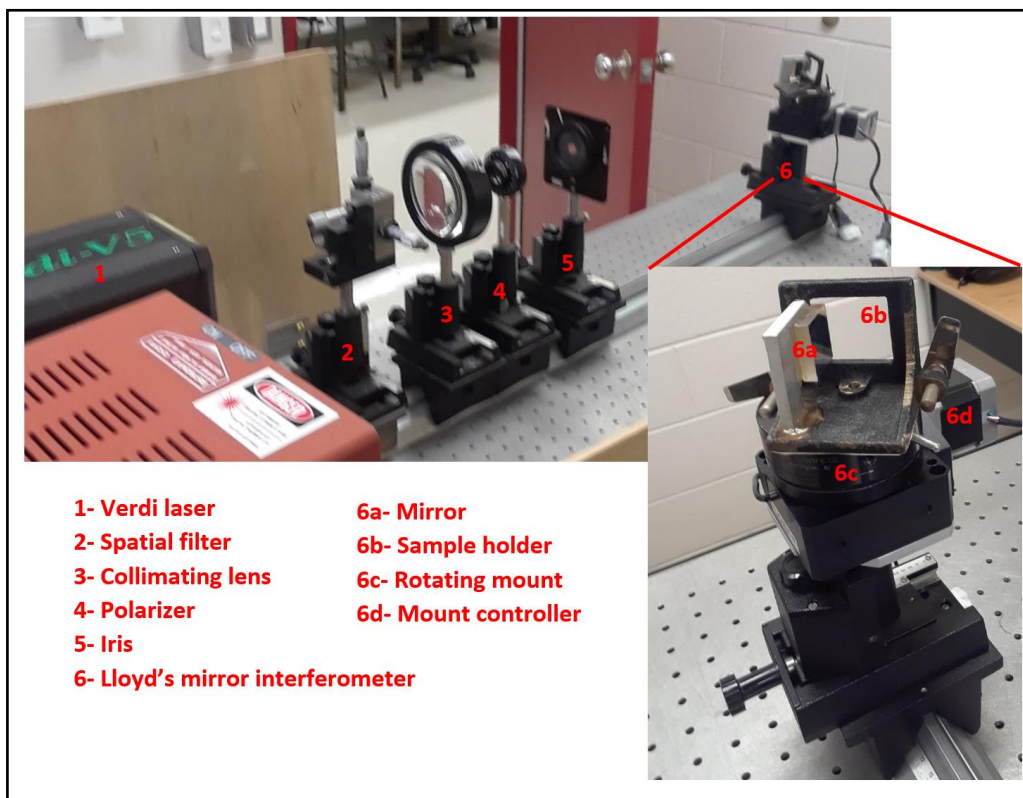
Figure 3.2. Surface relief grating station. This set-up was used to write SRGs on azobenzene thin films. The Lloyd's mirror interferometer is detailed in the inset.

The inset of Figure 3.2 shows the Lloyd's mirror interferometer. A mirror and sample holder were fastened at a 90˚ angle and mounted on a rotating platform. The platform was remotely controlled by a LabVIEW program and a Velmex Stepping Motor Controller which adjusted the angle of incidence of the laser beam, thus allowing control of the grating spacing as per Equation (2.63). The intersection axis between the mirror and sample holder was positioned at the center of the laser beam so that half of the laser beam was incident on the mirror's surface and half on the sample's surface.

### 3.3.1.2    Corona Poling Station

Figure 3.3 shows the equipment step-up used to pattern the azobenzene thin films by a custom-built corona poling apparatus fabricated in our laboratory. A Hewlett Packard 621B power supply and Omega Benchtop Controller connected to a temperature sensor were used to heat an copper hot plate. The copper hot plate was used as one of the poling electrodes, while the other electrode consisted of a thin wire suspended above the sample. A Hippotronics high-voltage DC power supply provided the corona discharge voltage. A cooling fan was used to cool the hot plate to room temperature after each heat cycle.
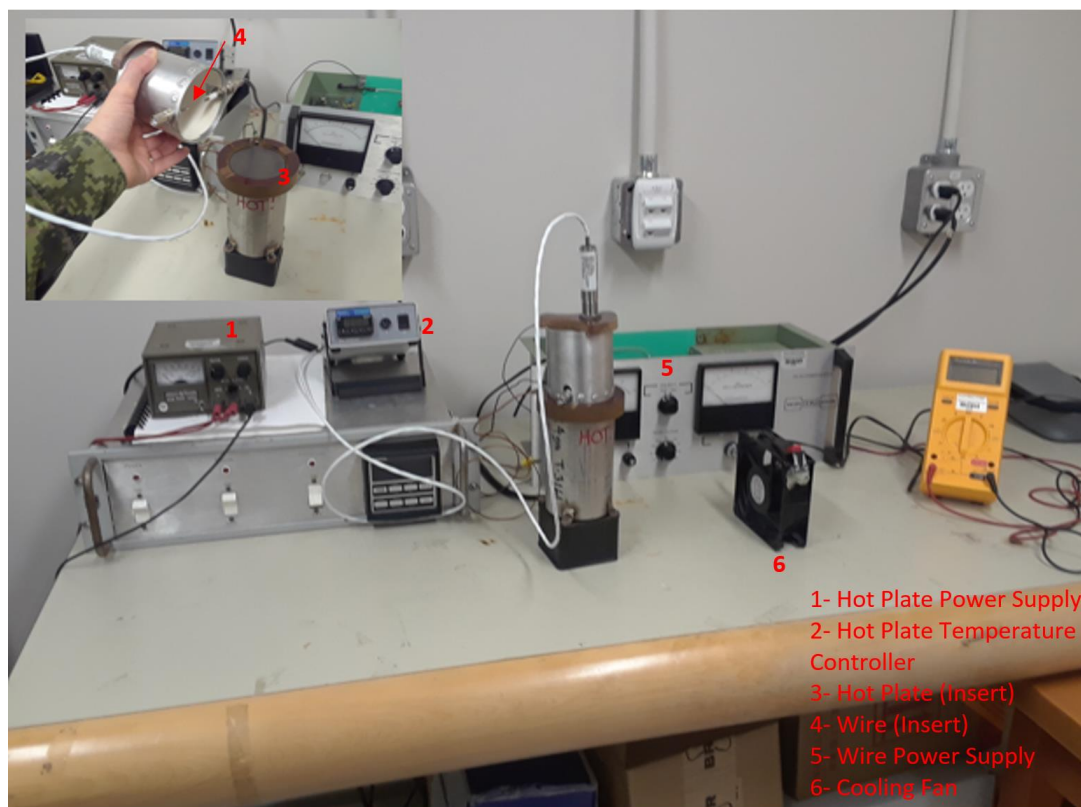
Figure 3.3. Corona poling set-up. The inset shows the wire suspended above the electrical hot plate.

### 3.3.2 Test Equipment

#### 3.3.2.1 *Spectrometry Stations*

Two set-ups were used for the measurement of transmission and absorption of thin films. The first set-up, shown in Figure 3.4 uses a Lambda LOS-R-12 regulated 120-volt power supply to power a halogen lamp. The beam of the lamp was then passed through vertical and horizontal slits. A neutral variable-density filter was used to ensure that the signal read by the spectrometer was not saturated. A variable iris controlled the diameter of the beam. The beam was then focussed on the sample by a converging lens, and the transmitted beam from the sample was then focussed again on an Edmond Optics BRC 11A-USB-VIS/NIR Charged Coupled Device (CCD) spectrometer by another converging lens. This set-up can be used to measure the transmission and absorption of thin films in the 300-1000 nm wavelength range.

1- Power Supply
2- Lamp
3- Vertical Slit
4- Horizontal Slit
5- Variable Neutral Filter
6- Iris
7- Converging Lens
8- Sample Holder
9- Converging Lens
10- CCD Spectrometer
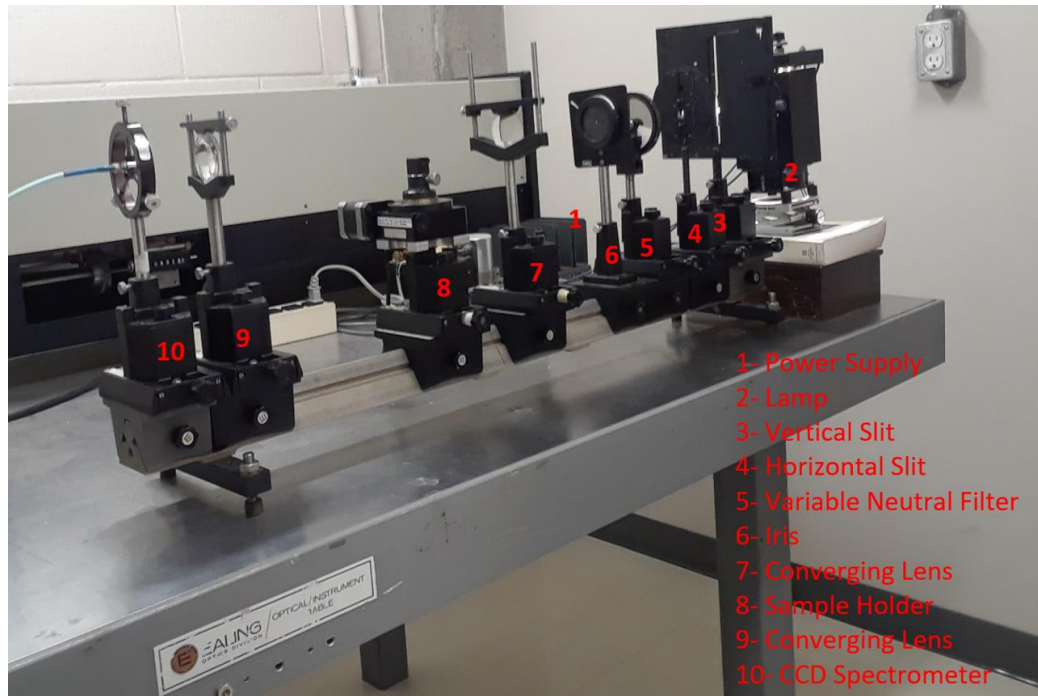
Figure 3.4. Spectrometry set-up #1. This set-up can be used to measure the transmission and absorption of thin films in the 300-1000 nm wavelength range.

The second set-up, shown in Figure 3.5 also uses a halogen lamp (behind the cardboard in Figure 3.5 and power supply. However, in this case, the light is split by a Scientech 9040 monochromator cycling through different wavelengths using a LabVIEW program. The resulting beam passes through a mechanical chopper controlled by a Stanford Research System SR540 chopper controller before being reflected by a mirror into the sample. Finally, the intensity of the light transmitted through the sample is measured by a photo-detector connected to a Stanford Research System SR865 2MHz DSP lock-in amplifier, which, in combination with the mechanical chopper, minimizes the signal noise from the background light. A Hughes 3227H-PC helium-neon laser powered by a Hughes 5000 power supply and a Uniblitz SD122B shutter drive unit are also included in the set-up to ensure proper alignment of the sample prior to taking measurements. This set-up can be used to measure the transmission and absorption of thin films in the visible and infrared range.
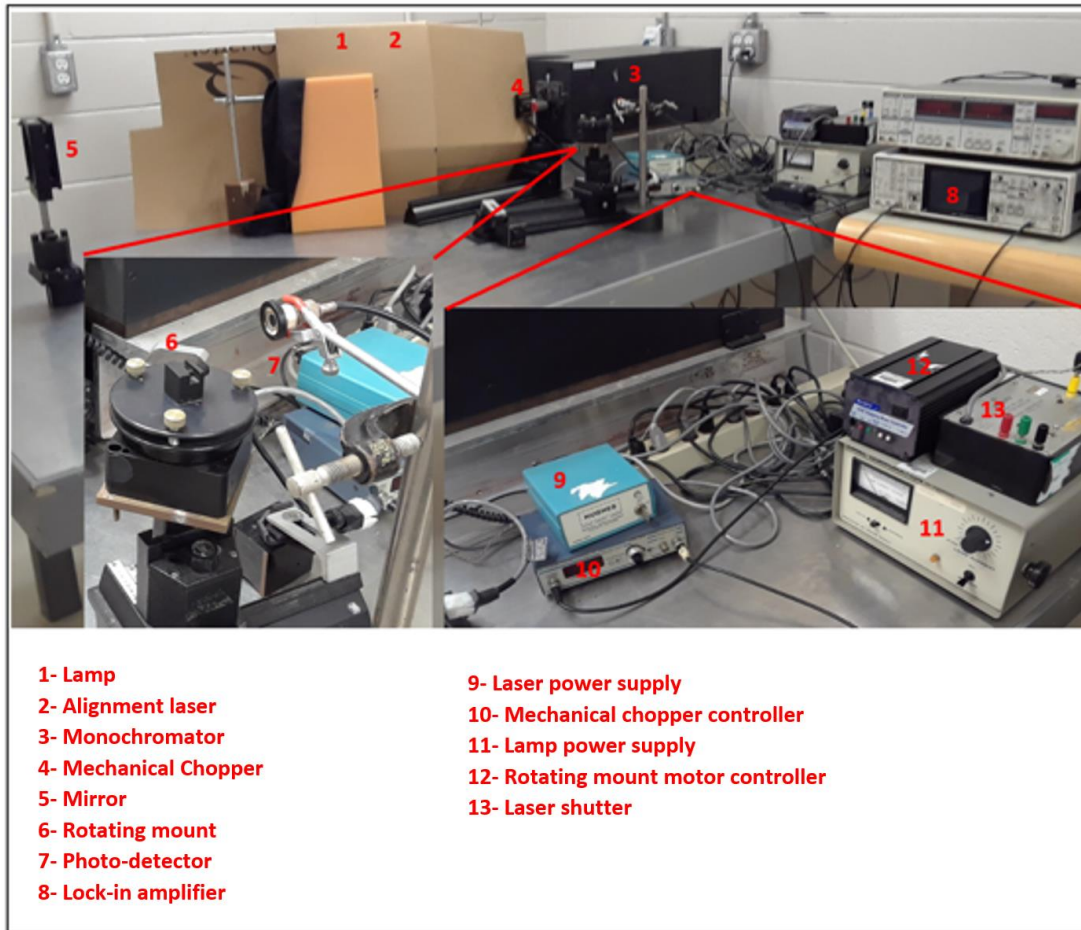
Figure 3.5. Spectrometry set-up #2. The source is provided by a halogen lamp (behind the cardboard in the picture). The light is then split by a monochromator before being reflected on the sample. A laser (also behind the cardboard in the picture) is used for sample alignment. Two insets give a closer look at the equipment # 6-13.

### 3.3.2.2 *Solar Cells Characterization Station*

As mentioned in section 2.2.5, the standard spectrum for measuring terrestrial solar cells efficiency is according to the AM1.5G, which is available in ASTM G-173-03(2006)[85]. The AM1.5G spectrum represents the total power per unit area that is received at the surface of the Earth at a solar zenith angle 48.2˚ on a clear sunny day. The integral of this spectrum over the entire spectrum is the $P_{in}$ used in the calculation of solar cells efficiency and has a value of 1000 W/m$^2$. This has become the standard intensity at which the efficiencies of solar cells are reported and is often referred to as 1 Sun condition[1].

A solar simulator is the equipment used to simulate the solar irradiance and spectrum to provide a controllable indoor test facility for the testing of solar cells. The classification of solar simulators is based on their spectral match to the reference spectral irradiance, spatial irradiance

uniformity and irradiance temporal stability, as specified in the ASTM E927 standard[156]. For this thesis, an in-house solar simulator was built using a light source and common optical system components. Three light sources were considered: a quartz tungsten halogen lamp, a xenon arc lamp and light emitting diodes (LEDs). Quartz tungsten halogen lamps provide a good spectral match to the reference spectrum in the infra-red but they are a very poor match across the visible range[157]. Xenon arc lamps provide a good spectral match in the visible range but have strong emission lines in the near infra-red region[157]. LEDs are commonly available and have longer lifetime than arc lamps but operate at discrete wavelengths[157]. A cluster of LEDs operating at different wavelengths would therefore be required to replicate a continuous spectrum. With the spectral match being an important factor in the quality of any solar cell testing set-up, an Oriel 66058 xenon arc lamp powered by an Oriel 200 W power supply was selected. To reduce the strong emissions of the xenon arc lamp in the infra-red region and achieve a closer spectral match, the lamp was paired with an Omega Optical AM1.5G optical filter. The normalized transmittance spectrum of the lamp with the AM1.5G filter, obtained from dividing the raw data of the transmission of the lam with AM1.5G filter by the raw data of the transmission of the lamp without the filter, is shown in Figure 3.6.
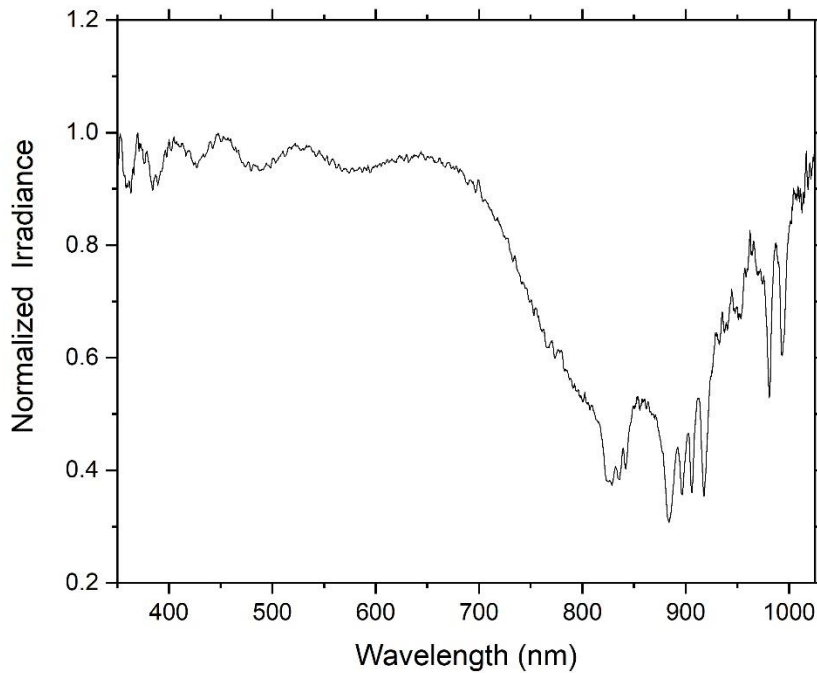


Figure 3.6. Normalized xenon arc lamp spectrum with an AM1.5G filter. The AM1.5G filter results in a reduction of the strong peaks of the xenon lamp in the near infra-red region to obtain a closer match with regards to the solar spectrum.

The solar cell characterization set-up was completed with a variable iris to control the illuminated area, a sample holder, a cooling and a Keithley 2601A System Source Meter to obtain the I-V characteristics of the solar cells, as shown in Figure 3.7.



Figure 3.7. Solar cells characterization station. The combination of a xenon lamp with an AM1.5G filter closely matches the solar spectrum.

In order to achieve the standard 1 Sun illumination testing condition, a Scientech 362 power energy meter equipped with a Scientech 380101 silicon detector was used to determine the required distance between the sample and the lamp. Even though the PCE is measured as a ratio of maximum output power from to solar cell to the input power, respecting the 1 Sun standard test condition is important as, at low light levels, the effect of the shunt resistance becomes increasingly important[159, 160], and therefore standardization of the input light intensity for testing and reporting purposes is required. However, due to the spectral-responsivity of the silicon detector, the 1 Sun condition could not be used as is to calibrate the solar simulator as it would lead to overestimation of the efficiency[158]. The chosen silicon detector can detect in the wavelength range of 280-1064 nm. This range contains 78.4% of the AM1.5G spectrum, or 784 W/m$^2$. Using $E = \frac{P}{A}$, where $P$ is the power level read on the power energy meter and $A$ is the area of the detector illuminated by the light, the position of the detector was therefore varied until $E = 784$ W/m$^2$ was achieved, thus ensuring that the sample actually received an illumination of 1000 W/m$^2$. With the lamp current set to maximum, this was achieved at a distance of 25.4 cm. The sample holder was therefore set at this position. The operating temperature also has an effect on the efficiency of the solar cell. While the open-circuit voltage decreases with increasing temperature, the short-circuit current and fill factor increase with increasing temperature, resulting in an overall increase of the energy

conversion efficiency[158, 160, 161]. A cooling fan was therefore added to the solar simulator set-up to ensure that the standard test conditions of 25˚C was maintained.

In addition to the two spectrometry and characterization stations, other test equipment used include a Sloan Dektak IIA/IID profilometer, which was used to measure the film thicknesses, a Bruker Dimension Edge AFM and a Fluke 89 IV True RMS multimeter.

## 3.4    FABRICATION OF CONTROL SOLAR CELLS

### 3.4.1    Fabrication of Indium-Tin-Oxide Solar Cells

Processing and testing procedures were verified using a well-studied design. From literature review, most bottom illuminated P3HT:PC$_{61}$BM solar cells in a direct structure (using ITO as bottom electrode, PEDOT:PSS as the HTL, an ETL and low work function metal top electrode combination such as Ca/Al or LiF/Al) have reported efficiencies between 3-4%[72]. As manufacturing ETL was not within our laboratory's capabilities, this layer was omitted and therefore a slightly lower solar cell efficiency was expected. The design used for the ITO solar cells is  illustrated in Figure 3.8.
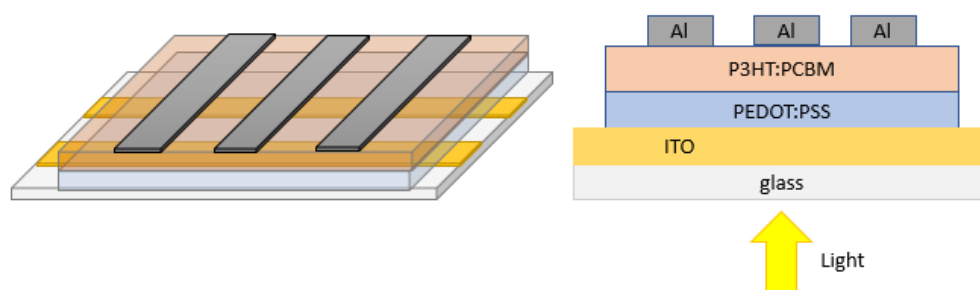


Figure 3.8. Schematic of direct structure ITO solar cell. This solar cell is a bottom-illuminated solar cell with an ITO layer as the anode, a PEDOT:PSS HTL, an active layer of P3HT:PC$_{61}$BM blend and an aluminium cathode. The patterning of the electrodes produces six solar cells per sample, with the active area of the solar cell defined as the overlap of the electrodes.

In a bottom-illuminated solar cell, the first layer is a transparent electrode. ITO-coated slides were patterned as per section 3.2 to create stripe electrodes, with some samples having electrodes of 6.25 mm width while others had electrodes of 2 mm width. Silver paste was then applied to improve the contact points where the aluminium electrodes would be deposited, as per Figure 3.9. The silver paste was cured in the oven at 120˚ for 20 minutes. The quality of the silver paste contacts was verified using a multimeter, a step which was critical as the silver paste contacts were sometimes found to be poor. In those cases, another layer of silver paste was applied.
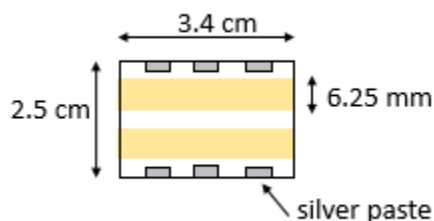
Figure 3.9. Silver paste pattern for ITO solar cells. Silver paste is deposited at the future contact location for the top electrodes in order to protect the thin aluminum film during connection to the measuring equipment.

As PEDOT:PSS is sensitive to moisture, and the active layer is sensitive to both light and oxygen, processing and testing from this point on were carried out promptly. Al 4083 was chosen as the HTL due to its ease of processing and high work function. Using a measured pipette, 0.7 ml of solution was spin-coating at 5000 revolutions per minute (RPM) for 60 seconds. The aluminum contacts were then exposed by cleaning them with a cleanroom swab dipped in deionized water. The HTL film was annealed at 120˚C for 10 mins under dinitrogen ($N_2$) atmosphere, resulting in a layer thickness of $\sim 30 - 50$ nm. For the active layer, 120 µl of P3HT:PC$_{61}$BM were spin-coated at 1100 RPM for 30 seconds. The contacts were then exposed by cleaning them with chlorobenzene, and the layer was annealed at 120˚C for 30 minutes under $N_2$ atmosphere, resulting in a layer thickness of $\sim 90$ nm.

The last layer the light encounters while going through a bottom-illuminated solar cell is the top electrode. Aluminium was used in this thesis due to its low work-function and high reflectance. The solar cells were completed by evaporating a $\sim 100$ nm thick layer of aluminium through an evaporation mask to form stripe electrodes of 4.72 mm or 3 mm width. The thickness deposition rate was closely monitored during the evaporation and kept between 3-5 Å/s, as a fast aluminium deposition rate can lead to concavity of the J-V plot due to the appearance of large voids at the interfaces[162], as illustrated in the inset of Figure 3.10. The overlap of the electrodes resulted in solar cells with active areas of 29.5 or 6 mm$^2$, depending on the ITO pattern and evaporation mask chosen.
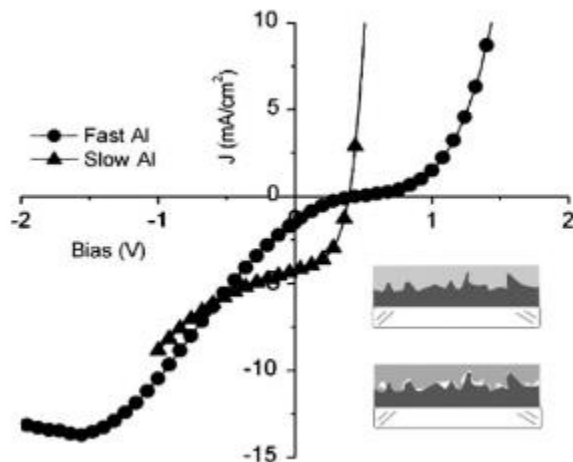
Figure 3.10. Effect of fast aluminium evaporation rate (200 nm/5 s) and slow evaporation rate (200 nm /100 s) on the J-V plot of a P3HT:PC$_{61}$BM solar cell. The interface morphology is shown in the inset, with the slow evaporation at the top and the fast evaporation at the bottom. The fast evaporation creates voids at the interface, leading to a concavity of the J-V curve. Adapted from (Gupta *et al.*, 2010)[162].

### 3.4.2    Fabrication of Solar Cells with a PC$_{61}$BM Over-layer

While most solar cells were made using a single active layer as per above, some were made with a layer of P3HT:PC$_{61}$BM followed by a thin PC$_{61}$BM over-layer, as illustrated in Figure 3.11. Spin-coating sequential layers require orthogonal solvents, i.e. the organic molecules from the under-layer must not be soluble by the solvent of the over-layer to avoid significant redissolution of the under-layer. This requirement adds to the complexity of the solar cell as most conjugated organic molecules are soluble in similar solvents. O-DCB and DCM were reported to be appropriate orthogonal solvents for the production of P3HT:PC$_{61}$BM bilayer solar cells[163, 164]. For the solar cells with a PC$_{61}$BM over-layer, the P3HT:PC$_{61}$BM in o-DCB layer was spin-coated at 600 RPM for 300 seconds. The solar cells were left to dry uncovered in the glovebox in the dark for 2 hours[165], resulting in an active layer thickness of ~150 nm. A thin layer of PC$_{61}$BM in DCM was then spin coated at 4000 RPM for 10 seconds on the dried P3HT:PC$_{61}$BM layer. The solar cells were completed with the evaporation of the aluminum electrode as per section 3.4.1.
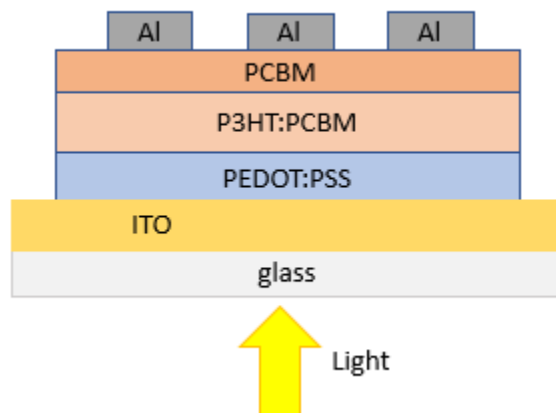
Figure 3.11. Schematic of an ITO solar cell with a $PC_{61}BM$ over-layer. A thin layer of $PC_{61}BM$ in DCM is deposited on top of a layer of $P3HT:PC_{61}BM$ in o-DCB.

### 3.4.3 Fabrication of PH1000 Electrodes

The ITO-based solar cells fabricated in section 3.4.1 were used to confirm appropriate manufacturing and testing methodologies. As mentioned in section 1.3, the goal of this thesis is to improve the efficiency of ITO-free organic solar cells through surface patterning of azobenzene thin films – thus requiring an alternative for the ITO electrode. One of the alternatives explored in this thesis is the use of a highly conductive formulation of PEDOT:PSS, namely PH1000, as a spin-coated electrode. Several challenges needed to be overcome: improving the conductivity of the PH1000 film, patterning the electrodes, and improving the wettability of PH1000 over a hydrophobic active layer.

To function as an electrode, the PH1000 film must have a high conductivity. Two methods were investigated to improve the conductivity of PH1000: PH1000 treated with DMSO post-spinning, and the addition of 5% wt DMSO in the PH1000 solution[91, 125]. Silver paste was deposited on three 3.8 cm x 3.8 cm slides, two of which were then spin-coated with pure PH1000 solution and the third one with a solution of PH1000 + 5% wt DMSO, all at 2800 RPM for 60 seconds. All three slides were then annealed at 120˚C for 10 minutes under $N_2$, resulting in films with a thickness around $\sim$100 nm. One of the pure PH1000 slides was then treated with DMSO by depositing 100 μl of DMSO on the dried film and letting it stand for three minutes before spin-coating it at 4000 RPM for 60 seconds and further annealing it at 120˚C for 10 minutes under $N_2$. The resistance $R$ of the films were then measured with a multimeter, and the resistivity and conductivity were calculated using:

$$R = \rho \frac{l}{A} = \frac{l}{\sigma wt} \tag{3.1}$$

where $\rho$, $l$, $A$, $\sigma$, $w$, and $t$ are respectively the resistivity of the electrode, its length, cross-sectional area, conductivity, width and thickness. As shown in Table 3.1, the addition of 5% wt DMSO to the PH1000 solution yielded the highest conductivity, which was on par with the resistivity value

given by the manufacturer (0.0012 Ohm-centimeter ($\Omega$cm) with the addition of 5% DMSO)[166]. Due to its higher conductivity and ease of fabrication, PH1000 + 5% wt DMSO was chosen as the transparent electrode.

Table 3.1. Conductivity of PH1000 at a pure state, with pre-spinning DMSO addition and post-spinning DMSO treatment.

|  | Thickness (nm) | Resistance ($\Omega$) | Resistivity ($\Omega$cm) | Conductivity (S/cm) |
|---|---|---|---|---|
| PH1000 | 108.5 | 94000 | 1.0199 | 0.98 |
| PH1000 + 5% wt DMSO | 105.4 | 140 | 0.0015 | 677.69 |
| PH1000 + DMSO rinsing | 93.1 | 173 | 0.0016 | 620.88 |

The resistance of the film can also be decreased by using a thicker electrode. However, this would be at the detriment of the transparency of the film. The thickness of the PH1000 film has already been optimized elsewhere, with film thicknesses of 80-100 nm providing good results[91].

Patterning of the solar cells' electrodes fabricated with PH1000 was the second challenge to overcome. The active area of the solar cells is defined by the overlap of the top and bottom electrodes and the active layer. This requires the patterning of at least one of the electrodes. However, recalling Equation (3.1), patterning the electrodes would affect their resistance as it would change the length and/or width of the electrodes. Since increasing the resistance of the electrodes increases the total series resistance of a solar cell which, as discussed in section 2.2.4, negatively impacts the efficiency of the solar cell[77-79], one should aim to minimise the increase in resistance caused by the patterning of the electrodes.

The aluminium conductivity is $3.77 \times 10^7$ S/m at 20°C[167], which gives a conductivity ratio of ~560 compared to that of the PH1000+5% wt DMSO. Therefore, the reduction in width caused by the patterning of the electrodes has a lesser impact on the resistance of aluminum electrodes than on the resistance of the PH1000 electrodes. The in-house fabricated evaporation mask used to evaporate the aluminium in the ITO/Al solar cells created three stripe electrodes with widths of 3 mm. When used in combination with patterned 2 mm ITO, this created six 6 mm$^2$ solar cells per sample. As it was decided not to pattern the PH1000 electrode, which was replacing the ITO (other than a thin strip on each side of the slide to prevent short-circuit at the contacts), a new evaporation mask was needed, or else it would result in only two large-area solar cells per sample. This was achieved by patterning a thin aluminium foil which was used in conjunction with the evaporation mask, with the resulting pattern illustrated in Figure 3.12. In order to further optimize the resistance of the PH1000 electrode, the design was changed to have the PH1000 electrode oriented along the shorter edge of the slide. This design resulted in four solar cells with active areas of 8.49 mm$^2$ per sample.
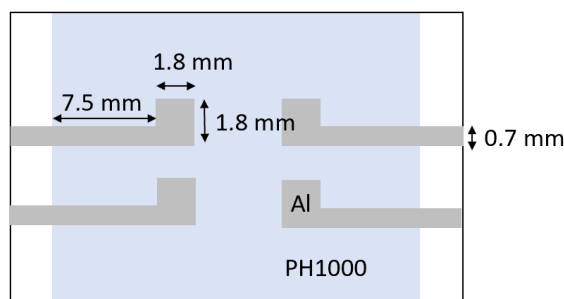
Figure 3.12. Schematic of the electrodes patterning of Al/PH1000 solar cells. To minimise the increase in the solar cell's series resistance, the aluminum was the electrode chosen for patterning.

While it was possible to connect directly to the ITO on ITO coated glass, connecting directly to the thin PH1000 film risked damaging the film. Three different contact designs were investigated: connecting directly to the thin film, pre-patterning an ITO-coated glass slide to remove all ITO but small ITO contact stripes at the edges of the slide or using silver paste for the contact areas. Thin films of PH1000 were spin-coated with identical thicknesses on slides with different contact designs and the resistance measured. As predicted, the conductivity was poor when connecting directly to the thin film, but no difference was found between the ITO or silver paste contact designs. The silver paste design, illustrated in Figure 3.13, was therefore chosen due to its ease of fabrication.
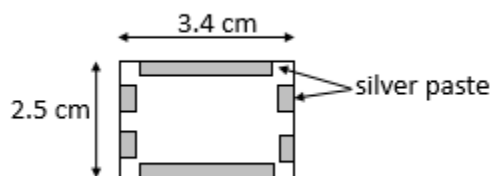


Figure 3.13. Silver paste pattern for PH1000 solar cells. The long stripes will be the PH1000 electrode contacts, while the shorter stripes will be the aluminium electrode contacts.

The final obstacle in the fabrication of PH1000 electrodes is the wettability of the spin-coated aqueous solution on a hydrophobic active layer. While some formulations of PEDOT:PSS, such as Heraeus Clevios[TM] HTL Solar, include surfactants to improve their wettability, the highly conductive PEDOT:PSS grade PH1000 cannot be used on top of the active layer without additional treatment. Several strategies have been tried in this thesis. Solutions made with the additions of 10% wt of isopropanol, 2% wt of PEG, a mix of 7% wt EG + 0.25% wt TX-100 or by mixing Al 4083 or HTL Solar with PH1000 at a 1:3 ratio[126] failed to provide a uniform film. Deposition of layers of Al 4083 or HTL Solar followed by PH1000 has also been unsuccessful[124, 126]. Transferring

a PH1000 film using PDMS stamp-transfer lamination technique was also tried, but without plasma treatment capabilities to tune the PDMS surface hydrophilicity[168, 169], the film would not spread well on the PDMS stamp. Finally, the addition of 0.5% wt TX-100 was found to be successful in providing good film morphology. It was found that this addition did not change the conductivity or transparency of the films, and that a similar thickness was obtained at the same RPM as films spin-coated from a solution that did not contained the surfactant.

### 3.4.4    Fabrication of Inverted Solar Cells with Transparent Top Electrodes

To excite SPR in inverted solar cells, the solar cells must have a transparent top electrode since the bottom electrode would be made of a metal with a SRGs. Two transparent top electrodes were tried in this thesis: a thin layer of silver or a layer of PH1000. Control solar cell designs without SRGs are illustrated in Figure 3.14.
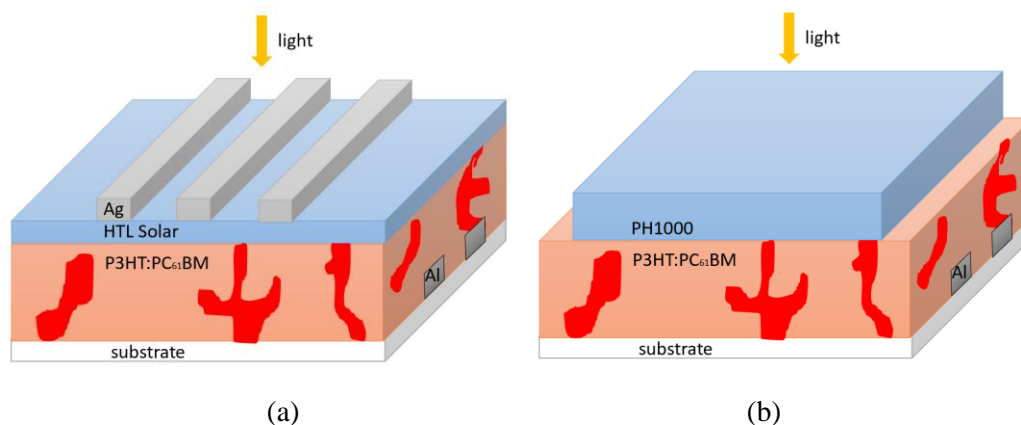


Figure 3.14. Transparent top electrode inverted solar cell designs. In (a) the anode is made of a thin layer of silver over an HTL, while in (b) PH1000 serves as both the HTL and anode. In both cases, the cathodes (visible on the right side of the solar cells) and the anodes are perpendicular in order to create several small area solar cells per sample.

For the design in Figure 3.14a, aluminium stripe electrodes of 2 mm width were evaporated at a rate of 3 Å/s through an evaporation mask on slides with silver paste contacts. The aluminum was kept thin, at 50 nm, to avoid the molding effect of the active layer. The thickness reduction of the bottom electrode was necessary, as our laboratories do not currently have the capability to fabricate ETL. Without the planarization effect of the ETL, it was found that the active layer thickness was only about 10 nm when spin-coated on top of 100 nm thick aluminum electrodes. However, when the thickness of the electrode was reduced to 50 nm, the active layer thickness was found to be similar to the ITO solar cells fabricated as per section 3.4.1 ($\sim$90 nm). The active layer and HTL were spin-coated and annealed as per section 3.4.1, however the HTL used in the inverted solar cells consisted of a grade of PEDOT:PSS that is more wettable than Al 4083 on top of the

hydrophobic active layer, namely HTL Solar. A thin 14 nm layer of silver was then evaporated at a rate of 3 Å/s through an evaporation mask to form stripe electrodes perpendicular to the aluminium stripe electrodes, thus creating six solar cells per sample with active areas of 4 mm$^2$.

For the design in Figure 3.14b, 50 nm thick aluminum electrodes were evaporated using the evaporation mask design illustrated in Figure 3.12 on slides with silver paste pattern as per Figure 3.13. The active layer was spin-coated and annealed as per section 3.4.1. PH1000 + 5% wt DMSO + 0.5% wt TX-100 served as both the HTL and the top electrode. Using a measured pipette, 0.7 ml of the mixture was spin-coated at 2800 RPM for 60 seconds to produce a ~100 nm thick film. The PH1000 film was then patterned with a cotton swap dipped in deionized water as per Figure 3.12 to produce four solar cells with 8.49 mm$^2$ area per sample. In order to avoid short-circuiting the solar cells, care was taken to not only remove the PH1000 film near the aluminum contact on the top surface of the slides, but also off the edges of the slides, as illustrated in Figure 3.15. The samples were then annealed at 120˚C for 10 minutes under N$_2$.
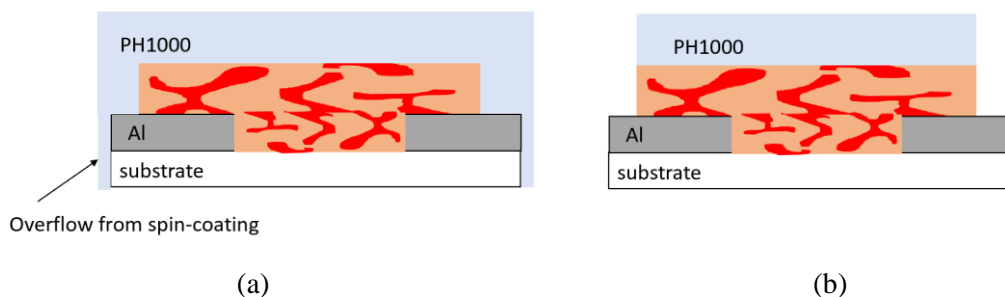


Figure 3.15. Overflow of PH1000 on the edges of a sample caused by spin-coating in (a) and clean edges in (b). Cleaning of the edges is a critical step to avoid short-circuiting the cell at the aluminum contact points.

### 3.4.5 Fabrication of Direct Solar Cells with Transparent Bottom Electrodes
The solar cells used in conjunction with bleached and nanostructured azobenzene thin films to test the efficiency enhancement of the solar cells through light scattering required transparent bottom electrodes. Control solar cells were made following a procedure similar to the one described in section 3.4.4. The PH1000 + 5% wt DMSO was first spin-coated, then two different kinds of active layers were used. P3HT:PC$_{61}$BM solar cells were also made with the annealing temperature reduced to 70˚C and the annealing time increased to 60 minutes for the active layer. While most solar cells were made using P3HT:PC$_{61}$BM processed and annealed as per the ITO-based solar cells, other solar cells used a solution of PTB7:PC$_{61}$BM for the active layer. For those solar cells, 120 µl of solution were spin-coated at 1000 RPM for 30 seconds and the samples were allowed to dry uncovered in the glovebox for 2 hours in the dark. The solar cells were completed by evaporating the aluminium electrodes. The aluminum thickness was set back to 100 nm for those solar cells. Figure 3.16 shows samples of P3HT:PC$_{61}$BM and a PTB7:PC$_{61}$BM solar cells in a direct structure with PH1000 bottom electrodes. Each sample contains four solar cells, identified on the back side of the samples with marker.
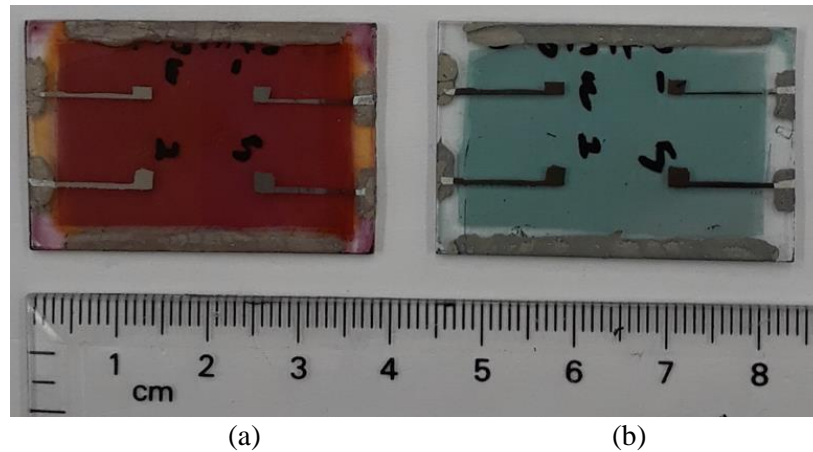
Figure 3.16. Image of (a) a P3HT:PC$_{61}$BM and (b) a PTB7:PC$_{61}$BM sample in a direct structure with PH1000 bottom electrodes. Each sample contains four solar cells.

In order to provide a direct comparison with solar cells with ITO bottom electrode, a P3HT:PCBM solar cell was also fabricated on an ITO covered glass slide etched with the same pattern as the PH1000 electrode.

## 3.5    INCORPORATION OF NANOSTRUCTURES IN SOLAR CELLS

### 3.5.1    Fabrication of Nanostructures on Azobenzene Thin Films

Thin films of azobenzene were prepared by spin-coating 60 µl of solution at 1000 RPM for 20 seconds. The films were cured in the oven at 95˚C for 30 minutes, producing films 150-200 nm thick with a root mean squared (rms) roughness $R_q = 0.5$ nm and a maximum profile height $R_{qmax} = 3.0$ nm. The films were then patterned through laser lithography to form cross-gratings or corona poling to form randomized nanostructures.

Crossed gratings were inscribed using the set-up detailed in section 3.3.1.1, with the laser irradiance set at 416 mW/cm$^2$ and grating spacing set at $\Lambda = 450$ nm for all gratings. The exposure time for the first grating was set at 120 s. The sample was then turned 90˚, and the exposure time for the second grating was set at 55 s, resulting in grating depth of ~85 nm for the first grating and ~60 nm for the second grating. Figure 3.17 shows an example of cross-grating inscribed using the above parameters.
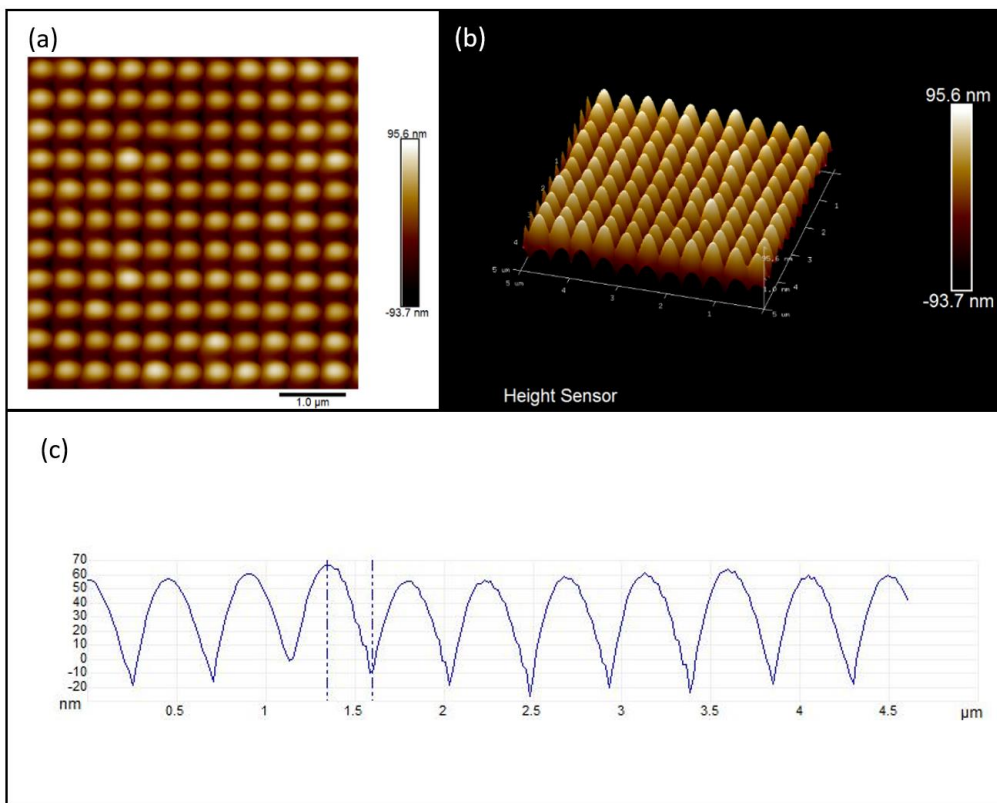
Figure 3.17. AFM (a) 2D image, (b) 3D image and (c) profile of a crossed grating on an azobenzene thin film. Parameters were laser irradiance of 416mW/cm$^2$, grating spacings of 450 nm and exposure times of 120 s and 55 s.

Randomized nanostructures were also fabricated on azobenzene thin films using the corona poling set-up described in section 3.3.1.2. The samples were first heated above their glass temperature, which is 71˚C for gDR1[170], to increase the molecular mobility, and an 8 kV corona discharge voltage was applied. The samples were then brought back to room temperature before the voltage was turned off in order to "freeze" the nanostructures in place. Nanostructures with different sizes were made by varying the exposure time from 150 seconds to 30 minutes, and the hot plate temperature from 75˚C to 90˚C, with longer exposures and higher temperatures resulting in larger nanostructures. Figure 3.18 and Figure 3.19 show two examples of randomized nanostructures fabricated by corona poling of azobenzene thin films.
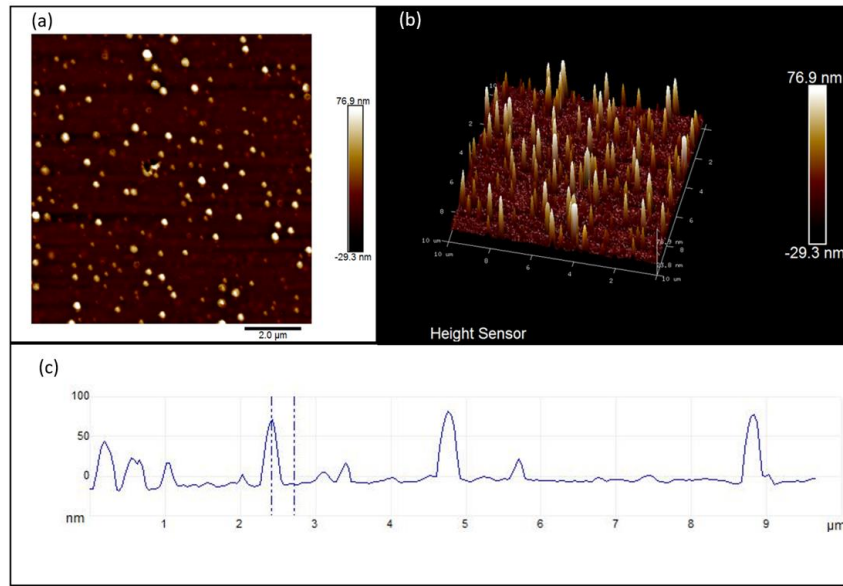
Figure 3.18. AFM (a) 2D image, (b) 3D image and (c) profile of nanostructures fabricated by corona poling of an azobenzene thin film heated at 75˚C. An exposure time of 30 minutes and discharge voltage of 8 kV were used.
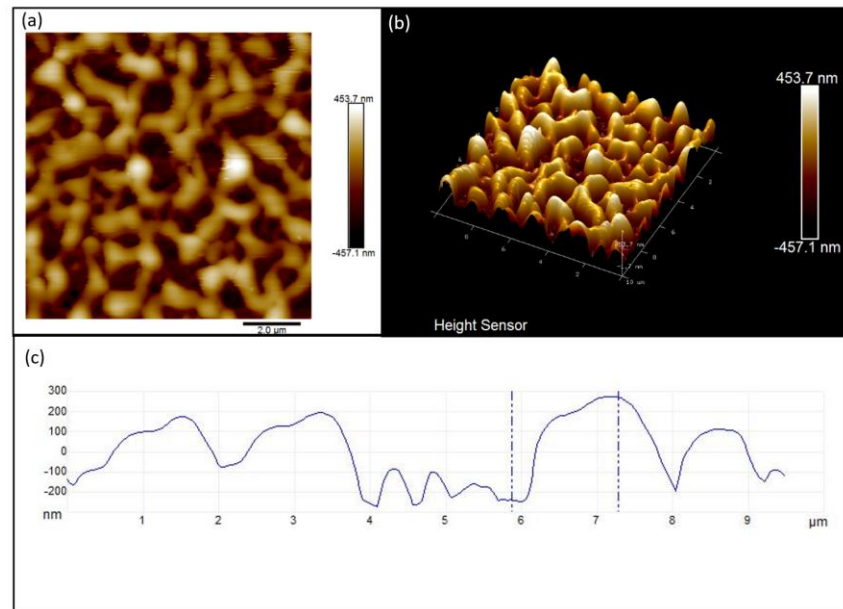


Figure 3.19. AFM (a) 2D image, (b) 3D image and (c) profile of a nanostructures fabricated by corona poling of an azobenzene thin film heated at 80˚C. An exposure time of 30 minutes and discharge voltage of 8 kV were used.

Figure 3.20 shows images of azobenzene thin films patterned with crossed gratings and randomized nanostructures by corona poling.



(a)                                                    (b)
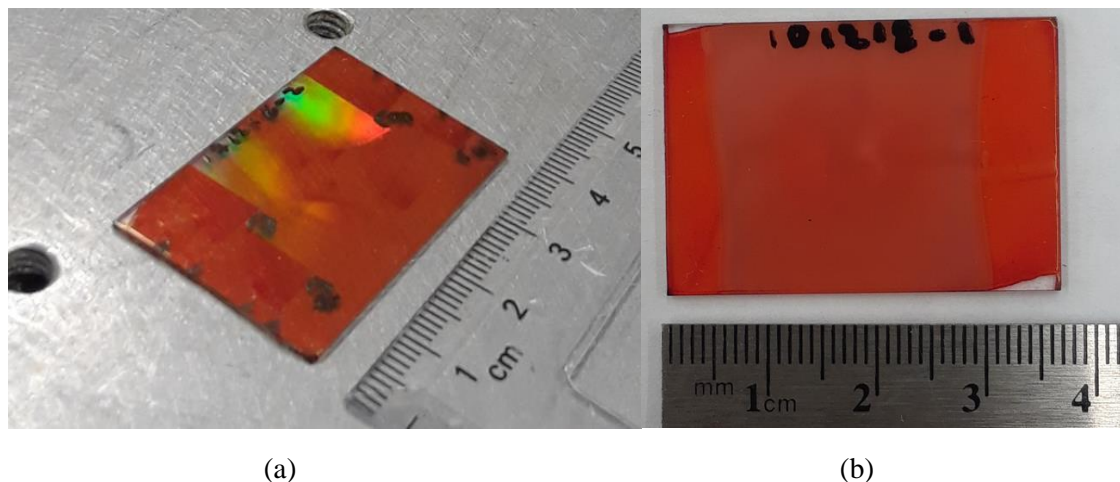
Figure 3.20. Azobenzene thin films patterned with (a) cross-gratings and (b) randomized nanostructures by corona poling.

### 3.5.2    UV treatment of Azobenzene Thin Films

To serve as reference solar cells, unstructured azobenzene thin films were bleached using a UV light, with the distance between the sample and the light set at 3.5 cm and the voltage of the lamp set at its maximum setting. No optical components such as filters or lenses were used between the lamp and the sample. The transmission of a treated azobenzene thin film was taken at different times using one of the spectrometry set-ups detailed in section 3.3.2.1. As illustrated in Figure 3.21, the transmission saturated after 20 hours of exposure.
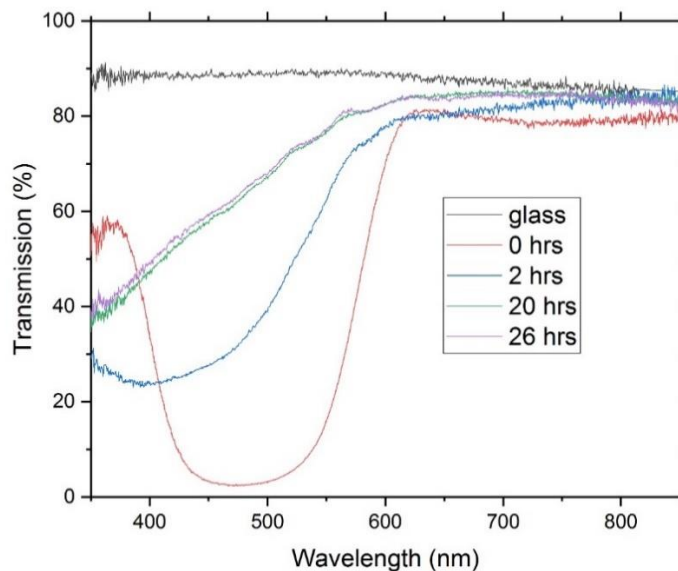
Figure 3.21. Transmission of an azobenzene thin film after UV exposure. The black line represents the transmission of glass only, and the color lines are the transmission of the azobenzene film and its glass substrate after different exposure times. The transmission saturated after a 20-hour exposure.

As discussed in section 2.5.3, there are two peaks in the spectrum changing over time, one near 300 nm and one near 490 nm, with the first peak associated with the *trans–cis* isomerization and the second peak with the irreversible photodegradation. The behaviour of the first peak corresponds to the reversible *trans-cis* isomerization process, which first gets stronger and then decreases as more and more molecules are damaged from continued photo-exposure. Figure 3.22 shows images of an azobenzene thin film before and after a 20-hour UV exposure.



(a)                                             (b)
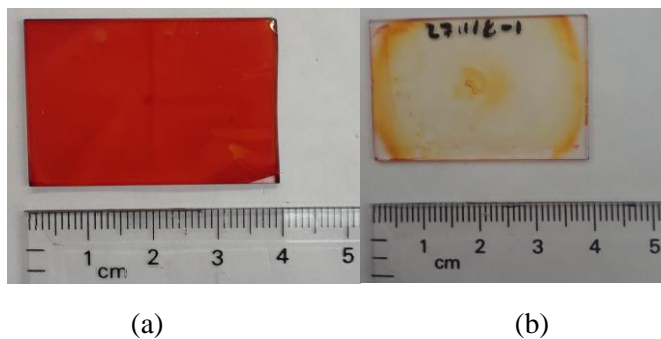
Figure 3.22. Azobenzene thin film (a) before and (b) after a 20-hour UV exposure.

Other unstructured azobenzene thin films and films patterned with cross-gratings or randomized nanostructures through corona poling were also bleached. As it was found that PH1000 was hard to remove once spin-coated on top of unbleached azobenzene, care was taken to clean the spin-coated overflow of azobenzene on the back side and edges of the slides with cleanroom swabs dipped in DCM. The azobenzene films were then bleached for 20 hours. However, the distance from the sample to the light was varied from 3.5 cm to 6 cm. Once the azobenzene films were bleached, solar cells were built either on top of the azobenzene thin films or on the other side of the substrate, as illustrated in Figure 3.23.

For the single-sided solar cell, applying the silver paste prior to poling the azobenzene thin film was found to be critical, or else the silver paste solvent would destroy the nanostructures. The mixture PH1000 + 5% wt DMSO + 0.5% wt TX-100 was used to help spread the electrode over the rough surface. Furthermore, in order for the PH1000 mixture to completely cover the nanostructures and have a similar resistance across the contacts to the ones of solar cells made without the azobenzene layer, the spin-coating speed was reduced to 1500 RPM. A low annealing temperature of 70°C was also used for those solar cells.

For the double-sided solar cells, the silver paste was applied after corona poling of the azobenzene film in order for the sample to be in direct contact with the corona apparatus hot plate and not to change the distance between the sample and the corona apparatus wire. The edges of the substrate were taped with the azobenzene film face down on another glass slide in order to spin-coat the PH1000 +5% wt DMSO mixture and active layers, with the spin-coated speed readjusted to 2800 RPM. A high annealing temperature of 120°C was used for those solar cells since, at this point, thermal stability of UV-treated azobenzene film had been observed, as will be further discuss in section 4.4.3. The additional glass slide used for spin-coating was then removed prior to the evaporation of the aluminium electrode.
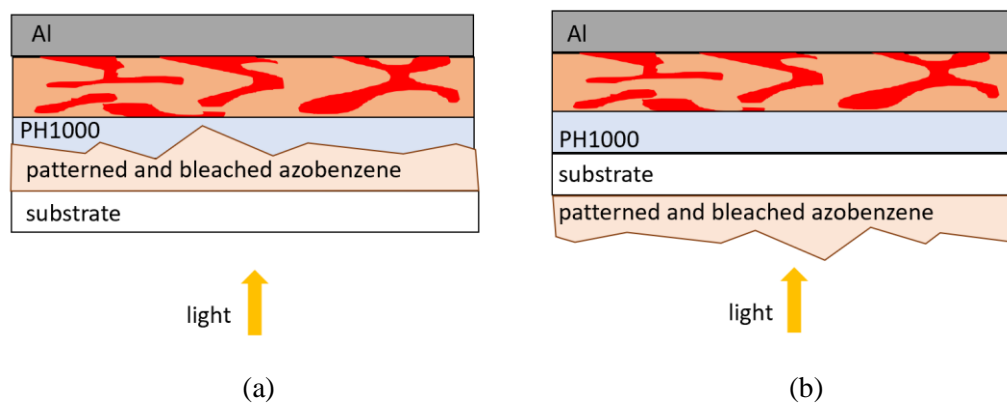


Figure 3.23. (a) Single-sided and (b) double-sided solar cells with patterned and bleached azobenzene thin films. The light is scattered by the patterned azobenzene films before entering the solar cells.

This chapter detailed the experimental procedures used to obtain the results in this thesis, including materials, substrates and solutions preparations, processing and test equipment, and the

fabrication of solar cells. Table 3.2 summarizes the processing parameters for the different solar cell designs used in this thesis. Results will be presented and discussed in Chapter 4.

Table 3.2. Summary of processing parameters for the different solar cell designs used in this thesis.

| | Processing Parameters |
|---|---|
| **Direct structure ITO solar cells** | **As per section 3.4.1, active area 29.5 mm$^2$ or 6 mm$^2$** |
| Etched ITO | As per Figure 3.1. |
| Silver paste | As per Figure 3.9, cured 120˚ for 20 minutes, conductivity verified. |
| Al 4083 | 0.7 ml, 5000 RPM/60 seconds, Al contacts cleaned with deionized water, annealed at 120˚C for 10 mins under N$_2$ atmosphere, thickness $\sim 30 - 50$ nm. |
| P3HT:PC$_{61}$BM | 120 µl P3HT:PC$_{61}$BM (1:0.8) 25 mg/ml in CB, 1100 RPM/30 seconds, contacts cleaned with CB, annealed at 120˚C for 30 minutes under N$_2$, thickness $\sim 90$ nm. |
| Aluminium | Evaporated through stripe electrode mask with width of 4.72 mm or 3 mm, deposition rate 3-5 Å/s, thickness $\sim 100$ nm. |
| **Direct structure ITO solar cells with PC$_{61}$BM over-layer** | **As per section 3.4.2, active area 29.5 mm$^2$** |
| Etched ITO | As per Figure 3.1. |
| Silver paste | As per Figure 3.9, cured 120˚ for 20 minutes, conductivity verified. |
| Al 4083 | 0.7 ml, 5000 RPM/60 seconds, Al contacts cleaned with deionized water, annealed at 120˚C for 10 mins under N$_2$ atmosphere, thickness $\sim 30 - 50$ nm. |
| P3HT:PC$_{61}$BM | 120 µl P3HT:PC$_{61}$BM (1.0.8) 2% w/v P3HT/o-DCB, 600 RPM/300 seconds, contacts cleaned with CB, dried uncovered in the glovebox in the dark for 2 hours, thickness $\sim 150$ nm. |
| PC$_{61}$BM | 120 µl PC$_{61}$BM 0.5% w/v in DCM, 4000 RPM/10 seconds, contacts cleaned with chlorobenzene. |
| Aluminium | Evaporated through stripe electrode mask with width of 4.72 mm, deposition rate 3-5 Å/s, thickness $\sim 100$ nm. |
| **Inverted structure with Ag top electrode solar cells** | **As per section 3.4.4, active area 4 mm$^2$** |
| Silver paste | Cured 120˚ for 20 minutes, conductivity verified. |
| Aluminium | Evaporated through stripe electrode mask with width of 3 mm, deposition rate 3-5 Å/s, thickness $\sim 50$ nm. |
| P3HT:PC$_{61}$BM | 120 µl P3HT:PC$_{61}$BM (1:0.8) 25 mg/ml in CB, 1100 RPM/30 seconds, contacts cleaned with CB, annealed at 120˚C for 30 minutes under N$_2$, thickness $\sim 90$ nm. |
| HTL Solar | 0.7 ml, 5000 RPM/60 seconds, Al contacts cleaned with deionized water, annealed at 120˚C for 10 mins under N$_2$ atmosphere, thickness $\sim 30 - 50$ nm. |
| Ag | Evaporated through stripe electrode mask with width of 3 mm, deposition rate 3-5 Å/s, thickness $\sim 14$ nm. |

| Inverted structure with PH1000 top electrode solar cells | As per section 3.4.4, active area 8.49 mm$^2$ |
|---|---|
| Silver paste | As per Figure 3.13, cured 120˚ for 20 minutes, conductivity verified. |
| Aluminium | Evaporated through electrode mask as per Figure 3.12, deposition rate 3 per -5 Å/s, thickness ∼50 nm. |
| P3HT:PC$_{61}$BM | 120 µl P3HT:PC$_{61}$BM (1:0.8) 25 mg/ml in CB, 1100 RPM/30 seconds, contacts cleaned with CB, annealed at 120˚C for 30 minutes under N$_2$, thickness ∼90 nm. |
| PH1000 | 0.7 ml PH1000 + 5% wt DMSO + 0.5% wt TX-100, 2800 RPM/60 seconds, Al contacts and edges cleaned with deionized water, annealed at 120˚C for 10 mins under N$_2$ atmosphere, thickness ∼100 nm. |
| **Direct structure PH1000 bottom electrode solar cells** | **As per section 3.4.5, active area 8.49 mm$^2$** |
| Silver paste | As per Figure 3.13, cured 120˚ for 20 minutes, conductivity verified. |
| PH1000 | 0.7 ml PH1000 + 5% wt DMSO, 2800 RPM/60 seconds, Al contacts and edges cleaned with deionized water, annealed at 120˚C for 10 mins under N$_2$ atmosphere, thickness ∼100 nm.<br><br>Low annealing temperature solar cells were also made by adjusting the annealing temperature to 70˚C, with a solution without surfactant, 0.7 ml PH1000 + 5% wt DMSO, and with surfactant, 0.7 ml PH1000 + 5% wt DMSO + 0.05% wt TX-100. |
| P3HT:PC$_{61}$BM or PTB7:PC$_{61}$BM | 120 µl P3HT:PC$_{61}$BM (1:0.8) 25 mg/ml in CB, 1100 RPM for 30 seconds, contacts cleaned with CB, annealed at 120˚C for 30 minutes under N$_2$, thickness ∼90 nm, or<br><br>120 µl P3HT:PC$_{61}$BM (1:0.8) 25 mg/ml in CB, 1100 RPM for 30 seconds, contacts cleaned with CB, annealed at 70˚C for 60 minutes under N$_2$, thickness ∼90 nm, or<br><br>120 µl PTB7:PC$_{61}$BM (1:2) 30 mg/ml in CB, 1000 RPM/30 seconds, contacts cleaned with CB, dried uncovered in the glovebox for 2 hours in the dark. |
| Aluminium | Evaporated through electrode mask as per Figure 3.12, deposition rate 3 per -5 Å/s, thickness ∼100 nm. |
| **Single-sided solar cells on azobenzene thin films** | **As per section 3.5, active area 8.49 mm$^2$** |
| Silver paste | As per Figure 3.13, cured 120˚ for 20 minutes, conductivity verified. |
| Azobenzene | 60 µl of gDR1 3% wt in DCM, 1000 RPM/20 seconds, back side, contacts and edges cleaned with DCM, cured at 95˚C for 30 minutes, thickness ∼150 − 200 nm.<br><br>Left unstructured or patterned by corona poling as per section 3.5.1, temperature varying between 75˚C-90˚C and exposure time varying between 2:30 – 30 minutes.<br><br>Bleached for 20 hours at various distances from UV lamp. |

| | |
|---|---|
| PH1000 | 0.7 ml  PH1000 + 5% wt DMSO + 0.5% TX-100 (single-sided solar cells) or PH1000 + 5% wt DMSO (double-sided solar cells), 1500 RPM/60 seconds, Al contacts and edges cleaned with deionized water, annealed at 70˚C for 10 mins under $N_2$ atmosphere. |
| P3HT:PC$_{61}$BM | 120 µl P3HT:PC$_{61}$BM (1:0.8) 25 mg/ml in CB, 1100 RPM for 30 seconds, contacts cleaned with CB, annealed at 120˚C for 30 minutes under $N_2$, thickness ∼90 nm, or |
| Aluminium | Evaporated through electrode mask as per Figure 3.12, deposition rate 3 per -5 Å/s, thickness ∼100 nm. |
| **Double-sided solar cells on azobenzene thin films** | **As per section 3.5, active area 8.49 mm$^2$** |
| Azobenzene | 60 µl of  gDR1 3% wt in DCM, 1000 RPM/20 seconds, back side, contacts and edges cleaned with DCM, cured at 95˚C for 30 minutes, thickness ∼150 − 200 nm.<br><br>Left unstructured, patterned by corona poling with temperature varying between 75˚C-90˚C and exposure time varying between 2:30 – 30 minutes, or patterned with cross-gratings  as per section 3.5.1.<br><br>Bleached for 20 hours at various distances from UV lamp. |
| Silver paste | As per Figure 3.13 on back side of substrate, cured 120˚ for 20 minutes, conductivity verified. |
| PH1000 | 0.7 ml  PH1000 + 5% wt DMSO + 0.5% TX-100 (single-sided solar cells) or PH1000 + 5% wt DMSO (double-sided solar cells), 2800 RPM/60 seconds, Al contacts and edges cleaned with deionized water, annealed at 120˚C for 10 mins under $N_2$ atmosphere, thickness ∼100 nm. |
| P3HT:PC$_{61}$BM or  PTB7:PC$_{61}$BM | 120 µl P3HT:PC$_{61}$BM (1:0.8) 25 mg/ml in CB, 1100 RPM for 30 seconds, contacts cleaned with CB, annealed at 120˚C for 30 minutes under $N_2$, thickness ∼90 nm, or<br><br>120 µl PTB7:PC$_{61}$BM (1:2) 30 mg/ml in CB, 1000 RPM/30 seconds, contacts cleaned with CB,  dry uncovered in the glovebox for 2 hours in the dark. |
| Aluminium | Evaporated through electrode mask as per Figure 3.12, deposition rate 3 per -5 Å/s, thickness ∼100 nm. |

# 4 RESULTS AND DISCUSSION

The results obtained from the solar cells built following Chapter 3 procedures are discussed in this chapter. In the first section of this chapter, ITO solar cells are characterized and analyzed to confirm appropriate fabrication procedures. Issues with fabricating solar cells with transparent top electrodes – a design compatible with a bottom metal structured electrode which is needed to excite SPR – are then discussed. Two transparent electrodes are investigated: an ultra-thin metal electrode and a spin-coated electrode. The third section of this chapter presents the results for spin-coated transparent bottom electrode solar cells, which are used as control solar cells for measuring the efficiency enhancements of the solar cells with scattering nanostructures. Solar cells made with azobenzene thin films patterned by corona poling are then presented. Next, solar cells with azobenzene thin films patterned by crossed gratings, using both P3HT:PC$_{61}$BM and PTB7:PC$_{61}$BM as active organic materials, are discussed. The last section of this chapter shows the J-V characteristic curves of the solar cells with the best efficiency enhancements compared to control solar cells obtained from the research done during this thesis. This section also includes a table summarizing the J-V characteristics of all the solar cells presented in this chapter.

## 4.1 INDIUM-TIN-OXIDE CONTROL SOLAR CELLS

Fabrication and testing procedures were verified using a well-studied design, as it is known that ITO solar cells with a structure similar to the one illustrated in Figure 3.8, but with the addition of an ETL, should produce an efficiency around 3-4%[72]. As the ETL was omitted in this thesis due to manufacturing limitations of our laboratory, a slightly lower efficiency was expected.

### 4.1.1 Large Area Indium-Tin-Oxide Solar Cells

The first solar cells produced were made using ITO patterned slides with stripe electrodes of 6.25 mm width, Al 4083 as HTL, P3HT:PC$_{61}$BM and 4.72 mm width aluminium top electrodes as per the processing parameters detailed in Table 3.2. The overlap of the layers created six solar cells with an active area of 29.5 mm$^2$ per sample. The active areas of the solar cells produced in this section are relative large, as most solar cells produced for research purposes have an active area between 5 and 15 mm$^2$ [72]. The characteristic J-V curve for the best solar cell obtained with the large area ITO solar cells design is given in Figure 4.1. The large area ITO solar cells exhibited a low average efficiency of $0.2 \pm 0.1\%$, with the best solar cell having a $J_{sc}$ of 2.76 mA/cm$^2$, a $V_{oc}$ of 0.56 V, a FF of 0.18 and an efficiency of 0.27%.
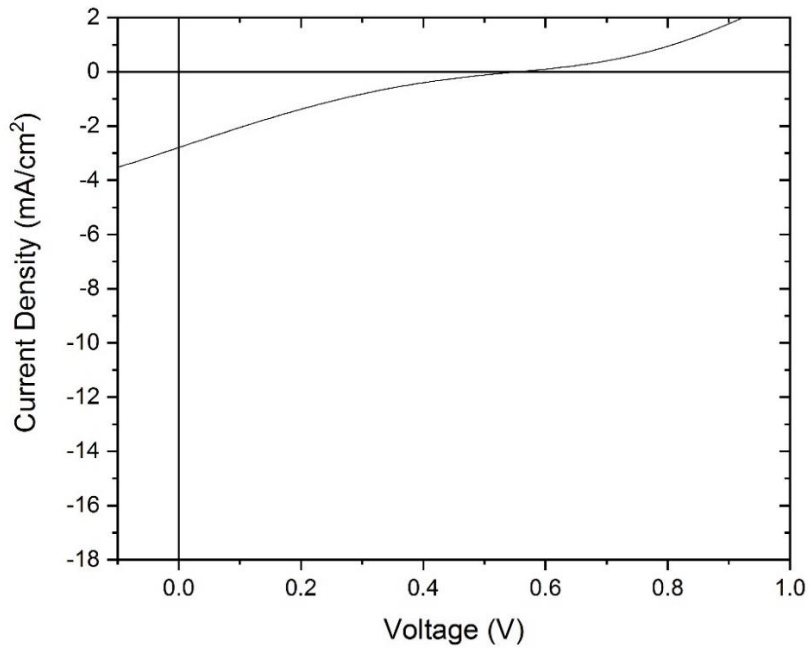
Figure 4.1. J-V characteristic curve of an ITO/Al 4083/P3HT:PC$_{61}$BM/Al solar cell with an active area of 29.5mm$^2$. This solar cell exhibited a good $V_{oc}$, but poor $J_{sc}$, FF and efficiency.

Before troubleshooting the issues with this design, the calibration of the in-house built solar simulator was verified. Solar cells were made with the same procedures as detailed above. They were then brought to Queen's University and tested with a calibrated solar simulator. The same solar cells were then tested at the Royal Military College of Canada in our laboratory. As there was a two-hour gap between the measurements taken at Queen's and the measurements taken our laboratory during which the solar cells, which were not encapsulated, were exposed to light, oxygen and moisture, a small decrease in efficiency was expected. The J-V characteristics of the best two solar cells tested with both solar simulators are presented in Table 4.1.

Table 4.1. J-V characteristics of two solar cells tested with Queen's University solar simulator, followed by the Royal Military College of Canada simulator.

| | Queen's University | | | | Royal Military College of Canada | | | |
|---|---|---|---|---|---|---|---|---|
| | $J_{sc}$ (mA/cm$^2$) | $V_{oc}$ (V) | FF | PCE (%) | $J_{sc}$ (mA/cm$^2$) | $V_{oc}$ (V) | FF | PCE (%) |
| Sample 1 | -3.44 | 0.50 | 0.22 | 0.37 | -2.74 | 0.55 | 0.22 | 0.32 |
| Sample 2 | -3.39 | 0.48 | 0.22 | 0.35 | -2.63 | 0.54 | 0.23 | 0.33 |
| Average | -3.41 | 0.49 | 0.22 | 0.36 | -2.69 | 0.55 | 0.23 | 0.33 |

As expected, the $J_{sc}$ – and consequently the PCE – values are slightly lower for the second testing, a sign of reduced absorption due to degradation of the solar cells after illumination from the first testing and ambient conditions exposure. Nevertheless, the results between the two sets of data are sufficiently similar to state that the poor performance of the solar cells is not due to a calibration issue of the solar simulator built in our laboratory.

Typical values for solar cells with a structure similar to those fabricated in this section are a $J_{sc}$ of 8-12 mA/cm$^2$, $V_{oc}$ ~0.6 V and a FF of 0.50-0.65[72]. Therefore, both the $J_{sc}$ and FF are of concerns. Furthermore, the J-V characteristic curve shown in Figure 4.1 exhibits a concavity $\left( \frac{d^2J}{d^2V} < 0 \right)$ in the fourth quadrant. Only a few papers investigating the origin of this concavity were found in the literature, but they seem to be pointing to a poor contact between the PC$_{61}$BM component of the active layer and the cathode[162, 171]. The results from an attempt to improve this contact are presented in the next section.

### 4.1.2    Solar Cells with a PCBM Over-layer

As discussed in 2.3.2, it has been widely reported that P3HT:PC$_{61}$BM blends suffer from a vertical phase separation during film formation with the PC$_{61}$BM, the electrons acceptor material, concentrating at the bottom of the film[31, 75, 104, 105]. This phase separation causes a hinderance for the electrons extraction in direct structure solar cells[171] since the cathode, the electrons collecting electrode, is the top electrode. Tremolet *et al.*[171] proposed that the poor contact between the PC$_{61}$BM and the cathode could be improved by inserting a thin layer of PC$_{61}$BM on the P3HT:PC$_{61}$BM layer, a solution which was tried in this thesis. Solar cells were made in accordance with the processing parameters detailed in Table 3.2. Orthogonal solvents were required for the P3HT:PC$_{61}$BM layer and the PC$_{61}$BM over-layer to avoid redissolution of the active layer. The active layer consisted of P3HT:PC$_{61}$BM in o-DCB (1:0.8, 2%w/v P3HT/o-DCB) while the over-layer was spin-coated from a solution of PC$_{61}$BM 0.5% w/v in DCM. The resulting solar cells were visually flaky in appearance, and some of the active layer seemed to have been washed out as a result of the deposition of the PC$_{61}$BM over-layer. This was confirmed by measuring the total thickness of the PEDOT:PSS, P3HT:PC$_{61}$BM and PC$_{61}$BM which was only 105 nm, compared to another solar cell made without the over-layer but otherwise identical parameters, which had a total thickness of 196 nm for the PEDOT:PSS and P3HT:PC$_{61}$BM. The efficiency of the solar cells produced with the over-layer was nevertheless measured. The J-V characteristic curve for the best solar cell obtained with a PC$_{61}$BM over-layer is shown in Figure 4.2.
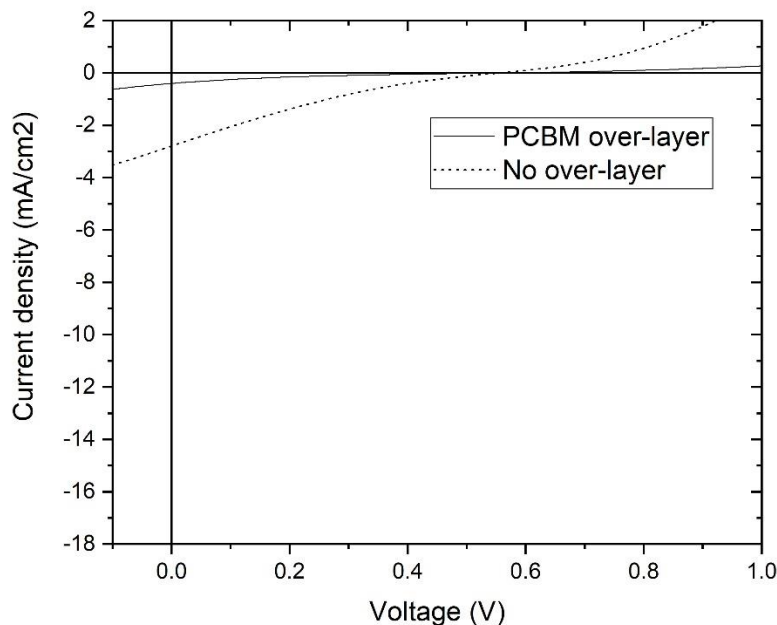
Figure 4.2. J-V characteristic curves of solar cells with and without a $PC_{61}BM$ over-layer. The $PC_{61}BM$ over-layer partially destroyed the under-layer, thus reducing the efficiency of the solar cell.

The efficiency of the best solar cell with a $PC_{61}BM$ over-layer was 0.03%, a net reduction from the solar cells presented in section 4.1.1. While other groups successfully reported bilayers solar cells using o-DCB and DCM as orthogonal solvent[163, 171], a $PC_{61}BM$ over-layer following the processing parameters detailed in Table 3.2 was deemed not to be the solution to improve the solar cells efficiency in this thesis as the under-layer was partly washed out by the over-layer.

Another option to improve the fullerene/cathode contact is to use a properly chosen ETL. As discussed in section 2.3.3.2, an ETL can improve the FF of solar cells by providing a protective layer preventing the diffusion of the metal from the cathode into the active layer and the subsequent electron quenching. As previously shown in Figure 2.24, a solar cell with an aluminium electrode but no ETL shows a concavity of the J-V curve similar to the one found in this thesis, while the concavity disappears and the $J_{sc}$ improves when a Ca or BCP ETL is used[120]. As manufacturing ETL is not within our laboratory's capabilities, the low FF was accepted as an unavoidable loss.

### 4.1.3  Small Area Indium-Tin-Oxide Solar Cells

The focus of the work was then shifted to the improvement of the low $J_{sc}$ of the solar cells fabricated in section 4.1.1. As mentioned in section 4.1.1, most solar cells produced for research purposes have an active area between 5 and 15 mm$^2$ and a $J_{sc}$ of 8-12 mA/cm$^2$ [72]. In comparison, the best solar cell fabricated in section 4.1.1 had an active area of 29.5 mm$^2$ and a $J_{sc}$ of 2.76 mA/cm$^2$. Similar results were obtained by Gupta et al.[162] with a solar cell with an active area of 25

mm$^2$, which had a $J_{sc}$ of 3.08 mA/cm$^2$. Several studies have been carried out on the effect of the solar cells active areas on their efficiency[78, 79, 172-174], with large area solar cells resulting in a sharp reduction of the efficiency. Figure 4.3 shows the efficiency of P3HT:PC$_{61}$BM solar cells as a function of their active area.
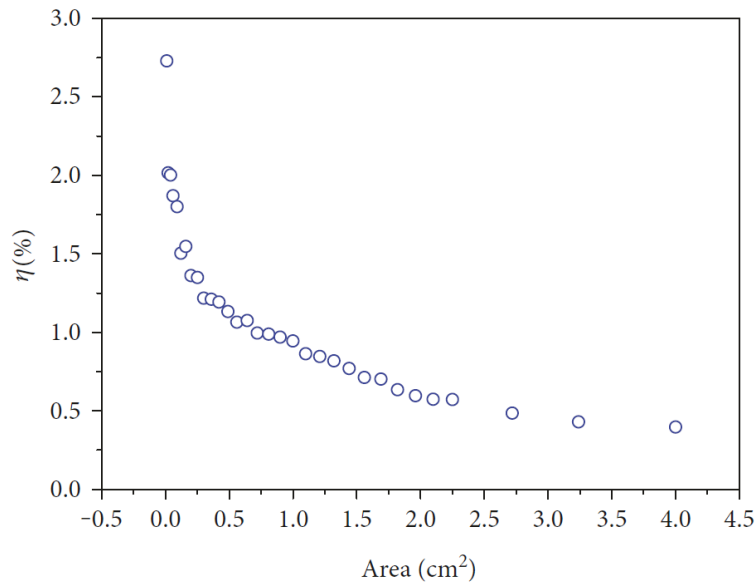


Figure 4.3. Area dependency of the efficiency of P3HT:PC$_{61}$BM solar cells. Large area results in a sharp reduction of the efficiency. Adapted from (Trindade and Pereira, 2017)[174].

Solar cells with smaller active areas were therefore fabricated as per the processing parameters detailed in Table 3.2. The patterning of the electrodes resulted in solar cells with active areas of 6 mm$^2$ and improved $J_{sc}$, as shown in Figure 4.4.
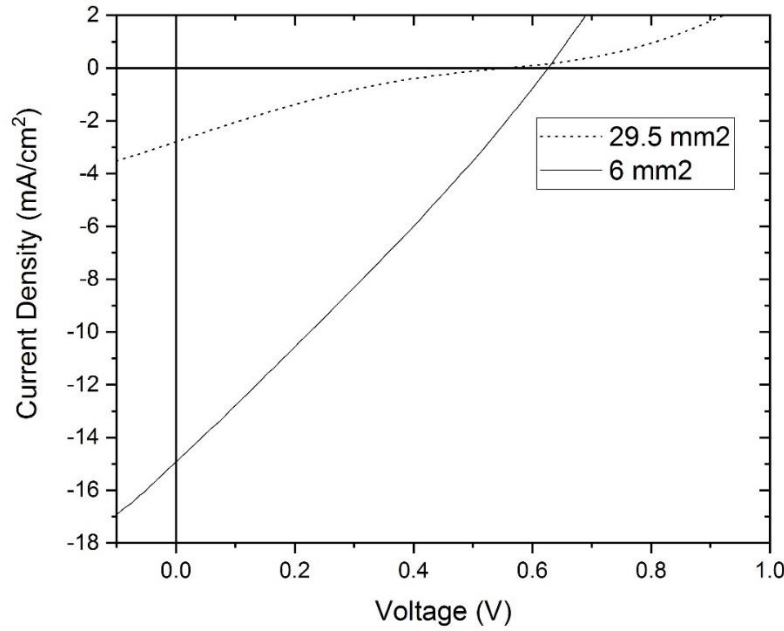
Figure 4.4. J-V characteristic curves for ITO solar cells with active areas of 29.5 and 6 mm$^2$. The solar cell with a smaller active area shows a marked increase in $J_{sc}$.

The $J_{sc}$ drastically improved with the reduction of the active area of the solar cell. The solar cells with an active area of 6 mm$^2$ exhibited an average efficiency of 1.7 $\pm$ 0.7% with the best cell having a $J_{sc}$ of 14.85 mA/cm$^2$, a $V_{oc}$ of 0.63 V, a FF of 0.27 and an efficiency of 2.48%, up from 0.27% for the 29.5 mm$^2$ solar cells. This increase in efficiency can be explained by looking at the effect of the series resistance $R_S$ of a solar cell, which would be higher for larger area of the active material and electrode. As discussed in 2.2.4, an increase in $R_S$ leads to a decrease in FF and current density[77-79]. From Figure 4.4, one can see that $R_S$, which is given by the inverse of the slope at the $V_{oc}$ point of the J-V characteristic curve, is much higher for the solar cell with the large active area (473.47 $\Omega$) than for the solar cell with the small active area (34.04 $\Omega$), thus negatively impacting the FF and current density. Furthermore, knowing that the power loss per unit area $P_R$ is given by[172]:

$$P_R = \frac{R_S I_{max}^2}{A} = \frac{R_S (J_{max} A)^2}{A} = R_S A J_{max}^2 \tag{4.1}$$

where $I_{max}, J_{max},$ and $A$ are respectively the maximum current, the maximum current density and the active area of a solar cell, it can be deduced that the effect of series resistance plays a more prominent role in solar cells with a larger area[78, 79, 173].

The small area solar cells fabricated in this section confirmed that appropriate fabrication procedures were used. The best solar cell with this design had an efficiency of 2.48% and serves

as the ITO reference solar cell for the remainder of this thesis. With a best cell efficiency of 2.48%, the efficiency is slightly lower than the 3-4%[72] reported in the literature. However, this was expected as the solar cells produced for this thesis do not have an ETL. In the next two sections, the ITO electrodes are replaced by PH1000 electrodes to fabricate ITO-free solar cells and allow the eventual integration of patterned azobenzene thin films within the solar cells.

## 4.2 INVERTED SOLAR CELLS WITH TRANSPARENT TOP ELECTRODES

One of the goals of this thesis was to use azobenzene crossed gratings to excite SPR and couple the light within an inverted solar cell. As discussed in section 1.2.3, linear and crossed gratings have been successfully used in the past to increase the efficiency of direct structure P3HT:PC$_{61}$BM solar cells[54]. However, inverted structures are becoming the dominating geometry due to advantages such as improved lifetime, air and moisture stability[31, 72, 73]. Only one example was found in the literature of SPR used in inverted P3HT:PC$_{61}$BM solar cells[56]. This study demonstrated an increase in photocurrent of inverted P3HT:PC$_{61}$BM solar cells[56], but solar cell efficiency measurements were not reported because of the difficulties encountered at that time with making a transparent top electrode. Two transparent top electrodes were tried in this thesis: an ultra-thin metal electrode and a spin-coated solution-processed electrode.

### 4.2.1 Metal Semi-Transparent Top Electrodes

Inverted solar cells with metal semi-transparent top electrodes were fabricated with 50 nm thick, 2 mm width stripe aluminium electrodes, P3HT:PC$_{61}$BM, HTL Solar, and 14 nm thick, 2 mm width stripe silver (Ag) electrodes, as per the processing parameters detailed in Table 3.2. The overlap of the layers created six solar cells with an active area of 4 mm$^2$ per sample. These solar cells exhibited a low average efficiency of $2.1 \times 10^{-4} \pm 0.7$ % with the best solar cell having a $J_{sc}$ of $5.16 \times 10^{-3}$ mA/cm$^2$, a $V_{oc}$ of 0.27 V, a FF of 0.19 and an efficiency of $2.6 \times 10^{-4}$ %. The characteristic J-V curve for the best solar cell obtained with this design is given in Figure 4.5. For this figure, the scale of the vertical axis has been changed from previous J-V plots reported in this chapter due to the low $J_{sc}$.
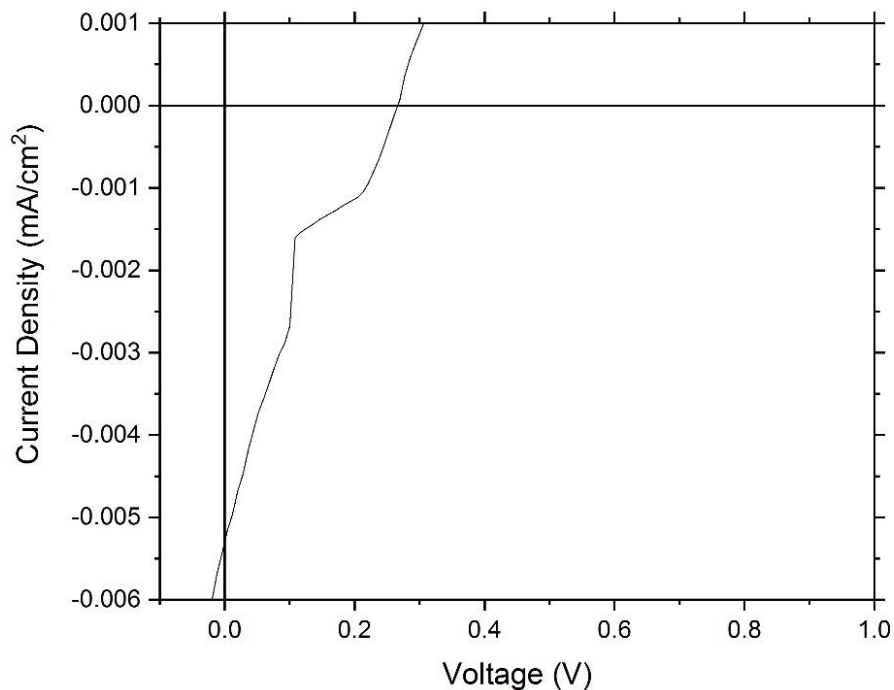
Figure 4.5. J-V characteristic curve of an inverted solar cell with a 14 nm Ag top electrode. This solar cell exhibited low $R_{SH}$, $J_{sc}$, $V_{oc}$, and FF.

The origin of the kink in the J-V characteristic curve is unknown. One possible explanation is that it is due to the charging of a capacitor, as the voltage swipe was done only once on the solar cell. While this is the technique used throughout this thesis, swiping back and forth several times should be done in future work. An analysis of the layers' thicknesses did not reveal any issues. The total thickness of the solar cell was measured to be 306 nm. With the bottom aluminium electrode having been reduced to 50 nm, the combined thickness of the active layer and HTL was therefore ~250 nm – a thickness which should not cause issues. However, while the $R_S$ - which can be estimated by the inverse of the slope at the $V_{oc}$ point - is low, as desired, the $R_{SH}$ - which can be estimated by the inverse of the slope at the $J_{sc}$ point – is also low, an indication of manufacturing defects. The total resistances of each solar cells on that sample varied from 0.9-4.0 MΩ. Combined with the active layer thickness of the solar cells, it is unlikely that the solar cells were short-circuited. One possible explanation for the low $R_{SH}$ could be the lack of an ETL. In a study on ZnO deposition technique, Noh et al. [175] fabricated inverted solar cells with a similar structure as the one built in this section, though theirs had a transparent bottom electrode. While the solar cells built in this thesis were made of Al/P3HT:PC$_{61}$BM/PEDOT:PSS/AG, the solar cells fabricated by Noh et al. had an ITO/optional ZnO/P3HT:PC$_{61}$BM/PEDOT:PSS/AG structure. The J-V characteristic

93

curves of the solar cells fabricated by Noh *et al.* are illustrated in Figure 4.6, with the characteristics shown in the first quadrant for this figure, instead of the fourth quadrant.
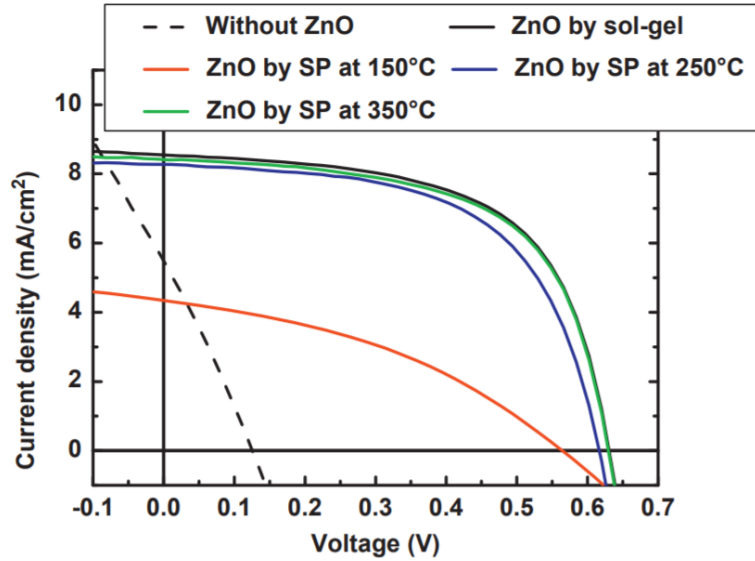


Figure 4.6. J-V characteristic curves of P3HT:PC$_{61}$BM solar cells with and without ZnO. The solar cell without a ZnO ETL displayed low $R_{SH}$, $J_{sc}$, $V_{oc}$, and FF. Adapted from (Noh *et al.*, 2013)[175].

Some similarities between Figure 4.5 and the J-V characteristics curve of the solar cell without the ZnO ETL in Figure 4.6 can be observed. In both cases, the solar cells exhibit low $R_{SH}$, $J_{sc}$, $V_{oc}$, and FF, and thus low efficiency. Delamination and dewetting[75], lack of a planarization layer over the bottom electrodes[13] and exciton quenching [31, 75, 104, 105] – which is more severe in an inverted solar cells due to vertical phase separation of the polymer/fullerene blend – are some of the reasons why and ETL is particularly important in an inverted structure.

Compounding the issue in this thesis is the use of an ultra-thin silver electrode without an anti-reflective coating. As discussed in section 2.3.3.3, ultra-thin layers of silver have been used as electrodes when combined with MoO$_3$ in a MoO$_3$/Ag/MoO$_3$ stack. While the top layer of the stack serves as a transparent conducting refractive index matching layer, reducing the large amount of reflection and lowering the series resistance, the bottom layer acts as a HTL to improve holes collection[121]. As manufacturing MoO$_3$ is not within our current laboratory capabilities, the top layer of the stack was omitted, while the bottom layer was replaced by PEDOT:PSS. The omission of the anti-reflective coating resulted in poor transmission of the light through the silver electrode, as illustrated in Figure 4.7.
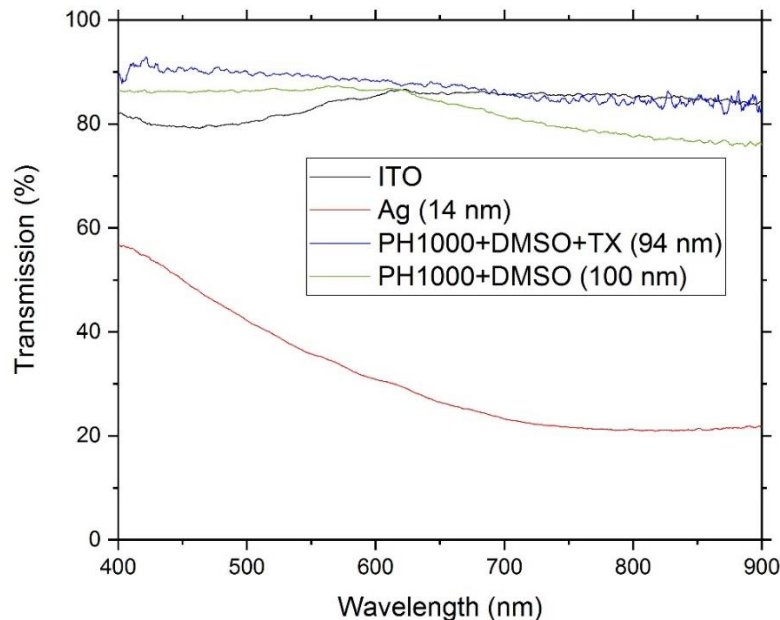
Figure 4.7. Transmission of ITO, PH1000 and Ag electrodes. While a ~100 nm PH1000 electrode is an acceptable alternative to ITO, a thin 14 nm layer of Ag without an anti-reflective coating has a significantly lower transmission in the visible range.

The combination of a lack of ETL and of anti-reflective coating for the ultra-thin metal electrode in the inverted solar cells structure resulted in solar cells with efficiency in the order of $10^{-4}$ – an efficiency far too low to serve as control solar cells. However, while Figure 4.7 shows that a 14 nm thick Ag electrode without an anti-reflective coating has poor transmission, it also shows that a 100 nm thick PH1000 electrode can be a suitable alternative to ITO. Furthermore, the addition of 0.5% wt of the surfactant TX-100, which was found essential to obtain good film morphology of the PH1000 electrode over the hydrophobic active layer, did not significantly alter the transmission of the film. Resistance measurements of PH1000 film with and without the addition of the surfactant also shows a trivial effect on the conductivity. Therefore, other attempts at fabricating top illuminated inverted solar cells were made, this time using PH1000 as the top electrode.

### 4.2.2 Spin-Coated Transparent Top Electrodes

Inverted solar cells with spin-coated transparent top electrodes were fabricated with 50 nm thick aluminium bottom electrodes, P3HT:PC$_{61}$BM, HTL Solar, and PH1000 + 5% wt DMSO + 0.5% wt TX-100 top electrodes, as per the processing parameters detailed in Table 3.2. The overlap of the layers created four solar cells with an active area of 8.49 mm$^2$ per sample. The best solar cell

obtained with this design had a $J_{sc}$ of $5.15 \times 10^{-3}$ mA/cm$^2$, a $V_{oc}$ of 0.50 V, a FF of 0.24 and an efficiency of $6.2 \times 10^{-4}$ %. The characteristic J-V curve for this solar cell is given in Figure 4.8.
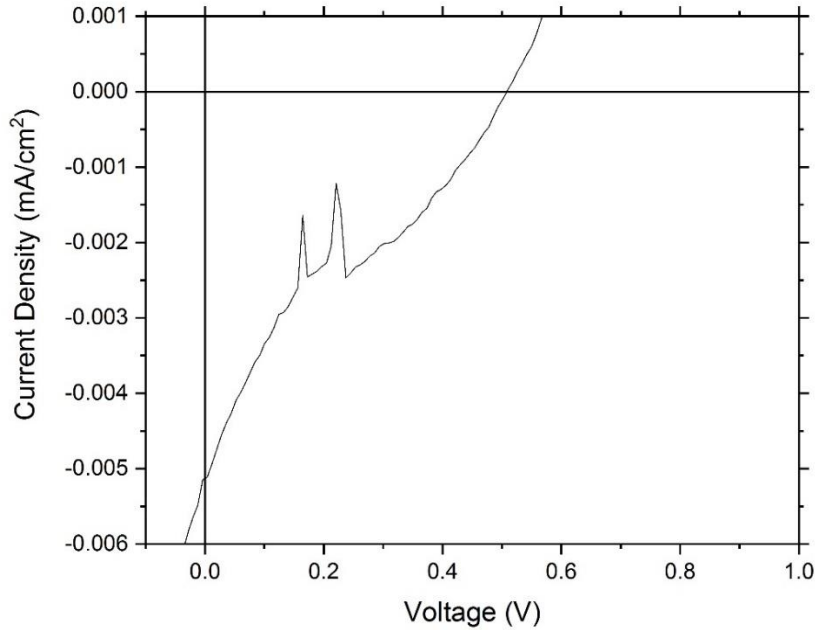


Figure 4.8. J-V characteristic curve of an inverted solar cell with a PH1000 top electrode. This solar cell displayed low $R_{SH}$ and $J_{sc}$.

The replacement of the top thin silver electrode by the PH1000 electrode resulted in improved $V_{oc}$ and FF with values closer to the ones obtained with the ITO control solar cell, as shown in Table 4.2. However, the $J_{sc}$ and PCE of the inverted/PH1000 solar cells remained very low.

Table 4.2. Comparison of the J-V characteristics of the ITO control solar cells and inverted solar cells.

| Solar Cell Design | $J_{sc}$ (mA/cm$^2$) | $V_{oc}$ (V) | FF | PCE (%) |
|---|---|---|---|---|
| Direct/ITO (area 6 mm$^2$) | 14.85 | 0.63 | 0.27 | 2.48 |
| Inverted/Ag (area 8.49 mm$^2$) | $5.16 \times 10^{-3}$ | 0.27 | 0.19 | $2.6 \times 10^{-4}$ |
| Inverted/PH1000 (area 8.49 mm$^2$) | $5.15 \times 10^{-3}$ | 0.50 | 0.24 | $6.2 \times 10^{-4}$ |

As PH1000 electrodes with similar resistance, thickness and transmission were successfully employed in this thesis in direct structure solar cells, as will be discussed in section 4.3, it is believed that the main issue with the inverted PH1000 top electrode is the lack of an ETL rather than choice and processing of the top electrode. Since inverted control solar cells could not be made with an acceptable efficiency, no attempts were made to integrate SRGs in inverted solar cells to excite SPR.

## 4.3    DIRECT SOLAR CELLS WITH PH1000 BOTTOM ELECTRODES

While the small-area ITO solar cells from section 4.1.3 confirmed appropriate manufacturing and testing procedures, it does not allow for the incorporation of a transparent nanostructure under the transparent electrode. Solar cells with PH1000 bottom electrodes were therefore fabricated to be used as control solar cells for measuring the efficiency enhancements of solar cells with scattering nanostructures.

### 4.3.1    High Annealing Temperature PH1000 Bottom Electrodes Solar Cells

Solar cells were fabricated with PH1000 + 5% wt DMSO bottom electrodes, P3HT:PC$_{61}$BM, and 100 nm thick top aluminium electrodes, as per the processing parameters detailed in Table 3.2. The overlap of the layers created four solar cells with an active area of 8.49 mm$^2$ per sample. These solar cells exhibited an average efficiency of 0.9 $\pm$ 0.4%. The characteristic J-V curve for the best solar cell obtained with this design is illustrated in Figure 4.9. This solar cell had a $J_{sc}$ of 13.62 mA/cm$^2$, a $V_{oc}$ of 0.54 V, a FF of 0.18 and an efficiency of 1.37%.
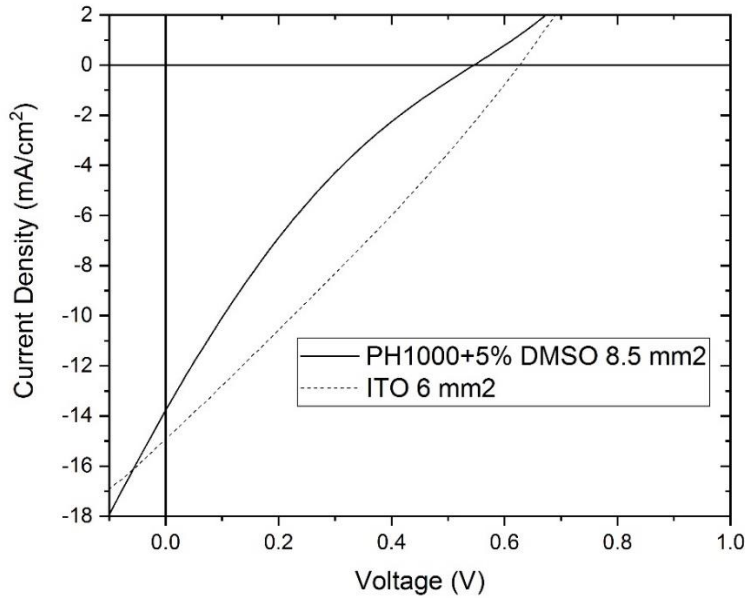


Figure 4.9. J-V characteristic curves of direct structure solar cells with ITO and PH1000 bottom electrodes. Though the PH1000-based solar cell shows a lower FF and current density, PH100 electrode remains an acceptable alternative to ITO.

With a best value of 1.37%, the PH1000 solar cell's efficiency is slightly lower than the 2.48% obtained for the ITO solar cell, but remains on par with results obtained by others[91]. The lower efficiency was expected due to both a lower conductivity of the PH1000 electrodes leading to a higher $R_S$ and, consequently, lower FF and current density, and a slight increase in the solar cells active area[77, 78]. The combined effect of the anode conductivity and solar cell active area on the performance of a P3HT:PC$_{61}$BM solar cell is modeled in Figure 4.10 below.
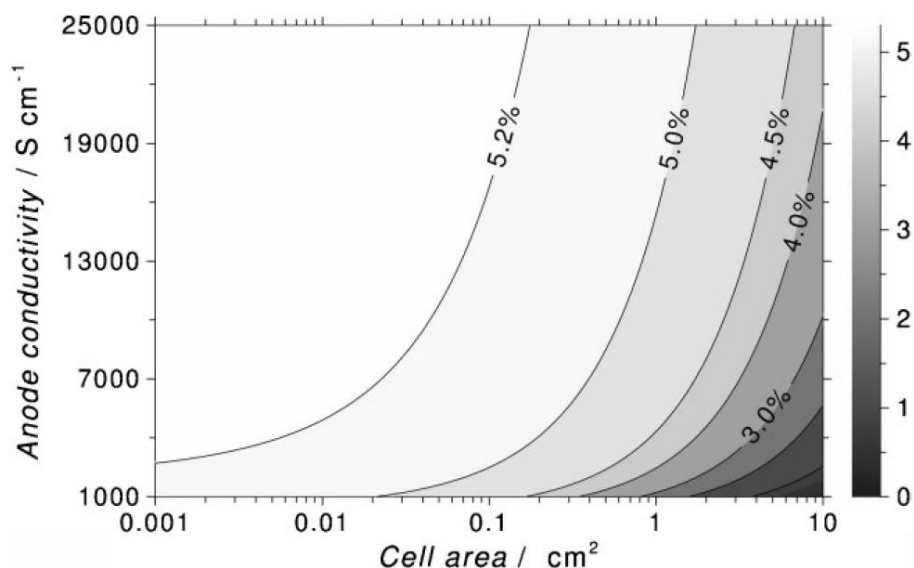


Figure 4.10. Effects of anode conductivity and solar cell area on the efficiency of P3HT:PC$_{61}$BM solar cells. The efficiency of the cell decreases with lower conductivity and higher active area. Adapted from (Servaites *et al.*, 2010)[77].

### 4.3.2 Low Annealing Temperature PH1000 Bottom Electrode Solar Cells

To scatter the light, a patterned thin layer of the azobenzene chromophore gDR1 will be incorporated in the solar cells. The glass transition temperature of gDR1 is 71˚C[170]. Although photobleaching by UV light exposure has shown to increase the glass transition temperature of some azobenzene chromophores above 150˚C[152-154], no reports were found on increasing the glass transition temperature through photobleaching of gDR1, the azobenzene chromophore used in this thesis. Therefore, solar cells were fabricated using a low 70˚C annealing temperature to serve as low annealing temperature control solar cells, in case the glass transition of gDR1 could not be increased.

The effect of a low annealing temperature on the PH1000 electrodes was first investigated. A 100 nm layer of PH1000 + 5% wt DMSO was spin-coated on a glass slide. The film was then annealed at 70˚C, and the resistance was measured at 0, 15, 30, 45 and 60 minutes intervals. It was found that longer annealing time had no effect on the resistance of the film, and that the film had similar conductivity at annealing temperatures of 70˚C and 150˚C. However, as seen in 2.3.3.1,

thermal annealing of P3HT:PC$_{61}$BM is responsible for the formation of networks allowing for a better movement of electrons and holes in the active material[18, 72, 107, 108]. A lower PCE was therefore expected for solar cells annealed at lower temperature.

Solar cells were built with identical methodology as the one in section 4.3.1, but with annealing temperature lowered to 70˚C and annealing time of the active layer adjusted to 60 minutes, as detailed in Table 3.2. The J-V curve for the best solar cell obtained with a low annealing temperature is illustrated in Figure 4.11.
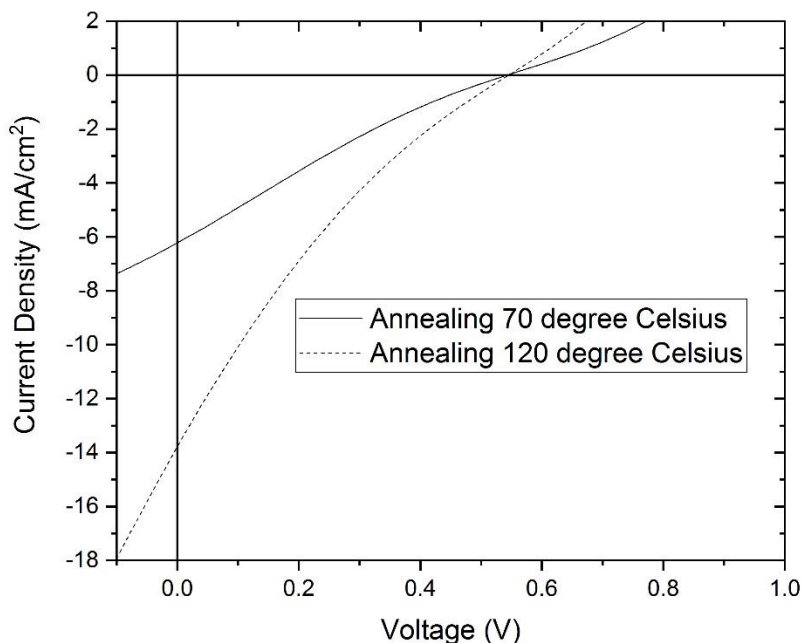


Figure 4.11. J-V characteristic curves of P3HT:PC$_{61}$BM solar cells with low and high annealing temperatures. The low annealing solar cell exhibits a reduced $J_{sc}$.

The solar cells made with a low annealing temperature exhibited an average efficiency of 0.69 $\pm$ 0.03% with the best solar cell having a $J_{sc}$ of 6.17 mA/cm$^2$, a $V_{oc}$ of 0.54 V, a FF of 0.22 and an efficiency of 0.72%. As expected, the change in the annealing temperature mainly affected the $J_{sc}$, a sign of poor percolation path for the electrons and holes. While the efficiency of this solar cell is lower than the 1.37% for the high annealing temperature, this solar cell can still function as a control solar cell shall the need arise to lower the annealing temperature due to the glass transition temperature of gDR1.

### 4.3.3 Effect of Surfactant on PH1000 Bottom Electrodes Solar Cells

In order to spread the PH1000 electrodes over structured azobenzene thin films, the surfactant TX-100 was added to the PH1000 + DMSO solution. Low annealing temperature solar

cells were made with the TX-100 surfactant as per the procedures detailed in Table 3.1, with the J-V characteristic curve for the best solar cell obtained with this design illustrated in Figure 4.12.
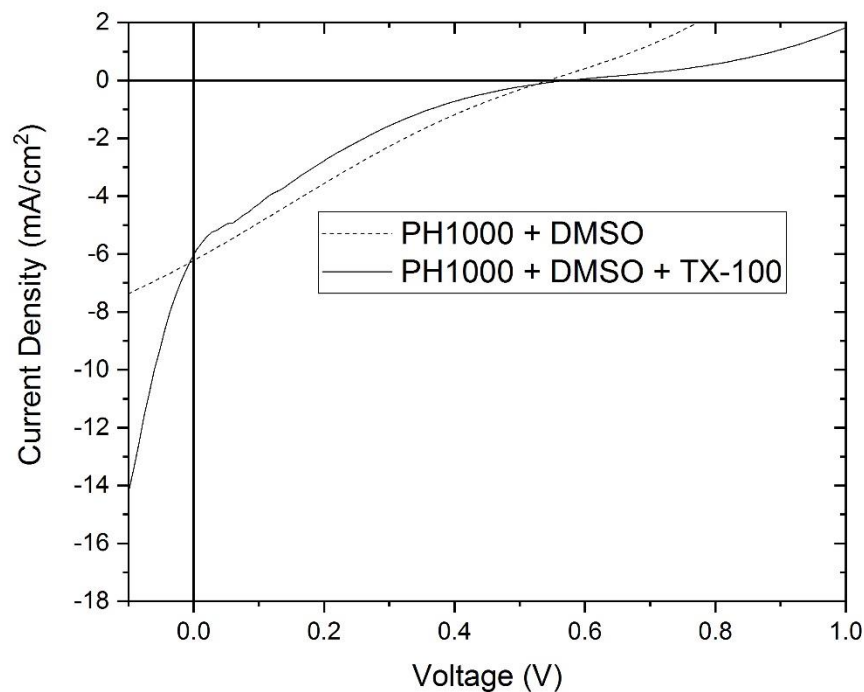


Figure 4.12. J-V characteristic curves of P3HT:PC$_{61}$BM solar cells fabricated with bottom a PH1000 electrodes with and without the addition of surfactant. The addition of 0.5% wt TX-100 to the PH1000 solution had minimal impact on the parameters of the solar.

The solar cells with the addition of the surfactant TX-100 exhibited an average efficiency of $0.4 \pm 0.2\%$ with the best solar cell having a $J_{sc}$ of 5.87 mA/cm$^2$, $V_{oc}$ of 0.57 V, a FF of 0.17 and an efficiency of 0.6%. Thus, the addition of 0.5% wt TX-100 to the PH1000 solution had minimal impact on the parameters of the solar cells. As discussed earlier in section 4.2.1, the small kinks in the J-V characteristic curve is unknown could be due to the charging of a capacitor, as the voltage swipe was done only once on the solar cell. Table 4.3 summarizes the parameters of the direct structure transparent bottom electrodes control solar cells used in this thesis.

Table 4.3. Parameters of the best direct structure transparent bottom electrode solar cells used as control solar cells.

| Solar Cell Design | $J_{sc}$ (mA/cm$^2$) | $V_{oc}$ (V) | FF | PCE (%) |
|---|---|---|---|---|
| ITO (area 6 mm$^2$) | 14.85 | 0.63 | 0.27 | 2.48 |
| PH1000 + DMSO/ high annealing temperature (area 8.49 mm$^2$) | 13.62 | 0.54 | 0.18 | 1.37 |
| PH1000 + DMSO/ low annealing temperature (area 8.49 mm$^2$) | 6.17 | 0.54 | 0.22 | 0.72 |
| PH1000 + DMSO + TX-100/ low annealing temperature (area 8.49 mm$^2$) | 5.87 | 0.57 | 0.17 | 0.60 |

## 4.4 SCATTERING IN SOLAR CELLS BY NANOSTRUCTURES ON CORONA-POLED AZOBENZENE THIN FILMS

With control solar cells characterized, focus was shifted to patterning azobenzene thin films in order to scatter the light in the solar cells to enhance their efficiency. This section presents the results of solar cells made with azobenzene thin films patterned by corona poling.

### 4.4.1 UV Treatment of Azobenzene Thin Films Patterned by Corona Poling

Randomized nanostructures were created on azobenzene thin films by corona poling as detailed in section 3.5.1, with Figure 3.18 and Figure 3.19 showing examples of nanostructures created following those procedures. The RMS roughness, $R_q$, could be controlled by varying the exposure temperature and exposure time. Figure 4.13 shows the $R_q$ obtained for azobenzene thin films poled at different temperatures with a constant exposure time of 30 minutes and constant corona discharge voltage of 8 kV, with average $R_q$ ranging from 86 nm to 420 nm, though only one sample was done at a temperature of 90˚C, as smaller structures were desired. An average $R_q =$ 41 nm was also achieved for azobenzene thin films poled at 75˚C for 150 seconds.
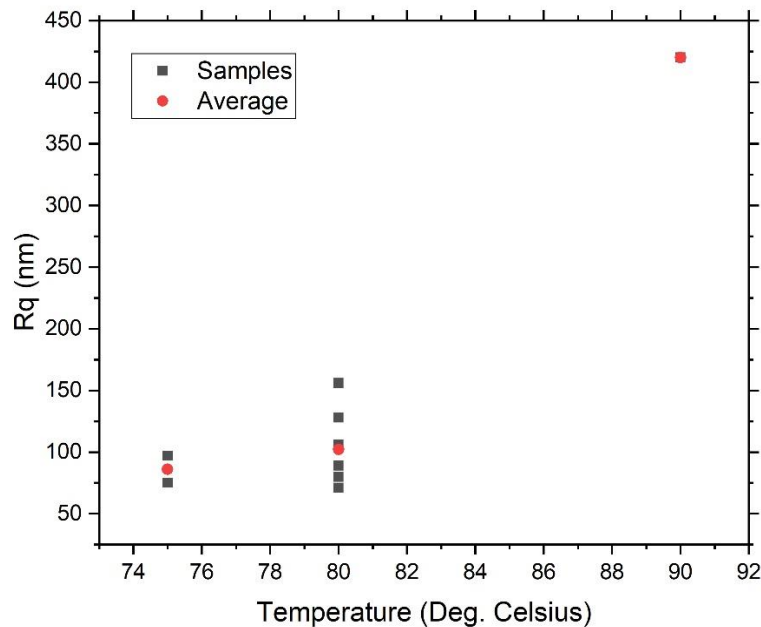
Figure 4.13. RMS roughness of corona-poled azobenzene thin films at different exposure temperatures. A higher exposure temperature resulted in an increase in $R_q$, with average values of $R_q = 86$ nm, $R_q = 102$ nm and $R_q = 420$ nm for exposure temperature of 75˚C, 80˚C and 90˚C respectively with a constant exposure time of 30 minutes and corona discharge voltage of 8 kV.

The corona-poled azobenzene thin films were then bleached by UV exposure as per the procedures detailed in section 3.5.2. It was observed that the bleaching of the thin films had two effects on the shape of the nanostructures. The first effect was the apparition of "volcano" like nanostructures, as illustrated in Figure 4.14.
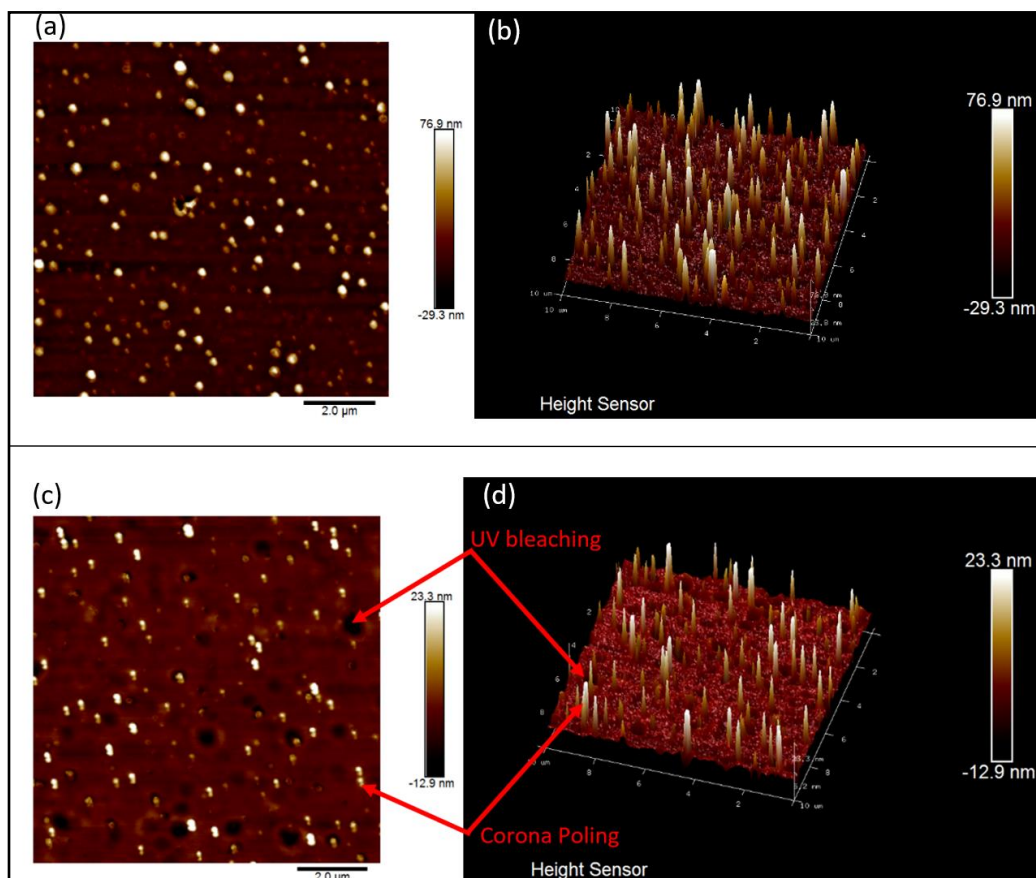
Figure 4.14. Formation of volcano-like nanostructures after UV treatment of a corona-poled azobenzene thin film. The 2D and 3D images of the untreated film are shown in (a) and (b) respectively, while (c) and (d) show the 2D and 3D images of the same film after a 20-hour UV exposure.

The formation of the volcano-like nanostructures also happened when an amorphous azobenzene thin film was exposed to UV light, as shown in Figure 4.15. The RMS roughness of the unbleached film was measured at $R_q = 0.5$ nm with the maximum roughness $R_{qmax} = 3$ nm. After a 20-hour UV exposure, the roughness was increased to $R_q = 2.1$ nm and $R_{qmax} = 40$ nm.
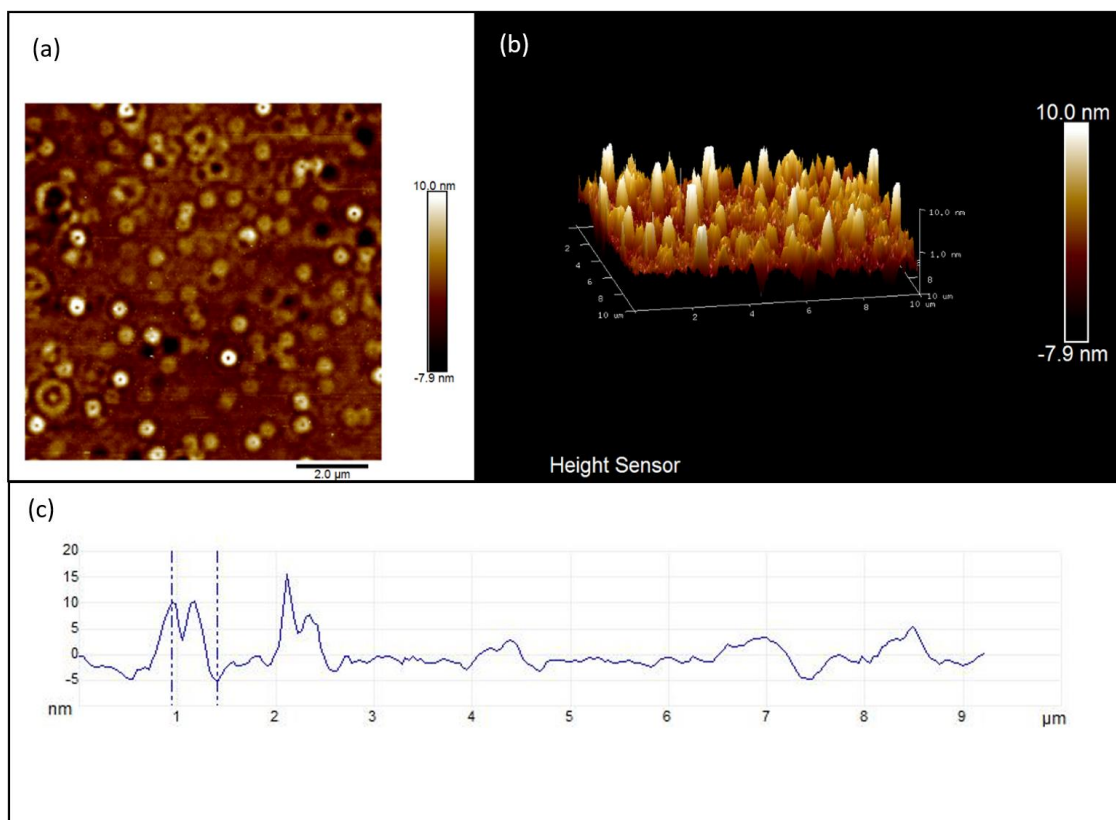
Figure 4.15. Nanostructures formation in as-cast azobenzene thin films exposed to UV light. Volcano-like nanostructures are shown in (a) 2D and (b) 3D with the profile shown in (c).The RMS roughness of the unbleached film was measured at $R_q = 0.5$ nm with the maximum roughness $R_{qmax} = 3$ nm. After UV light exposure, the roughness was increased to $R_q = 2.1$ nm and $R_{qmax} = 40$ nm.

The other effect of the UV exposure on the nanostructures of the corona-poled azobenzene thin films is their partial destruction. Figure 4.16 shows the profile of a corona-poled azobenzene thin film prior to and after UV exposure. The height of the nanostructures created from the corona poling were reduced from ~80 nm to ~40 nm.
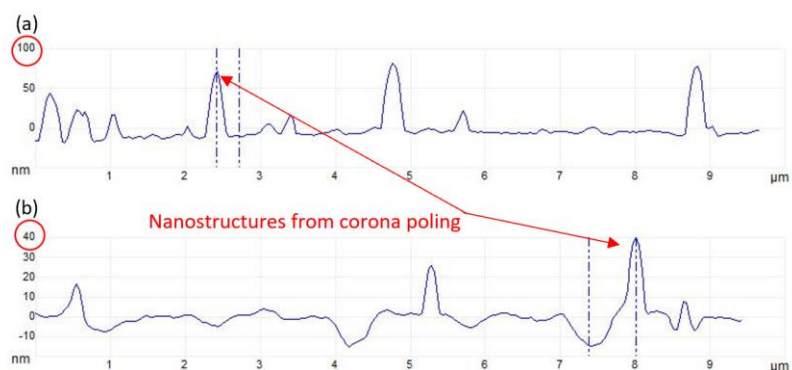
Figure 4.16. Profiles of a corona-poled azobenzene thin film (a) prior to and (b) after a 20-hour UV exposure. The UV exposure reduced the height of the nanostructures created by corona poling.

The partial destruction of the nanostructures after UV exposure was even more evident on larger structures created by corona poling at an elevated temperature, as shown by the scale difference in Figure 4.17.
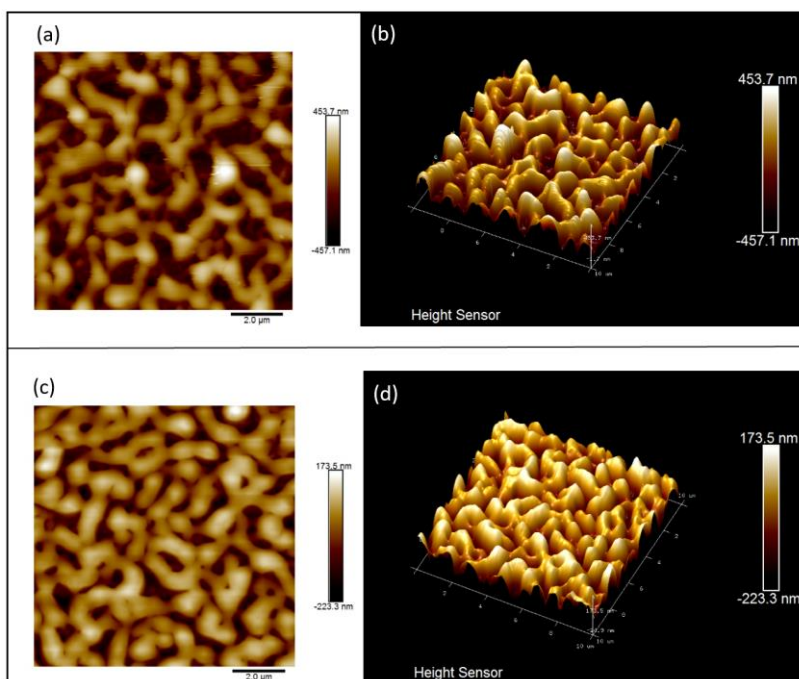


Figure 4.17. 2D and 3D images of large nanostructures on a corona-poled azobenzene thin film prior, (a) and (b), and after (c) and (d), a 20-hour UV exposure. The difference in the scales indicate a significant partial destruction of the nanostructures after UV exposure.

It was originally believed that the partial destruction of the nanostructures was a result of the films heating up when exposed to the UV light, thus allowing the azobenzene molecules to relax to their *trans* isomer. AFM measurements on a corona-patterned film after a 2-hour exposure effectively showed a decrease in $R_q$ from the original value. A cooling fan was then added to the UV station. AFM measurements taken every subsequent two hours showed no further reduction in $R_q$. However, a subsequent experiment with the cooling fan operating from the start of the exposure also showed a decrease in $R_q$ in the first two hours and stabilization of the nanostructure thereafter. A rise in the temperature of the sample was therefore not the cause for the partial destruction of the nanostructures. It is more likely that the initial absorption of the UV light energy allowed the azobenzene molecules to undergo a *trans-cis* isomerization. However, as discussed in section 2.5.3, the prolonged exposure to the UV light likely resulted in photodegradation of the film, which rendered the isomerization irreversible and stabilized the nanostructures.

### 4.4.2 Single-Sided Solar Cells with Corona-Poled Azobenzene Thin Films

Single-sided solar cells were fabricated as per the parameters detailed in Table 3.2, using a low 70˚C annealing temperature. The addition of a surfactant was found to be required to properly spread the PH1000 film over the rough azobenzene surface. The spin-coating speed of the PH1000 + 5% wt DMSO + 0.5% wt TX-100 was adjusted to 1500 RPM to completely cover the nanostructures and achieve a similar resistance across the electrode as the ones obtained for solar cells without the patterned azobenzene layer. Three single-sided solar cells designs were tried, and the J-V characteristic curves of the best solar cells for each design are presented in Figure 4.18. The first design included an azobenzene layer patterned uniquely by a 20-hour UV exposure at a distance of 3.5 cm from the lamp, creating volcano-like nanostructures and a film $R_q = 5.0$ nm. The other two designs were made by corona poling of azobenzene thin films, one with a 75˚C, 150 seconds exposure and the other with an 80˚C, 30 minutes exposure. Both were exposed to UV light for 20 hours, resulting in $R_q = 41$ nm and 49 nm respectively for corona-poled and bleached thin films.
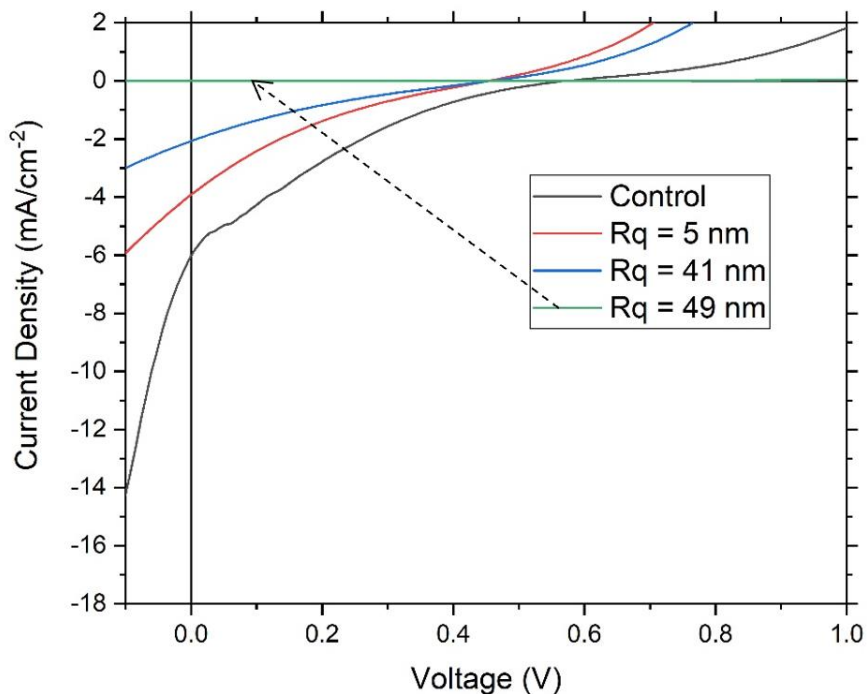
Figure 4.18. J-V characteristic curves of single-sided solar cells with azobenzene thin films patterned by corona poling. The efficiency of the solar cells quickly decreased with increasing values of $R_q$.

The solar cells with the azobenzene thin film patterned by UV exposure only exhibited an average efficiency of $0.24 \pm 0.06\%$ with the best solar cell having a $J_{sc}$ of 3.85 mA/cm², $V_{oc}$ of 0.45 V, a FF of 0.16 and an efficiency of 0.28%, down from 0.6% for the control solar cell (low annealing temperature with TX-100 surfactant, presented in section 4.3.3). The corona-poled solar cells with a $R_q = 41$ nm had an average efficiency of $0.12 \pm 0.06\%$ with the best solar cell having a $J_{sc}$ of 2.04 mA/cm², $V_{oc}$ of 0.46 V, a FF of 0.18 and an efficiency of 0.16%, while the one with a $R_q = 49$ nm had an average efficiency of $9 \times 10^{-5} \pm 3 \times 10^{-5}\%$ with the best solar cell having a $J_{sc}$ of 1.69x10⁻³ mA/cm², $V_{oc}$ of 0.47 V, a FF of 0.15 and an efficiency of $1.2 \times 10^{-4}\%$.

The spin-coated speed of the PH1000 mixture had been adjusted to 1500 RPM to provide electrodes with the similar resistance to those of the control solar cells. This technique worked relatively well for solar cells with small nanostructures, $R_q = 5$ nm and $R_q = 41$ nm with the PH1000 electrodes resistance measured at 141 Ω and 119 Ω respectively, compared to 122 Ω for the control solar cell. However, the PH1000 electrode resistance for the solar cell with the larger nanostructure, $R_q = 49$ nm, was measured at 256 Ω. It is possible that the random nature of the nanostructures was the origin of the issues with the morphology of the PH1000 film, with the PH1000 film being thick in some areas and thin in others – or worse not totally covering the peaks of the azobenzene film. This could have resulted in a non-continuous electrode. In order to isolate

the scattering effect of the nanostructures from the PH1000 morphology issue, double-sided designs were tried with the azobenzene layers and the solar cells on opposite side of the glass substrates. But first, the thermal stability of the bleached azobenzene films was investigated to identify if a higher annealing temperature could be used.

### 4.4.3 Thermal Stabilization of UV-Treated Azobenzene Nanostructures

As mentioned in section 4.3.2, the glass transition temperature of gDR1 is 71˚C[170]. The effect of heating a gDR1 azobenzene thin films at temperatures higher than its glass transition temperature was first investigated. Figure 4.19 shows the damage on a gDR1 azobenzene thin film cured at 120˚C for 30 minutes.



Figure 4.19. Damage on a gDR1 azobenzene thin film after curing at 120˚C for 30 minutes.

Heating a gDR1 azobenzene thin film at this temperature not only damaged the film, but also erased the nanostructures created by corona poling by allowing the azobenzene molecules to relax from their *cis* isomer to their *trans* isomer[67]. However, Takase *et al.*[153, 154] found that UV treated amorphous polymer containing DR1 could became thermally stable due to photocrosslinking, even at a temperature of 150˚C. Kimura *et al.*[152] found similar results using maleimide-based copolymers bearing azobenzene moieties. However, it is not believed that this demonstration was done for gDR1, the azobenzene chromophore used in this thesis. Patterned azobenzene thin films were therefore submitted to a 20-hour UV exposure to verify if they also became thermally stable. Figure 4.20 shows the 2D profile of an azobenzene thin film exposed to UV light before and after heating at 200˚C (the maximum safe operating temperature of the oven available in our laboratory) for 30 minutes.
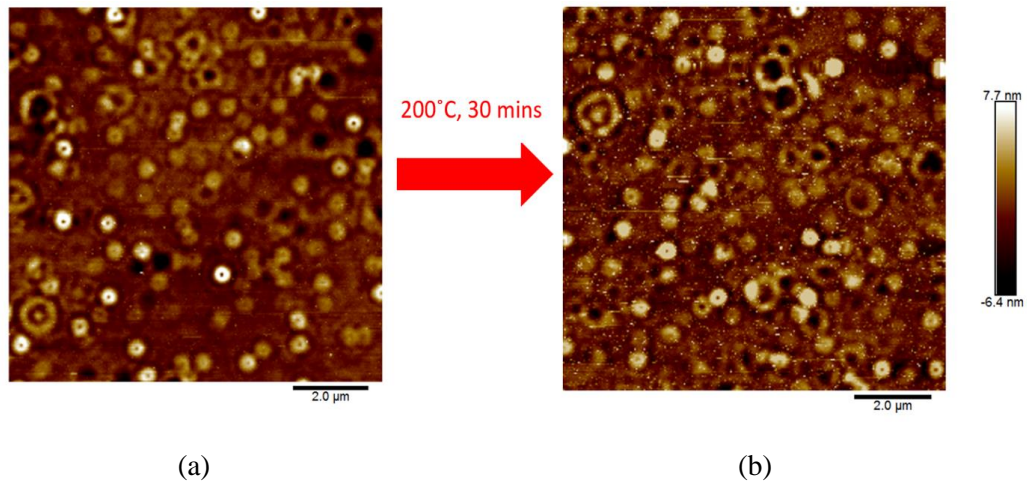
Figure 4.20. 2D profile of a UV treated azobenzene thin film (a) before and (b) after being heated at 200˚C for 30 minutes. The high temperature exposure had no apparent effect on the volcano-like nanostructures.

As discussed in section 4.4.1, the UV exposure created volcano-like nanostructures on the azobenzene thin film. The $R_q/R_{qmax}$ of the film before heating were measured at 2.14/40 nm and remained 2.14/40 nm after heating. Heating the UV treated film had no apparent effect on the nanostructures and did not seem to damage the film. Similar results were found after heating an azobenzene thin film patterned by corona poling and UV treated, as shown in Figure 4.21. This time, the film was heated at 120˚C, the chosen temperature for the thermal annealing of the solar cells.

.
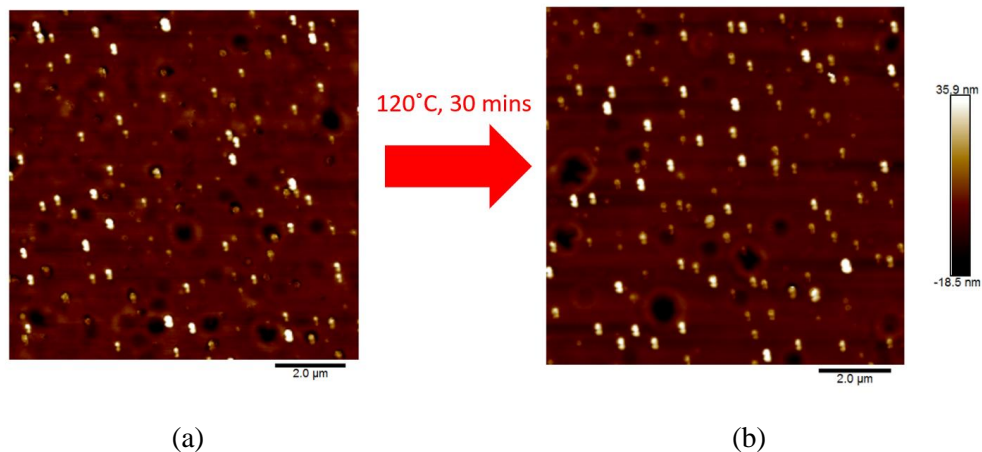


Figure 4.21. 2D profile of a corona-poled and UV treated azobenzene thin film (a) before and (b) after being heated at 120˚C for 30 minutes. The high temperature exposure had no apparent effect on the nanostructures.

The thermal stability of gDR1 after UV treatment is an interesting development for the incorporation of gDR1 nanostructures in solar cells. Recalling the results discussed in section 4.3.2, the control solar cell annealed at a low temperature of 70°C had an efficiency of 0.72%, while a higher annealing temperature of 120°C resulted in an efficiency of 1.37%. An annealing temperature of 120°C is therefore used for the remainder of this thesis. In the next sections, corona-poled and UV treated azobenzene thin films will be incorporated in double-sided direct solar cells with PH1000 bottom electrodes.

### 4.4.4 Double-Sided Solar Cells with Corona-Poled Azobenzene Thin Films

Double-sided solar cells with azobenzene thin films patterned by UV light exposure only ($R_q/R_{qmax} = 2.1/40$ nm) or a combination of corona poling and UV exposure ($R_q/R_{qmax} = 3.9/57$ nm, 6.2/71 nm, 5.5/72 and 6.5/371 nm) were fabricated as per the procedures detailed in Table 3.2, with a high annealing temperature of 120°C. The J-V characteristic curves for the best solar cells obtained with those designs are presented in Figure 4.22.
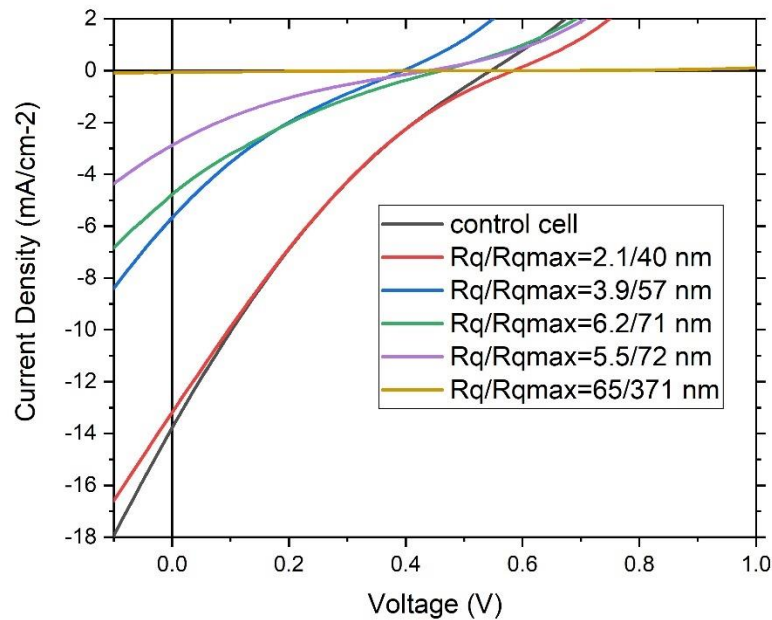


Figure 4.22. J-V characteristic curves for double-sided solar cells with azobenzene thin films patterned by corona poling and UV exposure. While the efficiencies of the solar cells showed some improvement with increased values of $R_q$, they quickly degraded with higher values of $R_{qmax}$.

Figure 4.22 has a few interesting details. The first point of interest is the J-V characteristics of the $R_q/R_{qmax} = 2.1/40$ nm solar cell, obtained by patterning the azobenzene thin film by UV

exposure only without corona poling (the only patterned solar cell without corona poling on the graph). This solar cell exhibited an average efficiency of $1.0 \pm 0.6\%$ with the best solar cell having a $J_{sc}$ of 13.49 mA/cm², $V_{oc}$ of 0.58 V, a FF of 0.19 and an efficiency of 1.47%, up from 1.37% for the best control solar cell (average of $0.90 \pm 0.06\%$) presented in section 4.3.1. With both the average and the best solar cell efficiencies surpassing those of the control solar cell, the efficiencies enhancements could possibly be attributed to scattering. However, as the efficiency gaps between the patterned solar cells and control solar cells are relatively small, a more in-depth analysis is required. Figure 4.23 shows the transmission of the patterned azobenzene thin films taken before building the solar cells on the other side of the glass substrates.
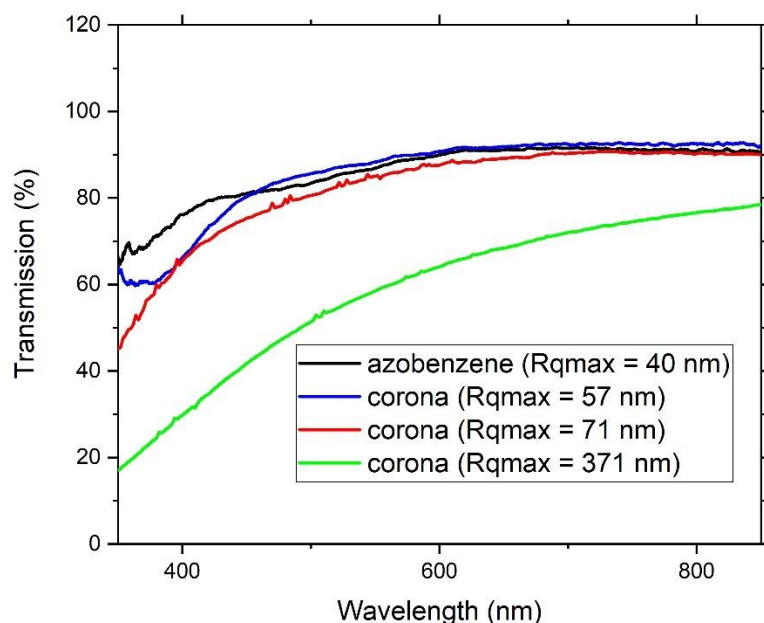


Figure 4.23. Transmission of azobenzene thin films patterned by UV exposure only ($R_{qmax} = 40$ nm) or a combination of corona poling and UV exposure ($R_{qmax} = 57,\ 71,\ 371$ nm). While the UV exposure resulted in good transmission for wavelengths above 500 nm, the transmissions of the thin films were not ideal for shorter wavelengths. High values of $R_{qmax}$ also resulted in poor transmission.

As it can be seen from Figure 4.23, even after 20 hours of bleaching, the transmissions of the azobenzene thin films and their glass substrate remain lower than the transmission of the glass substrate alone. Consequently, one should expect a lower efficiency from solar cells made with a layer of bleached azobenzene than a solar cell made without the additional layer. The increase in the efficiency of the solar cell with an azobenzene thin film patterned by UV exposure can therefore be attributed to the scattering of the light by the azobenzene, with the scattering effect slightly overcompensating for the loss in transmission.

With this promising result, one could expect that increasing the roughness of the azobenzene thin films should lead to further efficiency enhancements. However, patterning the azobenzene thin films by corona poling to increase their roughness did not yield successful results. As it can be seen from Figure 4.23, the transmission of the light through the corona-poled azobenzene thin films generally decreased with increasing roughness, resulting in decreasing values of $J_{sc}$, with $J_{sc} = 5.58$, 4.69, 2.83 and 0.06 mA/cm$^2$ obtained for $R_q/R_{qmax} = 3.9/57$ nm, 6.2/71 nm, 5.5/72 and 6.5/371 nm respectively. At first glance, it seems that increasing the roughness through corona poling and UV exposure does not lead to an efficiency enhancement, in contradiction to the result found with the patterning of the azobenzene thin film through UV exposure only. However, additional clues can be gained by analysing the average efficiencies obtained for the double-sided solar cells as a function of their $R_q$ and $R_{qmax}$, as shown in Figure 2.24.
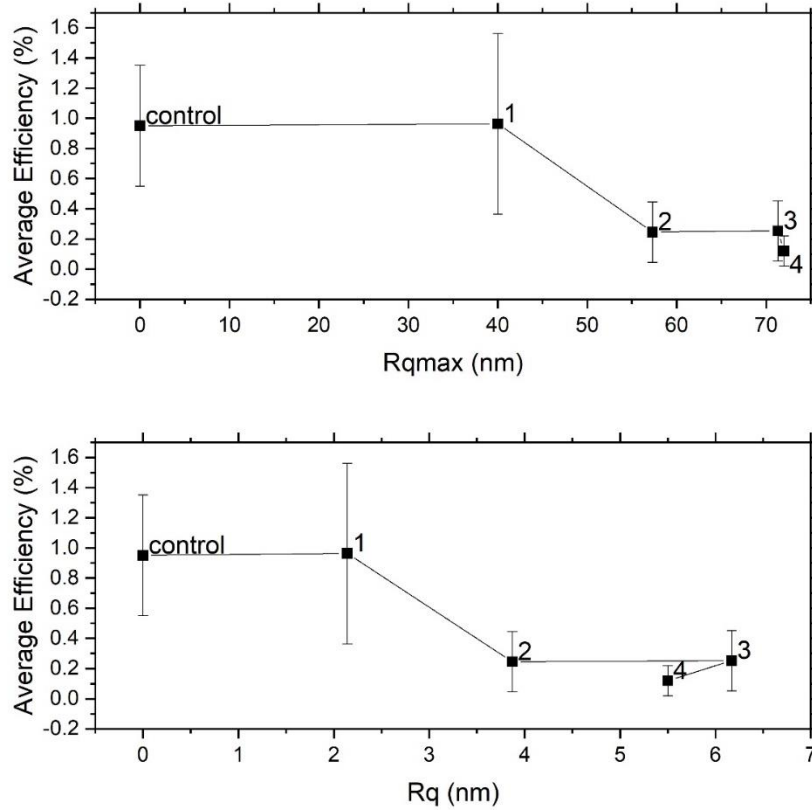


Figure 4.24. Average efficiencies of double-sided solar cells with patterned azobenzene thin films as a function of $R_{qmax}$ and $R_q$. The solid lines are guides for the eyes only.

As previously discussed, point 1, with a $R_q/R_{qmax} = 2.1/40$ nm, has a slightly better efficiency than the control solar cell. The efficiency then decreases sharply at point 2, which saw increases in both $R_q$ and $R_{qmax}$ with $R_q/R_{qmax} = 3.9/57$ nm. However, between point 2 and point 3 ($R_q/R_{qmax} = 3.9/57$ nm and 6.2/71 nm respectively), the efficiency slightly increased, with both $R_q$ and $R_{qmax}$ increasing. Meanwhile, at point 4 ($R_q/R_{qmax} = 5.5/72$ nm), the efficiency decreases, with the $R_q$ decreasing while $R_{qmax}$ is increasing. One can therefore conclude that an increase in $R_q$ can lead to an increase in efficiency due to a scattering effect, but a large $R_{qmax}$ negatively impacts the efficiency. This effect is probably due to the ratio of forward/total scattering.

Effectively, as discussed in section 2.5.1, in one of their experiments Baek *et al*.[60] incorporated AgNPs in the PEDOT:PSS layer of PTB7:PC$_{71}$BM inverted solar cells. They found that, initially, increasing the AgNPs size led to an enhancement of the efficiency. However, a further increase in AgNPs size caused a sharp reduction in the portion of forward scattering and, consequently, in the efficiency of the solar cell, with 67 nm being the optimized size for the nanoparticles for their particular case. In this thesis, promising results were obtained with an azobenzene thin film patterned by UV exposure only with a $R_{qmax} = 40$ nm, but a sharp decrease in efficiency was observed with an azobenzene thin film patterned by corona poling and UV exposure with a $R_{qmax} = 57$ nm. Taking those results in consideration, it is therefore hypothesized that if the $R_q$ of the azobenzene thin films could be increased without causing a further increase of the $R_{qmax}$ beyond 40 nm, better results could potentially be achieved. As corona poling, even at low temperature and exposure time, resulted in nanostructures with sizes superior to 40 nm, another patterning technique was chosen: crossed gratings.

## 4.5   SCATTERING IN SOLAR CELLS BY CROSS GRATINGS ON AZOBENZENE THIN FILMS
In this section, the UV treatment of crossed gratings on azobenzene thin films is discussed, and results of P3HT:PC$_{61}$BM and PTB7:PC$_{61}$BM solar cells with crossed gratings are presented.

### 4.5.1   Thermal Stabilization of UV-Treated Azobenzene Crossed Gratings
It has been seen in section 4.4.1 that UV exposure resulted in a partial destruction of azobenzene nanostructures. Therefore, crossed gratings with depth $\sim 60 - 90$ nm, that is deeper than the intended final depth, were fabricated as per the procedures detailed in section 3.5.1. Before building the solar cells on the other side of the substrate, the thermal stability of the UV treated gratings was verified. Figure 4.25 shows the 2D profile of a non-UV treated azobenzene thin film patterned with a crossed grating before and after being heated at 120°C for 30 minutes.
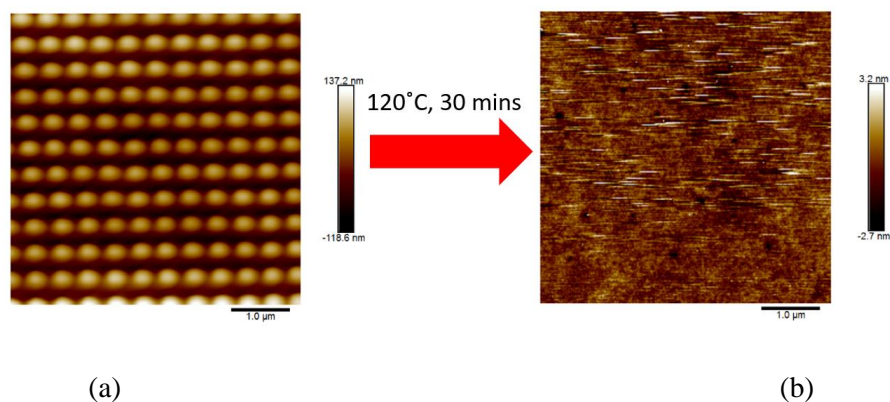
Figure 4.25. 2D profile of a crossed grating on an azobenzene thin film (a) prior to and (b) after heating at 120˚C for 30 minutes. Heating the azobenzene thin film above its glass transition temperature erased the grating.

As it can been seen from Figure 4.25, heating the azobenzene thin film patterned with crossed gratings above its glass transition temperature erased the gratings. Another grating was then fabricated and treated with UV light. Figure 4.26 shows crossed gratings after a 20-hours UV exposure. As it was the case with the corona-poled azobenzene thin films, the UV exposure resulted in a partial destruction of the existing nanostructures while creating volcano-like nanostructures.
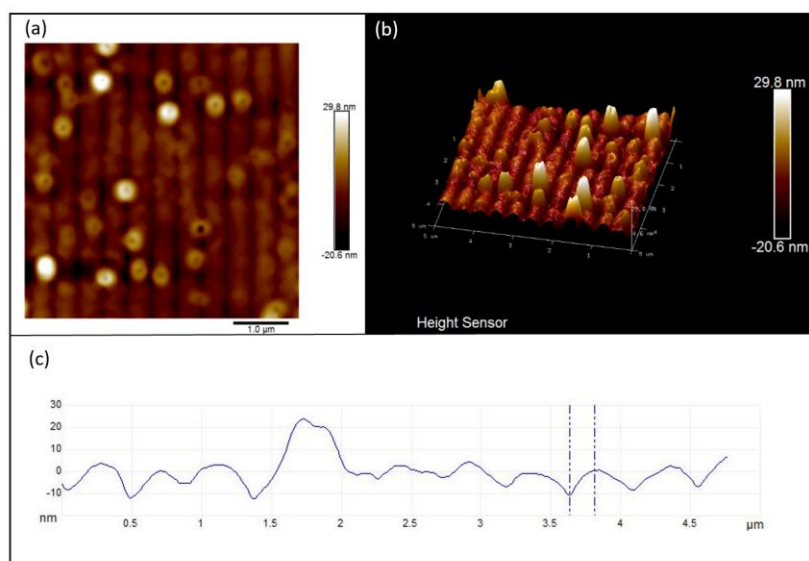


Figure 4.26. (a) 2D, (b) 3D and (c) profile of crossed grating on an azobenzene thin film after a 20-hour UV exposure. The UV exposure resulted in a partial destruction of the gratings and formation of volcano-like nanostructures.

Thermal stability of the UV treated films was then verified. Figure 4.27 shows a UV treated crossed grating before and after being heated at 120˚C for 30 minutes, with minimal changes caused by the heating cycle. The $R_q/R_{qmax}$ of the film before heating were measured at 4.56/53 nm and 5.09/57 nm after heating.
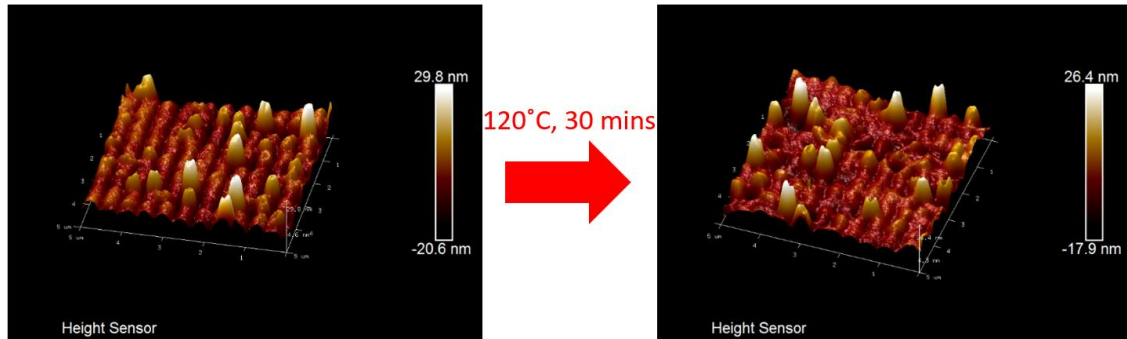


Figure 4.27. 3D Profile of a UV treated crossed grating on azobenzene thin film (a) before) and (b) after being heated at 120˚C for 30 minutes. The high temperature exposure had no apparent effect on the nanostructures.

### 4.5.2    Impact of UV Lamp Distance on the Nanostructures of the Azobenzene Thin Films

Under a constant exposure time, the distance of the azobenzene thin films to the UV lamp was found to have a critical impact on the size of the azobenzene nanostructures and the transmission of the film. Figure 4.28 shows the impact of the sample distance to the UV lamp on the grating depth, $R_q$ and $R_{max}$.
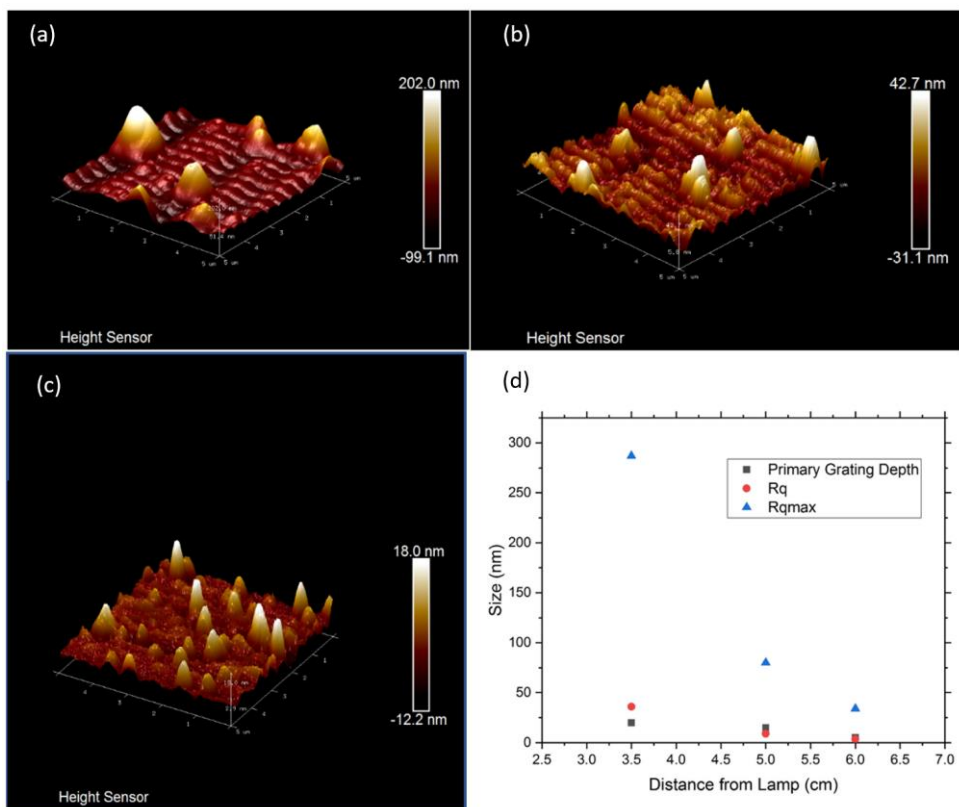
Figure 4.28. Effects of sample distance from the UV lamp on the size of the nanostructures. All three samples had identical original gratings and were exposed to UV light for 20 hours, with the distance to the lamp being (a) 3.5 cm, (b) 5 cm and (c) 6 cm.

The results from these experiments confirmed the hypothesis discussed in section 4.4.1: the partial destruction of the grating can not be due to the sample heating up under the UV lamp, as the destruction is more severe at an increased distance, as shown by the changing scales in Figure 4.28. It is more likely that the absorption of the UV energy allows the azobenzene to undergo a *trans-cis* isomerization responsible for the partial destruction of the grating, but the high intensity of the UV light causes an irreversible photodegradation of the azobenzene molecules, "freezing" the molecules in place. As the light would be more intense for a sample closer to the source, the photodegradation would be more rapid, therefore freezing the molecules in place at a faster rate. This would help preserve the grating and increase the $R_q$. However, a shorter distance to the lamp also has the unintended and undesired consequence of creating larger volcano-like nanostructures, as shown in Figure 4.28(a), thus greatly increasing the $R_{qmax}$.

Furthermore, even at a constant 20-hour exposure time – which, in Figure 3.21 was shown to be enough time to saturate the transmission gain at a distance of 3.5 cm from the lamp – the transmission of the patterned azobenzene thin films after UV exposure was found to also depend on the distance of the sample from the lamp, as illustrated in Figure 4.29.
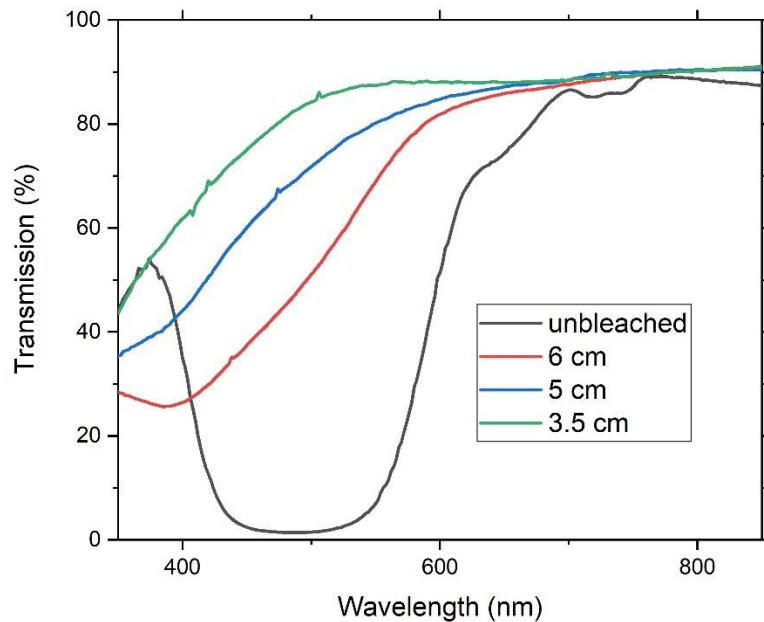
Figure 4.29. Transmission of patterned azobenzene thin films after a 20-hour UV exposure at different distance from the UV lamp. The films achieved a better transmission at a closer distance from the lamp.

As it can be seen from Figure 4.29, the films achieved a better transmission at a closer distance from the lamp. There are therefore competing requirements: while a high transmission and increased $R_q$ (increase preservation of the gratings) are desirable and require a short distance to the lamp, limiting the size of $R_{qmax}$ is critical and requires a longer distance from the lamp. In the next sections, azobenzene thin films patterned by crossed grating were exposed to UV light at different distances, resulting in different values of $R_q/R_{qmax}$. The patterned and bleached films were then incorporated in double-sided P3HT:PC$_{61}$BM and PTB7:PC$_{61}$BM solar cells.

### 4.5.3 Double-Sided Solar Cells with Crossed Gratings on Azobenzene Thin Films

Double-sided P3HT:PC$_{61}$BM solar cells with crossed gratings on azobenzene thin films were fabricated as per the procedures detailed in Table 3.2. The distance from the UV lamp was varied from 5 cm, resulting in $R_q/R_{qmax} = 3.9/41$ nm, to 3.5 cm, resulting in a $R_q/R_{qmax} = 14/136$ nm. The J-V characteristic curves for the best of those solar cells, the best solar cell made with the azobenzene thin film patterned only by the UV exposure ($R_q/R_{qmax} = 2.1/40$ nm) previously presented in section 4.4.4 and the control solar cell are shown in Figure 4.30. The reader should note that the scale of this graph was changed from previous graphs to accommodate a larger value of $J_{sc}$.
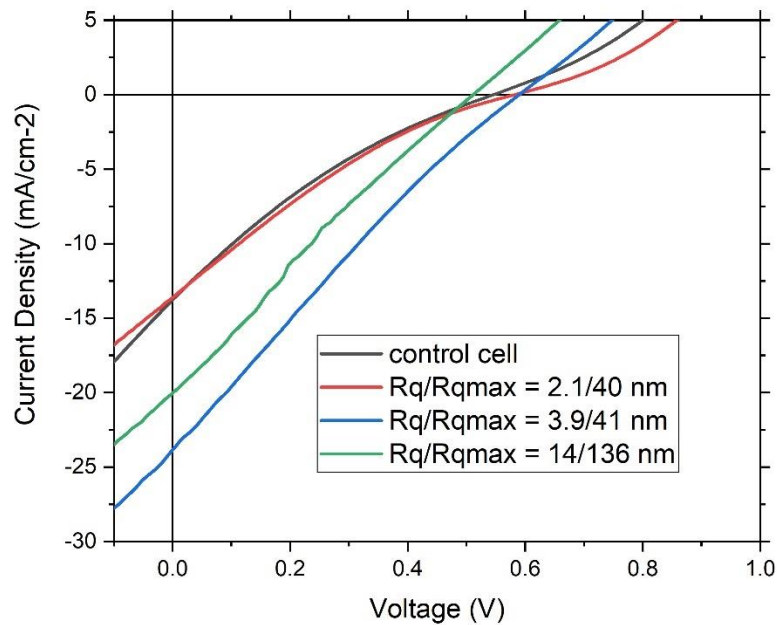
Figure 4.30. J-V characteristic curves for double-sided P3HT:PC$_{61}$BM solar cells with azobenzene thin films patterned by crossed gratings and UV exposure. The slight increase in $R_q$ from the crossed gratings, while keeping $R_{qmax}$ around ~40 nm, resulted in a significant increase in $J_{sc}$. A further increase in $R_{qmax}$ resulted in a smaller increase in $J_{sc}$.

The $R_q/R_{qmax} = 3.9/41$ nm solar cells had an increase average efficiency of $2 \pm 1\%$ (compared to $0.9 \pm 0.4\%$ for solar cells without the azobenzene layer). The best solar cell with $R_q/R_{qmax} = 3.9/41$ nm had a high $J_{sc}$ of 23.68 mA/cm$^2$ compared to 13.62 mA/cm$^2$ for the control solar cell, a strong indication of successful scattering within the solar cell leading to an increased absorption of the light. It also exhibited an improved $V_{oc}$ of 0.59 V, a FF of 0.23 and an efficiency of 3.19%, up from 1.37% for the best control solar cell - a significant efficiency enhancement of 133%. However, a further increase in $R_{qmax}$, with $R_q/R_{qmax} = 14/136$ nm, resulted in the best solar cell having a smaller increase in $J_{sc}$ of 19.89 mA/cm$^2$, $V_{oc}$ of 0.58 V, a FF of 0.19 and an efficiency of 2.32%.

As mentionned in section 4.5.2, the transmission of the azobenzene film decreases with the UV exposure distance. However, a short exposure distance is not possible due to the increase in $R_{qmax}$. This issue could be subsidiary in a polymer/fullerene blend less susceptible to the azobenzene absorbance. The absorbance spectrum of the P3HT:PC$_{61}$BM blend largely overlaps with the absorbance spectrum of gDR1, as shown in Figure 4.31. The wavelength range of 350 – 600 nm contains 90% of the gDR1 absorbance. P3HT:PC$_{61}$BM has 81% of its absorbance in the same range. Solar cells made from this blend would therefore be largely affected by the transmission of the azobenzene thin films. However, PTB7:PC$_{61}$BM only has 51% of its

absorbance in the 350 – 600 nm range. Double-sided PTB7:PC$_{61}$BM solar cells with patterned and UV treated azobenzene thin films should therefore have higher efficiency enhancements compared to a control solar cell than the ones observed for P3HT:PC$_{61}$BM solar cells with similar $R_q$, $R_{qmax}$, and transmission of the azobenzene thin films.
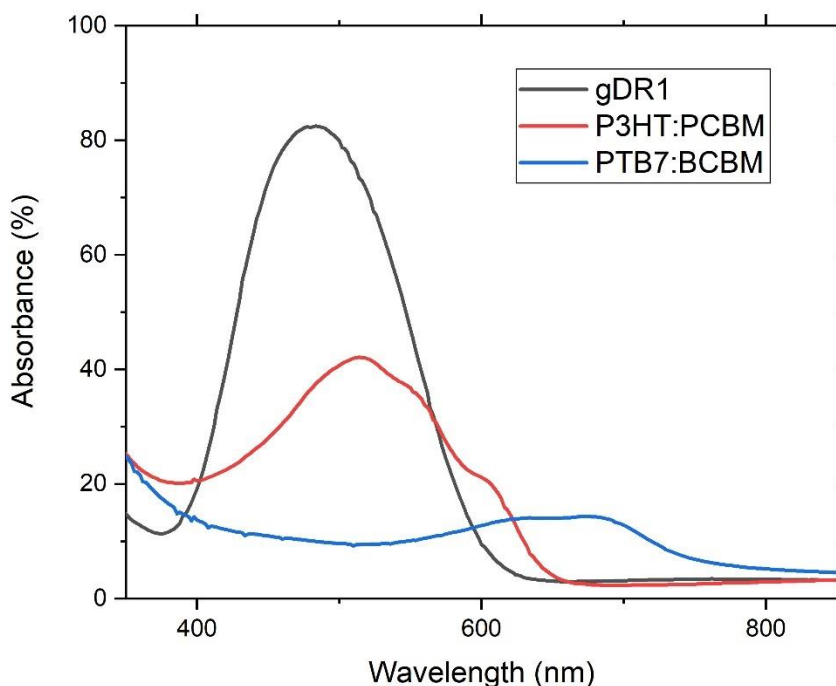


Figure 4.31. Absorbance spectra of thin films of gDR1, P3HT:PC$_{61}$BM and PTB7:PC$_{61}$BM. The azobenzene and P3HT:PC$_{61}$BM absorbance spectra largely overlap.

Control PTB7:PC$_{61}$BM solar cells without an azobenzene layer were fabricated as per the procedures detailed in Table 3.2. The best solar cell with this design exhibited a $J_{sc}$ of 5.24 mA/cm$^2$, $V_{oc}$ of 0.49 V, a FF of 0.21 and an efficiency of 0.53%, while the average efficiency was $0.4 \pm 0.2\%$. The low $J_{sc}$ of this solar cell is attributable to the use of PC$_{61}$BM instead of PC$_{71}$BM, which is the fullerene typically paired with PTB7[108]. Furthermore, the additive DIO is also normally used with PTB7 to increase the phase separation in PTB7 solar cells, resulting in a three-fold enhancement of the efficiency[108-112]. However, neither PC$_{71}$BM nor DIO were available in our laboratory. While PTB7:PC$_{71}$BM solar cells when processed with DIO have reached a high published efficiency of 9.2%[176], a much lower efficiency was expected for the PTB7:PC$_{61}$BM solar cells fabricated in this thesis. Therefore, as this thesis is mainly concerned with the efficiency enhancement due to scattering, and not the absolute efficiency, no attempts were made to further optimized the unstructured PTB7:PC$_{71}$BM solar cells made in this thesis and the efficiency of 0.53% serves as the control solar cell efficiency.

Double-sided PTB7:PC$_{61}$BM solar cells with azobenzene thin films patterned by UV exposure only or a combination of crossed gratings and UV exposure were fabricated as per the procedures detailed in Table 3.2 with various distance from the UV lamp, resulting in films with $R_q/R_{qmax}$ = 3.4/34 nm, 3.6/52 nm, 9.0/80 nm and 36/287 nm. The J-V characteristic curves for the best of those solar cells and the control solar cell are shown in Figure 4.32.
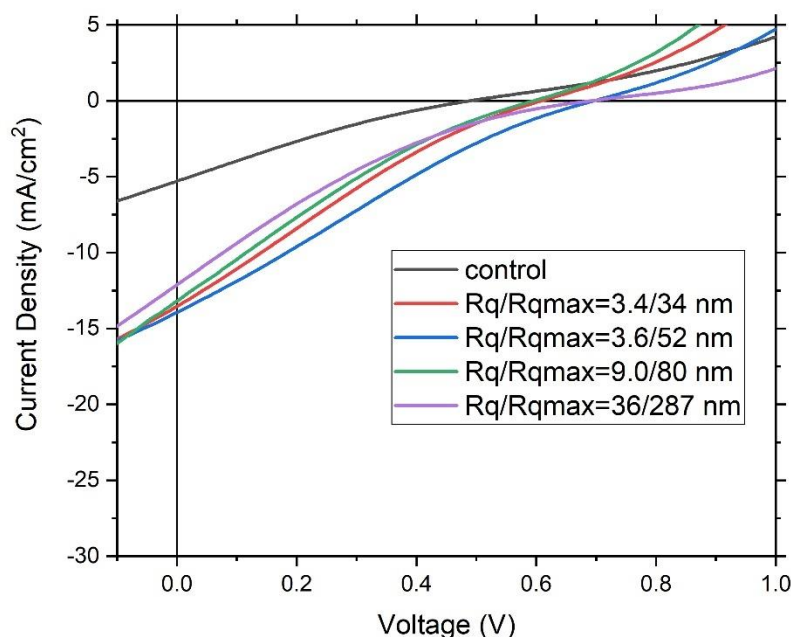


Figure 4.32. J-V characteristics curves for double-sided PTB7:PC$_{61}$BM solar cells with azobenzene thin films patterned by crossed gratings and UV exposure. As PTB7 solar cells are less susceptible to the transmission of azobenzene thin films than P3HT solar cells, the PTB7 patterned solar cells exhibited stronger efficiency enhancements than the P3HT solar cells.

With the bleaching of the azobenzene being a less dominant factor in PTB7:PC$_{61}$BM solar cells, less dispersed results were found for the patterned PTB7 solar cells, with all of them showing efficiency enhancements compared to the control solar cell. The best results were achieved using a $R_q/R_{qmax}$ = 3.6/52 nm, a value similar to the best results achieved with P3HT:PC$_{61}$BM ($R_q/R_{qmax}$ = 3.9/41 nm). This design had an average efficiency of 1.5 ± 0.3%, compared to 0.4 ± 0.2% for the control solar cells respectively. The best PTB7:PC$_{61}$BM solar cell exhibited a $J_{sc}$ of 13.97 mA/cm$^2$ compared to 5.24 mA/cm$^2$ for the control solar cell, a $V_{oc}$ of 0.69 V, a FF of 0.22 and an efficiency of 2.13%, up from 0.53% for the control solar cell. This represents an efficiency enhancement of 302%. The $R_q/R_{qmax}$ = 3.4/34 nm also exhibited an increased $J_{sc}$ and efficiency enhancement, although not as pronounced as the ones for the $R_q/R_{qmax}$ = 3.9/41 nm, probably due to a lower value of $R_q$. Both $R_q/R_{qmax}$ = 9.0/80 nm and 36/287 nm also showed $J_{sc}$ and

efficiency enhancements compared to the control solar cell, but it is believed that the enhancements were limited due the high $R_{qmax}$. The best solar cell with $R_{qmax} = 80$ nm had an efficiency of 1.56%, while the best solar cell with $R_{qmax} = 287$ nm had an efficiency of 1.39%.

Figure 4.33 shows the enhancements of the $J_{sc}$, $V_{oc}$, FF and PCE of the P3HT:PC$_{61}$BM and PTB7:PC$_{71}$BM solar cells for different values of $R_q/R_{qmax}$ of the azobenzene thin films. As it can be seen from this graph, in both P3HT:PC$_{61}$BM and P3HT:PC$_{71}$BM solar cells, the scattering mainly resulted in an improved $J_{sc}$ and PCE, with optimal values achieved with increased $R_q$ as long as the $R_{qmax}$ remained below $\sim 60$ nm. Stronger enhancements were achieved with PTB7:PC$_{71}$BM solar cells as PTB7 is less sensitive to the azobenzene bleaching than P3HT due to a different absorbance spectrum.
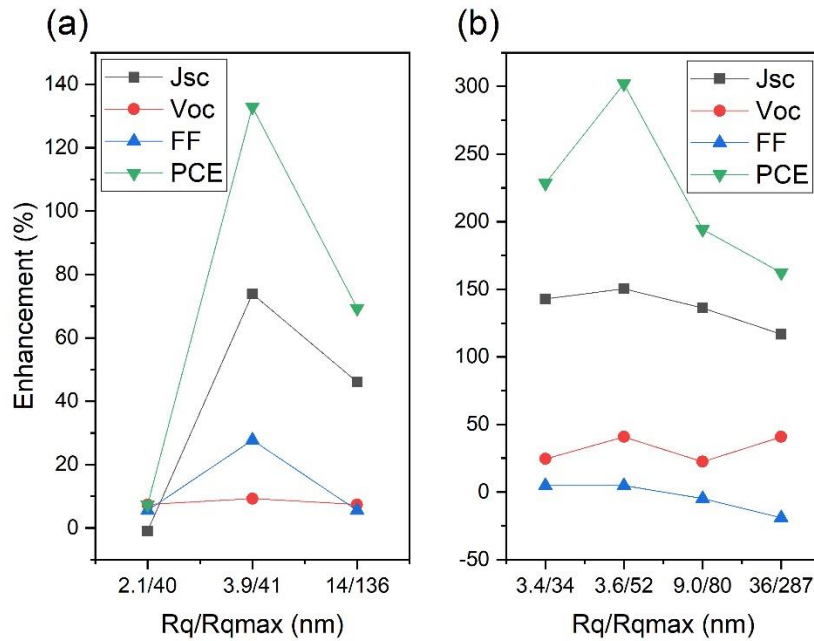


Figure 4.33. Enhancements of the solar cells characteristics of (a) P3HT:PC$_{61}$BM and (b) PTB7:PC$_{61}$BM solar cells after incorporation of azobenzene thin films patterned by crossed gratings and UV exposure. An improved $J_{sc}$ and PCE are observed, with optimal values achieved with increased $R_q$ as long as the $R_{qmax}$ remained below $\sim 60$ nm.

## 4.6    SUMMARY OF THE J-V CHARACTERISTICS OF THE SOLAR CELLS FABRICATED IN THIS THESIS

Figure 4.34 shows the J-V characteristic curves of the best P3HT:PC$_{61}$BM and PTB7:PC$_{71}$BM solar cells with azobenzene thin film patterned by crossed gratings and UV exposure obtained in this thesis along with their respective control solar cells. Efficiency

enhancements of 133% and 302% are reported for P3HT:PC$_{61}$BM and PTB7:PC$_{71}$BM solar cells, respectively.
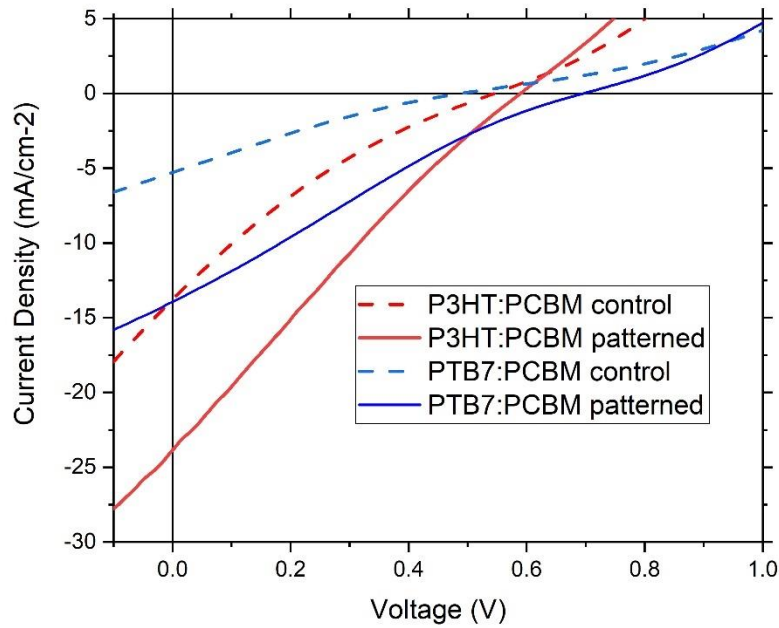


Figure 4.34. J-V characteristic curves of the best P3HT:PC$_{61}$BM and PTB7:PC$_{71}$BM solar cells with azobenzene thin film patterned by crossed gratings and UV exposure. PCE) enhancements of 133% and 302% compared to control solar cells were achieved for P3HT:PC$_{61}$BM and PTB7:PC$_{61}$BM solar cells, respectively.

The J-V characteristics of the solar cells presented in this thesis are summarized in Table 4.4.

Table 4.4. Summary of the J-V characteristics of the solar cells fabricated in this thesis.

| Design | Best $J_{sc}$ (mA/cm$^2$) | Best $V_{oc}$ (V) | Best FF | Best PCE % |
|---|---|---|---|---|
| ITO solar cells (section 4.1) | | | | |
| Area 29.5 mm$^2$ | 2.76 | 0.56 | 0.18 | 0.27 |
| With PCBM over-layer | 0.39 | 0.56 | 0.14 | 0.03 |
| Area 6 mm$^2$ | 14.85 | 0.63 | 0.27 | 2.48 |
| Inverted solar cells with transparent top electrodes (section 4.2) | | | | |
| Thin metal top electrode | $5.6 \times 10^{-3}$ | 0.27 | 0.19 | $2.6 \times 10^{-4}$ |
| PH1000 + DMSO + TX-100 top electrode | $5.15 \times 10^{-3}$ | 0.50 | 0.24 | $6.2 \times 10^{-4}$ |
| Direct solar cells with PH1000 bottom electrodes (section 4.3) | | | | |
| Annealed at 120˚C | 13.62 | 0.54 | 0.18 | 1.37 |
| Annealed at 70˚C | 6.17 | 0.54 | 0.22 | 0.72 |
| With TX-100 and annealed at 70˚C | 5.87 | 0.57 | 0.17 | 0.60 |
| Single-sided solar cells with azobenzene thin films patterned by corona poling (section 4.4.2) | | | | |
| Control | 5.87 | 0.57 | 0.17 | 0.60 |
| $R_q = 5$nm | 3.85 | 0.45 | 0.16 | 0.28 |
| $R_q = 41$ nm | 2.04 | 0.46 | 0.18 | 0.16 |
| $R_q = 49$nm | $1.69 \times 10^{-3}$ | 0.47 | 0.15 | $1.2 \times 10^{-4}$ |
| Double-sided solar cells with azobenzene thin films patterned by corona poling (section 4.4.4) | | | | |
| Control | 13.62 | 0.54 | 0.18 | 1.37 |
| $R_q/R_{qmax} = 2.1/40$ nm | 13.49 | 0.58 | 0.19 | 1.47 |
| $R_q/R_{qmax} = 3.9/57$ nm | 5.58 | 0.40 | 0.18 | 0.40 |
| $R_q/R_{qmax} = 6.2/71$ nm | 4.69 | 0.46 | 0.19 | 0.40 |
| $R_q/R_{qmax} = 5.5/72$ nm | 2.83 | 0.43 | 0.17 | 0.21 |
| $R_q/R_{qmax} = 6.5/371$ nm | 0.08 | 0.58 | 0.16 | $7.5 \times 10^{-4}$ |
| Double-sided P3HT:PC$_{61}$BM solar cells with azobenzene thin films patterned by crossed gratings (section 4.5.3) | | | | |
| Control | 13.62 | 0.54 | 0.18 | 1.37 |
| $R_q/R_{qmax} = 2.1/40$ nm | 13.49 | 0.58 | 0.19 | 1.47 |
| $R_q/R_{qmax} = 3.9/41$ nm | 23.68 | 0.59 | 0.23 | 3.19 |
| $R_q/R_{qmax} = 14/136$ nm | 19.89 | 0.58 | 0.19 | 2.32 |
| Double-sided PTB7:PC$_{61}$BM solar cells with azobenzene thin films patterned by crossed gratings (section 4.5.3) | | | | |
| Control | 5.24 | 0.49 | 0.21 | 0.53 |
| $R_q/R_{qmax} = 3.4/34$ nm | 10.14 | 0.64 | 0.22 | 1.74 |
| $R_q/R_{qmax} = 3.6/52$ nm | 13.93 | 0.69 | 0.22 | 2.13 |
| $R_q/R_{qmax} = 9.0/80$ nm | 13.09 | 0.60 | 0.20 | 1.56 |
| $R_q/R_{qmax} = 36/287$ nm | 12.00 | 0.69 | 0.17 | 1.39 |

# 5 CONCLUSION

## 5.1 SUMMARY

Climate change. The message is clear: we can still avoid disaster if we act now. But more than three years after nearly 200 countries signed a landmark climate agreement in Paris, we are still far off-track from preventing a severe global warming. If this trend continues, our children will learn from their history books how we were the generation who knew about the threat of climate change but failed to act. Why are we procrastinating? Why, when the sun offers a source of energy more than sufficient to meet our needs are our roofs not covered with solar panels? Cost. Current solar cells, which are mainly fabricated from inorganic materials such as silicon, are expensive to produce. The scientific community is developing a cheaper generation of solar cells using organic materials. However, these are not yet very efficient at harvesting the Sun's energy, particularly when using ITO-free solar cells which are more environmentally friendly, but typically have lower efficiencies.

Efficiency enhancement of organic solar cells can potentially be achieved by increasing the amount of light absorbed by the active layer. Two possible solutions for increasing the light absorption in organic solar cells were explored in this thesis. The first solution consisted of using azobenzene SRGs to couple the light in solar cells through the excitation of SPR. While this technique has been successfully used in the past to enhance the efficiency of direct structure solar cells[52, 52, 54], only one example was found in the literature of inverted solar cells with SPR excited by SRGs[56]. This study demonstrated an increase in photocurrent of inverted P3HT:PC$_{61}$BM solar cells, but solar cell efficiency measurements were not reported because of the difficulties encountered at that time with making a transparent top electrode.

Attempts were made in this thesis to fabricate top illuminated inverted solar cells with metal bottom electrodes and ultra-thin silver or solution-processed transparent top electrodes made from a PEDOT:PSS PH1000 formulation – a structure compatible with the integration of metal SRGs on the bottom electrodes. In the case of the ultra-thin silver electrodes, the poor results were partially attributed to high reflection of the light due to the use of a single layer of silver, instead of a MoO$_3$/Ag/MoO$_3$ stack. However, as it was shown with inverted PH1000 top electrodes solar cells, the low $J_{sc}$ and PCE of the inverted solar cells could not be attributed to reflection alone. As PH1000 electrodes with similar resistance, thickness and transmission were successfully employed in this thesis in direct structure solar cells, it is believed that the main issue with the inverted solar cells was the lack of an ETL rather than choice and processing of the top electrodes. Delamination and dewetting[75], lack of a planarization layer over the bottom electrodes[13] and exciton quenching [31, 75, 104, 105] – which is more severe in inverted solar cells due to vertical phase separation of the polymer/fullerene blend – are some of the reasons why an ETL is particularly important in an inverted structure. Since inverted control solar cells could not be made with an acceptable efficiency, no attempts were made to integrate SRGs in inverted solar cells to excite SPR.

The second method explored in this thesis to increase the amount of light absorbed by the active layer, and thus enhance the efficiency of ITO-free organic solar cells, used scattering principles. The thickness of the active material in an organic solar cell is critical: if the material is too thin, it will not be able to absorb a significant amount of the light energy. However, if the material is too thick, the charges generated inside the absorber would not be able to reach the electrodes within their lifetime. In this thesis, patterned and bleached gDR1 azobenzene thin films scattered the light before it entered the solar cells. The optical path of the light within the solar cells

was therefore extended without increasing the physical thickness of the solar cells, thus allowing a better absorption of the light while still keeping the electrodes within reach of the charges.

Prior to integrating the patterned azobenzene thin films into solar cells, the films were bleached by a 20-hour UV exposure to increase film transparency. The obtained transparency was found to vary with the distance of the sample from the UV lamp, with a transmission of 75% at a wavelength of 450 nm for an amorphous azobenzene thin film at a distance of 3.5 cm to the UV lamp, to 37% at a wavelength of 450 nm for a sample positioned at 6 cm from the lamp compared to 3% for an unbleached amorphous azobenzene thin film. Several other effects were noted due to the UV exposure. Firstly, it was noted that the UV exposure rendered the patterned gDR1 azobenzene thin films thermally stable, with minimal effects noted on the nanostructures at temperatures as high as 200˚C. This is believed to be caused by a photodegradation of the azobenzene chromophores, which was previously demonstrated in UV treated amorphous polymers containing DR1[153, 154] and maleimide-based copolymers bearing azobenzene moieties[152]. However, it is not believed that this demonstration was ever done for gDR1 thin films prior to this work.

The UV exposure of the patterned azobenzene thin films also resulted in the partial destruction of the nanostructures. It was demonstrated that this destruction was not caused by the samples heating up under the UV lamp, but more likely resulted from the absorption of the UV energy by the azobenzene thin films, which allowed the azobenzene chromophores to undergo a *trans-cis* isomerization responsible for the partial destruction of the nanostructures – a process rendered irreversible due to the photodegradation of the azobenzene molecules after UV exposure. As the light was more intense for samples closer to the source, the photodegradation was more rapid for those samples, resulting in a better preservation of the nanostructures. However, volcano-like nanostructures also appeared on azobenzene thin films when exposed to UV light, with a shorter distance to the lamp having the unintended and undesired consequence of creating larger volcano-like nanostructures.

Two patterning techniques were tried in this thesis. The first technique consisted of creating randomized nanostructures by corona poling of the azobenzene thin films. The experiments conducted with solar cells built on the back side of glass substrates with corona-poled and bleached azobenzene thin films led to the conclusion that an increase in $R_q$ could potentially lead to efficiency enhancements due to a scattering effect, but large $R_{qmax}$ negatively impacted the efficiency due to a disadvantageous ratio of forward/total scattering. In this thesis, promising results were obtained with a patterned azobenzene thin film with a $R_{qmax} = 40$ nm, but a sharp decrease in efficiency was observed with $R_{qmax} \geq 57$ nm. As corona poling, even at low temperature and exposure time, created nanostructures with sizes superior to $\geq 57$ nm, none of the corona-poled azobenzene thin films resulted in an efficiency enhancement. Therefore, another patterning technique was chosen: crossed gratings.

Double-sided P3HT:PC$_{61}$BM solar cells with crossed gratings on azobenzene thin films were fabricated, with the distance from the UV lamp varied from 5 cm to 3.5 cm, resulting in azobenzene thin films with $R_q/R_{qmax}$ between 3.9/41 nm to 14/136 nm. The best PH1000 P3HT:PC$_{61}$BM solar cell was achieved with a $R_q/R_{qmax} = 3.9/41$ nm. This solar cell exhibited a high $J_{sc}$ of 23.68 mA/cm$^2$ compared to 13.62 mA/cm$^2$ for the PH1000 control solar cell, a strong indication of successful scattering within the solar cell leading to an increased absorption of the light. It also exhibited an enhanced efficiency of 3.19%, up from 1.37% for the best PH1000 control

solar cell - a significant efficiency enhancement of 133%, which even surpassed the efficiency of the ITO solar cell (2.48%).

PTB7:PC$_{61}$BM, a polymer/fullerene blend less susceptible to the azobenzene absorbance, was also used to fabricate double-sided solar cells with azobenzene thin films patterned by crossed gratings. The distance of the samples to the UV lamp was once again varied to create azobenzene thin films with $R_q/R_{qmax}$ between 3.4/34 nm and 36/287 nm. The best results were achieved using a $R_q/R_{qmax} = 3.6/52$ nm, a value similar to the best results achieved with P3HT:PC$_{61}$BM ($R_q/R_{qmax} = 3.9/41$ nm). The best PTB7:PC$_{61}$BM solar cell exhibited a $J_{sc}$ of 13.97 mA/cm$^2$ compared to 5.24 mA/cm$^2$ for the control solar cell and an efficiency of 2.13%, up from 0.53% for the control solar cell, an efficiency enhancement of 302%.

The use of azobenzene thin films patterned by crossed gratings and bleached by a prolonged UV exposure to scatter the light in organic solar cells resulted in significant efficiency enhancements, with efficiencies above that of ITO-based solar cells. In the case of PTB7:PC$_{61}$BM solar cells, the efficiency was tripled compared to a control solar cell. Furthermore, patterning the azobenzene thin films used a process that was cheap, simple and compatible with mass-production, thus bringing affordable and efficient organic solar cells one step closer to commercialization.

## 5.2    FUTURE WORK

### 5.2.1    Testing of Solar Cells
To improve the accuracy of the J-V measurements and avoid reading the charging of a capacitor, the voltage should be swiped back and forth several times for each solar cell in future work. Scan rate and direction should be noted in the experimental procedures[177-179]. Dark current and Internal Photon to Current Efficiency (IPCE) measurements should also be taken, as it can provide additional clues in the analysis of the solar performance, such as the presence of trap-assisted recombination[180-183]. Encapsulation of the devices using glass cover and epoxy is also recommended in order to perform all the above testing, as the efficiency of devices exposed to air rapidly decreases, with decreases around 25% of the original values within 30 minutes and 80% of original values within 8 hours previously reported for some organic solar cells[184].

### 5.2.2    Surface Plasmons Resonance Excitation by Surface Reliefs Gratings in Organic Solar Cells
One of the goals of this thesis was the efficiency enhancement of inverted organic solar cells by using bottom metal SRGs electrode to couple the light in the solar cell through the excitation of SPR. However, difficulties were encountered in fabricating inverted control solar cells without SRGs. Future work on plasmonic solar cells could therefore be two-fold. On one hand, work could be done to enhance the efficiency of direct solar cells by patterning the top electrode, as illustrated in Figure 5.1 (though the inclusion of an HTL such as PEDOT:PSS between the ITO and the active layer would provide better results).
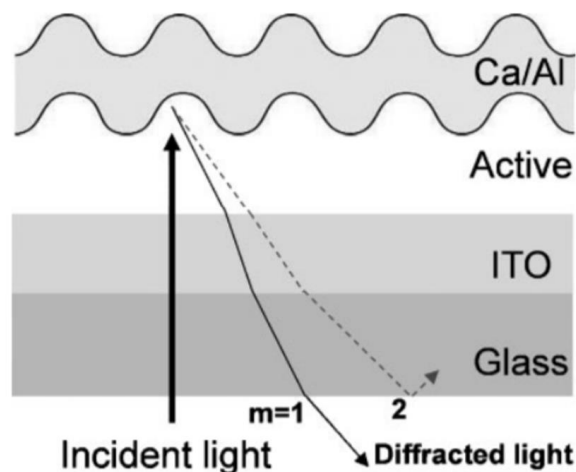
Figure 5.1. Schematic representation of the structure of a direct solar cell with a metal SRGs top electrode. The active layer is patterned by a PDMS mold before the evaporation of the top electrode. Adapted from (Na *et al.*, 2008)[54].

A soft lithography technique[54] could be used to create the structure in Figure 5.1. Azobenzene thin films can be patterned by laser lithography, as it was done in this thesis, to inscribe SRGs. PDMS molds could then be fabricated from these masters and used to imprint the active layer prior to evaporation of the top electrode – be it either Al, or a combination of Ca/Al or LiF/Al to improve the FF. While this method has been successfully used with linear and crossed gratings to enhance the efficiency of direct structure P3HT:PC$_{61}$BM solar cells[54], polymer/fullerene blends with extended absorption spectra could be used with novel grating geometry such as circular or chirped gratings[185, 186]. These novel gratings could lead to potentially larger efficiency enhancements due to a broadening of the SPR bandwidth.

On the other hand, as the inverted geometry is now predominant, inverted solar cells could be fabricated using a proper ETL, should our laboratory acquire this capability. ZnO is a popular choice of ETL, but normally requires a high annealing temperature above the 71˚C glass transition temperature of gDR1. As ZnO would be deposited and annealed after the patterning of the azobenzene layer, this would result in a destruction of the SRGs. One option could be to use ZnO nanoparticles that do not require annealing[31, 187] or other interfacial materials such as cesium carbonate (Cs$_2$CO$_3$)[188]. Alternatively, one could try to thermal stabilize the azobenzene gratings. In this thesis, it was shown that UV exposure resulted in thermally stability of gDR1, but also in partial destruction of the original nanostructures. While this was a viable option for scattering, a better conservation of the nanostructures would be required to excite SPR. Photocrosslinking has been shown to thermally stabilize other azobenzene compounds[152-154] with minimal SRGs degradation. This may be an interesting avenue to stabilize the gDR1 gratings in order to incorporate a ZnO ETL.

In addition to incorporating an ETL, a proper MoO$_3$/Ag/MoO$_3$ stack should be employed if using an ultra-thin metal top electrode. For a PH1000 top electrode, one could try the transfer technique employed by Bu *et al.*[166] and Yin *et al.*[167], though it is not believed that the deposition

technique or morphology of the PH1000 film with the TX-100 surfactant was the reason for the poor performance of the solar cells.

### 5.2.3 Scattering by Patterned and Bleached Azobenzene Thin Films in Organic Solar Cells

While efficiency enhancements of 133% and 302% were reported in this thesis for P3HT:$PC_{61}$BM and PTB7:$PC_{61}$BM solar cells respectively, further work is required to gain better control over the bleaching process. One limiting factor is the formation of the volcano-like nanostructures after UV exposure. These nanostructures were large when the samples were close to the lamp and caused a reduction in efficiency, possibly due to disadvantageous forward/total scattering ratio. If one could prevent or control the formation of these nanostructures, the samples could be positioned closer to the lamp. This would lead to a better transmission and preservation of the gratings – thus increasing $R_q$ and, consequently, improving the ratio of forward scattering/total scattering.

One possible explanation for those volcano-like structures is that the irradiation produces light-induced surface re-orientation and mass movement of the azobenzene molecules. This would create surface defects which in turn would act as seeds for Spontaneous Surface Reliefs Gratings (SSRGs)[189]. Mazaheri *et al.*[189] found that a different azobenzene compound with a slow rate of birefringence induction, namely Azoglass-530, prevented mass movement in the material at a rate necessary for SSRGs formation under a coherent laser beam. However, Azoglass-530 is not an appropriate material for SRGs either. It would be interesting to investigate if corona poling of this material could produce smaller nanostructures, and if the formation of the volcano-like nanostructures would be prevented when exposed to the UV light, thus allowing for a better control of the surface roughness of the azobenzene films. Additionally, better control may also be achieved with a more coherent UV light, or under different polarization conditions.

Other options would be to try again corona poling of gDR1, but with much shorter exposition time, 30 seconds for example. Alternatively, corona poling of other substances not requiring UV bleaching, such as mexylamiontriazine glasses[67], or substances creating concave structures instead of convex, could be attempted. Furthermore, other polymers/fullerenes with absorption different spectra different from the azobenzene spectrum could be explored.

With ternary blends (two donors and one acceptor, or one donor and two acceptors), the efficiencies of single-junction organic solar cells have now reached 12-14%[190]. However, there are still several factors limiting the future commercialization of organic solar cells, including low-level efficiency of large-size devices and poor reproducibility and stability. With continued research, organic solar cells could take their place in the energy market and replace fossil fuels and, maybe, we could then change the narrative in our children's history books. Finally, to quote the astrophysicist Neil deGrasse Tyson: "The dinosaurs never saw that asteroid coming. What's our excuse?"

## REFERENCES

1. Peter Würfel and Uli Würfel, <u>Physics of Solar Cells: From Basic Principles to Advanced Concepts</u>, 3rd ed. (Wiley-VCH, DE, 2016).

2. N. L. Panwar, S. C. Kaushik and Surendra Kothari, "Role of renewable energy sources in environmental protection: a review," Renewable and Sustainable Energy Reviews 15 (3), 1513-1524 (2011).

3. Government of Canada, Public Services and Procurement Canada, "Canada's greenhouse gas and air pollutant emissions projections .: En1-78E-PDF - Government of Canada Publications - Canada.ca," (2002).

4. UNFCCC, "Adoption of the Paris Agreement," (2015).

5. J. David Hughes, <u>Can Canada Expand Oil and Gas Production, Build Pipelines and Keep Its Climate Change Commitments?</u>, (Canadian Center for Policy Alternatives, 2016).

6. Luke Gibson, Elspeth N. Wilman and William F. Laurance, "How green is 'green'energy?" Trends in ecology & evolution 32 (12), 922-935 (2017).

7. Steven J. Strong and William G. Scheller, <u>The Solar Electric House: Energy for the Environmentally Responsive, Energy-Independent Home</u>, (Still River, Mass, Sustainability Press, 1987), .

8. Khaldun A. Salman, "Effect of surface texturing processes on the performance of crystalline silicon solar cell," Solar Energy 147, 228-231 (2017).

9. Jenny A. Nelson, <u>Physics Of Solar Cells, The</u>, (Imperial College Press, London, 2003).

10. Martin A. Green, "The path to 25% silicon solar cell efficiency: history of silicon cell evolution," Prog Photovoltaics Res Appl 17 (3), 183-189 (2009).

11. National Renewable Energy Laboratory, "Best Research-Cell Efficiencies," (2017).

12. Michael Grätzel, "Photovoltaic and photoelectrochemical conversion of solar energy," Philosophical Transactions of the Royal Society of London A: Mathematical, Physical and Engineering Sciences 365 (1853), 993-1005 (2007).

13. Dechan Angmo, Nieves Espinosa and Frederik Krebs, Indium Tin Oxide-Free Polymer Solar Cells: Toward Commercial Reality, in <u>Low-cost Nanomaterials</u>, (Springer, 2014), pp. 189-225.

14. Taesoo D. Lee and Abasifreke U. Ebong, "A review of thin film solar cell technologies and challenges," Renewable and Sustainable Energy Reviews 70, 1286-1297 (2017).

15. Kevin Bullis, "Mass Production of Plastic Solar Cells," (2019).

16. Scott Kirsner- Contributor, "Why did solar cell company Konarka fail? - The Boston Globe," (2019).

17. Tze-Chien Sum, Nripan Mathews and Bo Wu, Plasmonic Organic Solar Cells : Charge Generation and Recombination, (Springer, Singapore, 2016).

18. Gang Li *et al.*, High-efficiency solution processable polymer photovoltaic cells by self-organization of polymer blends, in Materials For Sustainable Energy: A Collection of Peer-Reviewed Research and Review Articles from Nature Publishing Group, edited by Anonymous (World Scientific, 2011), pp. 80-84.

19. Holger Spanggaard and Frederik C. Krebs, "A brief history of the development of organic and polymeric photovoltaics," Solar Energy Mater.Solar Cells 83 (2-3), 125-146 (2004).

20. Hwajeong Kim *et al.*, "Organic solar cells based on conjugated polymers: History and recent advances," Korean Journal of Chemical Engineering 31 (7), 1095-1104 (2014).

21. Veaceslav Coropceanu *et al.*, "Charge transport in organic semiconductors," Chem.Rev. 107 (4), 926-952 (2007).

22. Niyazi S. Sariciftci *et al.*, "Photoinduced electron transfer from a conducting polymer to buckminsterfullerene," Science 258 (5087), 1474-1476 (1992).

23. Hui Shi *et al.*, "Effective approaches to improve the electrical conductivity of PEDOT: PSS: a review," Advanced Electronic Materials 1 (4), 1500017 (2015).

24. Yun Zheng *et al.*, "Recent advances of conducting poly (3, 4-ethylenedioxythiophene) polystyrene sulfonate hybrids for thermoelectric applications," Journal of Materials Chemistry C, (2018).

25. Desalegn Alemu Mengistie, Pen-Cheng Wang and Chih-Wei Chu, "Highly conductive PEDOT: PSS electrode treated with polyethylene glycol for ITO-free polymer solar cells," ECS Transactions 58 (11), 49-56 (2013).

26. Desalegn Alemu Mengistie, Pen-Cheng Wang and Chih-Wei Chu, "Effect of molecular weight of additives on the conductivity of PEDOT: PSS and efficiency for ITO-free organic solar cells," Journal of Materials Chemistry A 1 (34), 9907-9915 (2013).

27. Yechuan Sun *et al.*, "Optimization of transparent electrode processing conditions for bulk heterojunction solar cells," Journal of Photonics for Energy 2 (1), 021005 (2012).

28. Desalegn Alemu *et al.*, "Highly conductive PEDOT: PSS electrode by simple film treatment with methanol for ITO-free polymer solar cells," Energy & environmental science 5 (11), 9662-9671 (2012).

29. Woon-Hyuk Baek *et al.*, "Use of fluorine-doped tin oxide instead of indium tin oxide in highly efficient air-fabricated inverted polymer solar cells," Appl.Phys.Lett. 96 (13), 133506 (2010).

30. Sung-Soo Yoon and Dahl-Young Khang, "Roles of Nonionic Surfactant Additives in PEDOT: PSS Thin Films," The Journal of Physical Chemistry C 120 (51), 29525-29532 (2016).

31. Sandro Lattante, "Electron and hole transport layers: their use in inverted bulk heterojunction polymer solar cells," Electronics 3 (1), 132-164 (2014).

32. Achilleas Savva *et al.*, "Synergistic effects of buffer layer processing additives for enhanced hole carrier selectivity in inverted organic photovoltaics," Organic Electronics 14 (11), 3123-3130 (2013).

33. Michael Vosgueritchian, Darren J. Lipomi and Zhenan Bao, "Highly conductive and transparent PEDOT: PSS films with a fluorosurfactant for stretchable and flexible transparent electrodes," Advanced functional materials 22 (2), 421-428 (2012).

34. R. H. Ritchie, "Plasma Losses by Fast Electrons in Thin Films," Physical Review 106 (5), 874-881 (1957).

35. C. J. Powell and J. B. Swan, "Origin of the Characteristic Electron Energy Losses in Aluminum," Physical Review 115 (4), 869-875 (1959).

36. Harry A. Atwater and Albert Polman, "Plasmonics for improved photovoltaic devices," Nature materials 9 (3), 205 (2010).

37. Srijit Nair, Carlos Escobedo and Ribal Georges Sabat, "Crossed surface relief gratings as nanoplasmonic biosensors," ACS sensors 2 (3), 379-385 (2017).

38. Srijit Nair *et al.*, "Selective Uropathogenic E. coli Detection Using Crossed Surface-Relief Gratings," Sensors 18 (11), 3634 (2018).

39. Johny P. Monteiro *et al.*, "SPR based biosensor using surface relief grating in transmission mode," Sensors Actuators B: Chem. 174, 270-273 (2012).

40. Lauren A. Austin *et al.*, "Plasmonic imaging of human oral cancer cell communities during programmed cell death by nuclear-targeting silver nanoparticles," J.Am.Chem.Soc. 133 (44), 17594-17597 (2011).

41. Pradeep Kumar Maharana, Triranjita Srivastava and Rajan Jha, "Ultrasensitive plasmonic imaging sensor based on graphene and silicon," IEEE Photonics Technology Letters 25 (2), 122-125 (2013).

42. Ting Xu *et al.*, "Plasmonic nanoresonators for high-resolution colour filtering and spectral imaging," Nature communications 1, 59 (2010).

43. Volker J. Sorger *et al.*, "Toward integrated plasmonic circuits," MRS Bull 37 (8), 728-738 (2012).

44. Rashid Zia *et al.*, "Plasmonics: the next chip-scale technology," Materials today 9 (7-8), 20-27 (2006).

45. Min-Ki Kwon *et al.*, "Surface-plasmon-enhanced light-emitting diodes," Adv Mater 20 (7), 1253-1257 (2008).

46. Dong-Ming Yeh *et al.*, "Localized surface plasmon-induced emission enhancement of a green light-emitting diode," Nanotechnology 19 (34), 345201 (2008).

47. Jelena Vučković, Marko Lončar and Axel Scherer, "Surface plasmon enhanced light-emitting diode," IEEE J.Quant.Electron. 36 (10), 1131-1144 (2000).

48. Luyao Lu *et al.*, "Cooperative plasmonic effect of Ag and Au nanoparticles on enhancing performance of polymer solar cells," Nano Letters 13 (1), 59-64 (2012).

49. Honghui Shen, Peter Bienstman and Bjorn Maes, "Plasmonic absorption enhancement in organic solar cells with thin active layers," J.Appl.Phys. 106 (7), 073109 (2009).

50. Seok-Soon Kim *et al.*, "Plasmon enhanced performance of organic solar cells using electrodeposited Ag nanoparticles," Appl.Phys.Lett. 93 (7), 305 (2008).

51. X. H. Li *et al.*, "Efficient inverted polymer solar cells with directly patterned active layer and silver back grating," The Journal of Physical Chemistry C 116 (12), 7200-7206 (2012).

52. Jingbi You *et al.*, "Surface Plasmon and Scattering-Enhanced Low-Bandgap Polymer Solar Cell by a Metal Grating Back Electrode," Advanced Energy Materials 2 (10), 1203-1207 (2012).

53. Xuanhua Li *et al.*, "Dual plasmonic nanostructures for high performance inverted organic solar cells," Adv Mater 24 (22), 3046-3052 (2012).

54. Seok-In Na *et al.*, "Efficient polymer solar cells with surface relief gratings fabricated by simple soft lithography," Advanced Functional Materials 18 (24), 3956-3963 (2008).

55. Ribal Georges Sabat, Marcos Jose Leite Santos and Paul Rochon, "Surface plasmon-induced band gap in the photocurrent response of organic solar cells," International Journal of Photoenergy 2010, (2010).

56. Justin Jefferies and Ribal Georges Sabat, "Surface-relief diffraction gratings' optimization for plasmonic enhancements in thin-film solar cells," Prog Photovoltaics Res Appl 22 (6), 648-655 (2014).

57. C. Cocoyer *et al.*, "Implementation of submicrometric periodic surface structures toward improvement of organic-solar-cell performances," Appl.Phys.Lett. 88 (13), 133108 (2006).

58. H. W. Deckman, C. B. Roxlo and E. Yablonovitch, "Maximum statistical increase of optical absorption in textured semiconductor films," Opt.Lett. 8 (9), 491-493 (1983).

59. Eli Yablonovitch and George D. Cody, "Intensity enhancement in textured optical sheets for solar cells," IEEE Trans.Electron Devices 29 (2), 300-305 (1982).

60. Se-Woong Baek *et al.*, "Plasmonic forward scattering effect in organic solar cells: a powerful optical engineering method," Scientific reports 3, 1726 (2013).

61. Dong Hwan Wang *et al.*, "Enhanced power conversion efficiency in PCDTBT/PC70BM bulk heterojunction photovoltaic devices with embedded silver nanoparticle clusters," Advanced Energy Materials 1 (5), 766-770 (2011).

62. Wei EI Sha *et al.*, "Near-field multiple scattering effects of plasmonic nanospheres embedded into thin-film organic solar cells," Appl.Phys.Lett. 99 (11), 199 (2011).

63. Chul-Hyun Kim *et al.*, "Silver nanowire embedded in P3HT: PCBM for high-efficiency hybrid photovoltaic device applications," ACS nano 5 (4), 3319-3325 (2011).

64. Se-Woong Baek *et al.*, "Au@ Ag core–shell nanocubes for efficient plasmonic light scattering effect in low bandgap organic solar cells," Acs Nano 8 (4), 3302-3312 (2014).

65. Xuanhua Li *et al.*, "Efficiency Enhancement of Organic Solar Cells by Using Shape-Dependent Broadband Plasmonic Absorption in Metallic Nanoparticles," Advanced Functional Materials 23 (21), 2728-2735 (2013).

66. P. Rochon, E. Batalla and A. Natansohn, "Optically induced surface gratings on azoaromatic polymer films," Appl.Phys.Lett. 66 (2), 136-138 (1995).

67. Hirohito Umezawa *et al.*, "Electric-Field-Induced Nanoscale Surface Patterning in Mexylaminotriazine-Functionalized Molecular Glass Derivatives," Langmuir 32 (22), 5646-5652 (2016).

68. Thomas Garm Pedersen *et al.*, "Quantum theory and experimental studies of absorption spectra and photoisomerization of azobenzene polymers," JOSA B 15 (11), 2721-2730 (1998).

69. Alexander Tofini *et al.*, "Erasure of surface relief gratings in azobenzene molecular glasses by localized heating using a CO 2 laser," Journal of Materials Chemistry C 6 (5), 1083-1091 (2018).

70. Juhwan Kim *et al.*, "A facile approach to improve light extraction for organic light emitting diodes via azobenzene surface relief gratings," Japanese Journal of Applied Physics 53 (8S3), 08NF02 (2014).

71. Alexey Bobrovsky *et al.*, "Comparative study of photoorientation phenomena in photosensitive azobenzene-containing homopolymers and copolymers," J.Photochem.Photobiol.A. 163 (3), 347-358 (2004).

72. Minh Trung Dang, Lionel Hirsch and Guillaume Wantz, "P3HT: PCBM, best seller in polymer photovoltaic research," Adv Mater 23 (31), 3597-3602 (2011).

73. Fujun Zhang *et al.*, "Recent development of the inverted configuration organic solar cells," Solar Energy Mater.Solar Cells 95 (7), 1785-1799 (2011).

74. A. Einstein, "On the Quantum Theory of Radiation," The Old Quantum Theory: The Commonwealth and International Library: Selected Readings in Physics , 167 (2016).

75. Hin-Lap Yip and Alex K-Y Jen, "Recent advances in solution-processed interfacial materials for efficient and stable polymer solar cells," Energy & Environmental Science 5 (3), 5994-6011 (2012).

76. J. Mazer, "Solar Cells: An Introduction to Crystalline Photovoltaic Technology," (1997).

77. Jonathan D. Servaites *et al.*, "Efficiency enhancement in organic photovoltaic cells: consequences of optimizing series resistance," Advanced Functional Materials 20 (1), 97-104 (2010).

78. A. K. Pandey *et al.*, "Size effect on organic optoelectronics devices: Example of photovoltaic cell efficiency," Physics Letters A 372 (8), 1333-1336 (2008).

79. Jun-Seok Yeo *et al.*, "Variations of cell performance in ITO-free organic solar cells with increasing cell areas," Semiconductor Science and Technology 26 (3), 034010 (2011).

80. A. Martí *et al.*, in E3S Web of Conferences, Anonymous (EDP Sciences, 2017) pp. 03004.

81. C. Riordan and R. Hulstron, in IEEE Conference on Photovoltaic Specialists, Anonymous (IEEE, 1990) pp. 1085-1088.

82. Green Rhino Energy, "Defining standard spectra for solar panels," (2016).

83. William Wolfgang Arrasmith, Systems Engineering and Analysis of Electro-Optical and Infrared Systems, 1st ed. (CRC Press, Baton Rouge, 2015).

84. C. A. Gueymard, D. Myers and K. Emery, "Proposed reference irradiance spectra for solar energy systems testing," Solar Energy 73 (6), 443-467 (2002).

85. Manajit Sengupta *et al.*, "Best Practices Handbook for the Collection and Use of Solar Resource Data for Solar Energy Applications," (2015).

86. Wikipedia, "Simple Model of the Atmospheric Radiative Transfer of Sunshine," (2013).

87. William Shockley and Hans J. Queisser, "Detailed balance limit of efficiency of p-n junction solar cells," J.Appl.Phys. 32 (3), 510-519 (1961).

88. Alan L. Fahrenbruch and Richard H. Bube, Fundamentals of solar cells: Photovoltaic Solar Energy Conversion, 1$^{st}$ ed. (Acad. Press, New York [u.a.], 1983).

89. Ana EP Maia *et al.*, "The thermalization process of photoexcited electrons and holes in the second kinetic stage of relaxation," physica status solidi (b) 180 (1), 213-222 (1993).

90. Foozieh Sohrabi, Arash Nikniazi and Hossein Movla, Optimization of third generation nanostructured silicon-based solar cells, in Solar Cells-Research and Application Perspectives, edited by Anonymous (InTech, 2013).

91. Seok-In Na *et al.*, "Efficient and flexible ITO-free organic solar cells using highly conductive polymer anodes," Adv Mater 20 (21), 4061-4067 (2008).

92. Said Karim Shah *et al.*, "Optimization of active-layer thickness, top electrode and annealing temperature for polymeric solar cells," AIMS MATERIALS SCIENCE 4 (3), 789-799 (2017).

93. Christoph J. Brabec *et al.*, "Polymer–fullerene bulk-heterojunction solar cells," Adv Mater 22 (34), 3839-3856 (2010).

94. William R. Salaneck, Richard H. Friend and Jean Luc Brédas, "Electronic structure of conjugated polymers: Consequences of electron–lattice coupling," Physics Reports 319 (6), 231-251 (1999).

95. Hideki Shirakawa *et al.*, "Synthesis of electrically conducting organic polymers: halogen derivatives of polyacetylene,(CH) x," Journal of the Chemical Society, Chemical Communications (16), 578-580 (1977).

96. Jenny Nelson, "Polymer: fullerene bulk heterojunction solar cells," Materials today 14 (10), 462-470 (2011).

97. Liang Gao *et al.*, "All-polymer solar cells based on absorption-complementary polymer donor and acceptor with high power conversion efficiency of 8.27%," Adv Mater 28 (9), 1884-1890 (2016).

98. Christian B. Nielsen *et al.*, "Non-fullerene electron acceptors for use in organic solar cells," Acc.Chem.Res. 48 (11), 2803-2812 (2015).

99. Gwan Ho Jung *et al.*, "BCP/Ag/MoO3 transparent cathodes for organic photovoltaics," Advanced Energy Materials 1 (6), 1023-1028 (2011).

100. Sung-Hyun Park *et al.*, "Large area roll-to-roll sputtering of transparent ITO/Ag/ITO cathodes for flexible inverted organic solar cell modules," Organic Electronics 30, 112-121 (2016).

101. Yue-Feng Liu *et al.*, "Highly flexible inverted organic solar cells with improved performance by using an ultrasmooth Ag cathode," Appl.Phys.Lett. 101 (13), 133303 (2012).

102. Harald Hoppe and Niyazi Serdar Sariciftci, "Organic solar cells: An overview," Journal of Materials Research 19 (7), 1924-1945 (2004).

103. Klaus Kuhnke *et al.*, "C 60 Exciton Quenching near Metal Surfaces," Phys.Rev.Lett. 79 (17), 3246 (1997).

104. Woon-Hyuk Baek *et al.*, "Composition-dependent phase separation of P3HT: PCBM composites for high performance organic solar cells," Organic Electronics 11 (5), 933-937 (2010).

105. Mariano Campoy-Quiles *et al.*, "Morphology evolution via self-organization and lateral and vertical diffusion in polymer: fullerene solar cell blends," Nature materials 7 (2), 158 (2008).

106. Martin Brinkmann *et al.*, "Highly oriented and nanotextured films of regioregular poly (3-hexylthiophene) grown by epitaxy on the nanostructured surface of an aromatic substrate," Macromolecules 43 (18), 7604-7610 (2010).

107. Mao-Yuan Chiu *et al.*, "Simultaneous use of small-and wide-angle X-ray techniques to analyze nanometerscale phase separation in polymer heterojunction solar cells," Adv Mater 20 (13), 2573-2578 (2008).

108. Katherine A. Mazzio and Christine K. Luscombe, "The future of organic photovoltaics," 44 (1), 78-9 (2014).

109. Juliane Kniepert *et al.*, "Effect of solvent additive on generation, recombination, and extraction in ptb7: Pcbm solar cells: A conclusive experimental and numerical simulation study," The Journal of Physical Chemistry C 119 (15), 8310-8320 (2015).

110. Samuel Foster *et al.*, "Electron collection as a limit to polymer: PCBM solar cell efficiency: effect of blend microstructure on carrier mobility and device performance in PTB7: PCBM," Advanced Energy Materials 4 (14), 1400311 (2014).

111. Wanjung Kim *et al.*, "Conflicted effects of a solvent additive on PTB7: PC71BM bulk heterojunction solar cells," The Journal of Physical Chemistry C 119 (11), 5954-5961 (2015).

112. Genene Tessema Mola *et al.*, "Co-solvent additives influence on the performance of PTB7: PCBM based Thin film organic solar cell," Materials Today: Proceedings 4 (14), 12558-12564 (2017).

113. Vytenis Pranculis *et al.*, "Influence of blend ratio and processing additive on free carrier yield and mobility in PTB7: PC71BM photovoltaic solar cells," The Journal of Physical Chemistry C 120 (18), 9588-9594 (2016).

114. Sun-Joo Park *et al.*, "Improvement of electrical conductivity for high-performance organic solar cells by multi-temperature solvent annealing," Japanese Journal of Applied Physics 54 (4S), 4 (2015).

115. Sadok Ben Dkhil *et al.*, "Toward high-temperature stability of PTB7-based bulk heterojunction solar cells: impact of fullerene size and solvent additive," Advanced Energy Materials 7 (4), 1601486 (2017).

116. Masaya Ohzeki *et al.*, "Performance improvement of flexible bulk heterojunction solar cells using PTB7: PC71BM by optimizing spin coating and drying processes," Japanese Journal of Applied Physics 53 (2S), 02BE04 (2014).

117. Kuan Sun *et al.*, "Review on application of PEDOTs and PEDOT: PSS in energy conversion and storage devices," J.Mater.Sci.: Mater.Electron. 26 (7), 4438-4462 (2015).

118. Bettina Friedel *et al.*, "Effects of layer thickness and annealing of PEDOT: PSS layers in organic photodetectors," Macromolecules 42 (17), 6741-6747 (2009).

119. M. Vogel *et al.*, "On the function of a bathocuproine buffer layer in organic photovoltaic cells," Appl.Phys.Lett. 89 (16), 163501 (2006).

120. Y. M. Kim *et al.*, "Combining Vacuum Deposited with Solution Processed Layers in Organic Solar Cell," Clean Technology , 69-71 (2010).

121. Chen Tao *et al.*, "Semitransparent inverted polymer solar cells with MoO3/Ag/MoO3 as transparent electrode," Applied Physics Letters 95 (5), 53303 (2009).

122. D. -T Nguyen *et al.*, "Effect of the thickness of the MoO3 layers on optical properties of MoO3/Ag/MoO3 multilayer structures," Journal of Applied Physics 112 (6), 63505 (2012).

123. M. N. Polyanskiy, "Refractive Index Database," *https://refractive index.info*, (2018).

124. Steven K. Hau *et al.*, "Indium tin oxide-free semi-transparent inverted polymer solar cells using conducting polymer as both bottom and top electrodes," Organic Electronics 10 (7), 1401-1407 (2009).

125. Xiaoqin Zhang *et al.*, "Highly conductive PEDOT: PSS transparent electrode prepared by a post-spin-rinsing method for efficient ITO-free polymer solar cells," Solar Energy Mater.Solar Cells 144, 143-149 (2016).

126. Yinhua Zhou *et al.*, "Optimization of a polymer top electrode for inverted semitransparent organic solar cells," Organic Electronics 12 (5), 827-831 (2011).

127. Richard BM Schasfoort, Handbook of surface plasmon resonance, (Royal Society of Chemistry, 2017).

128. J. R. Sambles, G. W. Bradbery and Fuzi Yang, "Optical excitation of surface plasmons: an introduction," Contemporary physics 32 (3), 173-183 (1991).

129. J. M. Pitarke *et al.*, "Theory of surface plasmons and surface-plasmon polaritons," Reports on progress in physics 70 (1), 1 (2006).

130. Frank L. Pedrotti, Leno M. Pedrotti and Leno S. Pedrotti, <u>Introduction to optics</u>, 3rd ed., (Pearson Prentice Hall, Upper Saddle River, NJ, 2007).

131. David J. Griffiths, <u>Introduction to electrodynamics</u>, 4th ed., (Pearson, Harlow, Essex, 2014).

132. E. I. Wei, Wallace CH Choy and Weng Cho Chew, "A comprehensive study for the plasmonic thin-film solar cell with periodic structure," Optics express 18 (6), 5993-6007 (2010).

133. Robert Martin Eisberg and Robert Resnick, <u>Quantum physics of atoms, molecules, solids, nuclei, and particles</u>, 2nd ed., (Wiley, New York u.a, 1985).

134. Anatoly V. Zayats, Igor I. Smolyaninov and Alexei A. Maradudin, "Nano-optics of surface plasmon polaritons," Physics reports 408 (3-4), 131-314 (2005).

135. Murray R. Spiegel, Seymour Lipschutz and John Liu, <u>Mathematical handbook of formulas and tables</u>, 4th ed., (McGraw-Hill, New York, NY [u.a.], 2013).

136. Tatsuya Fujino, Sergei Yu Arzhantsev and Tahei Tahara, "Femtosecond/Picosecond Time-Resolved Spectroscopy of trans-Azobenzene: Isomerization Mechanism Following S2 ($\pi\pi^*$)← S0Photoexcitation," Bull.Chem.Soc.Jpn. 75 (5), 1031-1040 (2002).

137. B. Bellini *et al.*, "Light-induced molecular motion of azobenzene-containing molecules: a random-walk model," Journal of Physics: Condensed Matter 18 (33), S1817 (2006).

138. Cristina Cojocariu and Paul Rochon, "Light-induced motions in azobenzene-containing polymers," Pure and applied chemistry 76 (7-8), 1479-1497 (2004).

139. M. Saphiannikova, V. Toshchevikov and J. Ilnytskyi, "Photoinduced Deformations in AzobenzenePolymer Films," Nonlinear Optics and Quantum Optics 41, 27-57 (2010).

140. H. Seidel *et al.*, "Anisotropic etching of crystalline silicon in alkaline solutions I. Orientation dependence and behavior of passivation layers," J.Electrochem.Soc. 137 (11), 3612-3626 (1990).

141. Eli Yablonovitch, "Statistical ray optics," JOSA 72 (7), 899-907 (1982).

142. Zongfu Yu, Aaswath Raman and Shanhui Fan, "Fundamental limit of nanophotonic light trapping in solar cells," Proceedings of the National Academy of Sciences 107 (41), 17491-17496 (2010).

143. H. E. Bennett and J. O. Porteus, "Relation between surface roughness and specular reflectance at normal incidence," JOSA 51 (2), 123-129 (1961).

144. Anis Rahman, "Poledfilm1," (2007).

145. Micol Alemani *et al.*, "Electric field-induced isomerization of azobenzene by STM," J.Am.Chem.Soc. 128 (45), 14446-14447 (2006).

146. Andrzej Miniewicz *et al.*, "On optical phase conjugation in polystyrene films containing the azobenzene dye Disperse Red 1," Pure and Applied Optics: Journal of the European Optical Society Part A 7 (4), 709 (1998).

147. Adriana Galvan-Gonzalez *et al.*, "Photodegradation of azobenzene nonlinear optical chromophores: the influence of structure and environment," JOSA B 17 (12), 1992-2000 (2000).

148. Adriana Galvan-Gonzalez *et al.*, "Effect of temperature and atmospheric environment on the photodegradation of some Disperse Red 1–type polymers," Opt.Lett. 24 (23), 1741-1743 (1999).

149. Natalie Wagner and Patrick Theato, "Light-induced wettability changes on polymer surfaces," Polymer 55 (16), 3436-3453 (2014).

150. Leonhard H. Urner *et al.*, "Online monitoring the isomerization of an azobenzene-based dendritic bolaamphiphile using ion mobility-mass spectrometry," Chemical Communications 51 (42), 8801-8804 (2015).

151. Xiaojuan Yu *et al.*, "cis-to-trans isomerization of azobenzene investigated by using thin films of metal–organic frameworks," Physical Chemistry Chemical Physics 17 (35), 22721-22725 (2015).

152. Tatsumi Kimura *et al.*, "UV-curable azobenzene polymer bearing photo-crosslinkable moiety for stabilization of photo-fabricated surface relief structure," Macromolecular Chemistry and Physics 203 (16), 2344-2350 (2002).

153. Hideaki Takase, Almeria Natansohn and Paul Rochon, "Immobilization of Surface Relief Gratings and Poled Alignment in Amorphous Azobenzene-containing Polymers by Photopolymerization," Journal of Photopolymer Science and Technology 14 (2), 189-192 (2001).

154. Hideaki Takase, Almeria Natansohn and Paul Rochon, "Photocrosslinked surface relief gratings on azobenzene-containing copolymer films," Polymer 44 (24), 7345-7351 (2003).

155. Robert Kirby *et al.*, "Disperse and disordered: a mexylaminotriazine-substituted azobenzene derivative with superior glass and surface relief grating formation," J. Mater. Chem. C 2 (5), 841-847 (2014).

156. "E927 Standard Specification for Solar Simulation for Photovoltaic Testing," (2015).

157. Wujun Wang and Björn Laumert, "Simulate a 'Sun' for Solar Research," (2014).

158. Vishal Shrotriya *et al.*, "Accurate measurement and characterization of organic solar cells," Advanced Functional Materials 16 (15), 2016-2023 (2006).

159. Gabriela E. Bunea *et al.*, in <u>2006 IEEE 4th World Conference on Photovoltaic Energy Conference</u>, (IEEE, 2006) pp. 1312-1314.

160. Ingo Riedel *et al.*, "Effect of Temperature and Illumination on the Electrical Characteristics of Polymer–Fullerene Bulk-Heterojunction Solar Cells," Advanced Functional Materials 14 (1), 38-44 (2004).

161. E. A. Katz *et al.*, "Temperature dependence for the photovoltaic device parameters of polymer-fullerene solar cells under operating conditions," J.Appl.Phys. 90 (10), 5343-5350 (2001).

162. Dhritiman Gupta, Sabyasachi Mukhopadhyay and K. S. Narayan, "Fill factor in organic solar cells," Solar Energy Mater.Solar Cells 94 (8), 1309-1313 (2010).

163. Alexander L. Ayzner *et al.*, "Reappraising the need for bulk heterojunctions in polymer−fullerene photovoltaics: the role of carrier transport in all-solution-processed P3HT/PCBM bilayer solar cells," The Journal of Physical Chemistry C 113 (46), 20050-20060 (2009).

164. Jordan C. Aguirre *et al.*, "Sequential Processing for Organic Photovoltaics: Design Rules for Morphology Control by Tailored Semi-Orthogonal Solvent Blends," Advanced Energy Materials 5 (11), 1402020 (2015).

165. Shilin Chen *et al.*, "Effect of preparation parameters on performance of P3HT: PCBM solar cells," Materials Science in Semiconductor Processing 39, 441-446 (2015).

166. "PEDOT:PSS," *https://www.ossila.com/products/pedot-pss*, accessed on 2019-02-15.

167. Raymond Serway, <u>Princples of Physics</u>, 2nd ed., (Saunders College Pub, Fort Worth, Texas, 1998).

168. Dhritiman Gupta, Martijn M. Wienk and René AJ Janssen, "Efficient polymer solar cells on opaque substrates with a laminated PEDOT: PSS top electrode," Advanced Energy Materials 3 (6), 782-787 (2013).

169. Yinhua Zhou *et al.*, "Efficient recyclable organic solar cells on cellulose nanocrystal substrates with a conducting polymer top electrode deposited by film-transfer lamination," Organic Electronics 15 (3), 661-666 (2014).

170. Jaana Vapaavuori *et al.*, "Submolecular plasticization induced by photons in azobenzene materials," J.Am.Chem.Soc. 137 (42), 13510-13517 (2015).

171. Bertrand Tremolet de Villers *et al.*, "Improving the reproducibility of P3HT: PCBM solar cells by controlling the PCBM/cathode interface," The Journal of Physical Chemistry C 113 (44), 18978-18982 (2009).

172. Seungkeun Choi, William J. Potscavage Jr and Bernard Kippelen, "Area-scaling of organic solar cells," J.Appl.Phys. 106 (5), 054507 (2009).

173. Dhritiman Gupta, Monojit Bag and K. S. Narayan, "Area dependent efficiency of organic solar cells," Appl.Phys.Lett. 93 (16), 384 (2008).

174. A. J. Trindade and L. Pereira, "Bulk heterojunction organic solar cell area-dependent parameter fluctuation," International Journal of Photoenergy 2017, (2017).

175. Yong-Jin Noh, Seok-In Na and Seok-Soon Kim, "Inverted polymer solar cells including ZnO electron transport layer fabricated by facile spray pyrolysis," Solar Energy Mater.Solar Cells 117, 139-144 (2013).

176. Zhicai He *et al.*, "Enhanced power-conversion efficiency in polymer solar cells using an inverted device structure," Nature photonics 6 (9), 591 (2012).

177. Wolfgang Tress *et al.*, "Understanding the rate-dependent J–V hysteresis, slow time component, and aging in CH 3 NH 3 PbI 3 perovskite solar cells: the role of a compensated electric field," Energy & Environmental Science 8 (3), 995-1004 (2015).

178. Henry J. Snaith, "The perils of solar cell efficiency measurements," Nature Photonics 6 (6), 337 (2012).

179. George Alexandru Nemnes *et al.*, "How measurement protocols influence the dynamic JV characteristics of perovskite solar cells: Theory and experiment," Solar Energy 173, 976-983 (2018).

180. GAH Wetzelaer *et al.*, "Origin of the dark-current ideality factor in polymer: fullerene bulk heterojunction solar cells," Appl.Phys.Lett. 99 (15), 153506 (2011).

181. J. Salinger, "Measurement of solar cell parameters with dark forward IV characteristics," Acta Polytechnica 46 (4), (2006).

182. Pablo P. Boix *et al.*, "Current-Voltage Characteristics of Bulk Heterojunction Organic Solar Cells: Connection Between Light and Dark Curves," Advanced Energy Materials 1 (6), 1073-1078 (2011).

183. A. G. Aberle, S. R. Wenham and M. A. Green, in <u>Conference Record of the Twenty Third IEEE Photovoltaic Specialists Conference-1993 (Cat. No. 93CH3283-9)</u>, Anonymous (IEEE, 1993) pp. 133-139.

184. Kenji Kawano *et al.*, "Degradation of organic solar cells due to air exposure," Solar Energy Materials and Solar Cells 90 (20), 3520-3530 (2006).

185. James Leibold and Ribal Georges Sabat, "Laser-induced controllable chirped-pitch circular surface-relief diffraction gratings on AZO glass," Photonics Research 3 (4), 158-163 (2015).

186. Erin Bailey and Ribal Georges Sabat, "Surface plasmon bandwidth increase using chirped-pitch linear diffraction gratings," Optics express 25 (6), 6904-6913 (2017).

187. Il Jeon *et al.*, "Air-processed inverted organic solar cells utilizing a 2-aminoethanol-stabilized ZnO nanoparticle electron transport layer that requires no thermal annealing," Journal of Materials Chemistry A 2 (44), 18754-18760 (2014).

188. Hua-Hsien Liao *et al.*, "Highly efficient inverted polymer solar cell by low temperature annealing of Cs 2 CO 3 interlayer," Appl.Phys.Lett. 92 (17), 156 (2008).

189. Leila Mazaheri *et al.*, "Unraveling the nucleation and growth of spontaneous surface relief gratings," Optical Materials 62, 378-391 (2016).

190. Hui Li *et al.*, "Thermostable single-junction organic solar cells with a power conversion efficiency of 14.62%," Sci.Bull 63 (6), 340-342 (2018).